

d-Block-p-Block Element Synergy for the Development of High-Performance Heterogeneous Catalysts

Zur Erlangung des akademischen Grades eines

DOKTORS DER NATURWISSENSCHAFTEN

(Dr. rer. nat.)

von der KIT-Fakultät für Chemie und Biowissenschaften

des Karlsruher Instituts für Technologie (KIT)

genehmigte

DISSERTATION

Von

Arjun Neyyathala

1. Referentin: TT.-Prof. Dr. Schirin Hanf

2. Referent: Prof. Dr. Jan-Dierk Grunwaldt

Tag der mündlichen Prüfung: 17.07.2025



This document is licensed under a Creative Commons Attribution 4.0 International License (CC BY 4.0): <https://creativecommons.org/licenses/by/4.0/deed.en>

Declaration

The work in this dissertation was carried out in the Institute for Inorganic Chemistry at the Karlsruhe Institute of Technology under the supervision of TT.-Prof. Schirin Hanf between December 2021 and June 2025. I, Arjun Neyyathala, declare that I have completed the present thesis independently and without illegitimate assistance from third parties. I have used no other than the specified sources and aids. The thesis has not been submitted to any examination body in this, or similar, form.

Karlsruhe,

City, Date

Signature

Abstract

The development of high-performing heterogeneous catalysts is of great industrial importance, as homogeneous catalysts, despite their typically encountered high activity and selectivity, face significant challenges, such as a difficult separation, limited reusability, and product contamination, which hinder their practical application. While supported or bulk transition metal nanoparticles are well-established as heterogeneous catalysts, which can enable a facile catalyst separation and reuse, they often suffer from limited activity, selectivity, and stability. A promising strategy to overcome these limitations involves incorporating a secondary element, such as a p-block element, into the crystal structure of the metal to form well defined binary-phase nanoparticles. In this work, supported catalysts were synthesized by applying this so-called “d-block-p-block element combination strategy” and evaluated for their catalytic performance in four different industrially relevant catalytic reactions. The catalysts exhibited promising performance across all reactions, which demonstrated the effectiveness of this approach. Additionally, through the modification of the support material with phosphorus, an approach referred to as support engineering, an improved metal leaching resistance could be achieved.

In chapter 3, silica-supported Pd_3P nanoparticles were synthesized and characterized by various analytic methods. The application of this catalyst in the Wacker-Tsuji oxidation of styrene, evaluated across four different reaction systems, led to promising results in terms of activity and selectivity. A comparison with a conventionally used supported Pd catalyst demonstrated the superior performance of the supported Pd_3P catalyst.

To overcome the metal leaching observed in the Wacker-Tsuji oxidation reactions, in chapter 4, the suppression of Pd leaching in the Heck coupling reaction is described through the deposition of Pd_3P nanoparticles on phosphorus-modified silica supports. Through this support engineering approach, a reduction in Pd leaching of up to 85 % was achieved compared to a Pd reference catalyst on an unmodified support. The enhanced leaching resistance can be attributed to a combined effect: anchoring of the nanoparticles by the phosphorus species present on the support and the stabilization of Pd provided by phosphorus within the crystal lattice.

In chapter 5, the supported Pd_3P catalyst was applied in alkoxy carbonylation reactions and has shown exceptional activity, outperforming many previously reported homogeneous and heterogeneous catalysts. The incorporation of phosphorus into palladium hereby led to more than a two-fold increase in the catalytic activity compared to the Pd-based reference catalyst.

In chapter 6, the hydroformylation of styrene using supported rhodium sulfide nanoparticles as catalysts revealed a phase-dependent activity trend, following the order $\text{Rh}_{17}\text{S}_{15} > \text{Rh}_2\text{S}_3 > \text{Rh}$. The surface structures of the catalysts were investigated using a combination of machine

learning and DFT calculations, and provided key insights into the observed differences in catalytic activity, which mainly result from the formation of spatially isolated Rh sites in $\text{Rh}_{17}\text{S}_{15}$. The superior activity and selectivity presented in these chapters from the d-block-p-block element combination catalysts, namely supported Pd_3P and supported $\text{Rh}_{17}\text{S}_{15}$, can be attributed to the formation of isolated active metal sites on the surface with tailored geometric and electronic properties induced by the incorporation of p-block elements into metal matrices. This strategy, combined with the support-engineering approach, has proven to be highly effective for developing high-performance catalysts in a variety of liquid-phase catalytic reactions.

Kurzzusammenfassung

Die Entwicklung leistungsfähiger heterogener Katalysatoren ist von großer industrieller Relevanz, da die mit homogenen Katalysatoren verbundenen Herausforderungen, wie etwa deren schwierige Abtrennung, eingeschränkte Wiederverwendbarkeit und potenzielle Produktkontamination, die breite Anwendung in industriellen Prozessen trotz hoher Aktivität und Selektivität erheblich einschränken. Obwohl der Einsatz von geträgerten oder ungeträgeren Übergangsmetallnanopartikeln als heterogene Katalysatoren, die eine einfache Trennung und Wiederverwertung ermöglichen, weitgehend etabliert ist, wird ihre Leistungsfähigkeit häufig durch eine begrenzte Aktivität, Selektivität und Stabilität limitiert. Eine effektive Strategie zur Leistungssteigerung von Übergangsmetallkatalysatoren besteht darin, ein zusätzliches Element, z.B. ein p-Block-Element, in die Kristallstruktur des Metalls zu integrieren, um wohldefinierte und phasenreine Nanopartikel zu bilden, ein Ansatz, der als “d-Block-p-Block-Element-Kombinationsstrategie“ bezeichnet wird. In dieser Arbeit wurden Katalysatoren gemäß diesem Prinzip hergestellt, auf Trägermaterialien aufgebracht und in vier industriell relevanten organischen Reaktionen hinsichtlich ihrer katalytischen Leistungsfähigkeit untersucht. Die Ergebnisse aller getesteten Systeme zeigten eine vielversprechende katalytische Leistung, was den Erfolg dieses strategischen Ansatzes unterstreicht. Darüber hinaus wurde durch die Modifizierung des Trägermaterials mit Phosphor (sogenanntes Support-Engineering) eine signifikante Verbesserung der Katalysatorstabilität in verschiedenen Reaktionssystemen erreicht.

Kapitel 3 beschreibt die Synthese von Pd_3P -Nanopartikeln auf Siliciumdioxid, sowie deren Charakterisierung mittels verschiedener analytischer Methoden. Der Einsatz dieses Katalysators in vier unterschiedlichen Reaktionssystemen in der Wacker-Tsuji-Oxidation von Styrol führte zu vielversprechenden Ergebnissen in Bezug auf Aktivität und Selektivität. Im Vergleich zu einem herkömmlichen geträgerten Pd-Katalysator zeigte Pd_3P eine deutlich überlegene Leistung.

Um den, in der Oxidationskatalyse beobachteten, Metallverlust vom Trägermaterial entgegenzuwerden, befasst sich Kapitel 4 mit der Unterdrückung des Palladiumverlusts in der Heck-Kupplungsreaktion durch den Einsatz von Pd_3P -Nanopartikeln auf phosphormodifizierten Siliciumdioxid. Durch diesen Support-Engineering-Ansatz konnte eine Reduktion des Metallverlusts um bis zu 85 % im Vergleich zum reinen Pd-Katalysator auf unmodifiziertem Trägermaterial erzielt werden.

Kapitel 5 zeigt, dass der geträgerte Pd_3P -Katalysator außergewöhnlich hohe Aktivitäten in der Alkoxy carbonylierung von Iodbenzol aufweist und dabei viele bisher publizierte homogene und heterogene Katalysatoren übertrifft. Die Einbindung von Phosphor führte zu mehr als einer Aktivitätsverdopplung im Vergleich zum reinen Pd-basierten Katalysator.

Kapitel 6 behandelt die Hydroformylierung von Styrol unter Verwendung von geträgerten Rhodiumsulfid-Nanopartikeln. Hierbei wurde ein phasenabhängiger Aktivitätstrend beobachtet: $\text{Rh}_{17}\text{S}_{15} > \text{Rh}_2\text{S}_3 > \text{Rh}$. Die Oberflächenstrukturen der Katalysatoren wurden mithilfe einer Kombination aus maschinellem Lernen und DFT-Rechnungen analysiert, wodurch entscheidende Einblicke in die beobachteten Unterschiede in der katalytischen Aktivität gewonnen wurden. Diese Unterschiede basieren hauptsächlich auf der Bildung von räumlich isolierten Rh-Zentren in $\text{Rh}_{17}\text{S}_{15}$.

Die überlegene Aktivität und Selektivität der d-Block-p-Block-Element-Kombinationskatalysatoren, insbesondere von Pd_3P und $\text{Rh}_{17}\text{S}_{15}$, ist auf die Bildung isolierter aktiver Zentren mit maßgeschneiderten geometrischen und elektronischen Eigenschaften zurückzuführen, die durch die Integration von p-Block-Elementen in Metalle induziert werden.

Die in diesen Kapiteln dargestellte überlegene Aktivität und Selektivität der Katalysatoren auf Basis der d-Block-p-Block-Elementkombination, insbesondere auf der Basis von Pd_3P und $\text{Rh}_{17}\text{S}_{15}$, lässt sich auf die Bildung isolierter aktiver Metallzentren an der Oberfläche zurückführen. Diese Oberflächenzentren weisen maßgeschneiderte geometrische und elektronische Eigenschaften auf, die durch die Einbindung von p-Block-Elementen in Metallmatrices hervorgerufen werden. Diese Strategie, in Kombination mit einem Support-Engineering-Ansatz, hat sich als äußerst effektiv für die Entwicklung leistungsfähiger Katalysatoren in einer Vielzahl flüssigphasenbasierter katalytischer Reaktionen erwiesen.

Contents

1	Introduction	4
1.1	Element synergy in heterogeneous catalysis.....	5
1.1.1	Heterogenized catalysts through p-block element incorporation	6
1.1.2	Metal phosphides and sulfides in catalysis	10
1.2	Stability enhancement of supported catalysts in liquid-phase reactions.....	13
1.3	Heterogeneous catalysis in oxidation and C–C bond formation reactions.....	14
1.3.1	Wacker-Tsuji oxidation	15
1.3.2	Heck coupling reaction	17
1.3.3	Alkoxycarbonylation reaction.....	20
1.3.4	Hydroformylation reaction	22
2	Project aims	26
3	Supported palladium phosphides as oxidation catalysts	28
3.1	Synthesis and characterization Pd _x P _y /SiO ₂	28
3.2	Catalytic performance in the Wacker-Tsuji oxidation	34
3.3	Theoretical insight into the activity improvement	40
3.4	Concluding remarks	42
4	Support engineering for Heck coupling reactions.....	43
4.1	Synthesis and characterization of palladium phosphide on phosphorus-modified supports.....	43
4.2	Catalytic performance in the Heck coupling reaction	49
4.3	Catalyst stability and leaching investigations	53
4.4	Theoretical insights into the stability and activity improvement	59
4.5	Concluding remarks	61
5	Alkoxycarbonylation reactions with supported palladium phosphide nanoparticles	63
5.1	Synthesis and characterization of Pd _x P _y /SiO ₂	63
5.2	Catalytic performance in the alkoxycarbonylation of aryl halides	66
5.3	Recovery and stability tests	74
5.4	Theoretical investigations of structure-activity relationships.....	75

5.5	Concluding remarks	77
6	Olefin hydroformylation reactions with supported rhodium sulfide nanoparticles	78
6.1	Synthesis and characterization of $\text{Rh}_x\text{S}_y/\text{SiO}_2$	79
6.2	Catalytic performance in olefin hydroformylation reactions	88
6.3	Recovery and stability tests.....	97
6.4	Theoretical investigations into Rh surface motifs.....	100
6.5	Concluding remarks	104
7	Conclusions and outlook	105
8	Experimental details	109
8.1	Material characterization techniques	109
8.2	Synthesis of materials	113
8.2.1	Chemicals	113
8.2.2	Preparation of phosphorus-modified supports	113
8.2.3	Synthesis of supported Pd_xP_y nanoparticles	113
8.2.4	Synthesis of supported Rh_xS_y nanoparticles	114
8.3	Catalyst testing procedures	115
8.3.1	General procedure for the Wacker Tsuji oxidation reactions.....	115
8.3.2	General procedure for Heck coupling reactions.....	116
8.3.3	General procedure for alkoxy carbonylation reactions	116
8.3.4	General procedure for hydroformylation reactions.....	116
8.3.5	Catalyst recovery tests	116
8.3.6	Filtration tests.....	117
8.3.7	GC-MS analysis of the reaction products	117
8.4	Estimation of performance parameters.....	118
8.5	Theoretical calculations	118
9	References.....	120
10	Appendix	137
10.1	Chapter 3: Supported palladium phosphides as oxidation catalysts	137
10.2	Chapter 4: Support engineering for Heck coupling reactions	139

10.3 Chapter 5: Alkoxycarbonylation reactions with supported palladium phosphide nanoparticles	146
10.4 Chapter 6: Olefin hydroformylation reactions with supported rhodium sulfide nanoparticles	150
11 Abbreviations	174
12 Personal data	176
12.1 Curriculum vitae	176
12.2 Attended conferences	177
12.3 List of publications and patents	177
13 Acknowledgements	179

1 Introduction

The development of high-performing catalysts is crucial in both academic and industrial contexts, since over 90 % of industrial processes, which are involved in producing fuels, fine chemicals, medicines, fertilizers, rely on catalytic reactions.^[1,2] Therefore, the development of active, selective, and stable catalysts is of significant importance. In this context, transition metal complexes have demonstrated exceptional activity and selectivity as homogeneous catalysts, primarily due to the tunability of the metal center's through tailored ligand systems and the formation of highly defined active sites.^[1,3] Beside the high catalytic activity and selectivity of homogenous catalysts, such systems are often difficult to separate from the reaction system after the reaction, thereby posing significant challenges in terms of large scale industrial application. Moreover, potential metal contaminations caused by homogeneous catalysts, can have serious implications for products related to life sciences.^[1] Therefore, the development of solid-state catalysts, also referred to as heterogeneous catalysts, depending on the reaction medium, are dominating the market of technically relevant catalysts. Such catalysts enable a facile catalyst recovery from the reaction mixture and reuse, and therefore promote industrial usage.

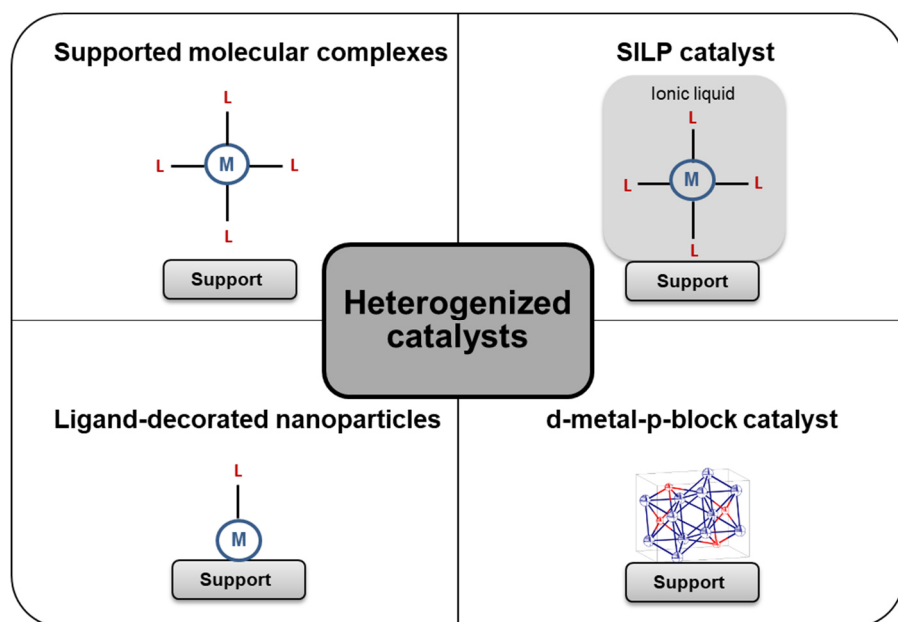


Figure 1: Strategies for combining the benefits of homogeneous and heterogeneous catalysis *via* heterogenized catalysts. L = ligand, SILP = supported ionic liquid phase.

Commonly used heterogeneous catalysts span a broad range of materials, such as porous materials (metal organic framework, zeolite, oxides, etc.),^[4–6] supported nanoparticles,^[7] bulk catalysts^[8] and structured catalysts.^[9] However, such heterogeneous systems often suffer from inherent limitations with respect to their catalytic activity and selectivity, due to the restricted tunability of their active metal centres.^[3,10] Also, in contrast to homogeneous catalysts, where

all metal atoms can potentially participate in the catalytic transformation, only a fraction of the surface metal centers in heterogeneous catalysts are typically involved in the catalytic cycle.^[11]

These pros and cons associated with homogeneous and heterogeneous systems initiated the approach for combining the benefits of both and developing so-called “heterogenized catalysts” (Figure 1).^[12,13] Several strategies have been reported for the implementation of this concept, such as the anchoring molecular complexes on supports,^[13,14] supported ionic liquid phase (SILP) catalysts,^[15,16] and ligand-decorated nanoparticles.^[17,18] These methods aim to create well-defined, substrate-accessible active sites, while simultaneously modulating the electronic structure of the metal center to tailor catalytic behavior and facilitate a facile catalyst recovery and reuse.

An alternative approach in the context of heterogenized catalysts involves the incorporation of a p-block element, such as P, S, Ga, or Sb, with a catalytically active transition metal, an approach which is referred to as “d-block-p-block element combination strategy”. The introduction of a secondary p-block element enables the electronic and geometric modulation of the metal center, influencing catalytic performance in a similar manner to that of a ligand in homogeneous catalysts. Several catalysts have been reported in this context, such as intermetallic compounds,^[19] alloys,^[20] metal chalcogenides,^[21] and pnictogenides^[22]. These catalysts exhibit significantly enhanced activity or selectivity compared to pure transition metal-based systems, primarily due to the tailored adsorption properties of substrates and reaction intermediates on the active sites at the surface.^[23–25]

1.1 Element synergy in heterogeneous catalysis

Element synergy in heterogeneous catalysis refers to the design and application of solid-state catalysts composed of two or more elements, which are integrated in the same crystal structure. The incorporation of a second element alongside the active metal to form a binary phase can significantly influence the catalytic performance compared to catalysts based solely on the pure metal.

For the description of such systems the concept of phases is an important aspect, since phases provide an insight into the structure, the properties and the application of materials. A phase is generally defined as a portion of matter, which is homogeneous and can be mechanically subdivided to portions, which are indistinguishable.^[26] Phases are typically characterized by their crystal structure, thermodynamic stability, and bonding characteristics, and can comprise one or more elements. Phases composed of multiple elements offer significant potential, as the properties of one element can be enhanced by carefully selecting suitable partner elements and tuning their compositions.^[27,28] In this context, combining a metal with another metal is particularly interesting, as it can lead to the formation of alloys or intermetallic compounds with tailored properties. For example, combining titanium (Ti) with gold (Au) to form the intermetallic

phase Ti_3Au , can result in a fourfold increase in hardness value compared to pure titanium. This is attributed to the short Ti–Au bond length in the crystal, the pseudo gap formation and an increase in the valance electron density.^[27] Similarly, the intermetallic compound composed of Fe and Ni, Fe_3Ni (invar), has a very low thermal coefficient of expansion (1.2 ppm/°C), which is approximately 10 times lower in comparison to commonly used steel materials. This property enables the use of invar for the manufacturing of precision devices, such as watches, delicate gauges or clocks.^[28] Just as phases can form through metal–metal interactions, various metal and non-metal combinations can also lead to the formation of distinct phases. One well-studied example is the iron–carbon (Fe–C) system, in which various structures can be obtained by altering the temperature and composition, thereby enabling a wide range of applications.^[29] Similarly, the incorporation of elements, such as phosphorus or sulfur into a metal matrix, resulting in the formation of binary phases, more precisely metal phosphides or sulfides, has also gained significant attention.^[24,30] These materials are particularly interesting because their metallic character (band gap) can be finely tuned by adjusting the metal to non-metal ratio. A notable application in the field of energy storage is the use of metal sulfides (M_xS_y) and phosphides (M_xP_y) as electrode materials for supercapacitor applications, due to their higher electrical conductivity, enhanced redox properties and theoretical capacitance in comparison to the commonly used oxide counterparts.^[31,32]

All the examples discussed above underscore the importance of phase formation achieved through the incorporation of secondary elements, as this approach allows for a precise tuning of the material properties and extends their applicability across a wide range of fields. In this context, phase diagrams serve as a pivotal tool for understanding the thermodynamic stability, synthesis conditions, and equilibrium reactions connected with different phases.^[33] Additionally, phase stability diagrams provide information about the thermodynamic stability of phases by plotting the calculated formation energies as a function of the phase composition. In these diagrams a convex hull is constructed by connecting the energies of all thermodynamically stable (ground state) phases. The energy above this convex hull is a key descriptor for assessing the phase stability and the subsequent synthetic accessibility. A value of energy above hull zero indicates a phase that lies on the convex hull and is thus thermodynamically stable, while higher values indicate metastable or unstable phases.^[33] With the assistance of both crystal structure information and phase stability data, researchers can design and synthesize materials with targeted properties for specific applications.

1.1.1 Heterogenized catalysts through p-block element incorporation

As mentioned before, an effective strategy for the development of heterogeneous catalysts involves the incorporation of a secondary element alongside the active metal (element synergy), potentially forming a new binary phase. In particular, the incorporation of p-block elements has gained significant attention, as some of these elements can effectively tailor the

catalytic performance of the active metal through both geometric and electronic modifications. In this regard, palladium–gallium (Pd_xGa_y)^[34] and nickel–gallium (Ni_xGa_y)^[35] intermetallic systems have been extensively studied in semi-hydrogenation reactions, demonstrating superior catalytic performance driven by element synergy. Notably, Pd_3Ga_7 , $PdGa$, and Pd_2Ga exhibited exceptional selectivity for the semi-hydrogenation of acetylene, surpassing established catalysts,^[34] while Ni_3Ga , Ni_5Ga_3 , and $NiGa$ nanoparticles showed remarkable selectivity in the semi-hydrogenation of phenyl acetylene.^[35] Beside the activity and selectivity enhancement, the incorporation of a p-block element into the metal matrix can reduce the noble metal content, thereby contributing to more sustainable use of scarce metal resources.

One key feature of materials prepared through element synergy is the potential formation of distinct active sites on the surface, facilitated by the site isolation imparted by the secondary element. These well-defined active sites can occur as single atoms or atom ensembles, with the p-block element providing the separation. Moreover, charge transfer between the elements can significantly modify the electronic structure of the metal centers, which is a key difference in comparison to pure metal-based systems.^[23,24,30] These effects are similar to the behavior seen in metal complexes used as homogeneous catalysts, where interactions between the metal centre and ligands influence the underlying catalytic properties. Hence, the major impact of element synergy relevant to catalysis are geometric and electronic effects, as depicted in Figure 2. The geometric effects can be categorized into ensemble, ordering, and steric effects, while the electronic effects are primarily classified as ligand and strain contributions.^[23]

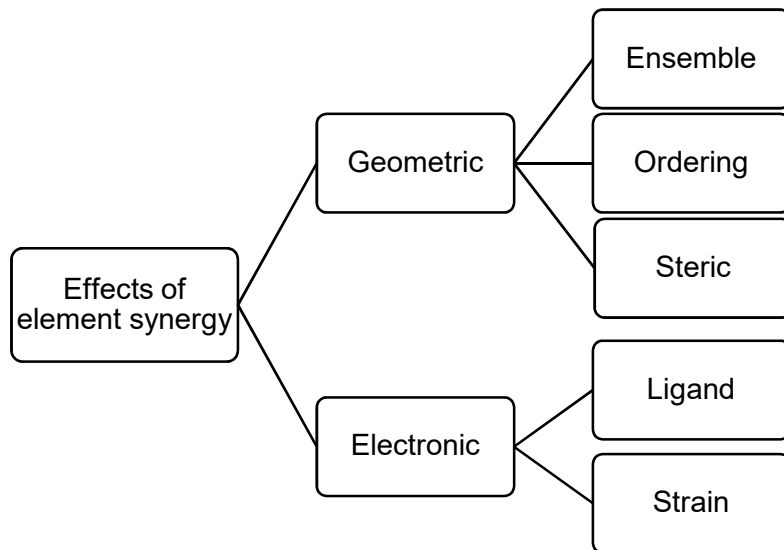


Figure 2: Various effects relevant to catalysis achieved through element synergy.^[23]

Ensembles are arrangements of similar atoms on the surface of the catalyst, which can potentially act as active sites. Their size, number of atoms and arrangement type can impact the adsorption of substrates, intermediates and products, thereby influencing the overall catalytic performance.^[36] Through alloying of a metal with a p-block element, the dilution of the

metal matrix is achieved thereby possibly creating such ensembles.^[23] These ensembles are often site isolated, due to the spacing created by the p-block element, and therefore also referred to as “frustrated single catalytic sites”, which is a well-known concept in homogeneous catalysis.^[12,30,37,38] The catalytic activity can also be tuned through controlling the size of such ensembles *via* tailored synthetic strategies.^[39] Recently, there have been examples reported, that show the importance of such surface motifs formed *via* d-block-p-block element synergy in catalysis. For example, the ensembles consisting of dimers and trimers in Pd_2Sn show exceptional activity and selectivity in the selective hydrogenation of acetylene.^[40] Similarly, the well-known Lindlar catalyst (Pd-Pb/CaCO_3) shows 2D isolated ensembles, which efficiently catalyze alkyne semi-hydrogenation reactions.^[41] In contrast, the solid solution of Pd_3Bi , with Pd ensembles constituted by more than 5 atoms show a lower activation energy for methanol oxidation.^[36] Some selected illustrative examples of ensembles from the literature are presented in Figure 3.

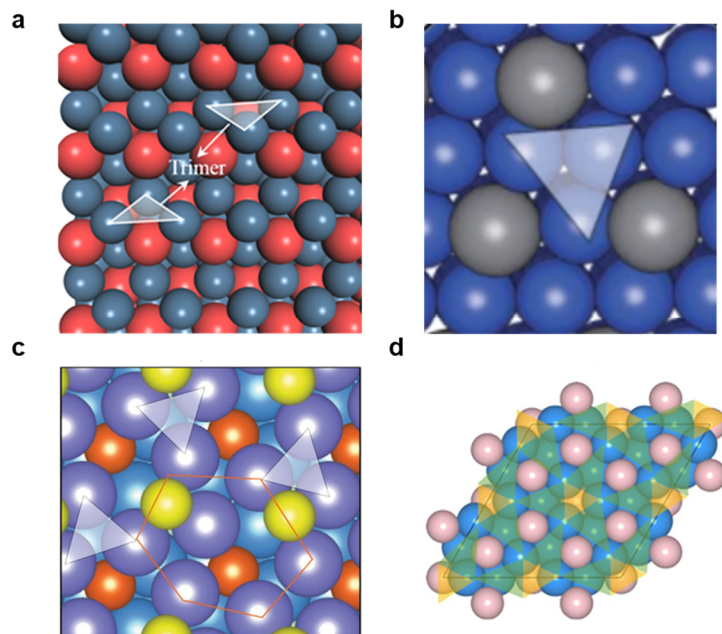


Figure 3: Some examples of ensembles reported in the literature present in a) Pd_2Sn ,^[40] b) PdPb ,^[21] c) Pd_3S ^[21] and d) Ni_2P ^[42] surfaces, which are relevant in the context of heterogeneous catalysis.

Ordering effects are present in both ordered and disordered structures. In alloys, the atomic arrangement is typically random, while in intermetallic compounds, the constituent atoms adopt a well-defined, ordered structure.^[43] These differences in atomic ordering often lead to variations in catalytic performance, primarily due to changes in the surface atomic configuration. This explains the change in activity or selectivity between intermetallic compounds and solid solutions that consist of the same elements and share identical compositions.^[23] The ordering effect is also evident in analogous element combinations, such as RhGa and RhGe intermetallic catalysts for propane dehydrogenation, where RhGa has

been reported to exhibit enhanced propylene selectivity compared to RhGe.^[44] The **steric effects** are caused by the difference in atomic sizes of the elements, leading to a hindrance in adsorption of the molecules or variation in diffusivity due to the separation of active metal centres.^[23] The enhanced activity observed for the Pd–Bi system during amine oxidation reactions can be attributed to such steric effects, resulting in a promotion of imine desorption.^[45]

Other important factors, which have an impact on the catalytic performance, are **electronic effects**, which alter the electronic structure of the active metal centers. This modulation can generally be categorized into **ligand effects** and **strain effects**.^[25] **Ligand effects**, named in analogy to concepts well-known in homogeneous catalysis, can be achieved by varying the neighboring atoms of the central metal atom, leading to changes in the metal center's electronic structure through local charge transfer processes.^[23,46] The local charge transfers arise from variations in electronegativity or work function of the constituent elements, whereby the presence of an electron-withdrawing counterpart enhances the cationic nature of the active metal.^[23] Thus formed cationic sites are indeed favorable for the adsorption and activation of species, such as alkenes, or nitro groups, which are electron rich in nature.^[23] For example, the exceptional performance of Pd₂Si supported on carbon nanotubes (CNT) in hydrodesulfurization reactions (higher activity in comparison to several commercially available catalysts) was attributed to an electron transfer from Pd to Si, rendering Pd more cationic.^[47] Such an effect on the catalyst surface can be analyzed through advanced analytic techniques, such as X-ray photoelectron spectroscopy (XPS), X-ray absorption near edge structure (XANES) or diffuse reflectance IR spectroscopy (DRIFT) in combination with theoretical interpretations based on quantum chemical calculations.^[23,48]

Furthermore, the incorporation of a secondary p-block element alters the d-band of the transition metal, thereby influencing its interaction with adsorbates. In this context, a widely used model for approximately describing the binding of adsorbate on transition metal surfaces is the d-band center model, which simplifies the d-state bands involved in bonding to a single energy level, known as the d-band center.^[49,50] The shift of the d-band center with respect to the Fermi level can be correlated to a variation in the binding energy of the adsorbate on the surface, thereby providing insight into the catalytic performance.^[49,50] During the chemisorption process, the valence state of the adsorbate interacts with the s- and d-states of the transition metal. The formed bond is governed by the extent to which the antibonding orbital, resulting from the interaction between the adsorbate and the metal d-states, is occupied.^[49,50] Since antibonding states always have higher energies than d-states, the bond strength can be effectively approximated by the relative position of the d-band center with respect to the Fermi level.^[49,50] An upward shift of the d-band center, which corresponds to higher energy levels of antibonding states relative to Fermi level, indicates a stronger adsorption or binding energy.^[49,50] Such shift of the d-band center can be induced by the alloying of a metal with

another element. For instance, alloying Sn with Co improves the electrocatalytic ammonia production by modifying the d-band center, which strengthens the NO_3^- adsorption and enhances the thermodynamic favourability of the reaction.^[51] Also, the alloying of Sn with Pt induces a downward shift in the d-band center as the Sn content increases, resulting in a weaker propyl and propylene binding on the catalyst surface, which results in a higher activation energy for the propylene dehydrogenation. This promotes the selective dehydrogenation of propane to propylene by suppressing other side reactions, including the further dehydrogenation to propyne.^[52]

Lattice strains, induced by the incorporation of a secondary element into a metal, can also modify the d-band structure. The strain from alloying increases the interatomic distance between metal atoms, thereby reducing the d-state overlap and narrowing the d-band. This narrowing leads to an upward shift of the d-band center relative to the Fermi level. Since this effect arises from both geometric modifications and electronic restructuring, strain effects can be considered at the intersection of geometric and electronic factors.^[23,53]

1.1.2 Metal phosphides and sulfides in catalysis

The exploitation of elemental synergy between d-block elements and phosphorus or sulfur has gained significant attention for the development of high-performance heterogeneous catalysts.^[54] By varying the metal to phosphorus or metal to sulfur ratio and exploring the structural diversity, the catalytic performance of such systems can be tailored to specific reactions.^[24]

Phosphine-based ligands are well known in homogeneous catalysis, with notable examples such as the Wilkinson catalyst for hydroformylation reactions, $[\text{RhCl}(\text{PPh}_3)_3]$,^[55] $[\text{Ni}(\text{PPh}_3)_4]$ in the presence of dppp (dppp: 1,3-bis(diphenylphosphino)propane) for Heck coupling reactions,^[56] palladium complexes with the ylide-substituted phosphines (YPhos ligand) for C–C and C–N coupling reactions,^[57,58] $[\text{PdCl}_2(\text{PPh}_3)_2]$ in carbonylation reactions,^[59] Even though these homogeneous catalysts exhibit excellent activity and selectivity, they pose inherent challenges in terms of catalyst separation and reuse.^[25] In order to overcome this challenge, the introduction of phosphorus into a metal matrix and the subsequent formation of metal phosphides, has been investigated (Figure 4). Through this approach the concept of molecular phosphine complexes can somehow be transferred to the solid-state. The incorporation of elemental phosphorus into the metal matrix modulates the binding energies of substrates and intermediates during catalysis. Moreover, phosphorus leads to the separation of the active sites (isolated sites) and also enables the fixation of metal atoms leading to an enhanced catalyst stability.^[24,25] Another important aspect of the metal phosphide surfaces is the formation of ensembles consisting of more than two metal atoms.^[24,42] Also, as mentioned

before, the (noble) metal content can be reduced through the incorporation of phosphorus, which is highly advantageous with respect to the limited availability of many metals.

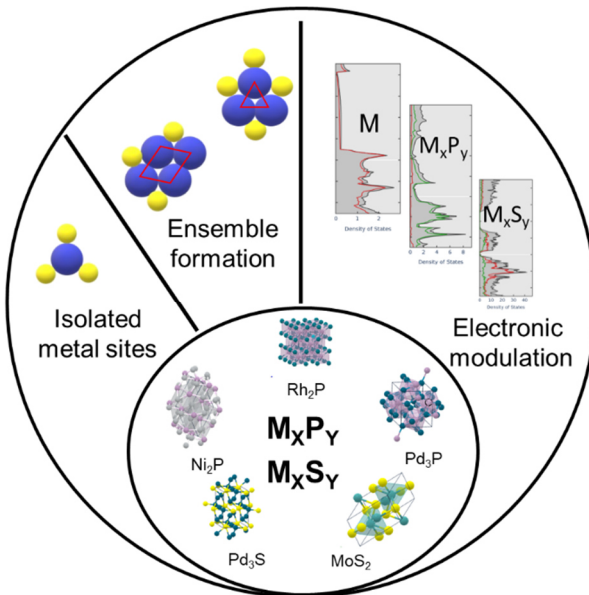


Figure 4: Schematic representation of the major effects relevant to catalysis in metal phosphides and sulfides. Crystal structure and DOS images taken from “The Materials Project”.^[33]

The application of metal phosphides in hydrotreating reactions has been investigated, especially for the phosphides of nickel, rhodium, palladium, molybdenum and cobalt.^[37] Through the decomposition of metal phosphine complexes, Habas *et al.*^[60] synthesized Ni₂P nanoparticles and applied them for the hydrodeoxygenation of acetic acid. Hereby, CO, CH₄ and H₂O were detected as the primary products. An important selectivity difference was observed when pure Ni was used instead of Ni₂P as the catalyst, where the primary products were H₂ and CO, due to the gasification of acetic acid. This selectivity difference already shows the substantial effect of P incorporation.^[60] Similarly, a comparison of the activity in the hydrodesulfurization (HDS) of dibenzothiophene (DBT) using silica supported rhodium phosphide nanoparticles(Rh₂P/SiO₂), Rh nanoparticles (Rh/SiO₂) and commercially available Ni-Mo/Al₂O₃ as catalysts demonstrated the superior performance of the Rh₂P/SiO₂ catalyst. The higher activity of the rhodium phosphide catalyst (145 nmol DBT/g_{cat}·s), in comparison to pure rhodium (44 nmol DBT/g_{cat}·s) and the commercial catalyst (123 nmol DBT/g_{cat}·s) has been attributed to the crystal structure of Rh₂P. The bonding scenario in the Rh₂P crystal is dominated by Rh–P interactions (weak Rh–Rh and P–P interactions), which modifies the electronic environment of Rh in comparison to pure Rh. Moreover, Rh₂P/SiO₂ exhibited an excellent tolerance towards sulfur poisoning.^[61]

An interesting example for the selectivity tuning through an ensembles design is reported by Albani *et al.*^[42] by preparing nickel phosphides using solid-state synthesis methods. The rate and selectivity for the semi hydrogenation of 1-hexyne and 2-methyl-3-butyn-2-ol was

observed to be higher with nickel phosphides (Ni_2P and Ni_5P_4) in comparison to pure nickel. The spatially isolated nickel trimers on the nickel phosphide surfaces were identified as the key feature. Moreover, the calculation of the reaction energy barriers over pure Ni, Ni_2P and Ni_5P_4 demonstrated more favorable semi-hydrogenation conditions on nickel phosphide surfaces, caused by the shift in the d-band centre and subsequent changes in the adsorption energy of the alkene and alkyne.^[42] From the above discussion, it is evident that elemental phosphorus can modify the metal center both geometrically, by creating ensembles and isolating active sites, and electronically, similar to a phosphine-based ligand. This dual influence enhances the catalytic behavior and highlights the potential for developing phosphide-based catalysts.

Adjacent to phosphorus in the periodic table, sulfur plays a significant role in catalysis, though it is often regarded as a catalyst poison.^[62,63] However, when incorporated into the metal lattice to form metal sulfides, sulfur can positively influence the catalytic performance. The application of metal sulfide-based catalysts, for example, has been reported in the context of semi-hydrogenation reactions,^[21,64] electro-catalysis,^[65,66] or hydrodesulfurization reactions^[67]. In this context palladium sulfides have been identified as promising catalyst candidates. For example, it has been shown that a weak binding of organic intermediates, facilitated by palladium trimer ensembles formed on graphitic carbon nitride supported palladium sulfide ($\text{Pd}_3\text{S/C}_3\text{N}_4$), resulted in the highly selective semi-hydrogenation of alkynes to alkenes.^[21] In another study, Pd_4S supported on carbon nanofibers ($\text{Pd}_4\text{S/CNF}$) exhibited an exceptional alkene selectivity of 86 % and 95 % in the performed hydrogenation of a mix of C3 and C2 alkynes.^[68] Further, molybdenum sulfide catalysts, specifically MoS_2 , have been investigated with respect to their activity in the electrochemical hydrogen evolution reaction (HER), where edge sites have been reported as active catalytic sites.^[69,70] The activity of MoS_2 , measured in terms of exchange current density, has shown to be 2 order of magnitude higher in comparison to pure Mo-based system.^[69] Moreover, the application of cobalt sulfide (CoS) in the HER reaction, as reported by Aslan *et al.*,^[66] demonstrated superior performance compared to Pt and Pd, which are traditionally known for their high efficiency in HER.^[66,69]

Metal phosphide and sulfide catalysts are commonly synthesized either as bulk materials or supported nanoparticles for catalytic applications. Typical metal sources include elemental metals,^[71,72] metal nitrates,^[22] chlorides,^[73] oxides,^[74] hydroxides,^[75] and acetylacetones,^[76] while phosphorus sources include elemental phosphorus,^[77] phosphoric acid (H_3PO_4),^[22] diammonium hydrogen phosphate ($(\text{NH}_4)_2\text{HPO}_4$),^[78] sodium hypophosphite (NaH_2PO_2),^[79] etc. Sulfur sources typically consist of elemental sulfur,^[80] hydrogen sulfide (H_2S),^[81] sodium sulfide (Na_2S),^[82] etc. Supported metal phosphide and sulfide nanoparticles are synthesized by impregnating the precursor solution(s) into the pores of a support material,^[22] followed by a thermal treatment in atmospheres, such as hydrogen,^[83] argon,^[84] or forming gas (5-10 % H_2 ,

rest N_2)^[22] at elevated temperatures. Bulk nanoparticles can be synthesized using solvothermal syntheses, where precursors undergo the transformation into metal phosphide/sulfide nanoparticles while forming a colloid.^[85] These nanoparticles can either be used directly or immobilized on supports for catalytic applications. Alternatively, solid-state synthesis techniques, such as ball milling of the pure elements (metals, P, or S) or precursors, or simple heating of the constituent elements at elevated temperatures, can also be employed to produce the targeted binary phases.^[42,86]

1.2 Stability enhancement of supported catalysts in liquid-phase reactions

One of the key challenges in catalytic reactions is the catalyst deactivation. This can occur due to various phenomena, such as coking, poisoning, sintering, and mechanical degradation.^[87] In addition, in liquid-phase reactions, metal leaching can occur, whereby the active metal species are transferred from the solid catalyst into the liquid reaction medium. Leaching can occur through the direct dissolution of the catalyst, for example metal hydroxides present in the catalyst can dissolve in water.^[88] Another mechanism involves the formation of a soluble species (most often molecular complexes) through chemical transformations under reaction conditions and the subsequent transfer to the liquid phase.^[89] Catalyst leaching results in a gradual decline in catalytic activity, eventually leading to a complete loss of catalytic activity. Therefore, the development of catalysts with a high resistance towards leaching is essential to enhance their recyclability, reduce metal contamination in the product stream, and to support the overall sustainability. To address this, various strategies have been investigated to strengthen the interaction between the support material and the metal species in order to prevent any metal leaching.

The strategies for preventing leaching mainly comprise of the modification of the support material,^[90] using alloys or intermetallic nanoparticles,^[91] modifying synthesis procedures,^[92] or the addition of protectants in the reaction system.^[93] For instance, the modification of the support material carbon with nitrogen is a promising tool for the suppression of leaching. For example cobalt nanoparticles stabilized on nitrogen-rich graphitic carbon for the chemoselective hydrogenation of nitroarenes^[94] and Co nanoparticles supported on N-doped carbon for transfer hydrogenations^[90] showed no measurable leaching into the liquid phase. This enhanced stability can be attributed to the improved metal-support interaction. Similarly, in the context of hydroformylation reactions, a substantial reduction in leaching was achieved by incorporating nitrogen into a cobalt catalyst supported on carbon ($\text{CoN}_x@\text{NC}$). Nitrogen-stabilized Co nanoparticles also exhibited significantly lower leaching of only 2 %, compared to 49 % observed for pure Co nanoparticles ($\text{Co}@\text{C}$).^[95]

Beyond the support modification, the concept of element synergy has also proven to be effective. Through adapting this concept in hydroformylation catalysis, a higher stability of

CoGa (CoGa/SiO₂) intermetallic nanoparticles as catalyst in comparison to supported Co nanoparticles (Co/SiO₂) was observed. Hereby, the Ga atoms act as anchoring sites for Co, providing an enhanced stability and leading to a substantial reduction in leaching from 84 % for Co/SiO₂ to only 4 % for CoGa/SiO₂.^[91] Similarly, through the incorporation of C into Mo, and the subsequent formation of molybdenum carbide nanoparticles on carbon nanotubes (Mo₂C/CNT), an excellent leaching resistance, outperforming the Pd catalyst (noble metal catalyst), was observed in the hydrodeoxygenation of vegetable oils.^[96]

Moreover, interesting improvements in the catalyst stability can also be achieved through the modification of the synthesis conditions. For example, the acid site leaching of an arenesulphonic SBA-15 (SBA-15 = Santa Barbara Amorphous-15, mesoporous silica) catalyst in xylose dehydrogenation reactions was observed to be dependent on the aging temperature. A comparison of the decline in surface acidity after the reaction demonstrated a significant drop (roughly 50 %) for the catalyst aged at 100 °C, whereas at 160 °C and 180 °C, the decline was marginal, indicating the importance of the catalyst synthesis conditions.^[92]

1.3 Heterogeneous catalysis in oxidation and C–C bond formation reactions

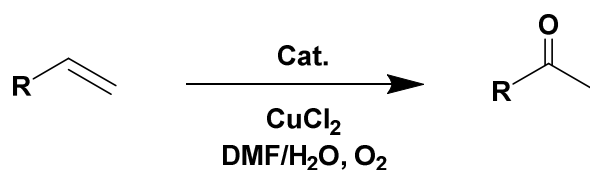
Oxidation and C–C bond formation reactions are two important classes of industrially relevant organic transformations, which are performed mostly with homogeneous catalysts, consisting of Pd,^[97] Ni,^[98] Rh,^[55] Co^[99] and ligand systems forming molecular complexes. Investigation into these transformations holds significant promise for expanding synthetic access to structurally diverse and functionally rich organic compounds. In the context of oxidation reactions, the Wacker-Tsuji oxidation, performed mostly with Pd compounds or complexes, is an efficient method for obtaining aldehydes or methyl ketones from terminal alkenes.^[100] Whereas, carbon–carbon (C–C) bond formation reactions play a central role in organic synthesis enabling the construction of carbon framework of organic molecules. This includes both coupling reactions between diverse organic molecules^[101] and carbonylation processes,^[102] such as alkoxy carbonylation and hydroformylation, where a carbon monoxide (CO) molecule is incorporated into an organic substrate. These transformations are vital to produce a wide range of high-value compounds.

Many of these reactions have been extensively studied in the context of homogeneous catalysis, with detailed information available in the literature regarding their mechanisms and kinetics. Given the industrial relevance of these reactions, there is a growing demand for their application using heterogeneous catalysts. However, in comparison to their homogeneous counterparts, mechanistic insights into heterogeneously catalyzed reactions remain limited. A common approach is to adapt the known mechanisms from homogeneous systems on the active sites of heterogeneous catalysts.^[12,103,104] Nevertheless, several additional factors must be considered when discussing heterogeneous reaction mechanisms. These include pore

diffusion, metal dispersion, the nature of active sites (e.g., steps, terraces, edges), poisoning, leaching, the choice of support material, and particle size effects. Advanced characterization techniques, such as *in situ* and *operando* spectroscopy and microscopy-combined with computational methods, now allow for detailed investigations into changes occurring at active sites.^[105–108] These tools enable the elucidation of reaction pathways and can significantly contribute to the design of more efficient catalysts.

1.3.1 Wacker-Tsuji oxidation

The Wacker-Tsuji oxidation refers to the catalytic conversion of terminal olefins to carbonyl compounds, often in the presence of a catalyst and co-catalyst in a mixture of water and an organic solvent (Scheme 1).^[109,110] In a typical reaction, a terminal olefin is converted into a carbonyl compound through its reaction with a water molecule (nucleophile), whereby a molecular Pd(II) species acts as catalyst. During this transformation, the Pd(II) species is reduced to Pd(0), which is then re-oxidized to Pd(II) with the assistance of a Cu(II) species (co-catalyst). The reduced copper species is subsequently re-oxidized by an oxidizing agent, such as H₂O₂ or molecular oxygen/air, thereby sustaining the catalytic cycle.^[100,110,111]



Scheme 1: Wacker-Tsuji oxidation reaction of an alkene towards a ketone with the use of a catalysts and a co-catalyst.

The first transition metal-mediated industrial process for the manufacture of acetaldehyde is the oxidation reaction of ethylene in an acidic medium with PdCl_2 as the catalyst and cupric salt (CuCl_2) as co-catalyst. This reaction was performed at Wacker-Chemie GmbH and is therefore referred to as Wacker oxidation. This process was further modified by Tsuji by using a DMF and water system for the selective oxidation of terminal olefins.^[100] Today, with these advancements, the Wacker-Tsuji oxidation accounts for the synthesis of various industrially important carbonyl compounds, which are applied in the production of fragrances, flavours, cosmetics and other valuable chemicals.^[100,112]

Numerous homogeneous catalysts, such as PdCl_2 ,^[100] $[\text{PdCl}_2(\text{PhCN})_2]$,^[113] $[\text{Pd}(\text{Quinox})\text{Cl}_2]$ (Quinox = 2,3-bis(2-pyridyl)quinoxaline),^[114] $\text{Pd}(\text{OAc})_2$,^[115] $\text{Pd}(\text{acac})_2$ (acac = acetylacetone)^[116] and $\text{Pd}(\text{TFA})_2$ (TFA = trifluoroacetate)^[117] have been reported in the context of Wacker-Tsuji oxidation reactions. The development of efficient heterogeneous catalysts was also studied in the past with the aim to make the process more industrially viable. In this context, supported Pd nanoparticles on zirconia (Pd/ZrO_2) were investigated by Zhang *et al.*^[118] for the Wacker oxidation of olefins. A study of the influence of the support on the Wacker oxidation of

styrene, based on the acetophenone yield, demonstrated a support dependence following the activity order: Pd/ZrO₂ (98 %) > Pd/CeO₂ (79 %) > Pd/Al₂O₃ (38 %) > Pd/TiO₂ (16 %). Further, an investigation concerning the Pd particle size impact on the acetophenone yield resulted in an optimum particle size range of 4 to 12 nm.^[118] Other heterogeneous catalysts reported in this contexts are Cu–Pd zeolites,^[119] Pd-doped vanadium pentoxide,^[120] and palladium nanoparticles supported on carbon nanotube (Pd/CNT).^[121] Several co-catalysts other than CuCl₂ have also been reported for the re-oxidation of Pd(0) to Pd(II), such as Cu(OAc)₂,^[122] CrO₃,^[123] KBrO₃,^[124] H₂O₂,^[110] Fe₃O₄ nanoparticles,^[110] and benzoquinone,^[125] which can avoid the possible chlorine contamination of the product mixture.

In addition to purely heterogenous catalysts, also, palladium complexes (bis-imidazoline dichlorido palladium(II) complexes) immobilized on hollow mesoporous silica material were reported by Vafaeenezadeh *et al.*^[126] In this work a comparison with several homogeneous and heterogeneous catalysts was carried out and a superior performance was observed using the synthesized heterogenized catalyst.^[126]

The literature reports on the mechanism of the heterogeneously catalyzed Wacker–Tsuji oxidation often observed similar to that of the homogeneous counterpart.^[121,127,128] Therefore, adapting the homogeneous mechanism provides a reasonable basis for understanding the heterogeneous process. In the generally accepted mechanism of the Wacker–Tsuji oxidation using a water-organic solvent system (Figure 5), the olefin first coordinates to the palladium center (**1**), followed by the nucleophilic attack of water (**2**), which leads to the formation of a hydroxyl-palladium intermediate.^[100] The addition of water to the terminal olefins occurs in accordance with the Markovnikov rule and results in the selective formation of the methyl ketone as product (**3**). This is followed by the catalyst regeneration with the assistance of a co-catalyst (**4**) and the co-catalyst re-oxidation (**5**). *Via* substrate variation, the addition of water (**2**) can be redirected to anti-Markovnikov product, namely an aldehyde. This selectivity can be achieved through the presence of a heteroatom in the allylic or homo-allylic position.^[129] This clearly indicates the selectivity dependence of the Wacker–Tsuji oxidation on the substrates undergoing oxidation. However, through the use of a suitable catalyst and co-catalyst even challenging substrates can be converted to the corresponding ketones.^[100,109,114]

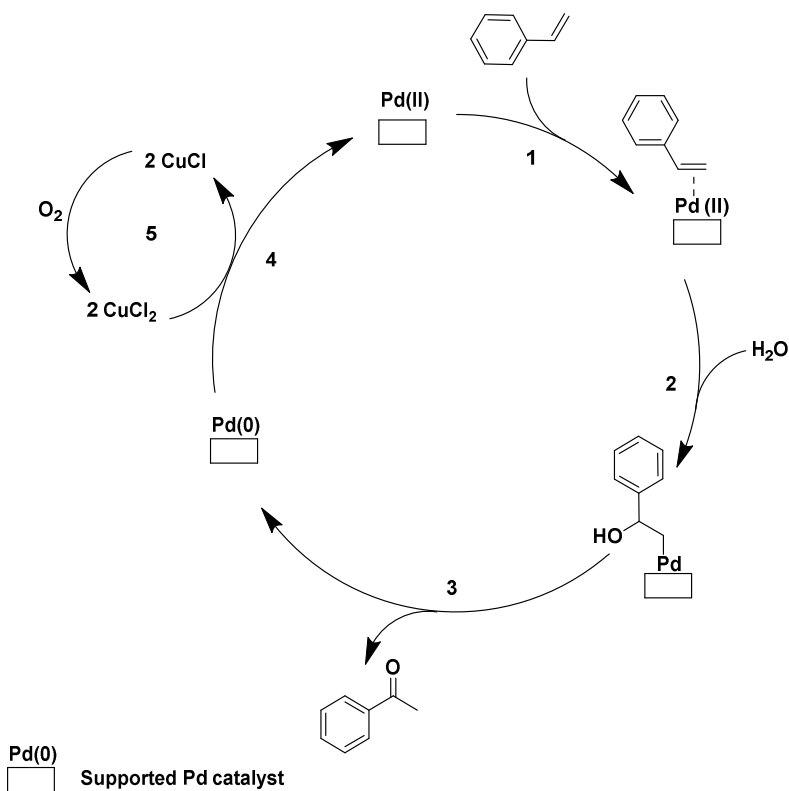
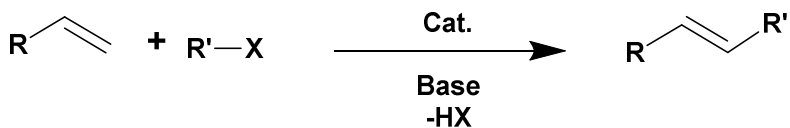


Figure 5: Simplified reaction mechanism of the heterogeneously catalyzed Wacker-Tsui oxidation of styrene with a CuCl_2/O_2 system, adapted from the field of homogeneous catalysis.

1.3.2 Heck coupling reaction

Coupling reactions, which involve the formation of C–C bonds, are important transformations in organic chemistry. One prominent example is the palladium catalyzed Heck coupling reaction of organic halides or triflates and an alkene (Scheme 2). This reaction results in an intermolecular C–C bond formation with the assistance of a base and the generation of a substituted alkene.^[130–133] The chemicals synthesized *via* Heck coupling reactions find widespread application for the production of pharmaceuticals, agrochemicals, and fine chemicals.^[130,133,134] Notably, the Heck coupling reaction enables the synthesis of biologically important molecules, such as stilbenoids and anticancer agents, like resveratrol, DMU-212, taxol, or singulair, chantix.^[130,135] The particular interest in the Heck coupling reaction is primarily due to its simplicity, high efficiency, and the advantage of not requiring an organometallic coupling partner, which typically involves multistep and expensive synthesis procedures.^[130,134] Moreover, the Heck reaction often exhibits a good stereo- and regioselectivity mostly favoring the *trans* products.^[135] Initial studies focussed on the coupling of an aryl bromide or iodide with an olefin. However the substrate scope was further extended to aromatic diazonium salts, aryl chlorides, aryl sulphonyl chlorides and aryl silanols, expanding the possible coupling products.^[134,135]



Scheme 2: Heck coupling reaction of an alkene and an aryl/alkyl halide. R and R' = C₆H₅, C₆H₄–OMe, C₆H₄–CH₃ and X = I, Cl, Br.

A large number of molecular palladium complexes were investigated as catalysts for the Heck coupling reaction. Some of the promising homogeneous catalysts reported are Pd(OAc)₂/PPh₃,^[136] palladium(II)-porphyrin complexes,^[137] Pd(OAc)₂/TPPTS (TPPTS = phosphanetriyltris(benzenesulfonic acid) trisodium salt),^[138] [Pd(dppe)(OTf)₂] (dppe: 1,2-bis(diphenylphosphino)ethane),^[139] Pd(OAc)₂/LHX (LHX = 1,3-dialkyl-3,4,5,6-tetrahydropyrimidinium salts),^[140] Pd₂(dba)₃/P(t-Bu)₃ (dba = dibenzalacetone),^[141] etc. The addition of a ligand along with palladium precursors, such as [Pd₂(dba)₃] and Pd(OAc)₂, largely prevent the formation of Pd black and enhances the stability of the catalyst.^[132] However, these systems are still associated with a challenging catalyst separation process, loss of precious metal and possible product contamination, which explains the need for the development of highly active and stable solid-state catalysts.

Therefore, palladium nanoparticles supported on carbon have been reported as active heterogeneous catalysts for the Heck coupling reaction, demonstrating broad applicability across a variety of substrates.^[142,143] The reaction of 4-bromonitrobenzene with methyl vinyl ether, carried out by Hallberg *et al.* using palladium on charcoal as a catalyst, achieved an 81% yield of the desired coupling product.^[142] In another study, Beller *et al.* reported the first heterogeneously catalyzed Heck coupling of aryl diazonium salts with acrylic acid esters using Pd/C, successfully synthesizing cinnamic acid esters with yields up to 92 % at a very mild reaction temperature of 60 °C.^[143] Several other metallic palladium catalysts were explored by Wagner *et al.* by synthesizing the nanoparticles on oxidic support materials, such as SiO₂, ZnO, MgO, Al₂O₃, TiO₂ or, ZrO₂. A difference in catalytic activity was observed depending on the support material in the reaction of bromobenzene and styrene at 140 °C.^[144] Moreover, polymer-based materials were used by various research groups as efficient support materials for Pd nanoparticles, such as cross-linked polyaniline,^[145] polystyrene,^[146] and N-heterocyclic carbene-based microporous organic polymer (NHC-MOP).^[147]

Further heterogenized catalysts were synthesized by immobilizing active palladium complexes on solid supports. For instance, iminopyridylphosphine palladium complexes were immobilized on cross-linked polyallylamine polymers by Liu *et al.* and applied in Heck coupling reactions. An excellent stilbene yield of 90 % was reported for the reaction of styrene and iodobenzene in dioxane as solvent under reflux conditions. The catalyst also exhibited good stability, as recycling experiments showed no decline in activity up to five rounds of reuse.^[148] There are

numerous examples available in the literature with exceptional performance achieved through the heterogenization of molecular species, such as polyacrylonitrile supported Pd complexes (m-PAN-Pd),^[149] palladium N-methylimidazolium supported complexes,^[150] amine-Pd complex on silica,^[151] silica-immobilized tridentate diphosphinoaryl ligand (PCP-type) palladium complex,^[152] or Pd Schiff base complexes supported on MCM-41 (MCM-41 = Mobil Composition of Matter, mesoporous silica).^[153] The ability to combine the benefits of homogeneous catalysts, namely the well defined and separated active sites and fine tunability, and heterogeneous catalysts, such as the high stability and the recycling potential can be considered as the strengths of such heterogenized catalysts.

The mechanism of homogeneously catalyzed Heck coupling reactions is well known and an adaption of the same in the heterogeneous catalysis context is reasonable (Figure 6).^[154] The catalytic cycle essentially starts with the oxidative addition of organic halide to Pd(0), forming an organopalladium halide complex on the support (**1**). Further, the alkene is coordinated to Pd, and migrates to insert into the Pd–R bond (**2 and 3**). The formed complex is decomposed *via* β -hydride elimination, thereby releasing the coupled product and generating a hydrido palladium halide complex (**4**). This complex undergoes a reductive elimination regenerating the active Pd(0) species (**5**), followed by the subsequent neutralization of formed HX by a base.^[155,156]

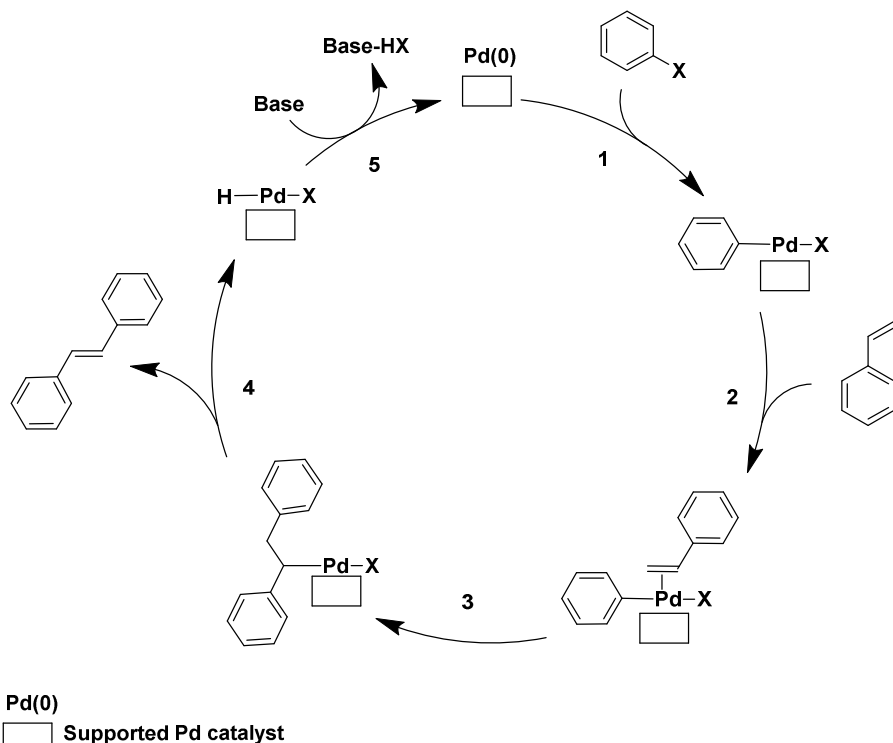


Figure 6: Reaction mechanism for the heterogeneously catalyzed Heck coupling reaction.

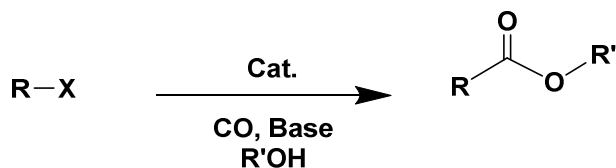
Even though considerable research was conducted in the context of heterogeneously catalyzed Heck coupling reactions, the true heterogeneity of the catalyst is still under debate.

The formation of soluble Pd species on the surface, followed by metal leaching to the liquid reaction mixture, which can then catalyze the reactions were discussed in the literature.^[157–159] Such active Pd species can potentially also redeposit on the support, whereby a “release and catch” mechanism is enabled.^[157, 158] However, it is important to mention that the development of a stable catalyst with higher tolerance towards metal leaching, thereby limiting the product contamination and facilitating reuse, are the most significant aspects in an industrial context. The same can be achieved through enhancing the metal-support interaction, through carefully selecting and tailoring the support materials.

1.3.3 Alkoxy carbonylation reaction

An important class of carbonylation reactions is the alkoxy carbonylation, through which esters and amides can be synthesized.^[89] Various substrates such as alkenes, alkynes, aryl or alkyl halides can be used for this transformation.^[160] Hereby, alkoxy carbonylation reactions, involving C–X bonds, hold significant relevance, owing to the wide commercial availability and low cost of various substituted aryl halides.^[161] In the alkoxy carbonylation reaction, organic halides react with a nucleophile (alcohol) and carbon monoxide in the presence of a base, resulting in the formation of esters (Scheme 3). The products obtained can be directly used or further converted to aldehydes, ketones, carboxylic acids to produce pharmaceuticals, detergents, flavors, fragrances, polymers, etc. Numerous homogeneous Pd-based catalysts have been reported and extensively studied for this transformation, where a significant contribution was given by Heck *et al.* providing the first insight in to the mechanism and kinetics of the aryl halide alkoxy carbonylation.^[162]

As homogeneous catalysts, palladium-based compounds, such as $\text{Pd}(\text{OAc})_2$ or PdCl_2 in combination with ligands, such as PPh_3 (triphenylphosphine),^[163] dppf (1,1'-bis(diphenylphosphino)ferrocene),^[97] DIBPP (1,3-bis(diisobutylphosphino)propane),^[164] and Xantphos (9,9-dimethyl-9H-xanthene-4,5-diyl) bis(diphenylphosphane),^[165] can be used to form the active species *in-situ*. Also, ready made molecular complexes such as $[\text{PdCl}_2(\text{dppp})]$ (dppp = 1,3-bis(diphenylphosphino)propane),^[166] $[\text{Pd}(\text{2-}(\text{CH}_3\text{NH})\text{Py-}\text{PPh}_2)_2](\text{OAc})_2$ ^[167] and $[\text{Pd}(\text{PPh}_3)_4]$ ^[168] have been applied. While most of these catalysts show promising performance in the alkoxy carbonylation of aryl halides, significant challenges remain regarding catalyst separation, noble metal loss, and product contamination. Considering the extensive industrial relevance of this reaction, the development of heterogeneous catalysts is therefore crucial to substitute homogeneous systems and mitigate these challenges.



Scheme 3: Alkoxy carbonylation of an aryl/alkyl halide producing an ester. R = C₆H₅, C₆H₄—OMe, C₆H₄—CH₃ and X = I, Cl, Br.

An approach for the development of heterogeneous catalysts through the synthesis of supported nanoparticles of Pd on carbon (Pd/C), was investigated by Dufaud *et al.*^[169]. Interestingly, the authors reported a six-fold increase in turnover frequency (TOF) upon introducing a promoter to this reaction, such as K₂Cr₂O₇. This effect is attributed to the re-oxidation of large Pd metal particles into highly dispersed Pd(II) species, which are subsequently reduced under CO atmosphere, thereby resisting palladium sintering and deactivation. However, a very high reaction temperature of 200 °C was required.^[169] A similar catalyst was used by Liu *et al.*^[170] with 5 wt.% Pd loading (5 % Pd/C) and applied in the alkoxy carbonylation of iodobenzene and resulted in 94 % yield of the corresponding ester using a comparatively milder reaction temperature of 130 °C. The milder reaction conditions can be attributed to the higher leaving ability of iodine compared to chlorine, which facilitates the reaction to proceed at lower temperatures. The catalyst also exhibited good stability, as only a slight decline in activity was observed in recycling experiments.^[170] Similarly, palladium particles on various supports, such as Pd/Fe₃O₄,^[104] Pd1/CeO₂,^[171] Pd/SiO₂,^[172] and palladium supported on nitrogen doped carbon (Pd/PdO/NGr-C, NGr-C = N doped carbon),^[173] were investigated.

The application of immobilized molecular complexes has also been also reported in the context of alkoxy carbonylation reactions of aryl halides, thereby combining the benefits of homogeneous and heterogeneous catalysis. For instance, Antebi *et al.* immobilized palladium complexes on PAMAM (polyaminoamido) dendrimers supported on silica. The catalysts were prepared through the complexation of [Pd(RCN)₂Cl₂] (R = Me, Ph) or [Pd(tmeda)Me₂] (tmeda: tetramethylethylenediamine) with phosphinated (PPh₂) PAMAM (polyaminoamido) dendrimers supported on silica. An excellent methyl ester yield up to 100 % and turn over number (TON) up to 652 was reported for the alkoxy carbonylation of iodobenzene performed at 100 °C.^[174] Moreover, the silica supported palladium phosphine complex (PdCl₂—PPh₂Et@SiO₂) prepared by Mane *et al.* exhibited superior activity in comparison to a conventionally used Pd/C catalyst. In the alkoxy carbonylation of iodobenzene to methyl benzoate 99 % yield to the target ester was obtained with [PdCl₂—PPh₂Et]@SiO₂ in 3 h at a reaction temperature of 100 °C. Contrary, Pd/C resulted in only 73 % yield, revealing the success of heterogenization approach. Several other examples of immobilized palladium complexes were reported in the literature, such as palladium(II) organometallic complexes encapsulated in Y zeolite,^[175] palladium ions in ionic

liquids immobilized on graphene-oxide (Pd@GOIL),^[176] palladium-bisoxazoline-supported catalysts (Pd-BOX-M),^[177] or an immobilized Pd ionic liquid complex (ImmPd-IL).^[178]

The mechanism of the heterogeneously catalyzed alkoxycarbonylation of aryl halides can partly be adapted from the homogeneous counterpart (Figure 7). The catalytic cycle begins with the oxidative addition of the aryl halide to palladium (1), forming an aryl-palladium complex. This step is followed by CO insertion (2), leading to the formation of an acyl-palladium complex, and subsequent alcoholysis of the complex (3), which yields the target ester and a hydridopalladium species. The active catalyst is regenerated through the decomposition of the hydridopalladium species, and the resulting HX is neutralized by the added base (4).^[162] A simplified catalytic cycle is depicted in Figure 7. In this context, the ease of oxidative addition (1) at the active sites of the heterogeneous catalyst can be considered a plausible descriptor for its catalytic performance; however, this process can be hindered by the formation of metal carbonyl species on the surface.^[179]

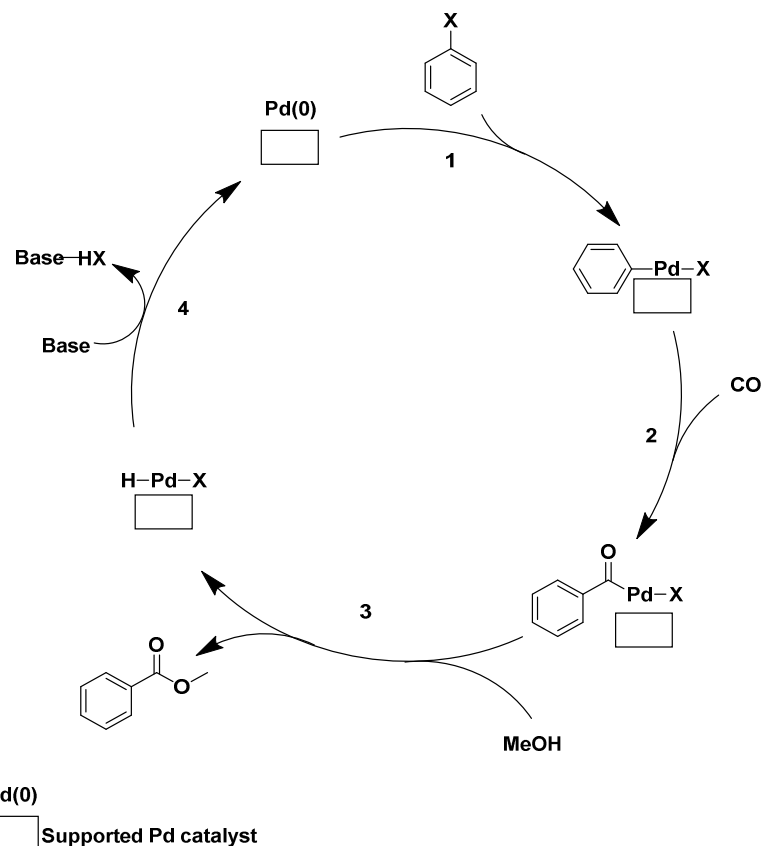
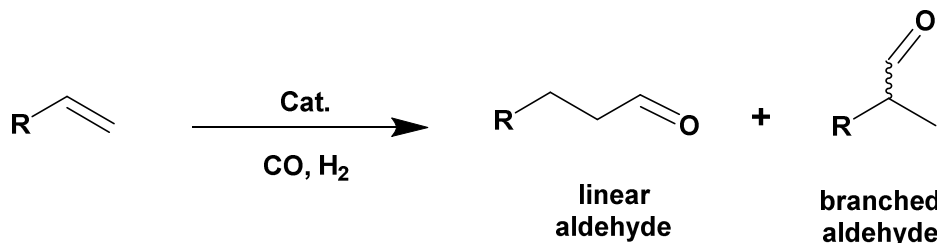


Figure 7: Simplified reaction mechanism of the heterogeneously catalysed alkoxycarbonylation of aryl halides.

1.3.4 Hydroformylation reaction

The hydroformylation reaction is a key catalytic process that converts olefins into aldehydes using syngas (CO and H₂), typically employing cobalt- or rhodium-based catalysts.^[180] Originally discovered by Otto Roelen in the 20th century during his research on Fischer-Tropsch chemistry at Ruhrchemie, hydroformylation has since become a major homogeneously

catalyzed industrial process.^[180,181] The aldehydes synthesized with this reaction can either be used directly or further transformed into other fine chemicals.^[182–184] Through hydroformylation reactions both linear and branched aldehydes can be produced (Scheme 4), whereby for longer-chain olefins, a mixture of branched and linear aldehydes is typically formed. Today, this reaction accounts for the global production of over 24 million metric tons of oxo chemicals annually.^[183]



Scheme 4: Hydroformylation of alkenes producing linear and branched aldehydes. R = CH₃, C₂H₅, C₆H₅.

In industrial settings, the hydroformylation reaction is predominantly catalyzed by molecular complexes of rhodium or cobalt, despite their inherent challenges in the catalyst separation and reuse. The most commonly used homogeneous rhodium catalysts are based on phosphine ligands, such as $[\text{RhCl}(\text{PPh}_3)_3]$,^[55] $[\text{RhX}(\text{CO})(\text{PPh}_3)_2]$ (X: Cl, Br, I)^[56] and Rh/TPPTS complexes^[185] (TPPTS = sodium salt of sulfonated triphenylphosphine). In contrast, the adoption of heterogeneous catalysts has been limited, primarily due to concerns regarding their potential constraints with respect to their activity and selectivity. Hence, the development of high-performing solid-state catalysts is important for the chemical industry and a considerable number of investigations were reported in this context.

Heterogeneous catalysts for hydroformylation reactions include supported nanoparticles,^[22] single atom catalysts,^[186] immobilized complexes,^[187] and supported ionic liquid based catalysts.^[188] Interestingly, some of these catalysts exhibits intrinsic activities comparable to or even higher than commonly used homogeneous catalysts, while showing an excellent stability. One example is the superior performance of a single atom rhodium-based catalyst supported on ZnO nanowire (Rh/ZnO-nw) showing a turn over frequency of 3333 h⁻¹ (calculated from TON) in comparison to 1583 h⁻¹ estimated for the Wilkinson's catalyst ($[\text{RhCl}(\text{PPh}_3)_3]$) for the hydroformylation of styrene under similar reaction conditions.^[189] Similarly, zeolite-encaged isolated Rh ions (Rh@Y) outperformed $[\text{HRh}(\text{CO})(\text{PPh}_3)_3]$, where a lower apparent activation energy of 60.6 kJ·mol⁻¹ has been reported with the heterogeneous catalyst in comparison to the homogeneous counterpart (117 kJ·mol⁻¹), with an excellent recyclability up to 5 cycles in the hydroformylation of 1-hexene.^[190]

All these promising results highlight the immense potential for developing high-performance heterogeneous hydroformylation catalysts, ultimately paving the way for an industrial application. In this context, several catalysts using the concept of element synergy in both gas

and liquid-phase hydroformylation reactions have been reported. Silica supported rhodium phosphide nanoparticles ($\text{Rh}_2\text{P}/\text{SiO}_2$) were reported to perform exceptionally in the hydroformylation of ethylene^[22] and styrene.^[25] The separated under-coordinated rhodium sites formed at the Rh terminated surfaces are postulated to act like rhodium-phosphine complexes, thereby exhibiting good activity (TOF: 190 h^{-1}) and selectivity of 80 % towards the ethylene hydroformylation to propionaldehyde.^[12] In the context of styrene hydroformylation, the enhanced activity, compared to pure rhodium nanoparticles on silica (Rh/SiO_2), was attributed to a d-band modification. This modification enabled a band structure equivalent to the benchmark $[\text{RhCl}(\text{PPh}_3)_3]$ complex, thereby providing a suitable CO binding energy on the Rh_2P surface.^[25] Similarly, for the styrene hydroformylation, Chen *et al.* reported a threefold enhancement in catalytic activity compared to the traditional Wilkinson catalyst (TOF: 966 h^{-1}) by employing SBA-15-supported RhZn intermetallic nanoparticles (RhZn/SBA-15), which exhibited a TOF of 3090 h^{-1} . A comparison of the intrinsic activity with Rh/SBA-15 revealed a six-fold increase in TOF upon using RhZn/SBA-15 . The alloying of Zn with Rh leads to the formation of RhZn (110) surfaces with a stoichiometrically balanced Rh–Zn composition, which results in a lower binding strength for reaction intermediates and a significantly reduced activation energy barrier compared to the Rh (111) surface.^[191] Also, the incorporation of cobalt to rhodium results in the formation of Rh–Co hybrid sites and Rh_3 ensembles, which significantly improve selectivity toward C_3 oxygenates in the hydroformylation of ethylene in comparison to pure Rh, by minimizing undesired hydrogenation side reactions. This effect is particularly evident in RhCo_3 supported on MCM-41 ($\text{RhCo}_3/\text{MCM-41}$), where a significantly higher selectivity of nearly 30 % for C_3 oxygenates was achieved, compared to 16 % for Rh/MCM-41 .^[192]

For the design of an efficient heterogeneous catalyst, it is important to understand the mechanism of the hydroformylation reaction. According to the widely accepted Heck and Breslow mechanism,^[193] the homogeneously catalyzed reaction proceeds through the formation of an active hydrido-metal carbonyl species (**1**). A similar mechanism can be assumed for the heterogeneously catalyzed hydroformylation reaction,^[12] where the surface metal atom transforms to hydrido-metal carbonyl species in the presence of syngas (**1**). A key step in the catalytic cycle involves the olefin insertion (**2**), leading to the formation of a metal–alkyl complex *via* hydride migration (**3**). This is followed by CO insertion (**4**) and, ultimately, aldehyde formation through hydrogenolysis of the metal–acyl bond (**5–8**). A proposed mechanism of the heterogeneously catalyzed hydroformylation of styrene with rhodium catalyst is depicted in Figure 8. Herein, the formation of the active hydrido–rhodium carbonyl species is observed to have a significant impact on the catalytic activity. Hence, the CO binding strength to the surface can be treated as one of the key descriptors for predicting the catalyst performance.^[25]

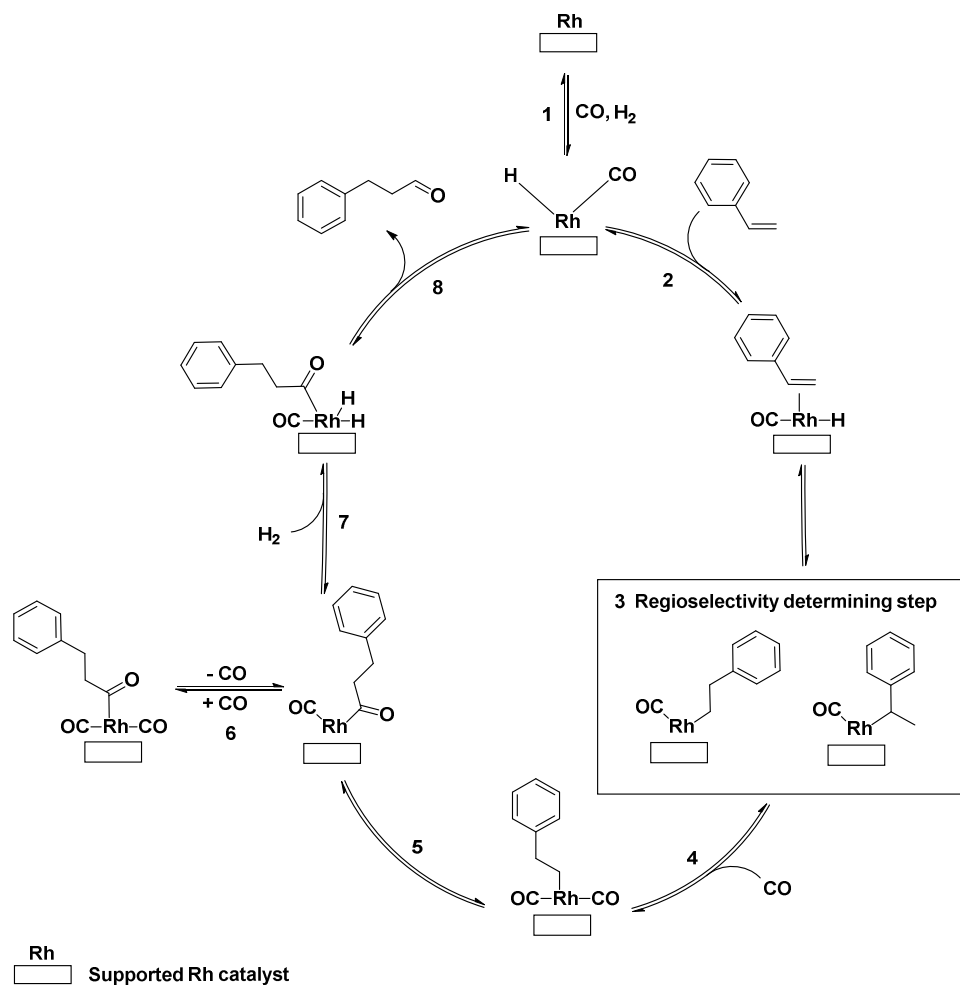


Figure 8: Reaction mechanism of the rhodium-catalyzed heterogeneous hydroformylation of styrene.

2 Project aims

One of the strategies for the development of high-performing heterogeneous catalysts involves the incorporation of a p-block element into a transition metal matrix to form a well-defined d-block-p-block element-based phase. Such binary phases can be considered as heterogenized catalysts, with modified metal sites compared to the pure metal. Such systems can potentially exhibit an exceptional catalytic performance, with respect to their catalytic activity and selectivity, through the tailor-made modification of the geometric and electronic properties of the metal centers. This approach remains totally underexplored for many industrially relevant reactions so far. The present work therefore investigates the application of the “d-block-p-block element combination strategy” to synthesize active catalysts for various organic transformations (Figure 9). Palladium and rhodium are chosen as the d-block elements, while phosphorus and sulfur serve as the p-block elements; accordingly, metal phosphide and sulfide nanoparticles are studied. Additionally, efforts are made to control the metal leaching and to enhance the catalyst stability in liquid-phase reactions by the choice and modification of support materials. The aim of this work is to provide valuable insights for the rational design of highly active and stable catalysts for a set of industrially important organic reactions.

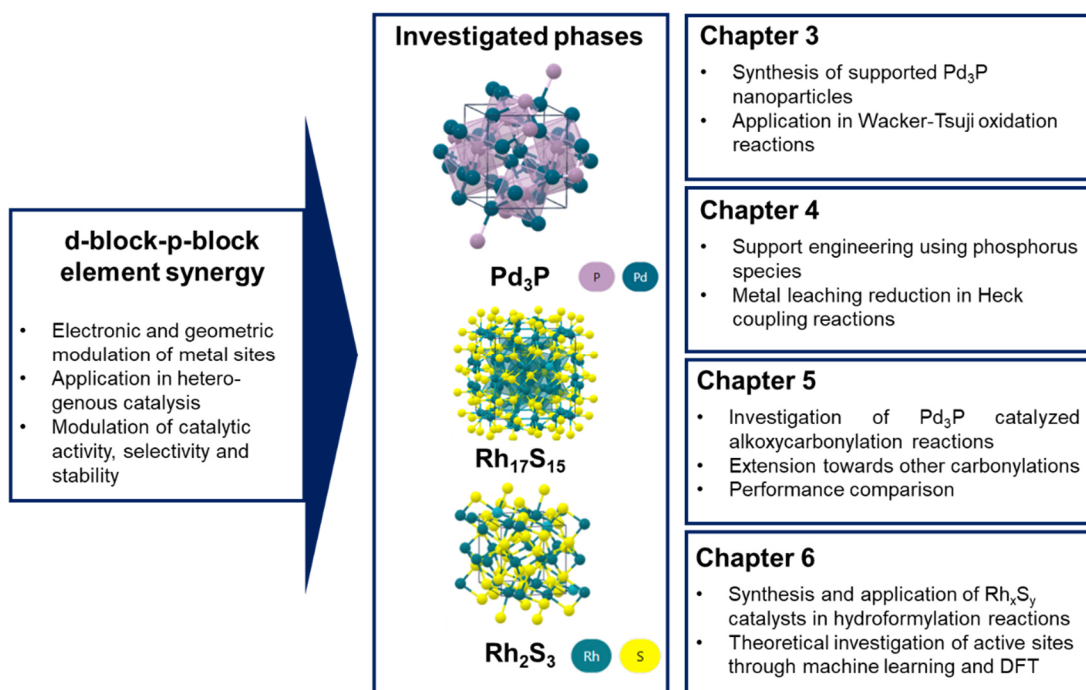


Figure 9: Overview of the research aims of this thesis, focusing on exploring the potential of element synergy in heterogeneous catalysis. Crystal structure images taken from “The Materials Project”.^[33]

Chapter 3: Supported palladium phosphides as oxidation catalysts

The synthesis and characterization of a supported palladium phosphide catalyst, namely $\text{Pd}_3\text{P}/\text{SiO}_2$, for the application in the Wacker-Tsuji oxidation of styrene in various reaction systems will be studied. The potential to achieve an enhanced activity and ketone selectivity, compared to a conventional supported palladium catalysts, will also be investigated.

Chapter 4: Support engineering for Heck coupling reactions

The suppression of metal leaching, which leads to catalyst deactivation, will be addressed by suitably modifying (engineering) a silica support with phosphorus species. The impact of synthesizing Pd_3P on such engineered supports, particularly in terms of enhancing catalyst stability, will also be an integral part of this study.

Chapter 5: Alkoxycarbonylation reactions with supported palladium phosphide nanoparticles

The application of supported Pd_3P catalysts in the alkoxycarbonylation of aryl halides is investigated, along with exploring their potential use in amino- and phenoxy carbonylation reactions. Based on the advantages of the d-block-p-block element combination strategy, the project will attempt to synthesize a catalyst with superior performance compared to conventionally used supported Pd catalysts, as well as previously reported homogeneous and heterogeneous systems.

Chapter 6: Olefin hydroformylation reactions with supported rhodium sulfide nanoparticles

The use of sulfur, a well-known catalyst poison, as a promoter for hydroformylation catalysis will be explored by incorporating sulfur into the crystal structure of rhodium to form rhodium sulfide nanoparticles. The resulting catalysts will be investigated both experimentally and theoretically to understand the effects and outcomes of this approach.

3 Supported palladium phosphides as oxidation catalysts

The results discussed in this chapter were published in:

A. Neyyathala, F. Flecken, S. Hanf, *ChemPlusChem* **2023**, 88, e202200431 under the license CC BY-NC 4.0.

Figures 10, 11, 12, 13, 15, 16, S2, S3 & S4 and Tables 2, 3, 4 and S1 are adapted from this publication.

The Wacker-Tsuji oxidation, for the synthesis of methyl ketones or aldehydes from terminal olefins, is an industrially relevant organic transformation typically catalyzed by palladium-containing compounds. The thereof resulting chemicals have wide spread use in the production of fine chemicals, pharmaceuticals, organic intermediates and agrochemicals.^[100,194] Therefore, the development of high-performing solid-state catalyst is very relevant in this context, whereby supported Pd-based catalysts have been investigated by various research groups.^[118,194,195] Going away from purely Pd-based catalysts, an element synergy strategy is applied in this work to synthesize a Pd-based supported catalyst, where phosphorus is incorporated into the Pd matrix forming palladium phosphide nanoparticles. A special focus was laid on one Pd–P phase, namely Pd₃P, as there is sufficient phosphorus present in the crystal structure to dilute the Pd matrix, but the metallic character is still maintained. Silica supported Pd₃P nanoparticles (Pd₃P/SiO₂) were synthesized *via* an impregnation method and characterized by powder X-ray diffraction (PXRD), scanning electron microscopy (SEM), energy-dispersive X-ray (EDX) spectroscopy, inductively coupled plasma-atomic emission spectroscopy (ICP-AES) and XPS. The synthesized catalyst was applied in the Wacker-Tsuji oxidation of styrene in four reaction systems. In all cases the synthesized catalyst was found to be active with an excellent selectivity up to 100 % towards acetophenone. A comparison with silica supported Pd nanoparticles (Pd/SiO₂) and other reported catalyst revealed the superior performance of Pd₃P/SiO₂, showing the success of the underlying catalyst design strategy.

3.1 Synthesis and characterization Pd_xP_y/SiO₂

Prior to the synthesis of the palladium phosphide catalysts, Pd–P phases were studied by looking into the phase diagram and formation energies. The phase stability diagram was generated with “The Materials Project” using the “Phase Diagram” application.^[33] Through this calculated diagram for this system (Figure S1) Pd₆P, Pd₃P, Pd₇P₃, and PdP₂ were identified as the most stable Pd_xP_y phases as the energy above hull for these compositions are estimated as zero (Table 1), pointing towards the possibility to synthesize these materials. The synthesis was focused on the Pd₃P phase, as it represents an optimal midpoint among the metallic Pd₆P,

Pd_3P and Pd_7P_3 phases. Unlike PdP_2 which exhibits semiconducting behavior, due to its band gap of 0.34 eV,^[33] Pd_3P maintains sufficient metallic character, while incorporating enough phosphorus to effectively dilute the palladium matrix.

Table 1: Thermodynamic stability of Pd_xP_y phases represented in terms of energy above hull. Values were extracted from “The Materials Project”.^[33]

Entry	Phase	Pd/P	Energy above hull (eV)
1	PdP_2	0.5	0
2	Pd_7P_3	2.3	0
3	Pd_3P	3	0
4	Pd_6P	6	0
5	Pd_{15}P_2	7.5	<0.01
6	Pd_4P	4	0.02
7	PdP_3	0.33	0.06

Supported palladium phosphide nanoparticles were synthesized using a wet impregnation method. Silica was selected as the support material accounting to it's chemical and thermal stability, wide spread industrial application, defined porosity, high adsorption capacity and high surface area.^[196] Palladium acetate ($\text{Pd}(\text{OAc})_2$) and ammonium dihydrogen phosphate ($\text{NH}_4\text{H}_2\text{PO}_4$) were selected as palladium and phosphorus precursors. In order to prepare the precursor solution, $\text{Pd}(\text{OAc})_2$ and $\text{NH}_4\text{H}_2\text{PO}_4$ were dissolved in hydrochloric acid with quantities corresponding to a Pd to P molar ratio of 0.5 in order to synthesize the desired Pd_3P phase. Herein, a six-fold excess with respect to the stoichiometrically required quantity of the phosphorus precursor was used as reported by Wu *et al.* in a similar synthesis for the formation of phase pure Pd_3P on silica.^[197] Further, the precursor solution was added to silica *via* wet impregnation, to achieve a Pd loading of 10 wt.% on the support material ($\text{Pd}_3\text{P}/\text{SiO}_2$, 10 wt.% Pd). The impregnated precursors were dried overnight at 60 °C and underwent thermal treatment.

In order to facilitate the reduction process and phase formation, pure hydrogen was selected as the thermal treatment atmosphere. Varying temperatures of 200, 300 and 400 °C were applied for 4 h in stagnant H_2 atmosphere to observe the impact of reduction temperature and evolution of the phase formation. The reduction of the impregnated precursors performed at 200 °C resulted in the formation of a pure Pd phase (Figure 10, I). An increase in temperature to 300 °C resulted in a mixed phase consisting of Pd_3P and Pd, as the reflex corresponding to Pd at a diffraction angle of 46° is still visible in the diffractogram (Figure 10, II). Upon further increasing the temperature to 400 °C, phase pure Pd_3P on silica was obtained, as evidenced by the appearance of well-defined reflexes corresponding to the orthorhombic crystal structure of Pd_3P , in agreement with data from the ICSD database (Figure 10, III). The PXRD patterns

recorded at different reduction temperatures suggest a mechanism indicative of the Pd_3P phase formation. The decomposition of the palladium precursor and the formation of Pd occurs at low temperature (200 °C). Further on increase in temperature, phosphorus starts incorporating into the Pd matrix and forming a mixed phase at higher temperature (300 °C). Finally, the phase formation of Pd_3P was completed through the incorporation of sufficient P at even higher temperature (400 °C), thereby obtaining phase pure Pd_3P supported on silica ($\text{Pd}_3\text{P}/\text{SiO}_2$, 10 wt.% Pd). The evolution of ammonia and water vapor during the thermal treatment can be concluded from the decomposition equation of ammonium dihydrogen phosphate reported in the literature.^[198]

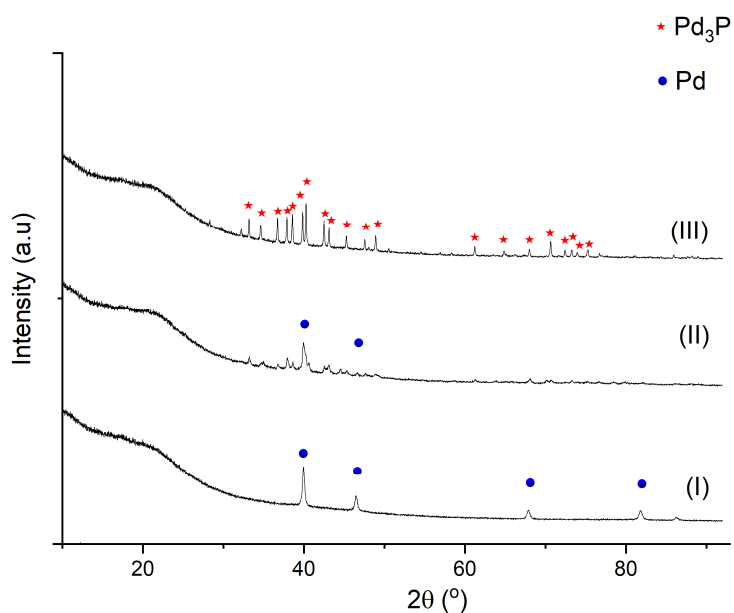


Figure 10: PXRD patterns obtained after performing the thermal treatment of the impregnated precursors at varying temperatures of I) 200 °C, II) 300 °C and III) 400 °C for the synthesis of $\text{Pd}_3\text{P}/\text{SiO}_2$ (10 wt.% Pd). Reference patterns for the phase identification - Pd_3P : ICSD 85525 and Pd: ICSD 52251. This figure has been adapted from reference^[199] (license CC BY-NC 4.0).

The significance of the thermal treatment atmosphere was studied through the application of argon atmosphere. After performing the thermal treatment for 4 h at 500 °C in argon, the resulting product was analyzed by PXRD, which revealed the formation of Pd_6P (Figure 11, I). The formation can be attributed to the thermal decomposition of the Pd precursor and the reducing effect of ammonia, which is formed during the decomposition of ammonium dihydrogen phosphate. However, the incorporation of phosphorus was limited leading to the formation of the Pd rich palladium phosphide phase Pd_6P . A further increase in temperature to 700 °C resulted in the formation of pure Pd, indicating the loss of P from the structure at high temperatures (Figure 11, II). Hence, the selection of thermal treatment atmosphere and temperature is very crucial for the formation of the target Pd_3P phase on support silica.

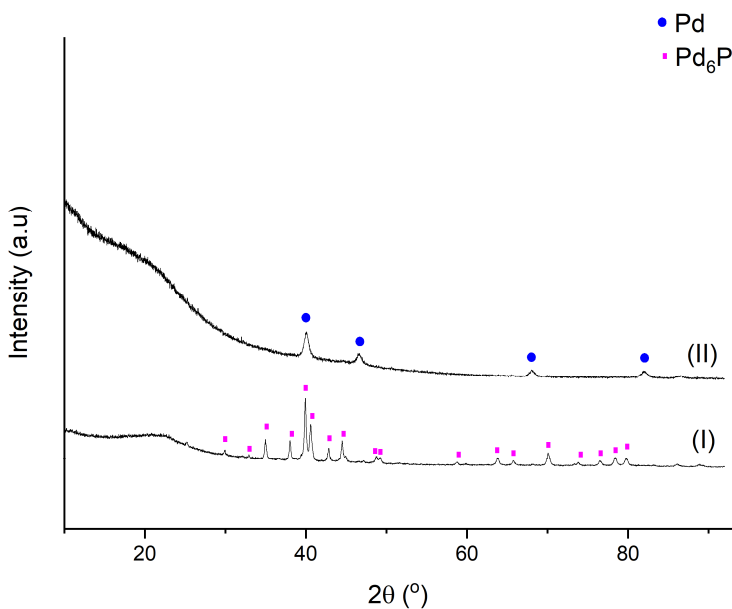


Figure 11: PXRD patterns of the supported catalysts after performing the thermal treatment in argon atmosphere at I) 500 °C and II) 700 °C. Reference patterns for the phase identification - Pd₆P: ICSD 26898 and Pd: ICSD 52251. This figure has been adapted from reference^[199] (license CC BY-NC 4.0).

In order to ensure the complete decomposition of the impregnated precursors at the selected reduction temperature of 400 °C, a thermogravimetry analysis coupled with differential thermal analysis was performed (TG-DTA). An understanding of the effect of thermal treatment is very important to ensure the complete decomposition of the catalytically active palladium precursor (Pd(OAc)₂). This will essentially assist to rule out the possibility of non-decomposed palladium precursors as true catalysts in the homogeneous phase. Due to safety concerns and the absence of equipment for thermal treatment in pure hydrogen, the analysis was carried out under a nitrogen atmosphere. A mass loss of approximately 15 wt.% accompanied by an endothermic spike was observed till 290 °C, indicating the complete decomposition of the precursors at this temperature (Figure S2). Hence, the presence of catalytically active palladium acetate residue can be completely ruled out in the catalyst synthesized at 400 °C. A reference Pd catalyst (Pd/SiO₂, 10 wt.% Pd) was also synthesized under similar conditions (without the addition of P precursor) and characterized by PXRD (Figure S3, I).

For the more in-depth characterization of Pd₃P/SiO₂ (10 wt.% Pd) scanning electron microscopy (SEM) and energy-dispersive X-ray (EDX) spectroscopy were utilized. Imaging Pd₃P nanoparticles on the silica support using SEM was challenging, due to the low contrast between the particles and the support material, low resolution of SEM as well as the porous nature of the support (Figure S4). However, EDX elemental mapping provided valuable insights into the distribution of palladium and phosphorus on the silica support. Quantitative EDX analysis performed at multiple positions across the sample, followed by averaging, resulted in a P/Pd molar ratio of approximately 2.27. This value is slightly higher than the

expected ratio of 2.0, based on the quantity of the precursor materials. EDX maps revealed a non-uniform distribution of Pd and P, with Pd-rich regions suggesting the presence of Pd_3P nanoparticles (Figure 12a). The phosphorus enriched areas are attributed to residual phosphorus species from excess precursors that did not participate in the formation of the Pd_3P phase and remained distributed over the support (Figure 12a).

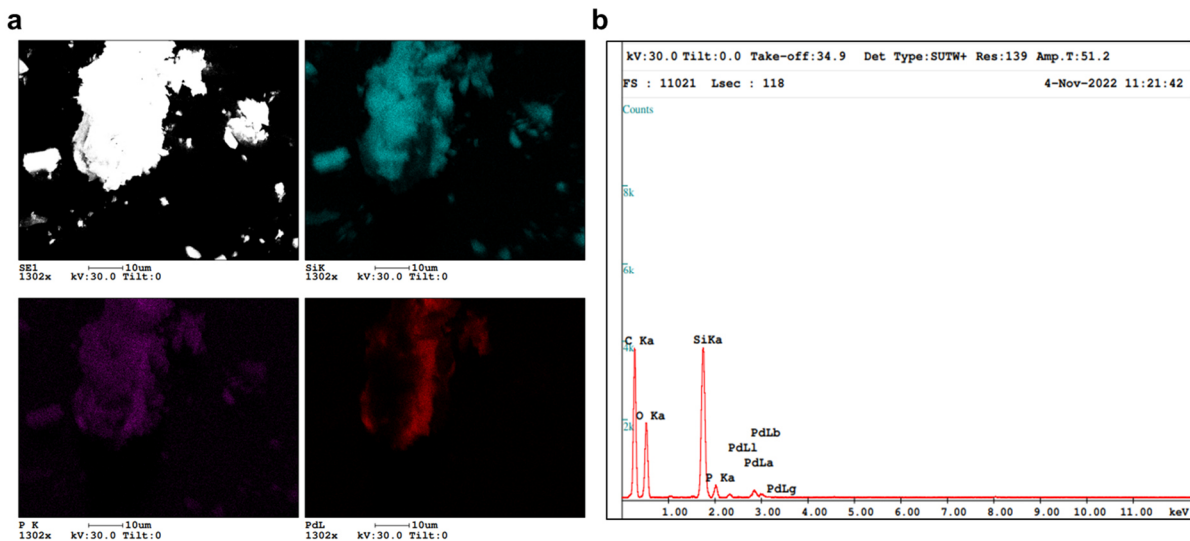


Figure 12: a) SEM image of $\text{Pd}_3\text{P}/\text{SiO}_2$ (10 wt.% Pd) and EDX mapping of Si, P as well as Pd and b) sample EDX spectra collected for the quantification of Pd and P. This figure has been adapted from reference^[199] (license CC BY-NC 4.0).

To obtain accurate quantification of Pd and P in $\text{Pd}_3\text{P}/\text{SiO}_2$ (10 wt.% Pd), inductively coupled plasma atomic emission spectroscopy (ICP-AES) analysis was performed. The quantification showed 9.28 wt.% of Pd and 5.23 wt.% of P in the sample, corresponding to a Pd/P molar ratio of 2.0, which is in good agreement with the precursor quantities used. Thereby it can be inferred that the difference in molar ratio observed from EDX may be originated from the non-uniform distribution of Pd and P in the sample.

Surface analysis

XPS measurements were performed for $\text{Pd}_3\text{P}/\text{SiO}_2$ (10 wt.% Pd) to investigate its surface characteristics (Figure 13). In the literature, for metallic palladium at zero oxidation state, Pd^0 , the binding energies are assigned as 340.5 eV and 335.2 eV for $3\text{d}_{3/2}$ and $3\text{d}_{5/2}$, respectively.^[200] In the case of silica supported Pd (Pd/SiO_2), Pd $3\text{d}_{5/2}$ is assigned in the range of 335.1 eV to 335.4 eV, due to metal-support interactions.^[201] In the performed measurement of $\text{Pd}_3\text{P}/\text{SiO}_2$ (10 wt.% Pd), signals were observed at slightly higher binding energies of 340.9 eV and 335.6 eV, which can be attributed to $3\text{d}_{3/2}$ and $3\text{d}_{5/2}$ signals of palladium in a slightly oxidized state ($\text{Pd}^{\delta+}$), revealing an electron transfer from Pd to P. Two P2p signals were observed at binding energies of 134.0 eV and 134.9 eV, corresponding to PO_4^{3-} , which most likely stems from the excess of ammonium dihydrogen phosphate used for the synthesis.^[202] However, signals corresponding to other phosphorus species were not

observed, possibly due to the low concentration of $P^{\delta-}$ (result of the charge transfer between Pd and P) or any other species. A table showing the assignments of species is provided in the appendix as Table S1. Hence the XPS measurement provided an indication about the charge transfer between Pd and P, indicating an electronic modulation due to phosphorus incorporation.

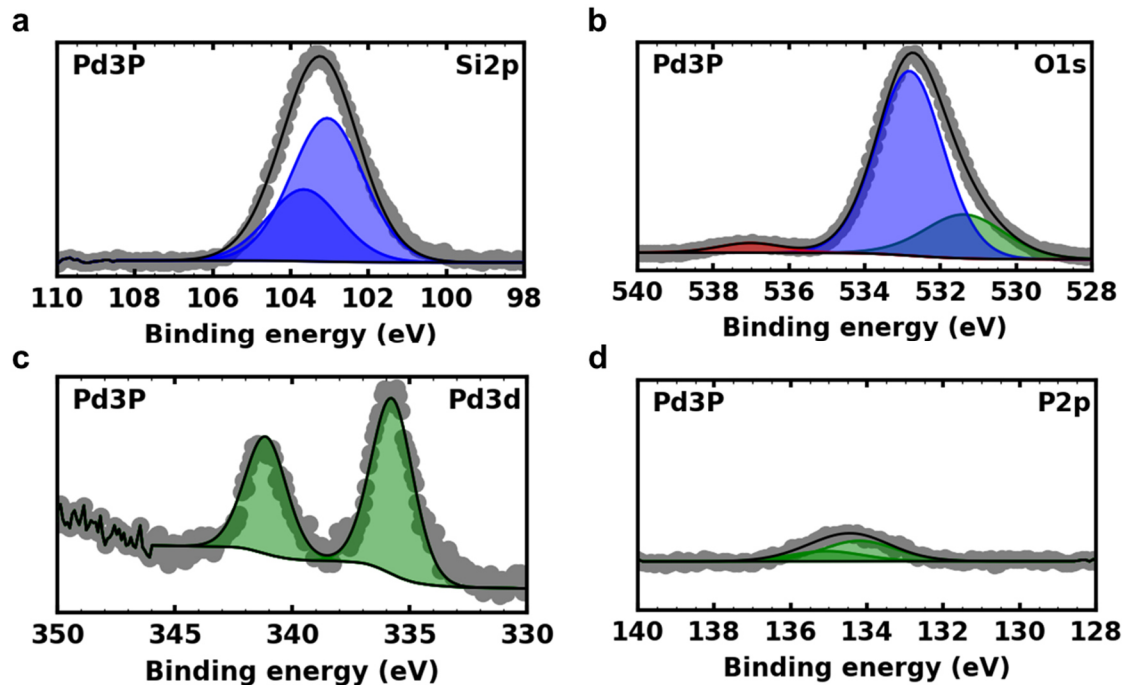
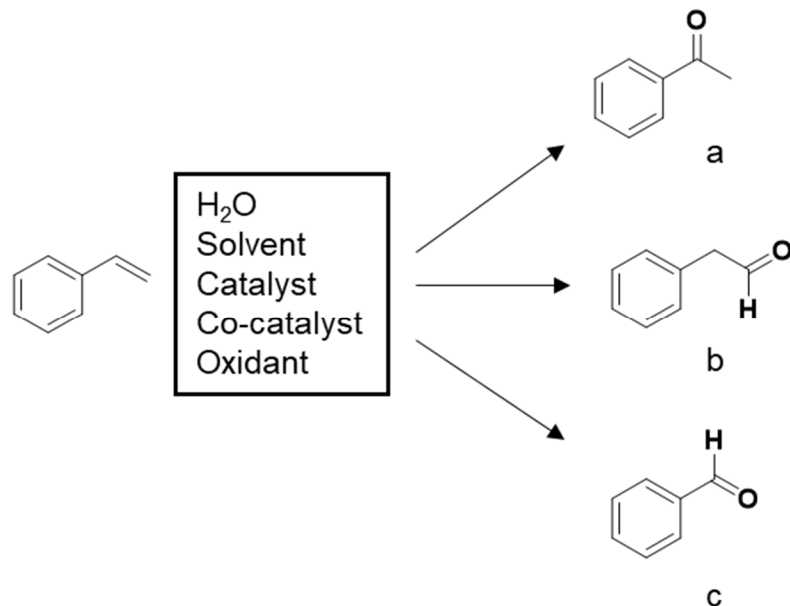


Figure 13: XP spectra of a) Si, b) O, c) Pd and d) P species of Pd_3P/SiO_2 (10 wt.% Pd) catalyst. This figure has been adapted from reference^[199] (license CC BY-NC 4.0).

3.2 Catalytic performance in the Wacker-Tsuji oxidation

The synthesized $\text{Pd}_3\text{P}/\text{SiO}_2$ (10 wt.% Pd) catalyst was applied in the Wacker-Tsuji oxidation of styrene in batch mode. This oxidation reaction of styrene can result in two products, namely acetophenone (Markovnikov) and phenylacetaldehyde (anti-Markovnikov). A possible side reaction of the styrene oxidation to benzaldehyde with oxidants, such as hydrogen peroxide^[203] or oxygen,^[204] can also be expected (Scheme 5).



Scheme 5: Possible reaction products expected while performing the Wacker-Tsuji oxidation of styrene: a) acetophenone, b) phenylacetaldehyde and c) benzaldehyde.

Various reaction systems have been developed for Wacker-Tsuji oxidation reactions,^[121,126,205] and four representative systems were selected for the investigation in this study. The details of the reaction systems are provided below in Table 2.

Table 2: Reaction systems used in this work for the Wacker-Tsuji oxidation of styrene. This table has been adapted from reference^[199] (license CC BY-NC 4.0).

System	Substrate	Reagents	Reference
A	Styrene	CuCl , O_2 (1.4 bar), $\text{THF}/\text{H}_2\text{O}$ (4:1)	Donck <i>et al.</i> ^[121]
		CuCl_2 , O_2 (1.4 bar), $\text{THF}/\text{H}_2\text{O}$ (4:1)	Donck <i>et al.</i> ^[121]
C		H_2O_2 , H_2SO_4 , MeCN	Xia <i>et al.</i> ^[205]
D		H_2O_2 , H_2O , CH_3COOH	Vafaeenezadeh <i>et al.</i> ^[126]

The investigation of the catalyst performance was started with system A using $\text{Pd}_3\text{P}/\text{SiO}_2$ (10 wt.% Pd) as catalysts and cuprous chloride (CuCl) as co-catalyst. A co-catalyst is important in order to re-oxidize the $\text{Pd}(0)$ species to the catalytically active $\text{Pd}(\text{II})$ during the catalytic

cycle, as shown before in the reaction mechanism (Figure 5). The reaction was performed for 6 h at 50 °C, with 2 mol% catalyst concentration, calculated based on the Pd and the substrate content. A styrene conversion of 20 % was observed, with 100 % selectivity towards acetophenone (Table 3, entry 1). A further increase in reaction time to 16 h did not show any further progress in conversion, indicating the termination of the catalytic cycle (Table 3, entry 2). This can be explained by the possible disproportionation of Cu(I) to Cu(II) and inactive Cu, resulting in an hindered re-oxidation of Pd (0).^[206] However, the use of CuCl₂ instead of CuCl in this reaction system under the same conditions resulted in very promising results. A reaction carried out for 6 h resulted in a styrene conversion of 51 % with 90 % selectivity to acetophenone (Table 3, entry 4). A further increase in reaction temperature to 16 h led to 95 % styrene conversion and an acetophenone selectivity of 73 % (Table 3, entry 5). A drop in selectivity of acetophenone can be observed at higher level of conversion, with 26 % benzaldehyde formation and trace amounts (1 %) of phenylacetaldehyde. The formation of benzaldehyde can be explained by the oxidation of styrene (side reaction), possibly catalyzed by the silica support under the oxygen atmosphere (1.4 bar pressure) in the reaction system during the prolonged reaction time of 16 h.^[204] Blank tests conducted without a catalyst for the reaction systems A and B for 16 h resulted in no conversion of styrene, indicating the crucial role of a catalyst for performing the Wacker-Tsuji oxidation reaction (Table 3, entry 3 and 6).

The Wacker-Tsuji oxidation of styrene was further investigated in a chlorine free system by avoiding the use of copper chlorides and using a different oxidant. Therefore, reaction system C was employed with H₂O₂ and H₂SO₄ as alternative oxidants. A reaction performed for 6 h at 50 °C, with 2 mol% catalyst concentration resulted in 44 % styrene conversion with 100 % selectivity to acetophenone (Table 3, entry 7). A blank test performed (without a catalyst) showed no conversion of styrene to acetophenone (Table 3, entry 8). Even though the results were promising, post reaction analysis showed the complete digestion of the catalyst, due to the presence of H₂O₂ and H₂SO₄ essentially creating a piranha solution effect. Also, slight damages to the reactor interiors were observed after performing the system C based reactions. Hence, no further reactions were performed under these conditions.

The investigation of the reaction systems was extended to system D using hydrogen peroxide and acetic acid. A promising styrene conversion of 60 % with 100 % acetophenone selectivity was observed when the reaction was performed for 6 h at 50 °C, with 2 mol% catalyst concentration (Table 3, entry 9). An increased conversion of 70 % with a drop in selectivity of acetophenone to 86 % was witnesses when the reaction time was increased to 16 h. Benzaldehyde and trace amount of phenylacetaldehyde were hereby observed as side products (Table 3, entry 10). In order to gain an insight into the dependency of the reaction with respect to the catalyst concentration, the Pd concentration in the reaction was doubled to 4 mol%. A reaction performed for 6 h resulted in 10 % higher conversion amounting to 71 %

(Table 3, entry 11), while maintaining the selectivity to acetophenone (100 %). This result indicates the positive correlation between the catalyst concentration and the reaction progress.

Table 3: Results of the catalysts testing in various reaction systems. This table has been adapted from reference^[199] (license CC BY-NC 4.0).

Entry	System	Catalyst	Catalyst concentration (mol%)	Temp. (°C)	Time (h)	Conv. (%)	Ap. Select. (%)
1	A ^[a]	Pd ₃ P/SiO ₂	2	50	6	20	100
2	A ^[a]	Pd ₃ P/SiO ₂	2	50	16	20	100
3	A ^[a]	-		50	16	nil.	nil.
4	B ^[b]	Pd ₃ P/SiO ₂	2	50	6	51	90
5	B ^[b]	Pd ₃ P/SiO ₂	2	50	16	95	73
6	B ^[b]	-		50	16	nil.	nil.
7	C ^[c]	Pd ₃ P/SiO ₂	2	50	6	44	100
8	C ^[c]	-		50	6	nil.	nil.
9	D ^[d]	Pd ₃ P/SiO ₂	2	50	6	60	100
10	D ^[d]	Pd ₃ P/SiO ₂	2	50	16	70	86
11	D ^[d]	Pd ₃ P/SiO ₂	4	50	6	71	100
12	D ^[d]	Pd ₃ P/SiO ₂	2	80	6	77	60
13	D ^[d]	Pd ₃ P/SiO ₂	2	80	14	80	44
14	D ^[d]	-		80	6	70	nil.
15	B ^[e]	Pd/SiO ₂	2	50	16	80	63

^[a] Reaction conditions system A: styrene (1 mmol), CuCl (20 mol%), THF (2 mL), H₂O (0.5 mL), pressure(O₂) = 1.4 bar. ^[b] Reaction conditions system B: styrene (1 mmol), CuCl₂ (20 mol%), THF (2 mL), H₂O (0.5 mL), pressure (O₂) = 1.4 bar. ^[c] Reaction conditions system C: styrene (1 mmol), 30 % H₂O₂ (3 mmol), 70 % H₂SO₄ (0.013 mL), MeCN (2.5 mL). ^[d] Reaction conditions system D: styrene (1 mmol), 30 % H₂O₂ (3 mmol), acetic acid (1.4 mL), H₂O (0.6 mL). ^[e] Pd/SiO₂, 10 wt.% Pd was used as the catalyst. Catalyst concentration was calculated with based on styrene and Pd content in the catalyst. The selectivity was calculated as Ap. Select. (acetophenone selectivity) = moles of acetophenone formed/moles of styrene converted. The quantifications were performed using GC-MS analysis and *n*-decane as internal standard.

In order to minimize the precious metal utilization, further tests were conducted with 2 mol% catalyst concentration. The effect of the elevated temperature on the reaction was examined by increasing the temperature to 80 °C and conducting the reaction for 6 h. An increase in conversion by 17 % in comparison to the reaction performed at 50 °C, was observed with a severe drop in acetophenone selectivity to 60 % and (Table 3, entry 12) further to 44 % by increasing the reaction time to 14 h (Table 3, entry 13). An increase in reaction temperature

has clearly facilitated the benzaldehyde formation, due to the possible side reaction of styrene with hydrogen peroxide.^[203] Interestingly, a reaction at 80 °C for 6 h without a catalyst resulted in a styrene conversion of 70 %, (Table 3, entry 14) with benzaldehyde and 1-phenyl-1,2-ethanediol as major products. This clearly indicates the non-catalytic nature of the benzaldehyde formation under the applied reaction conditions. The formation of diols might result from the hydrolysis of an epoxide (styrene oxide), which is another possible product of the styrene oxidation with H₂O₂.^[207] No acetophenone was observed in the absence of the catalyst.

While analysing the performance of Pd₃P/SiO₂ (10 wt.% Pd) in the various reaction systems (A to D), system A with CuCl as the co-catalyst can be considered inferior to other systems. The inherently aggressive nature of system C, containing H₂O₂ and H₂SO₄, leads to the digestion/dissolution of the catalyst making this reaction system less applicable. A comparison between systems B and D leads to the following conclusions:

- A higher conversion of styrene was achieved with system B (95 %), in comparison to system D (70 %) when the reaction was performed under similar reaction conditions (50 °C, 16 h). However, the acetophenone selectivity for system B was lower (73 %) in comparison to system D (86 %). An overall assessment made by calculating the approximate acetophenone yield (selectivity · conversion) shows 69.4 % for system B and 60 % for system D, indicating a slightly better performance of system B.
- System B, which consists of CuCl₂, can lead to the formation of chlorinated by products and possible corrosion.^[206,208] Also chloride-containing systems can have a negative impact on the environment.^[208] Moreover, the presence of homogeneous Cu species in the system necessitates efforts to remove the metal after the reaction to avoid product contamination. System D has no such adverse effects.

A trade-off exists between catalytic performance and the operational and environmental drawbacks of the reaction systems. Hence in an application perspective, the selection should therefore be guided by the specific priorities and requirements.

Reference catalysts

The effect of the incorporation of phosphorus into Pd forming Pd₃P, during the catalytic performance was investigated considering system B. For this purpose, pure Pd nanoparticles supported on silica (Pd/SiO₂, 10 wt.% Pd) were synthesized using the same synthetic procedure, as described before, however without addition of any P precursor. A reaction performed with Pd/SiO₂ (10 wt.% Pd) for 16 h at 50 °C with 2 mol% catalyst concentration (Pd based) resulted in a styrene conversion of 80 % and a acetophenone selectivity of 63 % (Table 3, entry 15). Both conversion and selectivity are lower in comparison to Pd₃P/SiO₂ (10 wt.% Pd (Table 3, entry 5). Moreover, it was observed that 22 % phenylacetaldehyde (anti-

Markovnikov) product was formed during the reaction with Pd/SiO_2 (10 wt.% Pd) indicating a lower Markovnikov selectivity in comparison to the Pd_3P catalyst. These results point towards a superior performance of supported palladium phosphide (Pd_3P) in comparison to a purely Pd-based catalyst in the Wacker-Tsuji oxidation of styrene, indicating the success of the underlying catalyst design principle.

The performance comparison was further extended to several literature reported Pd-based heterogeneous catalysts, which were applied in conjunction with reaction system B. The Wacker-Tsuji oxidation of styrene performed by Byun *et al.* using $\text{Pd-Fe}_3\text{O}_4$ heterodimer nanocrystals^[209] at 70 °C for 18 h resulted in only 20 % acetophenone selectivity (calculated from the reported yield and conversion), whereas $\text{Pd}_3\text{P/SiO}_2$ (10 wt.% Pd) at even milder reaction conditions of 50 °C for 16 h showed 73 % acetophenone selectivity at similar levels of conversion (Table 3, entry 5). However, the authors have used a different solvent (ethanol) in comparison to this work. Zhang *et al.* reported the application of Pd nanoparticles on zirconia with 10 wt.% Pd loading (Pd/ZrO_2). With the same reaction system B, however without using a copper co-catalyst, Pd/ZrO_2 at 80 °C for 20 h only showed 32 % conversion of styrene with 15 % acetophenone yield.^[118] This example indicates the possibility of applying the catalyst in this work under a co-catalyst free conditions. No promising results without a co-catalyst were obtained till date, however this opens a wide possibility in terms of variation in reaction conditions and catalysts synthesis procedure.

Recovery and stability tests

The stability of $\text{Pd}_3\text{P/SiO}_2$ (10 wt.% Pd) was evaluated by performing recovery experiments considering reaction system D. A schematic diagram illustrating the procedure used for the recovery experiment is presented in Figure 14. The selection of system D was based on the ease of catalyst separation, as the CuCl_2 in system B made the catalyst separation challenging. The catalyst recovered from the first round of testing (Table 3, entry 10) was initially analyzed by PXRD to obtain information regarding the phase stability. The PXRD showed phase pure Pd_3P on silica, indicating the stability of the phase under the test conditions (Figure 15a). However, a reduced crystallinity was observed, which can indicate the possibility of catalyst leaching. The recovered catalyst was further applied in the Wacker-Tsuji oxidation reaction of styrene with system D under the same reaction conditions (condition as in Table 3, entry 10). A decline in activity was observed in the second round, as the styrene conversion was reduced by 20 % resulting in 50 % conversion. After this test, the catalyst was recovered and tested again in the oxidation reaction. A further decline in conversion to 40 % was observed, indicating the further loss of catalytic activity (Figure 15b). However, in all the three rounds the selectivity towards acetophenone remained the same (86 %).

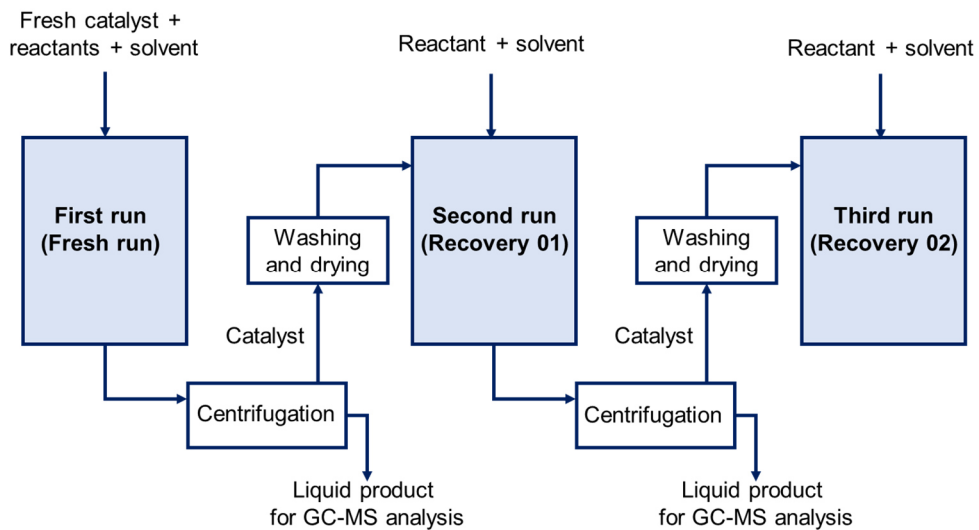


Figure 14: Schematic diagram showing the procedure for the recovery experiments.

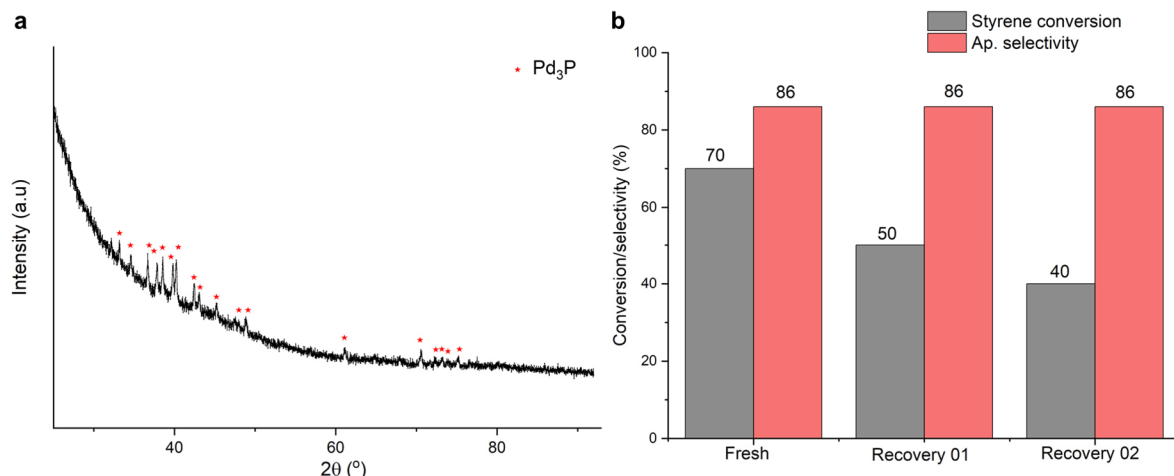


Figure 15: a) PXRD pattern of the recovered $\text{Pd}_3\text{P}/\text{SiO}_2$ (10 wt.% Pd) catalyst and b) catalyst recovery tests, showing the decline in activity. Reaction conditions system D: styrene (1 mmol), 30 % H_2O_2 (3 mmol), acetic acid (1.4 mL), H_2O (0.6 mL), catalyst (2 mol%, Pd basis), 50 °C, 16 h. This figure has been adapted from reference^[199] (license CC BY-NC 4.0).

The decline in catalytic activity observed during the recovery tests prompted an investigation into potential catalyst leaching. Subsequently, leaching was assessed using ICP-AES analysis of the recovered catalyst from the first round of testing applying reaction system D. Significant Pd leaching was observed, with losses ranging from 44 % to 75 %, depending on the test conditions, as determined by comparing the Pd content in the fresh and recovered catalysts (Table 4). This loss of catalytically active Pd sites can be seen as the primary reason for the loss of catalytic activity in the recovery runs. The severe leaching of Pd can be attributed to the presence of acetic acid in system D^[210] and possible loss of Pd₃P nanoparticles from the silica support, due to the poor metal-support interactions. Hence, strategies have to

investigated to minimize metal leaching and enhance metal-support interactions in order to develop stable palladium phosphide-based catalysts for oxidation reactions.

Table 4: Results of the ICP-AES analysis showing the metal leaching of the $\text{Pd}_3\text{P}/\text{SiO}_2$ (10 wt.% Pd) catalyst. This table has been adapted from reference ^[199] (license CC BY-NC 4.0).

Entry	Reaction temperature (°C)	Reaction time (h)	wt.% of Pd in the recovered catalyst	wt.% of Pd leached
1	50	6	3.25	65
2	80	6	5.25	44
3	50	16	2.30	75
4	80	14	3.02	67

Reaction conditions system D: styrene (1 mmol), 30 % H_2O_2 (3 mmol), acetic acid (1.4 mL), H_2O (0.6 mL), catalyst (2 mol%, Pd basis), 50 °C, 16 h.

3.3 Theoretical insight into the activity improvement

The improved performance of Pd_3P compared to pure Pd, in terms of both activity and selectivity, was observed during the catalyst testing. To gain insights into the possible reasons behind this enhancement, the crystal structures of Pd_3P and Pd were investigated. Pd_3P crystallizes in an orthorhombic structure with the *Pnma* space group, leading to two inequivalent Pd sites (Pd(1) and Pd(2)) based on their bonding environments (Figure 16). In contrast, Pd crystallizes in a cubic structure with the *Fm-3m* space group, where all Pd atoms are equivalent.^[33,211] This fundamental structural information itself highlights the difference in the spatial arrangement of Pd atoms in Pd_3P and Pd. In Pd_3P , the shortest distance between two Pd(1) sites is 2.77 Å, whereas other Pd–Pd are found to be slightly longer (Pd(1) and Pd(2): 2.83 Å, Pd(2) and Pd(2): 3.22 Å).^[211] Meanwhile, in pure Pd, all Pd–Pd bond lengths are uniformly 2.77 Å.^[33] The variation in Pd–Pd distances in Pd_3P , ranging from 2.77 Å to 3.22 Å, indeed arises from the phosphorus incorporation. As a result, spatially separated Pd sites, which can serve as active catalytic centers are present in Pd_3P , unlike in pure Pd. Furthermore, the presence of phosphorus introduces two inequivalent Pd sites with distinct bonding environments, resulting in electronically different active sites.

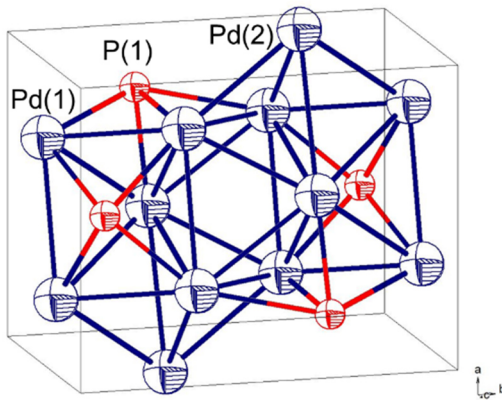


Figure 16: Crystal structure of Pd_3P showing the inequivalent Pd sites. This figure has been adapted from reference^[199] (license CC BY-NC 4.0).

The electron transfer from Pd to P in Pd_3P imparting a partial positive charge to Pd was observed in XPS analysis of $\text{Pd}_3\text{P}/\text{SiO}_2$ (10 wt.% Pd), pointing towards the electronic modulation of the palladium sites. Such partial charges on Pd were also reported in the XPS analysis of Pd_3P nanoparticles in other works, due to the Pd to P electron transfer.^[68] Thus, the separation of active sites and modulation of their electronic properties, which influences the binding characteristics of substrates and intermediates, can be considered a key reason for the improved catalytic performance of Pd_3P relative to Pd.

3.4 Concluding remarks

Supported palladium phosphide nanoparticles, with a phase corresponding to Pd_3P ($\text{Pd}_3\text{P}/\text{SiO}_2$, 10 wt.% Pd), were synthesized, comprehensively characterized and successfully applied in the Wacker-Tsuji oxidation of styrene. Four different reaction systems were explored to evaluate the catalyst performance, and the synthesized palladium phosphide catalyst demonstrated activity across all systems. Notably, $\text{Pd}_3\text{P}/\text{SiO}_2$ (10 wt.% Pd) exhibited superior activity and selectivity compared to the supported Pd reference catalyst (Pd/SiO_2 , 10 wt.% Pd). Only trace amounts of the anti-Markovnikov product were observed in reactions using $\text{Pd}_3\text{P}/\text{SiO}_2$, while the significant formation of the anti-Markovnikov product was seen using Pd/SiO_2 as catalyst. The exceptional performance of the palladium phosphide catalyst can potentially be attributed to spatially separated Pd sites with modified electronic structures, resulting from the phosphorus incorporation. Hence, the element synergy approach applied through the combination of a d-block metal (Pd) with a p-block non-metal (P) for the catalyst design was proven to be successful for the Wacker-Tsuji oxidation reaction.

Although the catalysts exhibited promising activity and selectivity, a poor stability was observed in the acetic acid and hydrogen peroxide-based reaction system, as shown by recovery experiments and metal leaching studies. This highlights the need to implement strategies that minimize active metal leaching and strengthen metal-support interactions. Also, for future work, specific approaches, such as the tuning particle size or altering the support material, should be explored to further enhance the catalytic performance. Additionally, testing a broader range of industrially relevant substrates for their compatibility with Pd–P catalysts is essential. As an initial step, in collaboration with the group of Prof. Dr. Michael Meier (IOC, KIT), successful reactions with methyl oleate were conducted using $\text{Pd}_3\text{P}/\text{SiO}_2$ as catalysts.

4 Support engineering for Heck coupling reactions

The results discussed in this chapter were published in:

A. Neyyathala, F. Flecken, F. Rang, C. Papke, S. Hanf, *Chem. Eur. J.* **2024**, *30*, e202302825 under the license CC BY-NC 4.0.

Figures 17, 18, 19, 20, 21, 22, 23, 24, S5, S6, S7, S8, S9, S10, S11, S12, S13, S14, S15 and Tables 5, 6, 7, 8, 9, S2, S3, S4 are adapted from this publication.

Liquid-phase reactions with heterogeneous catalysts always pose the challenge of catalyst deactivation, due to leaching of the active metal into solution. This effect was also observed in the palladium phosphide-catalyzed Wacker-Tsuji oxidation discussed in chapter 3, where a substantial decline in catalytic activity was noted in the recovery tests, resulting from significant palladium leaching. Therefore, the design of stable catalysts that prevent metal leaching is crucial for extending the catalyst lifetime and therewith for contributing to a more sustainable use and reuse of metal resources. Moreover, minimizing or preventing metal leaching helps to avoid any potential product contamination, thereby facilitating an industrial application.

A reaction in which metal leaching has been reported in a number of studies is the Heck coupling reaction.^[157,212] This reaction, which involves the reaction of an aromatic halide or triflate with an alkene, forming an intermolecular C–C bond formation, is an industrially relevant reaction typically catalyzed by molecular palladium complexes.^[130–133] Also, numerous heterogeneous catalyst systems have been explored for this reaction.^[144,145,148] As mentioned before, a major limitation of these systems is the leaching of metal species, leading to a significant decline in catalytic activity in subsequent reaction runs.^[157] In this study, a strategy combining element synergy (d-block-p-block element combination) and support modification is proposed to mitigate metal leaching in Heck coupling reactions. For this purpose, palladium phosphide (Pd_3P) and pure palladium nanoparticles were synthesized on silica modified with phosphorus species and applied in the Heck coupling reaction with various substrates. The modification of the support through the incorporation of phosphorus species, as carried out in this work, is hereafter referred to as “support engineering”, since the addition of these species effectively tailors the support’s properties.

4.1 Synthesis and characterization of palladium phosphide on phosphorus-modified supports

The ability of phosphorus species to enhance the stability of heterogeneous catalysts is discussed in the context of many reactions, such as dehydrogenation reactions,^[213] oxidation reactions,^[214] and dry reforming.^[215] Such exceptional stability is often due to an anchoring

effect between phosphorus species on the support with metal species through an improvement of the metal-support interactions.^[213,214] Based on this experimental evidence, phosphorus was selected for the support modification of silica as part of this work. Several phosphorus precursors were reported as suitable choices to modify supports, including phosphoric acid (H_3PO_4),^[216] triphenylphosphine (PPh_3),^[217,218] diammonium hydrogen phosphate ($(NH_4)_2HPO_4$),^[219] etc. Herein, ammonium dihydrogen phosphate ($NH_4H_2PO_4$) was selected to modify the silica support, due to the ease of handling, non-toxicity and non-corrosive character.

To synthesize phosphorus-modified SiO_2 , an aqueous solution of $NH_4H_2PO_4$ was impregnated on silica (incipient wetness impregnation) and calcined in air. Depending on the loading of phosphorus on silica (based on the added $NH_4H_2PO_4$ quantity), the P-modified supports were labelled as 0.5P- SiO_2 , 1P- SiO_2 and 5P- SiO_2 , corresponding to 0.5 wt %, 1 wt % and 5 wt % P loading, respectively. During the calcination, $NH_4H_2PO_4$ decomposes into ammonia (NH_3) and phosphoric acid (H_3PO_4),^[220] with the latter serving as a precursor for the final phosphorus species. To ensure the complete decomposition of $NH_4H_2PO_4$ and subsequent transformation of H_3PO_4 , an appropriate calcination temperature had to be selected. For this purpose, a TG-DTA analysis (Figure S5) was conducted using the 5P- SiO_2 precursor ($NH_4H_2PO_4$ impregnated on silica). Two endothermic peaks were observed near 200 °C and 350 °C (indicated as A and B in Figure S5), accompanied by a significant mass loss of approximately 7 % up to 400 °C. The initial endothermic event around 200 °C most likely corresponds to the decomposition of $NH_4H_2PO_4$ into NH_3 and H_3PO_4 .^[220] The continued mass loss and endothermic peak around 350 °C suggest further transformations of H_3PO_4 . Beyond 400 °C, a negligible mass loss and no significant thermal events were detected (Figure S5). Based on these observations, 600 °C was selected as the calcination temperature to facilitate the formation of phosphorus species on silica. Therefore, all P-modified supports (0.5P- SiO_2 , 1P- SiO_2 and 5P- SiO_2) were prepared by impregnation of $NH_4H_2PO_4$ followed by calcination in air at 600 °C.

PXRD analysis performed for the 5 wt.% P-containing impregnated support calcined at 600 °C (5P- SiO_2) showed an amorphous nature of the material with the absence of any reflexes (Figure S6). However, with the applied thermal treatment conditions the successful formation of phosphate species on the support can be assumed. This is also in accordance with literature reports concerning the formation of $Si_3(PO_4)_4$ and $Si(HPO_4)_2 \cdot H_2O$ on silica^[221,222] under similar reaction conditions, due to the reaction between H_3PO_4 and silica. In this study, the reflexes corresponding to such phosphate species were not observed via PXRD analysis due to the very low concentration of phosphate species on the support (Figure S6). The synthesized phosphorus-modified supports were further characterized using SEM-EDX to assess the distribution of phosphate species on the silica surface. EDX elemental mapping for 0.5P- SiO_2 was not successful, due to the phosphorus concentration being below the detection limit of the SEM-EDX technique. In contrast, successful EDX mapping of 1P- SiO_2 (Figure 17) and 5P-

SiO_2 (Figure S11) revealed a uniform distribution of phosphate species across the silica support. The elemental quantification indicated 0.86 wt.% and 3.67 wt.% phosphorus on silica corresponding to 1P- SiO_2 (Figure S10b) and 5P- SiO_2 (Figure S11b) respectively. The observed low concentration of phosphorus on the support, compared to the added amount of $\text{NH}_4\text{H}_2\text{PO}_4$, can be attributed to the loss of phosphorus during calcination at 600 °C. This analysis thereby provided an evidence for the successful support modification or support engineering with phosphorus. It is important to note that 5P- SiO_2 was synthesized only to optimize the preparation conditions of the phosphorus-modified supports by enabling clearer thermal events in TG-DTA analysis and facilitating characterization through SEM-EDX. These optimized conditions were subsequently applied to supports with lower phosphorus loading. The 5P- SiO_2 material itself was not used for any catalyst synthesis or testing.

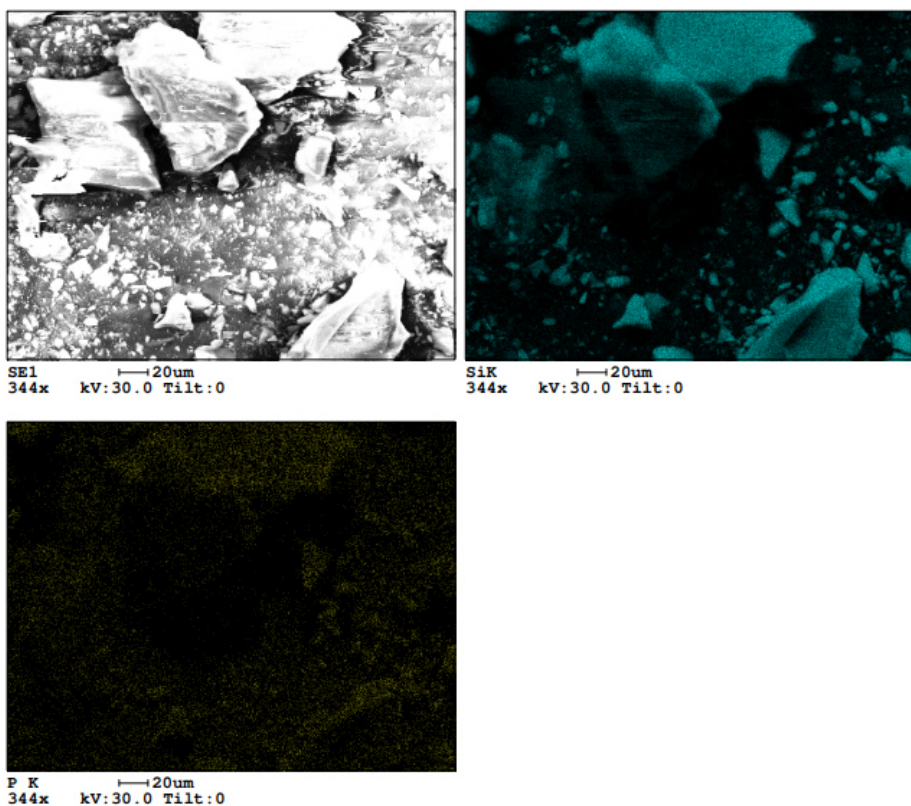


Figure 17: SEM-EDX elemental mapping of the 1P- SiO_2 support, showing the uniform distribution of P on silica. This figure has been adapted from reference^[223] (license CC BY-NC 4.0).

Synthesis of Pd_3P on phosphorus-modified supports

After the successful synthesis of phosphorus-modified supports, palladium phosphide nanoparticles were synthesized on the support using an incipient wetness impregnation approach. During the synthesis of supported Pd_3P nanoparticles as catalysts for Wacker-Tsuji oxidation reactions (chapter 3), it was observed that an excess of $\text{NH}_4\text{H}_2\text{PO}_4$ as P source was required with respect to the stoichiometric amount for the target phase formation. However, the presence of this excess P can result in the formation of further phosphorus species and

possibly interfere with the already being present phosphate species on the modified support. To circumvent this, it was important to perform a synthesis using a precursor, which limits the contribution of phosphorus species to the support, while it enables the formation of phase pure Pd_3P . Therefore, an attempt to synthesize Pd_3P nanoparticles on unmodified silica first was carried out with phosphoric acid as the P precursor of choice. Palladium acetate ($\text{Pd}(\text{OAc})_2$) was used as the Pd precursor to achieve a metal loading of 10 wt.% Pd on silica. $\text{Pd}(\text{OAc})_2$ and H_3PO_4 , with a Pd to P molar ratio of 3, were dissolved in HCl and impregnated on silica. After drying the impregnated precursors, the thermal treatment was carried out at 400 °C for 4 h in pure H_2 . When analyzing the sample by PXRD Pd_3P and Pd were both observed (Figure 18, I). Therefore, the thermal treatment/reduction time was extended to 8 h, which resulted in the formation of phase pure Pd_3P (Figure 18, II) on silica ($\text{Pd}_3\text{P}/\text{SiO}_2$, 10 wt.% Pd). This observation points towards the possible mechanism of the Pd_3P formation, which occurs through the decomposition of the precursors to Pd and further P incorporation to the metal matrix forming Pd_3P . Notably, through the application of H_3PO_4 as the phosphorus precursor, the synthesis of Pd_3P was achieved with stoichiometric quantities of precursors.

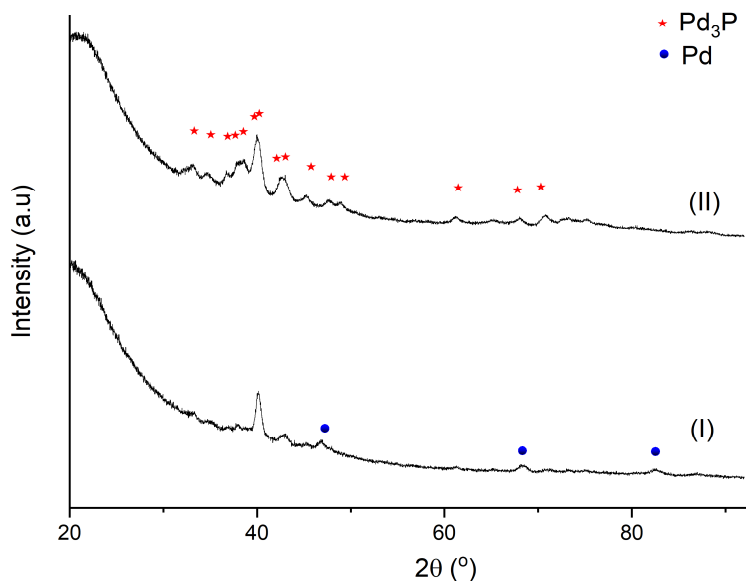


Figure 18: PXRD patterns for the impregnated precursors thermally treated under H_2 atmosphere at 400 °C for I), 4 h and II) 8 h. Reference patterns for the phase identification - Pd_3P : ICSD 85525 and Pd: ICSD 52251. This figure has been adapted from reference^[223] (license CC BY-NC 4.0).

After the successful synthesis of Pd_3P on unmodified silica, this method was further extended to the palladium phosphide nanoparticle synthesis on P-modified supports. Therefore, $\text{Pd}(\text{OAc})_2$ and H_3PO_4 with a Pd to P molar ratio of 3 were dissolved in HCl and impregnated on the P-modified supports ($0.5\text{P}-\text{SiO}_2$ and $1\text{P}-\text{SiO}_2$). The impregnated materials underwent thermal treatment for 8 h at 400 °C in stagnant H_2 atmosphere. The synthesized materials were characterized by PXRD and phase pure Pd_3P was observed in all cases (Figure 19a).

The synthesized Pd_3P on P-modified silica catalyst were labelled as $\text{Pd}_3\text{P}/0.5\text{P}-\text{SiO}_2$ (10 wt.% Pd) and $\text{Pd}_3\text{P}/1\text{P}-\text{SiO}_2$ (10 wt.% Pd). Using the same method Pd_3P nanoparticles were synthesized on 1P-SiO₂, with a reduced Pd loading of 5 and 1 wt.% ($\text{Pd}_3\text{P}/1\text{P}-\text{SiO}_2$, 5 wt.% Pd and 1 wt.% Pd). The PXRD analysis showed the formation of phase pure Pd_3P for $\text{Pd}_3\text{P}/1\text{P}-\text{SiO}_2$ (5 wt.% Pd), but with broadened reflexes possibly due to smaller crystallites in comparison to the 10 wt.% Pd loaded sample (Figure S7, II). No reflexes were observed for the $\text{Pd}_3\text{P}/1\text{P}-\text{SiO}_2$ (1 wt.% Pd) sample, due to smaller crystallites or the more amorphous nature of the sample (Figure S7, I).

Pure palladium catalysts as reference systems were also synthesized under similar conditions on the unmodified silica support (Pd/SiO_2 , 10 wt.% Pd) and on the 1P-SiO₂ support ($\text{Pd}/1\text{P}-\text{SiO}_2$, 10 wt.% Pd), and subsequently characterized by PXRD (Figure 19b). A reduced crystallinity was observed for the palladium nanoparticles synthesized on the P-modified silica ($\text{Pd}/1\text{P}-\text{SiO}_2$, 10 wt.% Pd) in comparison to Pd/SiO_2 (10 wt.% Pd). This points towards the ability of phosphorus species on the support to suppress sintering, resulting in smaller crystallites and possibility leading to the stabilization of small nanoparticles on the support.

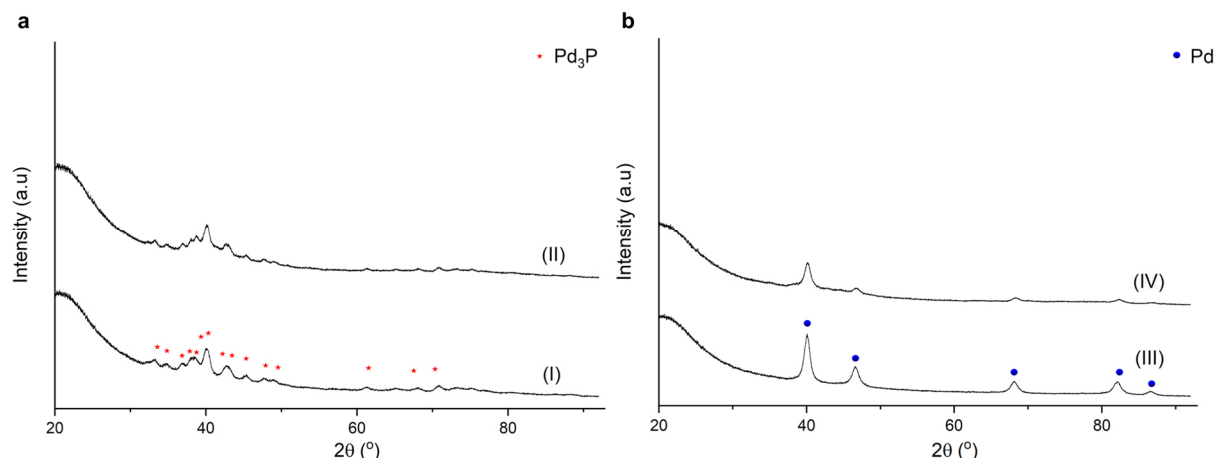


Figure 19: PXRD patterns of a) palladium phosphide on a modified supports with I) $\text{Pd}_3\text{P}/0.5\text{P}-\text{SiO}_2$ (10 wt.% Pd) and II) $\text{Pd}_3\text{P}/1\text{P}-\text{SiO}_2$ (10 wt.% Pd) and b) reference Pd catalyst on an unmodified and P-modified support with III) Pd/SiO_2 (10 wt.% Pd) and IV) $\text{Pd}/1\text{P}-\text{SiO}_2$ (10 wt.% Pd). Reference patterns for the phase identification - Pd_3P : ICSD 85525 and Pd: ICSD 52251. This figure has been adapted from reference^[223] (license CC BY-NC 4.0).

The SEM analysis of the samples to visualize the particles was challenging, due to the presence of the porous silica support and resolution limitations (Figure S12). However, EDX analysis of the samples coupled with SEM provided insights on the elemental compositions and the elemental distribution. The EDX analysis performed for the $\text{Pd}_3\text{P}/\text{SiO}_2$ (10 wt.% Pd) sample showed a uniform distribution of Pd and P on silica with a Pd to P molar ratio of 2.63 (Figure S13), which was higher than the ratio of 2.31 obtained from ICP-AES analysis (Table S3, entry 3). It is important to note that while ICP-AES provides information about the bulk elemental composition, EDX results are highly dependent on the specific spatial location of the

measurement. Similarly, EDX analysis was performed for the $\text{Pd}_3\text{P}/1\text{P}-\text{SiO}_2$ (10 wt.% Pd) catalyst from which again a uniform distribution of Pd and P on support silica was observed (Figure 20 and Figure S14a). The elemental quantification and determination of the Pd to P ratio (less than 3) indicated an excess of phosphorus corresponding to the phosphate species on silica, which was introduced for the support engineering (Figure S14b).

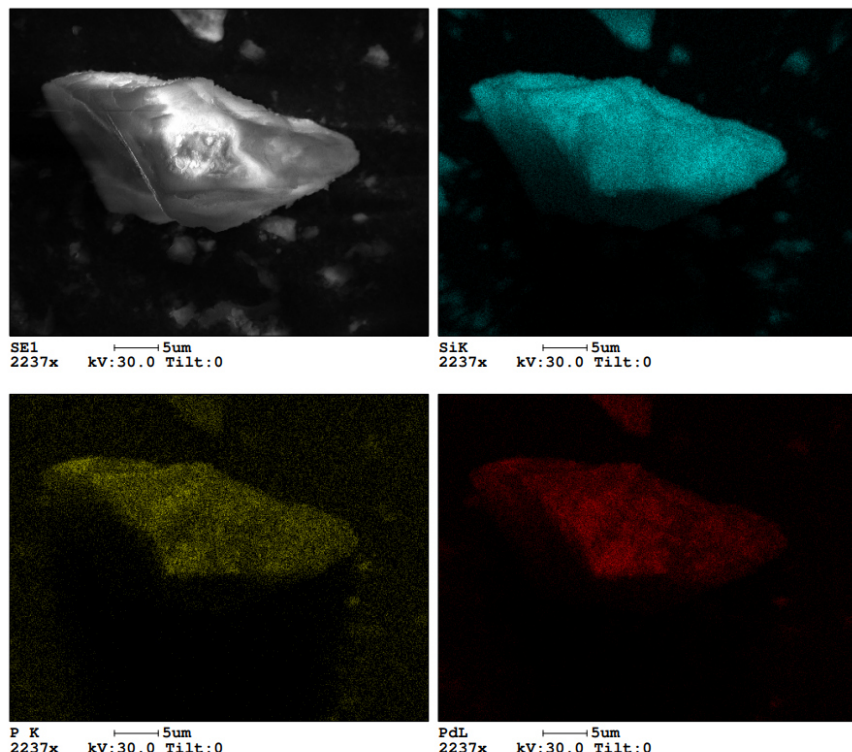


Figure 20: SEM image and EDX elemental mapping of $\text{Pd}_3\text{P}/1\text{P}-\text{SiO}_2$ (10 wt.% Pd). This figure has been adapted from reference^[223] (license CC BY-NC 4.0).

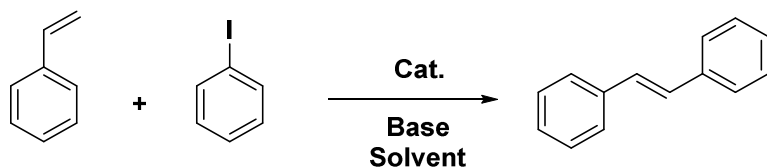
An overview of the catalysts synthesized in this work is given in Table 5 below.

Table 5: Overview of the catalysts synthesized in this work. This table has been adapted from reference^[223] (license CC BY-NC 4.0).

Catalyst	wt.% Pd	Support description
Pd/SiO_2 (10 wt.% Pd)	10	Unmodified silica
$\text{Pd}/1\text{P}-\text{SiO}_2$ (10 wt.% Pd)	10	1 wt.% P-modified silica
$\text{Pd}_3\text{P}/\text{SiO}_2$ (10 wt.% Pd)	10	Unmodified silica
$\text{Pd}_3\text{P}/0.5\text{P}-\text{SiO}_2$ (10 wt.% Pd)	10	0.5 wt.% P-modified silica
$\text{Pd}_3\text{P}/1\text{P}-\text{SiO}_2$ (10 wt.% Pd)	10	1 wt.% P-modified silica
$\text{Pd}_3\text{P}/1\text{P}-\text{SiO}_2$ (5 wt.% Pd)	5	1 wt.% P-modified silica
$\text{Pd}_3\text{P}/1\text{P}-\text{SiO}_2$ (1 wt.% Pd)	1	1 wt.% P-modified silica

4.2 Catalytic performance in the Heck coupling reaction

The synthesized samples were evaluated as catalysts in the Heck coupling reaction. All reactions were performed in batch mode. As an initial investigation, the coupling between iodobenzene and styrene was selected (Scheme 6). The substrate scope was subsequently expanded to include reactions between styrene and methyl 4-iodobenzoate, as well as iodobenzene and methyl acrylate. The synthesis of stilbene from iodobenzene and styrene was first examined with the $\text{Pd}_3\text{P}/\text{SiO}_2$ (10 wt.% Pd) catalyst. This reaction was used as starting point to optimize the reaction conditions. Since the Heck coupling reaction is significantly influenced by the choice of base and solvent, a range of bases and solvents was screened to identify the best reaction conditions. The inorganic base K_3PO_4 was used to screen the solvents, such as *N,N*-dimethylformamide (DMF), *N*-methyl-2-pyrrolidone (NMP) and dimethyl sulfoxide (DMSO). The reactions were carried out at 140 °C for 40 min (Table 6, entries 1-3). A superior performance with an iodobenzene (limiting reagent) conversion of 75 % was observed when DMSO was used as solvent. Subsequently, various bases including K_2CO_3 , Et_3N and K_3PO_4 were evaluated using DMSO as the solvent at 140 °C for 60 min. Hereby, comparable iodobenzene conversions were observed with K_3PO_4 (81 %) and Et_3N (79 %) (Table 6, entries 6 and 5), both of which are significantly higher than the 40 % conversion obtained with K_2CO_3 (Table 6, entry 4). Therefore, Et_3N and K_3PO_4 were selected as the preferred bases, with DMSO chosen as the solvent for the majority of subsequent reactions.



Scheme 6: Heck coupling reaction of styrene and iodobenzene to form stilbene.

A control experiment conducted in the absence of a base resulted in only 10 % conversion (Table 6, entry 7), highlighting the crucial role of a base in the Heck coupling reaction. This observation can be explained by the reaction mechanism (Figure 6), wherein the final step the regeneration of the $\text{Pd}(0)$ species, *via* reductive elimination, is base assisted. Therefore, the presence of a base is pivotal for restoring the active catalytic species and sustaining the catalytic cycle.

After the identification of suitable reaction conditions, the performance of various catalysts was investigated. Initially, the catalytic activities of $\text{Pd}_3\text{P}/\text{SiO}_2$ (10 wt.% Pd) and Pd/SiO_2 (10 wt.% Pd) were evaluated in the Heck coupling reaction of iodobenzene and styrene. These studies focused on assessing the influence of phosphorus incorporation within the metal matrix on the catalytic activity. Reactions were carried out using 1.6 mol% (Pd basis) catalyst, 1 equivalent of Et_3N (relative to styrene) in DMSO at 140 °C for 60 min. An iodobenzene conversion of

79 % to stilbene (Table 7, entry 3) was achieved with $\text{Pd}_3\text{P}/\text{SiO}_2$ (10 wt.% Pd), whereas Pd/SiO_2 (10 wt.% Pd) yielded a higher conversion of 92 % (Table 7, entry 1). These results indicate that the incorporation of phosphorus does not enhance the catalytic activity under the tested conditions. To gain more insights, both catalysts were applied in the same reaction, using K_3PO_4 as base instead of Et_3N . Under these conditions, with $\text{Pd}_3\text{P}/\text{SiO}_2$ (10 wt.% Pd) an iodobenzene conversion of 81 % was achieved (Table 8, entry 2), while Pd/SiO_2 (10 wt.% Pd) showed a slightly higher conversion of 86 % (Table 8, entry 1).

Table 6: Results of the Heck coupling reactions for the screening of various bases and solvents. This table has been adapted from reference^[223] (license CC BY-NC 4.0).

Entry	Reaction time (min)	Solvent	Base	Iodobenzene conversion (%)
1	40	DMF	K_3PO_4	20
2	40	NMP	K_3PO_4	57
3	40	DMSO	K_3PO_4	75
4	40	DMSO	K_2CO_3	40
5	60	DMSO	Et_3N	79
6	60	DMSO	K_3PO_4	81
7	60	DMSO	-	10

Reaction conditions: styrene (1 mmol), iodobenzene (0.6 mmol), base (1 mmol), solvent (10 mL), $\text{Pd}_3\text{P}/\text{SiO}_2$ (10 wt.% Pd) (10^{-3} mmol·mL⁻¹, Pd basis), 140 °C. Conversions were calculated considering the concentration of iodobenzene. The quantifications were performed using GC-MS analysis and *n*-decane as internal standard.

To further differentiate the activities of the P-containing and P-free catalyst, the reaction was monitored at an earlier stage, after 20 min (one-third of the total reaction time). Interestingly, a similar trend was observed at this lower conversion level, with $\text{Pd}_3\text{P}/\text{SiO}_2$ (10 wt.% Pd) and Pd/SiO_2 (10 wt.% Pd) yielding conversions of 54 % and 57 %, respectively (Table 8, entries 6 and 5). These findings suggest that, in both reaction systems (Et_3N and K_3PO_4), Pd_3P does not lead to any significant enhancement in catalytic activity in comparison to Pd. In all cases a 100 % selectivity to stilbene was observed.

Table 7: Catalysts testing results for the Heck coupling reaction of styrene and iodobenzene using Et₃N as base. This table has been adapted from reference^[223] (license CC BY-NC 4.0).

Entry	Catalyst	Pd (mol %)	Iodobenzene conversion (%)
1	Pd/SiO ₂ (10 wt.% Pd)	1.6	92
2	Pd/1P-SiO ₂ (10 wt.% Pd)	1.6	89
3	Pd ₃ P/SiO ₂ (10 wt.% Pd)	1.6	79
4	Pd ₃ P/0.5P-SiO ₂ (10 wt.% Pd)	1.6	90
5	Pd ₃ P/1P-SiO ₂ (10 wt.% Pd)	1.6	90
6	Pd ₃ P/1P-SiO ₂ (10 wt.% Pd) ^[a]	1.6	10
7	Pd ₃ P/1P-SiO ₂ (5 wt.% Pd)	1.6	89
8	Pd ₃ P/1P-SiO ₂ (1 wt.% Pd)	1.6	91
9	Pd ₃ P/1P-SiO ₂ (5 wt.% Pd)	0.8	96
10	Pd ₃ P/1P-SiO ₂ (1 wt.% Pd)	0.16	83

Reaction conditions: styrene (3 mmol), iodobenzene (1.8 mmol), base Et₃N (3 mmol), solvent DMSO (30 mL), catalyst (entry 1 – 8: 10⁻³ mmol·mL⁻¹, entry 9: 5·10⁻⁴ mmol·mL⁻¹, entry 10: 10⁻⁴ mmol·mL⁻¹, Pd basis), 140 °C, 60 min. ^[a]Reaction was carried out without a base. The quantifications were performed using GC-MS analysis and *n*-decane as internal standard.

The investigation was further extended towards support engineering. Interestingly, Pd₃P nanoparticles supported on phosphorus-modified silica exhibited a significantly higher iodobenzene conversion compared to Pd₃P/SiO₂ (10 wt.% Pd). Hereby, the reaction performed with 1.6 mol% (Pd basis) catalyst, 1 equivalent of Et₃N (relative to styrene) in DMSO at 140 °C for 60 min resulted in 90 % conversion using Pd₃P/0.5P-SiO₂ (10 wt.% Pd) and Pd₃P/1P-SiO₂ (10 wt.% Pd) (Table 7, entries 4 and 5). In contrast, when Pd₃P/SiO₂ (10 wt.% Pd) was used as catalyst, only 79 % conversion under the same reaction conditions could be achieved (Table 7, entry 3). These results indeed point towards the positive influence of the support engineering approach with respect to the catalytic activity. Surprisingly, no improvement in catalytic activity, due to modified supports, was observed when the reaction was performed with K₃PO₄ as base (Table 8, entries 2-8). The importance of the base is also shown by an experiment, which was conducted Pd₃P/1P-SiO₂ (10 wt.% Pd) as the catalyst in the absence of a base. The aim was to investigate the possibility to conduct the reaction base free with the assistance of engineered support. However, a significantly lower conversion of 10 % was observed (Table 7, entry 6) after 60 min of reaction at 140 °C underlining the importance of a base in the catalytic cycle.

Table 8: Catalyst test results for the Heck coupling reaction of styrene and iodobenzene using K_3PO_4 as base. This table has been prepared based on data from reference^[223] (license CC BY-NC 4.0).

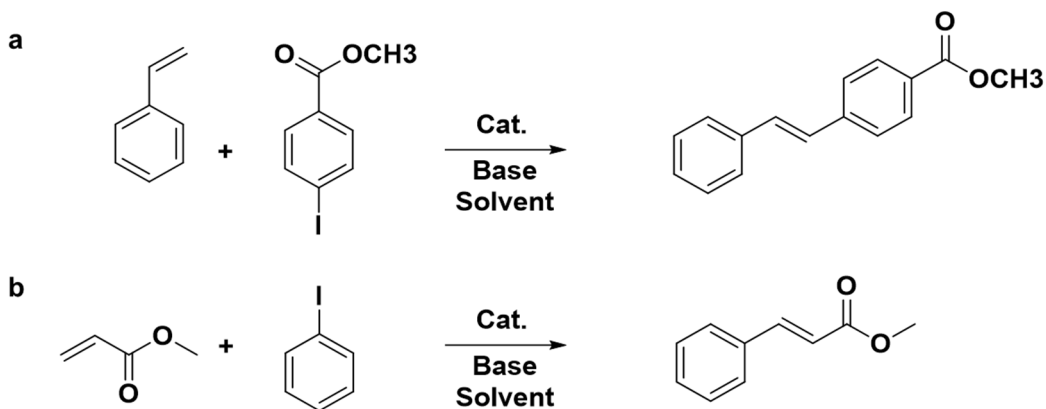
Entry	Catalyst	Reaction time (min)	Iodobenzene conversion (%)
1	Pd/SiO ₂ (10 wt.% Pd)	60	86
2	Pd ₃ P/SiO ₂ (10 wt.% Pd)	60	81
3	Pd ₃ P/0.5P-SiO ₂ (10 wt.% Pd)	60	86
4	Pd ₃ P/1P-SiO ₂ (10 wt.% Pd)	60	80
5	Pd/SiO ₂ (10 wt.% Pd)	20	57
6	Pd ₃ P/SiO ₂ (10 wt.% Pd)	20	54
7	Pd ₃ P/0.5P-SiO ₂ (10 wt.% Pd)	20	50
8	Pd ₃ P/1P-SiO ₂ (10 wt.% Pd)	20	43

Reaction conditions: styrene (0.1 mmol·mL⁻¹), iodobenzene (0.06 mmol·mL⁻¹), K_3PO_4 (0.1 mmol·mL⁻¹), solvent (DMSO), catalyst (10⁻³ mmol·mL⁻¹), 140 °C.

To reduce the precious metal content in the system and to explore the potential industrial application, Pd₃P /1P-SiO₂ prepared with a lower Pd loading were applied in the Heck coupling reaction. Initially, the tests were performed with 1.6 mol% catalyst concentration in the reaction system with Et₃N as the base, generative comparable data with the 10 wt.% Pd loaded catalysts. Both Pd₃P/1P-SiO₂ (5 wt.% Pd) and Pd₃P/1P-SiO₂ (1 wt.% Pd) exhibited excellent iodobenzene conversion of 89 % and 91 % with 100 % selectivity to stilbene after 60 min at a reaction temperature of 140 °C (Table 7, entries 7 and 8). Consequently, a test was performed with a reduced catalyst concentration (0.8 mol %) and the reaction was performed with Pd₃P/1P-SiO₂ (5 wt.% Pd). Hereby a conversion of 96 % (Table 7, entry 9) was achieved, underlining the performance of the catalyst also at lower catalysts concentrations. As a next step, the catalyst concentration in the reaction system was further reduced to 0.16 mol% (one tenth of the initially tested concentration), and the lowest Pd loaded catalyst Pd₃P/1P-SiO₂ (1 wt.% Pd) was used. Interestingly, a conversion of 83 % (Table 7, entry 10) towards stilbene was observed. This shows that the reduction of precious metal content does not affect the conversion significantly. However, these catalysts were not investigated further due to the challenges in the phase identification through PXRD for the recovered catalysts, which was inevitable for confirming the catalyst stability.

Substrate variation

The adaptability of the catalysts towards substituted aryl iodides were studied by conducting reactions with methyl 4-iodobenzoate and styrene as substrates (Scheme 7). Reactions performed with 1.6 mol% (Pd basis) catalyst, 1 equivalent of Et_3N (relative to styrene) in DMSO at 140 °C for 60 min showed very good conversions of methyl 4-iodobenzoate ranging from 82 % to 95 % with all the applied catalysts (Table S2).



Scheme 7: a) Heck coupling reaction of styrene and methyl 4-iodobenzoate and b) methyl acrylate and iodobenzene forming methyl cinnamate.

Furthermore, a reaction system investigated by Nuri *et al.*^[224] was adapted to perform tests with $\text{Pd}_3\text{P}/\text{P-SiO}_2$ (10 wt.% Pd) and $\text{Pd}_3\text{P}/\text{SiO}_2$ (10 wt.% Pd) catalysts (the best catalysts candidates in terms of stability in this work). Coupling reactions of iodobenzene and methyl acrylate were performed at 140 °C for 60 min with 0.2 mol% catalyst concentration, Et_3N as the base, dimethyl amine (DMA) as the solvent. Both catalysts exhibited excellent activity showing 100 % conversion of iodobenzene with 100 % selectivity to methyl cinnamate. The synthesized methyl cinnamate is an important ingredient for cosmetics industries for the production of body lotion, face cream, fine fragrances, etc.^[225]

4.3 Catalyst stability and leaching investigations

The testing study described above demonstrated the active nature of the synthesized catalysts in the Heck coupling reaction, as well as their adaptability towards various substrates. However, a significant difference in iodobenzene conversion, due to the phosphorus incorporation was not observed in all cases. It should be noted that, the fundamental goal of applying element synergy and support engineering in this project is to enhance catalyst stability. Accordingly, various tests and analyses were conducted to assess the stability of the catalysts.

The reusability of the catalysts was investigated through recovery tests conducted according to the procedure outlined in Figure 14. Each test began with a reaction using fresh catalysts, allowing sufficient time for high conversion levels to be achieved, while also enabling any

potential catalyst deactivation to occur during the course of the reaction. After the reaction, the catalyst was recovered *via* centrifugation, thoroughly washed with acetone multiple times, and dried. The recovered catalyst was then used in a second reaction under identical reaction conditions. This procedure was repeated for the desired number of recovery cycles. Initially, the reusability was examined for the Heck coupling reaction between styrene and iodobenzene, using Et_3N as base. A catalyst concentration of $10^{-3} \text{ mmol}\cdot\text{mL}^{-1}$ (Pd basis) was maintained throughout all the runs and the reactions were performed at 140°C for 60 min. The results of the recovery test are summarized in Figure 21.

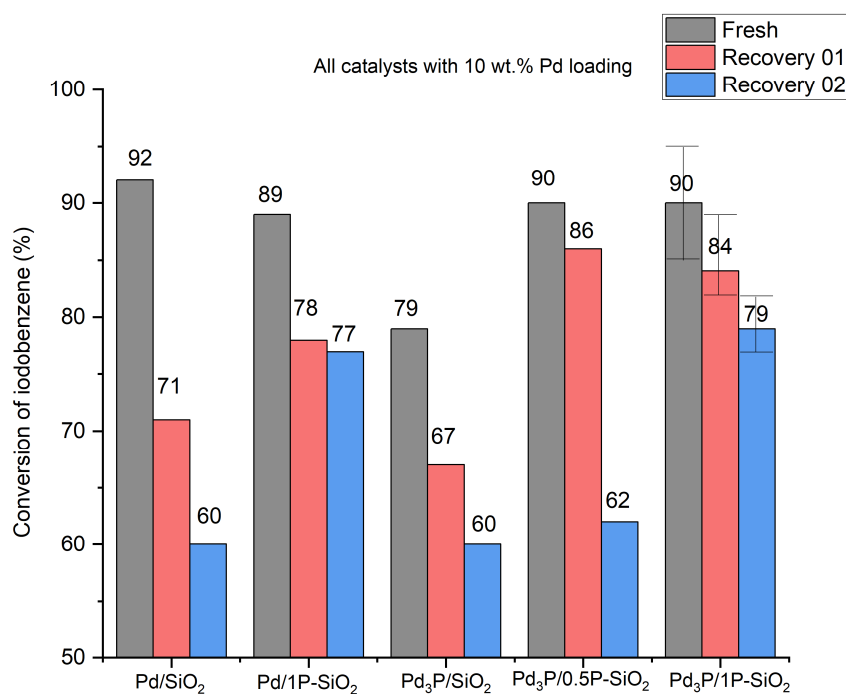


Figure 21: Results of the recovery test performed for the Heck coupling reaction of styrene and iodobenzene with the synthesized catalysts. Reaction conditions: styrene ($0.1 \text{ mmol}\cdot\text{mL}^{-1}$), iodobenzene ($0.06 \text{ mmol}\cdot\text{mL}^{-1}$), Et_3N ($0.1 \text{ mmol}\cdot\text{mL}^{-1}$), solvent (DMSO), catalyst ($10^{-3} \text{ mmol}\cdot\text{mL}^{-1}$, Pd basis), 140°C , 60 min. Conversions were calculated considering the concentration of iodobenzene. The quantifications were performed using GC-MS analysis and *n*-decane as internal standard. This figure has been adapted from reference^[223] (license CC BY-NC 4.0).

Three catalytic runs (one with fresh catalyst and two recovery cycles) were conducted for all five catalysts, and their performance was evaluated based on the iodobenzene conversion. In the case of the Pd/SiO₂ (10 wt.% Pd) catalyst, a significant decline in activity was observed. The conversion dropped by 21 % to 71 % in the first recovery run in comparison to the first test (92 %) with the fresh catalyst. This decline continued in the second recovery test, reaching 60%, a total decrease of 32 % from the initial conversion. These results showed poor reusability of the Pd/SiO₂ (10 wt.% Pd) catalyst under the tested conditions. The impact of the support engineering on Pd catalyst was evaluated by testing the Pd/1P-SiO₂ (10 wt.% Pd)

catalyst under similar conditions. Interestingly, a much lower decline in activity, only by 11 %, was observed after the first recovery test, which is almost half of the decline in conversion observed with Pd/SiO₂ (10 wt.% Pd). Further, a second recovery test with Pd/1P-SiO₂ (10 wt.% Pd) only showed a very slight decrease in conversion in comparison to the first recovery test. While combining all the three runs a total decrease in conversion by only 12 % was observed with Pd/1P-SiO₂ (10 wt.% Pd), which is almost 2.7 times lower than the decline in conversion observed with Pd/SiO₂ (10 wt.% Pd) catalyst. Hence, these results clearly indicate the success of support engineering approach in minimizing decline in activity even for pure metal-based nanoparticles (Figure 21).

The influence of the phosphorus-modified support was further evaluated by looking at the stability of supported Pd₃P nanoparticles. The Pd₃P/SiO₂ (10 wt.% Pd) catalyst showed a 12 % decrease in conversion during the first recovery run and a 19 % decrease in the second, relative to the initial performance with the fresh catalyst (Figure 21). Although some loss in activity was observed, it was significantly less than the decline seen with Pd/SiO₂ (10 wt.% Pd). These results clearly demonstrate the effectiveness of the element synergy strategy in enhancing the catalyst reusability. Most likely phosphorus already acts as inherent stabilization agent for palladium in Pd₃P.

When studying the reusability of the Pd₃P nanoparticles on the engineered supports very interesting results were observed. First of all, a significantly higher stability can be seen from the recovery tests of Pd₃P/1P-SiO₂ (10 wt.% Pd) as only a slight decline in conversion by 6 % was observed in the first recovery test (second run). This drop is nearly half of that observed for Pd₃P supported on unmodified SiO₂ and less than one-third of the activity loss seen with the Pd/SiO₂ (10 wt.% Pd) catalyst in the first recovery test. After the second recovery test, a total conversion loss corresponding to 11 % using Pd₃P/1P-SiO₂ (10 wt.% Pd) was observed, which is significantly lower than the 19 % observed with Pd₃P/SiO₂ (10 wt.% Pd) and 32 % observed with Pd/SiO₂ (10 wt.% Pd). These results further highlight the impact of support engineering for stability enhancement. Reducing the phosphorus content in silica to 0.5 wt.% (Pd₃P/0.5P-SiO₂, 10 wt.% Pd) led to only a slight drop in conversion by only 4% during the first recovery test. However, the second recovery run showed a sharp 28 % decline compared to the initial conversion. This indicates the critical role of the phosphorus content in maintaining a high catalytic activity.

Based on the reusability assessments from the recovery tests discussed above, Pd₃P/1P-SiO₂ (10 wt.% Pd) can be identified as the best-performing catalyst in terms of stability. In all of the above discussed cases 100 % selectivity towards stilbene was observed.

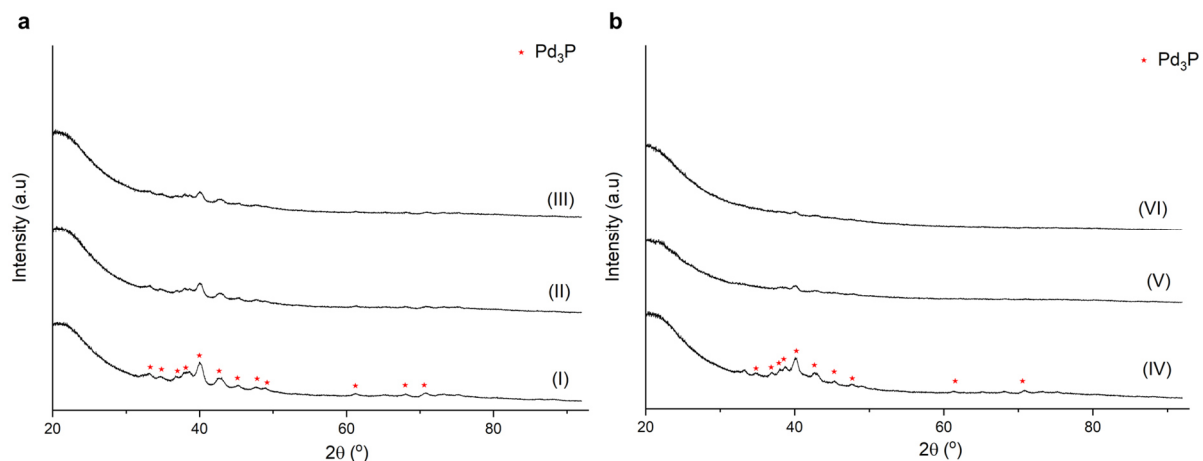


Figure 22: PXRD patterns for the recovered catalyst. a) $\text{Pd}_3\text{P}/\text{SiO}_2$ (10 wt.% Pd) with (I) fresh, (II) after the first run and (III) after second run. b) $\text{Pd}_3\text{P}/1\text{P}-\text{SiO}_2$ (10 wt.% Pd) with (IV) fresh, (V) after the first run and (VI) after second run. Reaction conditions: styrene ($0.1 \text{ mmol} \cdot \text{mL}^{-1}$), iodobenzene ($0.06 \text{ mmol} \cdot \text{mL}^{-1}$), Et_3N ($0.1 \text{ mmol} \cdot \text{mL}^{-1}$), solvent (DMSO), catalyst ($10^{-3} \text{ mmol} \cdot \text{mL}^{-1}$, Pd basis), 140°C , 60 min. Reference for the phase identification - Pd_3P : ICSD 85525. This figure has been adapted from reference^[223] (license CC BY-NC 4.0).

To gain deeper insights into the stability of the catalysts, the recovered catalysts after the first and second runs (after fresh run and the first recovery run) were characterized by PXRD. No phase changes were observed compared to the fresh catalyst, however, a progressive decline in crystallinity was noted after each run (Figure 22, Figure S8 and Figure S9). Such decline in crystallinity can often be associated with catalyst leaching. Moreover, the decrease in conversions observed after each run can also point towards catalyst deactivation through metal leaching. Hence to obtain a quantitative information on the loss of Pd during the reactions, ICP-AES analyses were performed for the fresh catalysts and after the first run (Table 9 and Table S3).

Table 9: Results of the Pd leaching determined by ICP-AES analysis. This table has been adapted from reference^[223] (license CC BY-NC 4.0).

Entry	Catalyst	Pd leaching (wt.%)
1	Pd/SiO_2 (10 wt.% Pd)	21
2	$\text{Pd}/1\text{P}-\text{SiO}_2$ (10 wt.% Pd)	25
3	$\text{Pd}_3\text{P}/\text{SiO}_2$ (10 wt.% Pd)	8
4	$\text{Pd}_3\text{P}/1\text{P}-\text{SiO}_2$ (10 wt.% Pd)	3

Reaction conditions applied on the catalyst: styrene ($0.1 \text{ mmol} \cdot \text{mL}^{-1}$), iodobenzene ($0.06 \text{ mmol} \cdot \text{mL}^{-1}$), Et_3N ($0.1 \text{ mmol} \cdot \text{mL}^{-1}$), solvent (DMSO, 30 mL), catalyst ($10^{-3} \text{ mmol} \cdot \text{mL}^{-1}$, Pd basis), 140°C , 60 min.

An extreme leaching of Pd amounting to 21 % (Table 9, entry 1) could be observed with Pd/SiO_2 (10 wt.% Pd) showing the very low stability of the catalyst. The significant decline in conversion observed in the first recovery test can now be substantiated with this extreme

leaching. Through the incorporation of phosphorus into the Pd matrix and the formation of Pd_3P , the Pd leaching was suppressed to 8 % (Table 9, entry 3). This was also reflected in the results of first recovery test, where the decrease in conversion for $\text{Pd}_3\text{P}/\text{SiO}_2$ (10 wt.% Pd) was almost half in comparison to Pd/SiO_2 (10 wt.% Pd). These results collectively provided the evidence of the stability enhancement through element synergy (d-block-p-block element combination strategy). An extremely low Pd leaching of just 3 % (Table 9, entry 4) was observed with $\text{Pd}_3\text{P}/1\text{P}-\text{SiO}_2$ (10 wt.% Pd), indicating superior performance of this catalyst in terms of stability, inline with the lower decline in conversion observed in the recovery tests. A combined effect of the support engineering and element synergy presumably made $\text{Pd}_3\text{P}/1\text{P}-\text{SiO}_2$ (10 wt.% Pd) the most superior candidate of this study.

The decreased levels of leaching observed with the lead candidates $\text{Pd}_3\text{P}/1\text{P}-\text{SiO}_2$ (10 wt.% Pd) and $\text{Pd}_3\text{P}/\text{SiO}_2$ (10 wt.% Pd) are indeed considerably lower in comparison to many reported catalysts for Heck coupling reactions. Some of the reported Pd leaching values are 17 % with Pd supported IRMOF-3,^[224] 26 % with Pd/C ,^[226] 79 % with $\text{Pd}/\text{Al}_2\text{O}_3$ and 100 % with Pd on ion exchange resin,^[227] 50 % with $[\text{PdMe}(\text{tmEDA})]/\text{SiO}_2$ (tmEDA: tetramethylethylenediamine),^[157] etc. These results point towards the superior leaching resistance of $\text{Pd}_3\text{P}/1\text{P}-\text{SiO}_2$ (10 wt.% Pd) and $\text{Pd}_3\text{P}/\text{SiO}_2$ (10 wt.% Pd) in comparison to many reported catalysts. A high leaching of 25 % was determined with $\text{Pd}/1\text{P}-\text{SiO}_2$ (10 wt.% Pd), which was not in line with recovery tests and required further investigations.

Recovery tests with variation in base and substrates

The recovery tests were further extended towards a base variation, whereby K_3PO_4 was used instead of Et_3N for the Heck coupling between styrene and iodobenzene. All other conditions remained the same. Due to the presence of undissolved K_3PO_4 being present in the reaction mixture, a separation of the base from the solid catalyst and a subsequent catalyst recovery was challenging. Hence, only one recovery test (2 runs) was performed and the results are summarized in Figure 23. The results were indeed confirming the superior recycling behaviour of $\text{Pd}_3\text{P}/1\text{P}-\text{SiO}_2$ (10 wt.% Pd) as no decline in conversion was observed in the recovery test, underlining the consistent performance of the catalyst. These results clearly indicate the positive effect of P incorporation in the support as with increase in P concentration in the support, the reusability has increased. A substantial decline in the conversion by 45 % (from 81 to 36 %) shown with $\text{Pd}_3\text{P}/\text{SiO}_2$ (10 wt.% Pd), could be reduced to 20 % through the use of 0.5 wt.% P-modified support ($\text{Pd}_3\text{P}/0.5\text{P}-\text{SiO}_2$ (10 wt.% Pd)). A further increase in phosphorus content in the support *via* support engineering, using $1\text{P}-\text{SiO}_2$ ($\text{Pd}_3\text{P}/\text{SiO}_2$, 10 wt.% Pd), resulted in a significant improvement in maintaining catalyst performance, as the conversion in the recovery test matched that of the initial run. This further confirms the effectiveness of the underlying support engineering strategy.

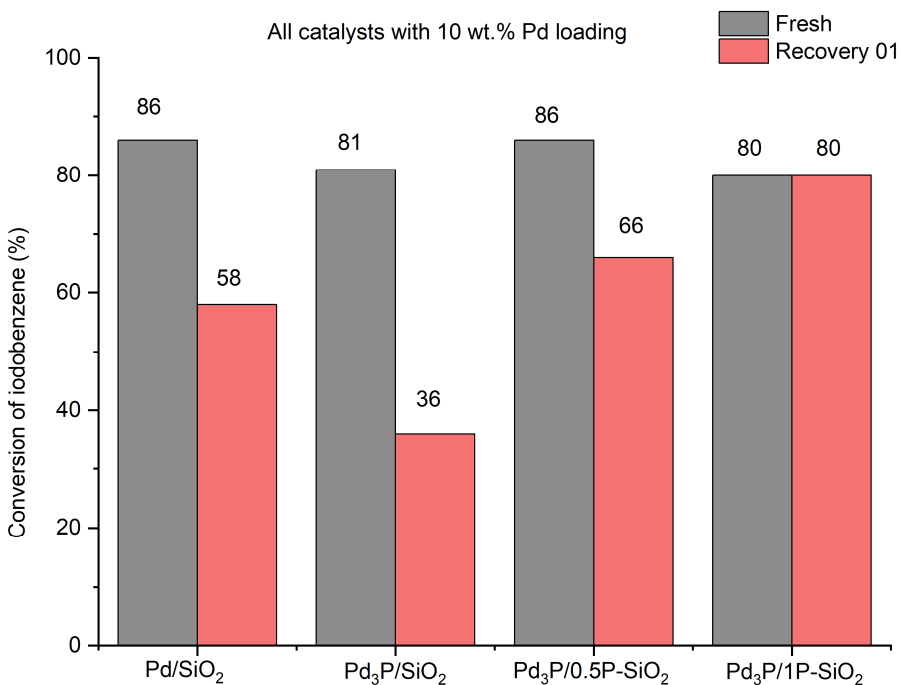


Figure 23: Results of the recovery experiments performed for the Heck coupling reaction of styrene and iodobenzene with K₃PO₄ as the base. Reaction conditions: styrene (0.1 mmol·mL⁻¹), iodobenzene (0.06 mmol·mL⁻¹), K₃PO₄ (0.1 mmol·mL⁻¹), solvent (DMSO), catalyst (10⁻³ mmol·mL⁻¹, Pd basis), 140°C, 60 min. The quantifications were performed using GC-MS analysis and *n*-decane as internal standard. This figure has been adapted from reference [223] (license CC BY-NC 4.0).

To evaluate the influence of phosphorus-modified supports on maintaining the catalytic activity with a different substrate, recovery tests were conducted using methyl 4-iodobenzoate and styrene in the presence of Et₃N in DMSO. Both Pd₃P/1P-SiO₂ (10 wt.% Pd) and Pd/1P-SiO₂ (10 wt.% Pd) exhibited a lower decrease in conversion after the first recovery test compared to their non-engineered counterparts (Figure S15). These results again confirm the adaptability of the support engineering approach across different substrates.

Heterogeneity of the catalyst

To confirm the heterogeneous nature of the catalysts, hot filtration tests were carried out. The reaction was allowed to proceed partially (low conversion) before the catalyst was removed by filtration, without cooling the reaction mixture, to prevent potential re-deposition of any potentially leached species onto the support. The resulting filtrate, free of any solid catalyst, was allowed to react further, and the conversions were monitored. Any significant conversion in the absence of the solid catalyst would indicate the presence of catalytically active leached species. However, negligible or no further conversions were observed for any of the catalysts, strongly supporting their heterogeneous nature. However, it may be possible that the leached Pd species from the catalysts during the reaction can be catalytically inactive or Pd species became inactive during the filtration process. One other possibility can be a fast re-deposition

of the catalytically active species on the support prior to filtration,^[228] however no evidence for the same were observed in the current data. The results of the filtration tests are presented in Table S4. In this context, *in-situ* X-ray absorption spectroscopy (XAS) analysis^[229,230] conducted for the reaction system can offer deeper insights into the role of leached species and surface-mediated reactions.

4.4 Theoretical insights into the stability and activity improvement

The experimental results described before reveal two important ways in which the phosphorus incorporation enhances the catalyst stability:

1. Improvement in stability through the incorporation of phosphorus into the Pd matrix, thereby forming the Pd₃P phase.
2. Improvement in stability through the support engineering approach *via* the incorporation of phosphate-type species on the silica support.

The analysis of the leaching data revealed a substantial reduction in metal leaching for Pd₃P nanoparticles (8 % Pd leaching) compared to supported Pd nanoparticles (21 % Pd leaching). This was in line with the observed iodobenzene conversions in the recovery test for the investigated systems. Based on the results, a hypothesis can be proposed regarding the stabilizing effect of phosphorus within the crystal structure. While analyzing the crystal structure of Pd₃P (Figure 16), it can be seen that two inequivalent Pd sites are bonded to P atoms. The Pd (1) site is bonded to three equivalent P atoms (3-coordinate geometry) with Pd–P bond distances ranging from 2.3 Å to 2.6 Å, whereas the Pd (2) site is bonded to two P atoms (2-coordinate geometry) with a Pd–P distance of approximately 2.3 Å.^[33,211] The sum of the van der Waals radii for Pd and P is 3.43 Å, which is significantly greater than the Pd–P bond length discussed above, indicating a strong interaction between these two atoms in the Pd₃P crystal structure. This clearly illustrates the close interaction between Pd and P in the Pd₃P crystal structure. The phosphorus present in the structure can thereby provide an additional anchoring effect on Pd sites, which helps to suppress potential Pd leaching. Similar observations, in which Ga acts as anchoring point, providing stability to a CoGa intermetallic system and reducing Co leaching during hydroformylation, have been reported by Zhao *et al.*^[91] Hence, the stabilization of Pd sites can be assumed *via* P-based anchoring sites in Pd₃P resulting in lower a leaching of Pd in Pd₃P/SiO₂ (10 wt.% Pd) in comparison to Pd/SiO₂ (10 wt.% Pd) in Heck coupling reactions.

Another interesting aspect to analyze is the effect of support engineering, which also leads to an enhanced stability. In almost all tested cases, a significant contribution of the phosphorus species on the support can be observed with respect to a reduction in activity loss. As explained in section 4.1, the presence of phosphate species on the support surface is a valid assumption, also in analogy to literature reports. The ability of phosphate species to stabilize

nanoparticles on the surface are discussed and described in the literature.^[213,231] In most of the cases P species are acting as anchoring points for the metal nanoparticles thereby providing an enhanced metal-support interaction.^[213,231] The stabilization of Pd_3P nanoparticles facilitated by phosphate anchoring points on the support can be considered responsible for the metal leaching reduction to mere 3 % based on the ICP-AES data of the recovered $\text{Pd}_3\text{P}/1\text{P}-\text{SiO}_2$ (10 wt.% Pd) catalysts in comparison to 8 % observed for the recovered $\text{Pd}_3\text{P}/\text{SiO}_2$ (10 wt.% Pd) catalyst. It is important to note that metal leaching can occur through two primary pathways in the selected reaction systems. First of all, soluble metal species can be formed and dissociate from the nanoparticles to the liquid phase,^[89] or secondly the detachment and migration of nanoparticles from the support into the reaction medium can take place. The first pathway can be inhibited by the presence of phosphorus within the Pd_3P crystal structure, while the latter one can be suppressed by phosphorus species on the support surface. These combined effects can be considered as "double anchoring", in the case of the $\text{Pd}_3\text{P}/1\text{P}-\text{SiO}_2$ (10 wt.% Pd) catalyst. A conceptual representation of the Pd_3P nanoparticles on phosphorus-modified silica is provided as Figure 24.

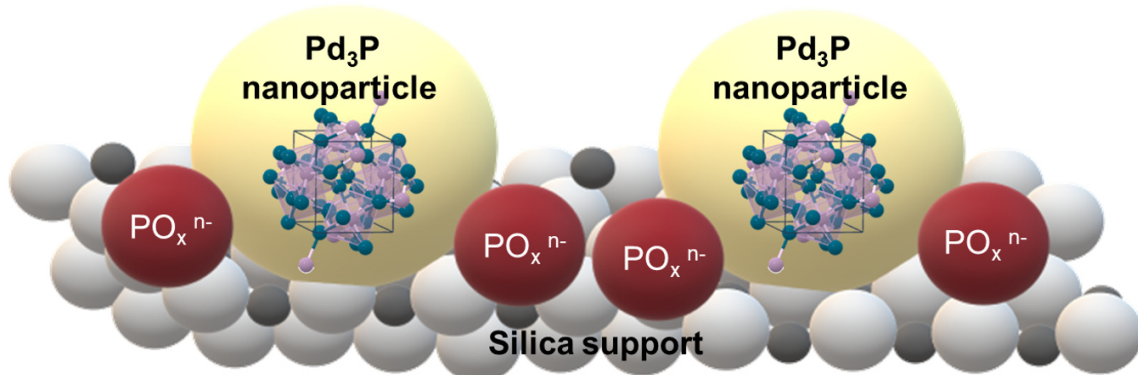


Figure 24: Conceptual representation of the stabilization of palladium phosphide nanoparticles on phosphorus-modified silica.

Beside the stability improvement *via* the support engineering, this modification of silica with phosphate species also has a positive impact on the catalytic activity. For example, the Heck coupling reaction of iodobenzene and styrene performed with $\text{Pd}_3\text{P}/\text{SiO}_2$ (10 wt.% Pd), Et_3N as base at 140°C for 60 min resulted in 79 % conversion (Table 7, entry 3). Whereas with Pd_3P nanoparticles prepared on the P-modified support $\text{Pd}_3\text{P}/1\text{P}-\text{SiO}_2$ (10 wt.% Pd) and $\text{Pd}_3\text{P}/0.5\text{P}-\text{SiO}_2$ (10 wt.% Pd) an increased conversion of 90 % (Table 7, entries 4 and 5) can be achieved. The support modification leads to the formation of phosphate species on silica, which can restrict the mobility of Pd_3P nanoparticles and potentially prevent sintering during the synthesis. This, in turn, enhances the dispersion of the active metal, resulting in higher catalytic activity compared to the non-engineered counterpart.

Similar observations are reported in the context of Pt nanoparticles on P-modified alumina applied in dehydrogenation reactions.^[213,231] Moreover, the charge transfer between the phosphate species on the support and the active Pd centres can result in an improved catalytic activity and an optimal interaction with reactants, intermediates and products. For instance, the charge transfer achieved for Pt on P-doped ceria (Pt₁/PO₄-CeO₂) has been reported as one of the major reasons for the increased hydrogenation activity in comparison to the undoped counter part.^[232] Hence, the electronic effects induced through support engineering can significantly influence the catalytic activity.

4.5 Concluding remarks

Palladium phosphide (Pd₃P) nanoparticles, synthesized on both unmodified silica and phosphorus-modified silica supports, were tested for their performance as catalysts in Heck coupling reactions with various substrates. In all tested cases, the catalysts exhibited good activity, and in some instances, the phosphorus modification of the support (support engineering) led to an enhanced catalytic activity in comparison to the catalyst prepared with non-modified support. For instance, the coupling reaction of iodobenzene and styrene using Et₃N as the base in DMSO resulted in a 79 % conversion with Pd₃P/SiO₂ (10 wt.% Pd), while an improved conversion of 90 % was achieved with Pd₃P/1P-SiO₂ (10 wt.% Pd).

A particularly interesting observation was the enhancement in stability achieved through the support engineering approach, as evidenced by a reduction in metal leaching and an improved catalyst reusability. In all cases, a much lower decline in catalytic activity was observed for Pd₃P nanoparticles supported on phosphorus-modified silica compared to those on unmodified silica. For example, in the Heck coupling reaction of iodobenzene and styrene using K₃PO₄ as the base in DMSO, a significant drop in conversion up to 45 % was observed during the recovery test with Pd₃P/SiO₂ (10 wt.% Pd). In contrast, the complete retention of conversion was observed when using Pd₃P/1P-SiO₂ (10 wt.% Pd) as catalyst. Additionally, the combined effect of element synergy and support engineering led to a substantial reduction in Pd leaching from 21 % with Pd/SiO₂ (10 wt.% Pd) to just 3 % with Pd₃P/1P-SiO₂ (10 wt.% Pd) highlighting the effectiveness of the overall strategy. Through the combination of element synergy (d-block-p-block element combination strategy) and support engineering, a significant reduction in Pd leaching and an improvement in catalyst stability were achieved in Heck coupling reactions. Moreover, the application of support engineering also contributed to an enhancement in catalytic activity, probably through a more effective charge transfer between the phosphate species on the support and the Pd centres.

For future work, use of support modifiers other than phosphorus, such as nitrogen, sulfur or boron can be investigated. The influence of alternative support materials such as carbon,

alumina, and ceria, as well as the impact of support engineering on these systems, also demand further studies.

5 Alkoxy carbonylation reactions with supported palladium phosphide nanoparticles

The results discussed in this chapter were published in:

A. Neyyathala, F. Jung, C. Feldmann, S.A. Schunk, S. Hanf, *ChemRxiv* **2025**, DOI = 10.26434/chemrxiv-2025-46zsr under the license CC BY NC ND 4.0.

Figures 25, 26, 27, 28, 29, 30, 31, S16, S17, S18, S19 and Tables 10, 11, S5, S6, S7, S8 are adapted from this publication.

Patent application EP25161927, Process for performing alkoxy carbonylation reactions, BASF SE and KIT, 05.03.2025.

The conversion of alkyl and aryl halides into high-value products, such as amides, esters, and azides *via* carbonylation reactions has gained significant research interest, owing to the wide industrial applicability of these compounds.^[89,178,233,234] Extensive studies on palladium-catalyzed homogeneous systems have provided valuable insights into the reaction mechanisms, thereby facilitating the systematic design of catalysts. Although heterogeneous catalysts have been reported for this class of reactions, no catalytic system using the element synergy strategy has been reported in the literature up to now. This in fact opens the possibility of investigating Pd_xA_y (A: p-block elements) binary-phase-based systems for their performance in the carbonylation reaction of alkyl/aryl halides.

In this study, the d-block-p-block element combination strategy was applied to develop a Pd-based heterogeneous catalyst for the alkoxy carbonylation of aryl halides. Supported palladium phosphide (Pd_3P) nanoparticles were synthesized on silica, characterized by PXRD, TEM, ICP-AES and CO chemisorption and evaluated for their catalytic performance in the alkoxy carbonylation of iodobenzene. The Pd_3P catalyst demonstrated exceptional activity, significantly outperforming a purely Pd-based reference catalyst and several other reported homogeneous and heterogeneous systems. The incorporation of phosphorus into palladium to form Pd_3P nanoparticles resulted in a more than 2.5-fold increase in turnover frequency compared to pure Pd. The catalyst was further tested with a range of substrates, including various substituted iodobenzenes and different alcohols. Additionally, the supported Pd_3P catalyst has proven to be effective in other carbonylation reactions, such as aminocarbonylation and phenoxy carbonylation reactions.

5.1 Synthesis and characterization of Pd_xPy/SiO_2

The successful synthesis of supported palladium phosphide nanoparticles using phosphoric acid, as described in chapter 4, was also applied in this study. Therefore, $Pd(OAc)_2$ and H_3PO_4

were combined in a molar ratio of Pd to P of 3:1, dissolved HCl, and then impregnated onto a silica support. The amounts of $\text{Pd}(\text{OAc})_2$ and silica were calculated to achieve a Pd loading of 5 wt.%. After impregnation, the material was dried and subsequently thermally treated in a pure hydrogen atmosphere at 400 °C for 8 h. PXRD analysis confirmed the formation of phase pure Pd_3P on the silica support (Figure 25a). Further, to verify the phase formation a high-resolution transmission electron microscope (HRTEM) analysis was performed for $\text{Pd}_3\text{P}/\text{SiO}_2$ (5 wt.% Pd). This analysis clearly demonstrated a lattice fringe distance of 2.0 Å, which is in good agreement with the d spacing corresponding Pd_3P (122), providing an additional proof for the formation of targeted phase (Figure 25b).

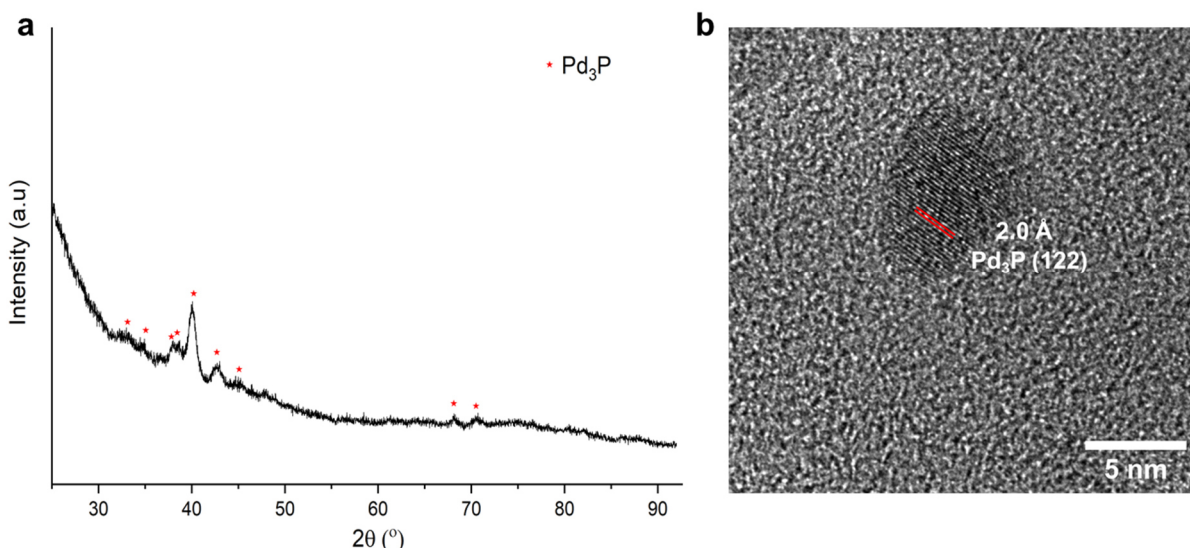


Figure 25: a) PXRD pattern of $\text{Pd}_3\text{P}/\text{SiO}_2$ (5 wt.% Pd) and b) HRTEM lattice fringe analysis confirming the phase formation. Reference of phase identification: Pd_3P (*Pnma*): $d_{122} = 1.999 \text{ \AA}$ (ICSD 85525). This figure has been adapted from reference^[235] (license CC BY-NC ND 4.0).

The elemental composition of the sample was analyzed through performing an EDX analysis coupled with scanning transmission electron microscopy (STEM). A uniform distribution of palladium and phosphorus on the silica support was observed in the EDX elemental mapping with an average Pd/P ratio of 3.03, closely matching the stoichiometry of the targeted Pd_3P phase (Figure 26). Further, the Pd content of $\text{Pd}_3\text{P}/\text{SiO}_2$ (5 wt.% Pd) sample was quantified with ICP-AES analysis and resulted in 4.95 wt.%, which is indeed close to the expected loading of 5 wt.%. As reference, a supported Pd catalyst was prepared applying the same synthesis procedure, however without the addition of phosphoric acid. Again, the phase identification performed by PXRD analysis (Figure S16) indicated the formation of phase pure Pd on silica (Pd/SiO_2 , 5 wt.% Pd).

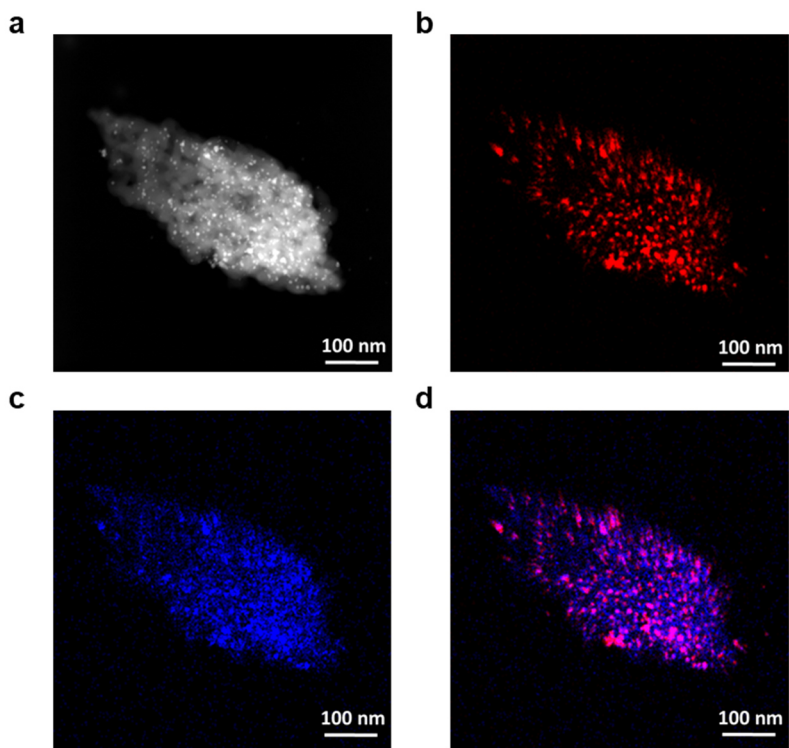


Figure 26: a) HAADF-STEM image of $\text{Pd}_3\text{P}/\text{SiO}_2$ (5 wt.% Pd), where the bright white spots indicate the Pd_3P nanoparticles and EDX mapping of the catalyst showing b) palladium, c) phosphorus and d) combined Pd and P (Pd: red, P: blue). This figure has been adapted from reference^[235] (license CC BY-NC ND 4.0).

Further characterization of the synthesized material was carried out using high-angle annular dark-field scanning transmission electron microscopy (HAADF-STEM). The HAADF-STEM images of $\text{Pd}_3\text{P}/\text{SiO}_2$ (5 wt.% Pd) revealed well dispersed, spherical Pd_3P nanoparticles uniformly distributed over the silica support (Figure 27a). This observation was enabled by Z contrast imaging, which clearly distinguished the Pd_3P nanoparticles due to their higher contrast relative to the lighter silica support. Subsequently, particle size analysis of the $\text{Pd}_3\text{P}/\text{SiO}_2$ (5 wt.% Pd) revealed an average nanoparticle size of approximately 5.6 nm (Figure 27b). Whereas, the particle size analysis performed for Pd/SiO_2 (5 wt.% Pd) catalyst showed a higher average value of 6.6 nm (Figure S 19b). In the PXRD analysis of $\text{Pd}_3\text{P}/\text{SiO}_2$ (5 wt.% Pd, Figure 25a), a reduced crystallinity indicated by broader reflexes compared to those of Pd/SiO_2 (5 wt.% Pd) becomes obvious, as demonstrated in Figure S16. These broader reflexes indicate the presence of smaller crystallites, aligning well with the smaller particle size observed for $\text{Pd}_3\text{P}/\text{SiO}_2$ (5 wt.% Pd). This difference in particle sizes can be attributed to the lower crystallization ability of the Pd_3P phase,^[236] which results in the formation of smaller crystallites and, consequently, smaller nanoparticles. Additionally, the presence of phosphorus within the crystal structure may contribute to an enhanced sintering resistance, further supporting the stabilization of smaller Pd_3P nanoparticles.

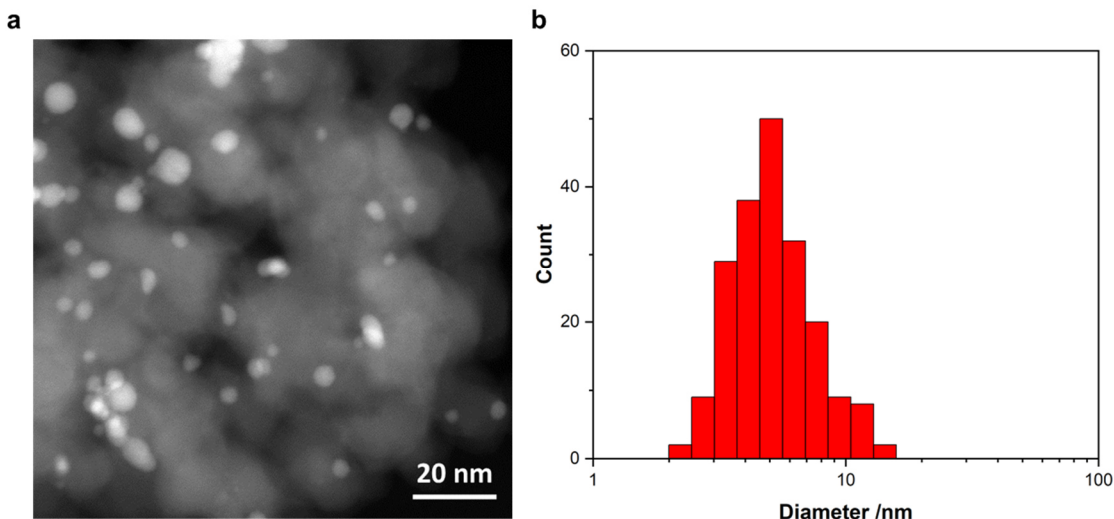


Figure 27: a) Example HAADF-STEM image of $\text{Pd}_3\text{P}/\text{SiO}_2$ (5 wt. % Pd), showing spherical nanoparticles distributed over silica and b) the particle size distribution histogram showing the average particle size of 5.6 ± 2.4 nm. This figure has been adapted from reference^[235] (license CC BY-NC ND 4.0).

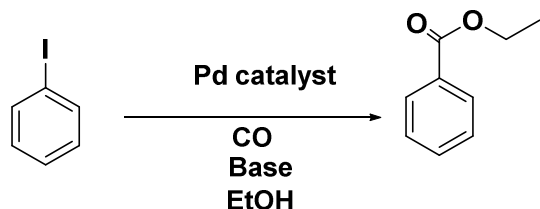
To determine the Pd dispersion of the catalysts, CO chemisorption measurements were performed for $\text{Pd}_3\text{P}/\text{SiO}_2$ (5 wt.% Pd) and Pd/SiO_2 (5 wt.% Pd). This data is important to later on asses the intrinsic activity of the catalyst by estimating turn over frequencies (TOF). Surprisingly, a slightly lower dispersion of 8.5 % was determined for palladium phosphide ($\text{Pd}_3\text{P}/\text{SiO}_2$, 5 wt.% Pd) in comparison to 9.9 % estimated for the pure Pd catalyst (Pd/SiO_2 , 5 wt.% Pd). This result is somewhat unexpected since smaller nanoparticles typically correlate with higher dispersion values. Despite the smaller particle size of $\text{Pd}_3\text{P}/\text{SiO}_2$ (5 wt.% Pd), the dispersion did not surpass that of the Pd/SiO_2 (5 wt.% Pd). This discrepancy may be attributed to surface phosphorus species potentially blocking Pd sites, especially given the stagnant conditions used during the thermal treatment. Alternatively, the lower dispersion could also originate from a reduced CO adsorption affinity or altered adsorption behavior on the Pd_3P surface, likely arising from electronic and/or geometric modulation of Pd sites induced by the phosphorus incorporation.

To asses the influence of the support Pd_3P nanoparticles were synthesized on carbon ($\text{Pd}_3\text{P}/\text{C}$, 5 wt. % Pd) and phosphorus-modified silica ($\text{Pd}_3\text{P}/\text{1P-SiO}_2$, 5 wt. % Pd). No reflexes were observed in the case of $\text{Pd}_3\text{P}/\text{C}$ (5 wt. % Pd), possibly due the formation of extremely small crystallites (Figure S18), whereas reflexes corresponding to Pd_3P were observed for $\text{Pd}_3\text{P}/\text{1P-SiO}_2$ (5 wt. % Pd, catalyst from chapter 4 was used, Figure S7, II).

5.2 Catalytic performance in the alkoxy carbonylation of aryl halides

The performance of the synthesized catalysts was assessed in the alkoxy carbonylation reaction of aryl halides. Catalytic tests were performed in a batch reactor with iodobenzene as the substrate, ethanol as the nucleophile (NuH) and the solvent, Et_3N as the base

(3 equivalents in comparison to substrate) and with a CO pressure of 6 bar (Scheme 8). A reaction performed with $\text{Pd}_3\text{P}/\text{SiO}_2$ (5 wt.% Pd) at 100 °C for 2 h resulted in an iodobenzene conversion of 97 % with 100 % selectivity towards ethyl benzoate (Table 10, entry 2). Extending the reaction time to 3 h resulted in a complete conversion of iodobenzene with a consistent selectivity towards ethyl benzoate (Table 10, entry 3).



Scheme 8: Alkoxy carbonylation of iodobenzene and ethanol forming ethyl benzoate.

After performing the first catalytic tests successfully, the influence of the base was investigated. A test conducted under similar condition, without the addition of a base resulted in a marginal iodobenzene conversion of 7 % to ethyl benzoate after 2 h reaction time (Table 10, entry 1). This reveals the significance of a base in order to enhance the progress of the reaction and achieve higher levels of conversion. This fact can be explained by looking at the mechanism of the reaction (Figure 7). The acyl palladium complex $[\text{ArCO}(\text{L}_n)\text{PdX}]$ formed after the CO insertion step undergoes alcoholysis leading to the release of the ester product and the formation of a hydridopalladium species. Pd (0), the catalytically active species, is subsequently formed through base-assisted decomposition of the hydridopalladium intermediate and neutralization of the generated HX.^[89,162,234] Therefore, in the absence of a base, the catalyst regeneration can be challenging, moreover the added base significantly influences the rate of the reaction.^[89,234,237] One other possibility can be the catalyst deactivation through poisoning caused by the HI (iodide) species, which can be prevented by the neutralization with a base.^[238] Hence, further carbonylation tests for the aryl iodides were performed with the addition of a base.

The catalytic reactions with $\text{Pd}_3\text{P}/\text{SiO}_2$ (5 wt.% Pd) were performed with NaOAc , KOH and K_2CO_3 for 2 h and resulted in iodobenzene conversions of 40 %, 70 %, 56 % respectively (Table 10, entries 4, 5 and 6). All of which are substantially lower than the conversion obtained with Et_3N (97 %). One of the reasons for the higher conversion when using Et_3N is the higher solubility of the base in comparison to other bases. The superior alkoxy carbonylation performance of Et_3N based systems has also been reported in other studies, where the authors investigated heterogeneous catalysts.^[239,240] Considering the above, all subsequent tests were conducted using Et_3N as the base.

Table 10: Catalytic test results for the alkoxycarbonylation reaction of iodobenzene. This table has been adapted from reference^[235] (license CC BY-NC ND 4.0).

Entry	Catalyst	Base	Reaction time (min)	Conversion of iodobenzene (%)
1	Pd ₃ P/SiO ₂ (5 wt.% Pd)	-	120	7
2	Pd ₃ P/SiO ₂ (5 wt.% Pd)	Et ₃ N	120	97
3	Pd ₃ P/SiO ₂ (5 wt.% Pd)	Et ₃ N	180	100
4	Pd ₃ P/SiO ₂ (5 wt.% Pd)	NaOAc	120	40
5	Pd ₃ P/SiO ₂ (5 wt.% Pd)	KOH	120	70
6	Pd ₃ P/SiO ₂ (5 wt.% Pd)	K ₂ CO ₃	120	56
7	Pd ₃ P/SiO ₂ (5 wt.% Pd)	Et ₃ N	60	80
8	Pd/SiO ₂ (5 wt.% Pd)	Et ₃ N	60	50
9	Pd ₃ P/SiO ₂ (1 wt.% Pd)	Et ₃ N	60	41
10	Pd ₃ P/SiO ₂ (5 wt.% Pd)	Et ₃ N	10	37
11	Pd ₃ P/1P-SiO ₂ (5 wt.% Pd)	Et ₃ N	10	30
12	Pd ₃ P/C (5 wt.% Pd)	Et ₃ N	10	44

Reaction conditions: iodobenzene (1 mmol), base (3 mmol), CO (6 bar), ethanol (4 mL), catalyst (0.5 mol %, Pd basis), 100 °C, 1000 rpm.

The effect of element synergy was subsequently investigated by conducting alkoxycarbonylation reactions with the synthesized reference catalyst (Pd/SiO₂, 5 wt.% Pd). Therefore, the alkoxycarbonylation of iodobenzene and ethanol was performed with Pd/SiO₂ (5 wt.% Pd) with 0.5 mol% catalyst concentration (Pd basis) at 100 °C for 1 h and resulted in an iodobenzene conversion of 50 % with 100 % selectivity to ethyl benzoate (Table 10, entry 8). Under the same reaction conditions, a significantly improved conversion of 80 % (Table 10, entry 7) was observed using the Pd₃P/SiO₂ (5 wt.% Pd) catalyst. This finding clearly indicates the superior activity of Pd₃P in comparison to Pd, thereby pointing towards the positive influence of phosphorus incorporation. Tests conducted at shorter reaction times also yielded consistent results and demonstrate the superior catalytic performance of Pd₃P/SiO₂ (5 wt.% Pd) over its Pd/SiO₂ counterpart. In all cases higher iodobenzene conversions were achieved with Pd₃P/SiO₂ (5 wt.% Pd) with respect to the reference catalyst (Figure 28b).

Further, turnover frequencies for the palladium phosphide and reference catalysts were estimated based on the metal dispersion obtained from CO chemisorption measurements. This comparison offers insights into the enhancement of intrinsic activity enabled by phosphorus incorporation. A TOF value of 7680 h⁻¹ was estimated for Pd₃P/SiO₂ (5 wt.% Pd), whereas a significantly lower value of 2830 h⁻¹ was calculated for the reference Pd/SiO₂ (5 wt.% Pd) catalyst. These results demonstrate the remarkable improvement in active site engineering *via* the formation of the Pd₃P phase and highlight the success of the underlying d-block-p-block

element combination strategy. The electronic and geometric modulations achieved through the P incorporation can be considered as the reason for the superior activity exhibited by Pd_3P catalyst in comparison to pure Pd.

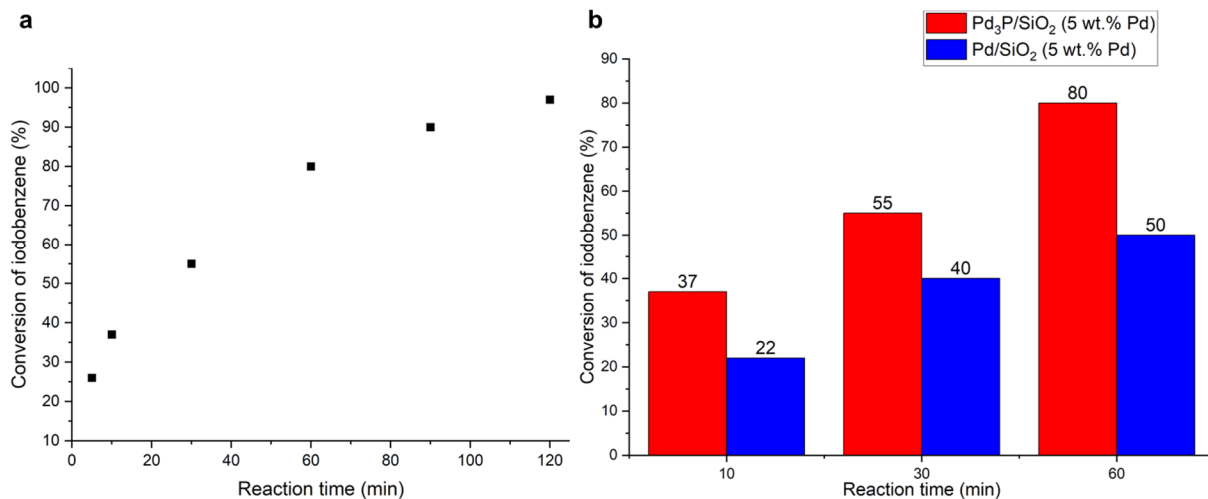


Figure 28: a) Conversion versus time plot for the alkoxy carbonylation of iodobenzene with $\text{Pd}_3\text{P}/\text{SiO}_2$ (5 wt.% Pd) and b) activity comparison of Pd and Pd_3P . Reaction conditions: iodobenzene (1 mmol), Et_3N (3 mmol), CO (6 bar), ethanol (4 mL), catalyst (0.5 mol%, Pd basis), 100 °C, 1000 rpm. The quantifications were performed using GC-MS analysis and *n*-decane as internal standard. This figure has been adapted from reference^[235] (license CC BY-NC ND 4.0).

Various strategies were adapted to further improve the catalytic activity of the supported Pd_3P nanoparticles. The dependency of the particle size on the catalyst performance is well known, where smaller particles often outperform the bigger ones in terms of catalytic activity.^[241–243] Hence, an attempt was made to improve the catalytic activity of Pd_3P by reducing the particle size. For the same, the catalyst was synthesized, adapting the procedure discussed above. However, the Pd impregnation loading on silica was reduced to 1 wt.%. The PXRD analysis of the material obtained, $\text{Pd}_3\text{P}/\text{SiO}_2$ (1 wt.% Pd), showed no reflexes (Figure S17), indicating the formation of smaller crystallites in comparison to $\text{Pd}_3\text{P}/\text{SiO}_2$ (5 wt.% Pd). The synthesized $\text{Pd}_3\text{P}/\text{SiO}_2$ (1 wt.% Pd) catalyst was further tested for the alkoxy carbonylation of iodobenzene at 100 °C for 1 h. However, the results demonstrated a considerably reduced conversion of 41 % with $\text{Pd}_3\text{P}/\text{SiO}_2$ (1 wt.% Pd, Table 10, entry 9) in comparison to 80 % obtained with $\text{Pd}_3\text{P}/\text{SiO}_2$ (5 wt.% Pd). This decline in activity observed for $\text{Pd}_3\text{P}/\text{SiO}_2$ (1 wt.% Pd) most likely arises from the strong binding of substrates and intermediates to the extremely small nanoparticles, leading to surface poisoning effects.^[244]

Effect of support variation

In another approach, the influence of support materials was investigated by preparing Pd_3P on support engineered silica (1P- SiO_2 , from chapter 4) and carbon. The assessment of the catalytic activity was hereby performed at lower conversion levels of iodobenzene to examine the difference in activity. After a reaction time of 10 min, the reaction performed with $\text{Pd}_3\text{P}/1\text{P}$ -

SiO_2 (5 wt.% Pd) showed 30 % conversion (Table 10, entry 11), which is slightly lower than the 37 % (Table 10, entry 10) observed with $\text{Pd}_3\text{P}/\text{SiO}_2$ (5 wt.% Pd). This suggests that the engineered support did not significantly improve the catalytic activity. A slightly improved conversion of 44 % (Table 10, entry 12) was achieved by employing the carbon support ($\text{Pd}_3\text{P}/\text{C}$, 5 wt.% Pd), which might be caused by an improved metal-support interaction. Hence, it can be concluded that by varying support material for the synthesis of supported Pd_3P nanoparticles, the alkoxy carbonylation activity can be tailored. However, a major challenge with using carbon as the support material was the phase identification *via* PXRD, as no reflexes were observed for the carbon-supported catalyst with 5 wt.% Pd loading (Figure S18). Additionally, the low density of the carbon support resulted in handling difficulties, leading to contamination of the Schlenk line during the thermal treatment. Given these issues, further investigations with carbon supports were not pursued, and Pd_3P prepared on silica was used for the remaining tests.

Kinetic investigation

After examining the strategies for improving the catalytic activity, further investigations on the catalytic performance of $\text{Pd}_3\text{P}/\text{SiO}_2$ (5 wt.% Pd) were carried out.

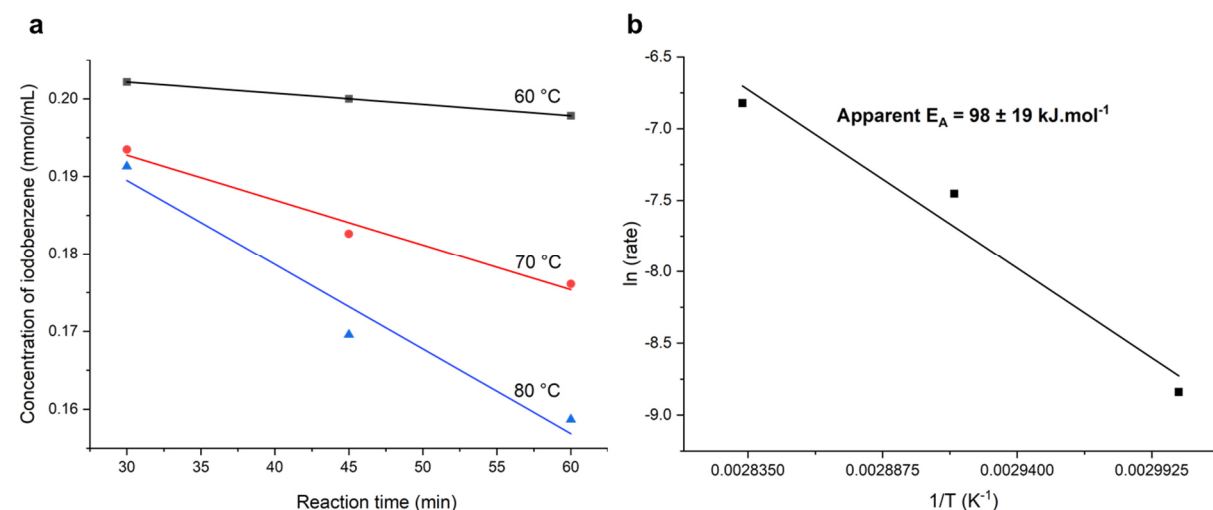


Figure 29: Estimation of the apparent activation energy of the $\text{Pd}_3\text{P}/\text{SiO}_2$ (5 wt.% Pd) catalyzed alkoxy carbonylation of iodobenzene showing a) plot prepared for the determination of rate of reaction and b) Arrhenius plot to determine the apparent activation energy. Reaction conditions: iodobenzene (1 mmol), Et_3N (3 mmol), CO (6 bar), ethanol (4 mL), catalyst (0.5 mol%, Pd basis), 1000 rpm. The quantifications were performed using GC-MS analysis and *n*-decane as internal standard. This figure has been adapted from reference^[235] (license CC BY-NC ND 4.0).

Reaction kinetic investigations were performed by estimating the apparent activation energy of the reaction conducted with $\text{Pd}_3\text{P}/\text{SiO}_2$ (5 wt.% Pd). The reactions were performed at temperatures between 60-80 °C and the rates of the reactions were assessed at low iodobenzene conversions (<30 %). From the slope of the Arrhenius plot ($\ln(\text{rate})$ versus $1/T$),

the apparent activation energy was estimated as $98 \pm 19 \text{ kJ}\cdot\text{mol}^{-1}$ (Figure 29). In comparison, Ito *et al.* reported an apparent activation energy of $104 \text{ kJ}\cdot\text{mol}^{-1}$ for the alkoxy carbonylation of iodobenzene with Pd black using a $\ln(k)$ v/s $1/T$ plot, prepared in the temperature range of 70–100 °C.^[237]

Influence of CO pressure and base concentration

An experiment performed with a higher CO pressure of 24 bar (4 times the previously applied pressure), at 100 °C using $\text{Pd}_3\text{P}/\text{SiO}_2$ (5 wt.% Pd) resulted in substantial drop in conversion, with a calculated TOF of 820 h^{-1} (Table S5, entry 1). This result points towards the negative influence of a very high CO pressure in the progress of the reaction. At higher CO pressures, the availability of active sites for the oxidative addition is reduced due to the metal carbonyl formation, essentially blocking the Pd sites.^[168,179] The CO ligand reduces the electron density of palladium, which in turn increases the activation energy barrier towards the oxidative addition step. This reduced affinity towards oxidative addition substantially reduces the rate of the reaction, resulting in lower conversion values. Also, tests were performed to evaluate the influence of the base concentration. A variation of Et_3N concentration did not result in a significant change in TOF when reduced to one third (Table S5, entry 4), indicating the possibility of performing the reaction with 1 equivalent of base with respect to the substrate.

NuH and aryl halide variation

The tests were further expanded by carrying out the alkoxy carbonylation of iodobenzene with various alcohols (NuH) at 100 °C under 6 bar CO pressure for 2 h using $\text{Pd}_3\text{P}/\text{SiO}_2$ (5 wt.% Pd) as catalyst. The reaction with methanol resulted in 97 % conversion of iodobenzene to methyl benzoate, while isopropanol gave 96 % conversion to isopropyl benzoate (Table 11, entries 1 and 2). Further studies were conducted using various substituted aryl halides, including p-iodotoluene, p-bromo-iodobenzene, and p-idoanisole, with ethanol at 100 °C under 6 bar CO pressure. Excellent conversions ranging from 98 % to 100 % were achieved (Table 11, entries 3 to 6), demonstrating the broad applicability of the synthesized $\text{Pd}_3\text{P}/\text{SiO}_2$ (5 wt.% Pd) catalyst toward different substituted aryl iodides.

Table 11: Alkoxy carbonylation reactions using $\text{Pd}_3\text{P}/\text{SiO}_2$ (5 wt.% Pd) as catalyst with various substrates and nucleophiles (NuH). This table has been adapted from reference^[235] (license CC BY-NC ND 4.0).

Entry	Substrate	NuH	Conversion	Product formed (Selectivity)
1	p-Iodobenzene	Methanol	97 %	Methyl benzoate (100 %)
2		i-Propanol	96 %	Isopropyl benzoate (100 %)
3	p-bromoiodobenzene	Ethanol	99 %	<i>p</i> -(ethoxycarbonyl)phenyl bromide (98 %)
4				Diethyl terephthalate (2 %)
5	p-iodotoluene	Ethanol	98 %	Ethyl- <i>p</i> -methylbenzoate (100 %)
6	p-iodoanisole	Ethanol	100 %	Ethyl- <i>p</i> -methoxybenzoate (100 %)
7	Iodobenzene ^a	Phenol	30 %	Phenyl benzoate (100 %)

Reaction conditions: substrate (1 mmol), Et_3N (3 mmol), CO (6 bar), NuH (4 mL), catalyst (0.5 mol %, Pd basis), 100 °C, 2h. The quantifications were performed using GC-MS analysis and *n*-decane as internal standard.

^a Iodobenzene (1 mmol), phenol (2 mmol), Et_3N (3 mmol), CO (6 bar), toluene as solvent (4 mL), catalyst (Pd 0.5 mol %), 100 °C, 7 h. The quantifications were performed using GC-MS analysis and *n*-decane as internal standard

Benchmarking the catalyst

The activity of $\text{Pd}_3\text{P}/\text{SiO}_2$ (5 wt.% Pd) was compared with several homogeneous catalysts for the alkoxy carbonylation reaction. Reactions were carried out using iodobenzene and ethanol at 100 °C under 6 bar CO pressure, with a catalyst loading of 0.5 mol%. Initially, $\text{Pd}(\text{OAc})_2$, which is commonly employed as a homogeneous pre-catalyst for alkoxy carbonylation reactions, was investigated.^[179] The TOF was determined to be 620 h^{-1} , (Table S7, entry 1), which is substantially lower than the TOF achieved with $\text{Pd}_3\text{P}/\text{SiO}_2$ (5 wt.% Pd) under similar conditions. A similar study using $\text{Pd}(\text{NO}_3)_3 \cdot 2\text{H}_2\text{O}$ yielded a TOF of 700 h^{-1} (Table S7, entry 2). Thus, $\text{Pd}_3\text{P}/\text{SiO}_2$ (5 wt.% Pd) exhibits superior catalytic performance compared to these two homogeneous catalytic systems.

It is also important to benchmark the performance of the herein reported Pd_3P -based catalysts against other heterogeneous Pd catalysts reported for the alkoxy carbonylation reaction. For

example, methyl benzoate yields of 85 % and 73 % were reported with Pd-BOX (BOX: bisoxazoline)^[177] and Pd/C^[239] (Table S8, entries 1 and 2) as catalysts for the alkoxycarbonylation of iodobenzene performed at 100 °C. Under the similar condition Pd₃P/SiO₂ (5 wt.% Pd) catalyst achieved a significantly higher methyl benzoate yield of 98 % (Table S8, entry 14). Similarly, the alkoxycarbonylation in ethanol using 5 % Pd/C^[245] afforded an 80 % yield, but required elevated reaction temperature of 140 °C and a reaction time of 6 h (Table S8, entry 6). In comparison, Pd₃P/SiO₂ (5 wt.% Pd) delivered a superior 97 % yield under much milder conditions of 100 °C and a shorter reaction time of 2 h (Table S8, entry 15). Table S8 in the appendix shows the comparison with various heterogeneous catalysts reported in the literature. From these examples, the superior performance of the palladium phosphide catalyst compared to several heterogeneous catalysts can be concluded.

Other carbonylation reactions

In the field of carbonylation reactions, phenoxy carbonylation and aminocarbonylation represent two other important transformations. Accordingly, this catalytic study was further extended to evaluate the applicability of the palladium phosphide catalyst in these reactions. Interestingly, Pd₃P/SiO₂ (5 wt.% Pd) was found to be active towards both the reactions. The phenoxy carbonylation of iodobenzene performed with toluene as the solvent at 100 °C, 7 h with 0.5 mol% catalyst resulted in 30 % conversion to phenyl benzoate (Table 11, entry 7). Subsequently, the amide synthesis *via* aminocarbonylation was investigated using Pd₃P/SiO₂ (5 wt.% Pd) by reacting iodobenzene with aniline. The reaction carried out at 100 °C under 10 bar CO pressure in toluene for 5 h resulted in a modest 10 % conversion to benzylidene (Table S6, entry 1). Increasing the reaction temperature to 120 °C and 140 °C significantly improved the conversion of iodobenzene, resulting in 56 % and 78 % conversion, respectively (Table S6, entries 2 and 3). In all cases a 100 % selectivity to benzylidene was observed. These results demonstrate the successful application of the synthesized Pd₃P catalyst in both amino and alkoxycarbonylation reactions.

5.3 Recovery and stability tests

After the successful application of the palladium phosphide catalyst in the alkoxy carbonylation reaction, the reusability of the catalyst was verified. The catalyst recovered after the fresh test (first run) was washed 3 times with acetone, dried and used again without any reactivation step. No decline in activity was observed with $\text{Pd}_3\text{P}/\text{SiO}_2$ (5 wt.% Pd) in the second run (first round with recovered catalyst). However, a significant drop in conversion to 50 % from the initial value of 97 % was observed in the third run (second recovery run), indicating a substantial loss of catalytic activity (Figure 30). Further, the Pd content of the recovered catalyst after the first run was quantified *via* ICP-AES analysis to estimate the loss of precious metal. Hereby, a reduction of the Pd content from 4.94 to 3.70 wt.% was estimated, indicating severe metal leaching. To obtain more insights into the mechanism of leaching, a simple analysis of the reaction mixture after centrifugation was carried out. Shining a beam of light through the supernatant indicated a clear Tyndall effect, proving the presence of particles in the sample. Therefore, a loss of Pd_3P particles from the silica support was concluded, possibly due to the reaction conditions and mechanical milling effect induced by the fast-rotating stirrer. This requires the implementation of strategies to improve metal-support interactions to limit the loss of nanoparticles from the support.

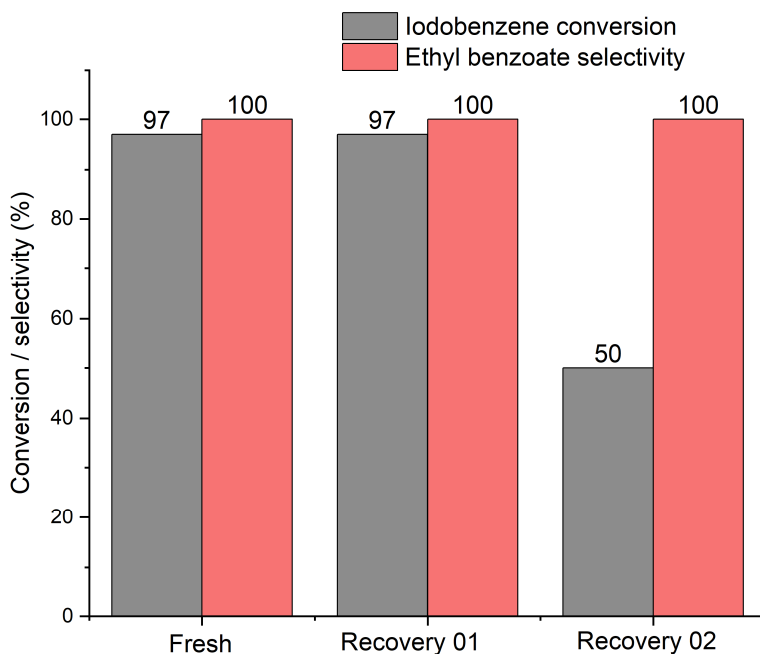


Figure 30: Results of the recovery tests performed using $\text{Pd}_3\text{P}/\text{SiO}_2$ (5 wt.% Pd) as catalyst for the alkoxy carbonylation reaction. Reaction conditions: iodobenzene (0.25 mmol/mL), Et_3N (0.75 mmol/mL), CO (6 bar), ethanol, catalyst (0.5 mol%, Pd basis), 100 °C, 2 h. The quantifications were performed using GC-MS analysis and *n*-decane as internal standard. This figure has been adapted from reference^[235] (license CC BY-NC ND 4.0).

Subsequently, an electron microscopy-based analysis was conducted for the recovered $\text{Pd}_3\text{P}/\text{SiO}_2$ (5 wt.% Pd) catalyst after the first run. The HRTEM lattice fringe-based assessment

confirmed the structural integrity of the catalyst as the measured d spacing of 2.0 \AA is in good agreement with Pd_3P (122), clearly demonstrating no phase transition during catalysis (Figure 31a). However, the particle size analysis revealed nanoparticle sintering, evidenced by an increase in the average particle size from 5.6 nm to 7.0 nm after the first run (Figure 31b). This sintering can be attributed to the presence of CO in the reaction.^[89,169] Such sintering and increase in particle size can also lead to the observed decline in activity in the recovery test.

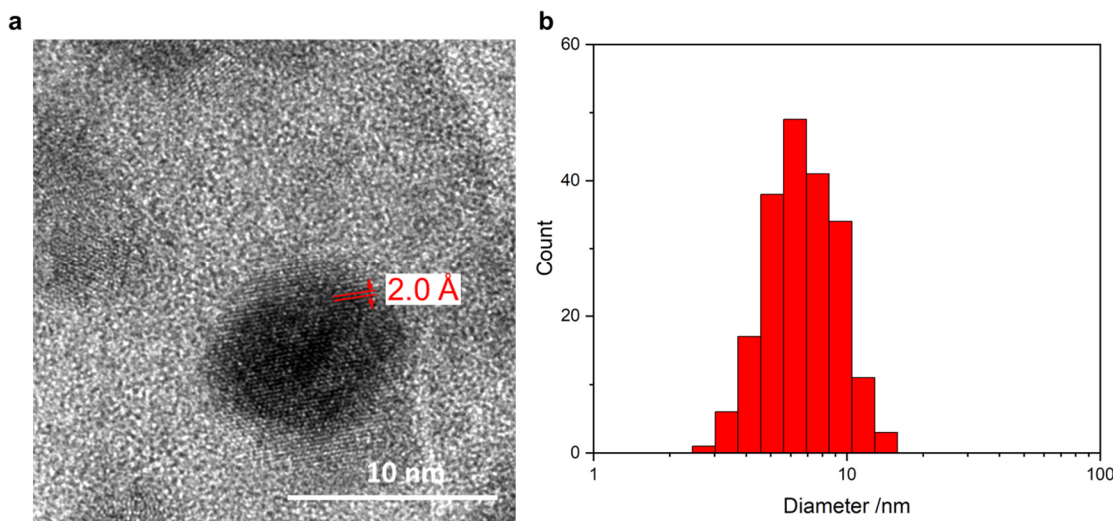


Figure 31: a) HRTEM lattice fringe analysis of the recovered $\text{Pd}_3\text{P}/\text{SiO}_2$ (5 wt.% Pd) catalyst, indicating a d spacing of 2.0 \AA and b) particle size distribution showing an average particle size of 7.0 ± 2.3 nm. Reference for phase identification- Pd_3P (Pnma): $d_{122} = 1.999 \text{\AA}$ (ICSD 85525). Reaction conditions: iodobenzene (0.25 mmol/mL), Et_3N (0.75 mmol/mL), CO (6 bar), ethanol, catalyst (0.5 mol%, Pd basis), 100 $^{\circ}\text{C}$, 2 h. The quantifications were performed using GC-MS analysis and *n*-decane as internal standard. This figure has been adapted from reference^[235] (license CC BY-NC ND 4.0).

5.4 Theoretical investigations of structure-activity relationships

The exceptional activity of supported palladium phosphide nanoparticles observed in this study essentially proves the success of d-block-p-block element combination strategy. The crystal structure discussion of Pd_3P provided in chapter 3, essentially points towards the enhanced Pd site separation in Pd_3P in comparison to pure Pd. The effect of phosphorus specifically on the surface can be investigated through analyzing the possible surface structures of Pd_3P . Herein, low miller indices surfaces (100), (101) and (001) of Pd_3P are studied (Figure 32). Independent of the Miller indices, the surface structure images reveal separated Pd sites resulting from phosphorus incorporation (Figure 32). This clearly indicates the possibility of the unhindered oxidative addition of bulkier aryl halides. Moreover, various structural motifs, such as Pd dimers (Pd_2), Pd trimers (Pd_3) and Pd tetramers (Pd_4) can be identified on the surfaces, which are well separated and can potentially act as active sites. In contrast, on Pd surfaces, all sites possess identical Pd neighbours, and no significant site separation is observed, which can lead to oxidative addition being limited by steric hindrance.

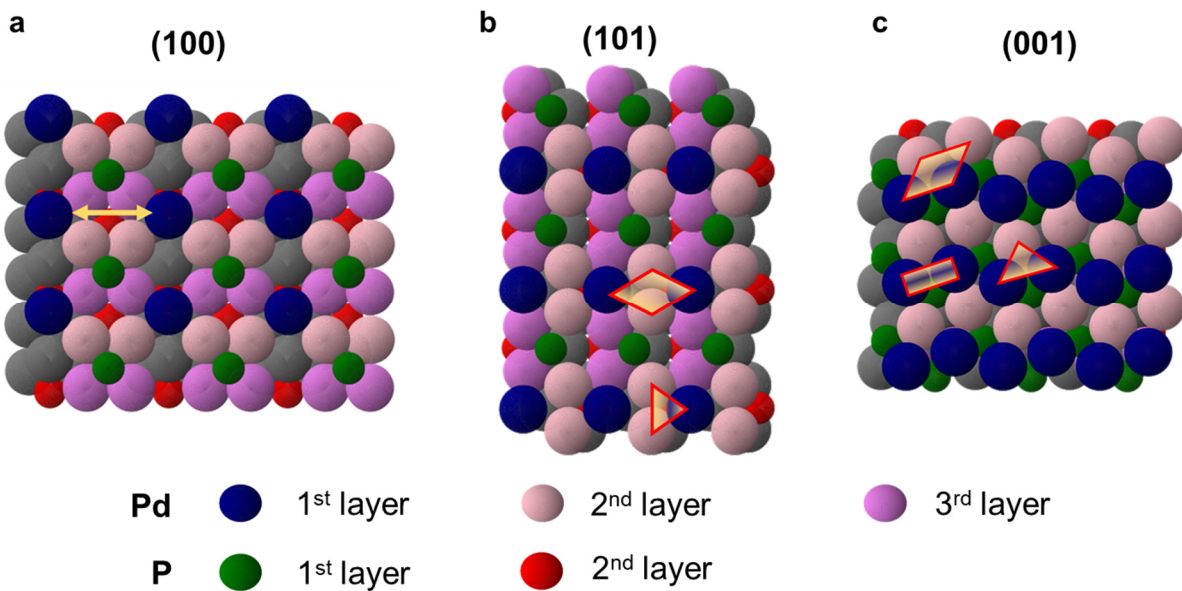


Figure 32: Surface structure of Pd_3P , indicating the formation of various structural motifs and the separation of active sites. The crystal structure data for the generation of the images was obtained from “The Materials Project”^[33] (ID: mp19879).

As evident from the experiments, a higher CO pressure considerably decelerated the reaction, due to the possible formation of metal carbonyl species on the surface. This indirectly point towards the fact that a higher CO affinity of the catalyst surface can possibly result in lower activity. Therefore, approximate CO binding energies were estimated for various Pd_3P and Pd surfaces to assess their CO affinity using the “Open Catalyst Project”.^[246] The calculated CO adsorption energies on Pd_3P (100), Pd_3P (101) and Pd_3P (001) are -1.167 eV, -1.287 eV and -1.216 eV respectively. Whereas, the CO adsorption energies calculated for the preferable Pd (110) and Pd (111) surfaces^[21] are -1.718 eV and -1.740 eV, respectively, which are considerably higher than that on Pd_3P surfaces. The stronger Pd–CO interaction in pure Pd surfaces is likely to promote the formation of metal carbonyl species, which can in turn increase the activation energy barrier for the oxidative addition of aryl halides. Conversely, the weaker CO adsorption on Pd_3P surfaces suggests a lower likelihood for metal carbonyl formation, thus facilitating oxidative addition steps. These findings are consistent with CO chemisorption experiments, where a reduced CO uptake on Pd_3P surfaces relative to pure Pd surfaces was seen. Therefore, CO poisoning is expected to be significantly suppressed on Pd_3P surfaces, resulting in a greater number of available active sites for the oxidative addition of aryl halides and contributing to the enhanced catalytic activity observed.

5.5 Concluding remarks

The application of the element synergy approach, specifically through a d-block-p-block element combination strategy, was successfully demonstrated in the context of alkoxy carbonylation reactions for the first time. Silica-supported palladium phosphide nanoparticles with the Pd_3P phase ($\text{Pd}_3\text{P}/\text{SiO}_2$, 5 wt.% Pd) were synthesized and characterized by PXRD, HAADF-STEM, HRTEM, EDX, CO chemisorption and ICP-AES analyses. The $\text{Pd}_3\text{P}/\text{SiO}_2$ (5 wt.% Pd) catalyst showed superior performance in the alkoxy carbonylation of iodobenzene, outperforming a reference Pd catalyst as well as several reported heterogeneous and homogeneous systems. A significant improvement in intrinsic activity, assessed through TOF values, was achieved through the incorporation of phosphorus and the formation of the Pd_3P phase. The enhanced Pd site separation, the formation of distinct surface motifs, and the tuning of the electronic structure, leading to a favorable adsorption behavior, are proposed as key factors responsible for the exceptional performance of the synthesized palladium phosphide catalyst. Furthermore, the $\text{Pd}_3\text{P}/\text{SiO}_2$ (5 wt.% Pd) catalyst demonstrated excellent activity across a range of substituted aryl halides and alcohols (NuH). Its effectiveness in phenoxy carbonylation and aminocarbonylation reactions further highlights the broad applicability of the developed catalyst in various carbonylation reactions.

Despite its excellent catalytic activity, the stability of the catalyst remains a challenge, as significant nanoparticle detachment from the support and a corresponding decline in activity were observed upon reuse, limiting its long-term applicability. To address this, improving the metal-support interactions is essential. Strategies, such as the use of alternative supports and support engineering, as discussed in chapter 4, could offer effective solutions. Additionally, expanding the scope of the alkoxy carbonylation reactions to include alkenes and alkynes would provide valuable insights into the versatility of the Pd_3P catalyst. Beyond Pd_3P , further investigations into other Pd_xP_y and Pd_xA_y (A: p-block elements, such as S, Sb, or Ga) systems are important to explore the full potential of this class of catalysts in alkoxy carbonylation reactions. A theoretical investigation using density functional theory (DFT) to analyze the energetics of the catalytic cycle, combined with machine learning, could provide valuable insights into the behavior of Pd_xP_y and Pd_xA_y surfaces, thereby enabling more rational and efficient catalyst design.

6 Olefin hydroformylation reactions with supported rhodium sulfide nanoparticles

The results discussed in this chapter were published in:

A. Neyyathala, E. Fako, S. De, D. Gashnikova, F. Maurer, J. Grunwaldt, S. A. Schunk, S. Hanf, *Small Struct.* **2025**, 6, 2400260 under the license CC BY 4.0.

Figures 33 to 48, S21 to S51 and Tables 12, 13 S9 to S17 are adapted from this publication

Patent application 230651EP01, Rhodium Sulfides as Hydroformylation Catalysts, BASF SE and KIT, 08.12.2023.

The theoretical calculations were performed by E. Fako and S. De at BASF SE.

The data of this study are available at [<https://doi.org/10.5281/zenodo.11082359>], reference number [11082360].

Hydroformylation, the synthesis of aldehydes *via* the reaction of alkenes with CO and H₂, is one of the most important industrial reactions.^[102,183,247] The primary catalysts for this transformation are cobalt and rhodium-based homogeneous systems, with rhodium demonstrating significantly higher activity than cobalt.^[102,248,249] Several heterogeneous rhodium catalysts, such as rhodium-based nanoparticles,^[22,191] supported rhodium complexes,^[12,187] and Rh containing zeolite^[250] have also demonstrated promising performance in hydroformylation reactions.

A catalyst design strategy based on element synergy has been successfully applied in hydroformylation reactions using systems, such as Rh-Zn,^[191] Rh-P,^[22,25] and Rh-Co^[251] in the form of supported nanoparticles. These examples highlight the potential of extending this approach to other element combinations. Notably, Rh₂P nanoparticles have outperformed pure Rh in both liquid^[25] and gas phase^[22] hydroformylation reactions. All of these findings are motivating to start the exploration of neighboring elements for the incorporation into Rh. In this context, sulfur, traditionally regarded as a catalyst poison,^[63] was investigated as a promoter as part of this work in combination with rhodium. It is worth noting that many metal sulfides have shown excellent catalytic performance in semi-hydrogenation,^[21] CO₂ reduction,^[252] and methanol carbonylation^[253] reactions. These findings point towards the potential of applying the underlying d-block-p-block element combination strategy, with Rh and S as the participating elements, to boost oxo chemistry.

In this study, supported rhodium sulfide nanoparticles, specifically phases assigned to Rh₁₇S₁₅ and Rh₂S₃, were synthesized and extensively characterized by PXRD, HAADF-STEM, HR-

TEM, EDX, XPS, ICP-AES, DRIFT, and XAS. These Rh_xS_y nanoparticles ($x = 17$, $y = 15$ or $x = 2$, $y = 3$) were evaluated in the liquid-phase hydroformylation of olefins. In particular, the $\text{Rh}_{17}\text{S}_{15}$ phase demonstrated superior catalytic activity in the hydroformylation of styrene, outperforming pure Rh and several reported homogeneous and heterogeneous catalysts. A combined theoretical investigation using DFT and machine learning revealed that rhodium sulfide catalysts possess spatially isolated active sites with a wide range of CO binding energies.

6.1 Synthesis and characterization of $\text{Rh}_x\text{S}_y/\text{SiO}_2$

An analysis of the phase stability diagram, generated using “The Materials Project”^[33], (Figure S20) identified $\text{Rh}_{17}\text{S}_{15}$, Rh_3S_4 and Rh_2S_3 as the thermodynamically stable rhodium sulfide phases, each exhibiting an energy above hull of 0.0 eV.^[33,254] The investigation was started considering the most Rh rich $\text{Rh}_{17}\text{S}_{15}$ ($\text{Rh}/\text{S} = 1.13$) and lean Rh_2S_3 ($\text{Rh}/\text{S} = 0.66$) to analyze the difference in performance originate from the crystal structure and metal content. Silica supported rhodium sulfide nanoparticles were synthesized *via* the incipient wetness impregnation method, using rhodium acetate ($\text{Rh}(\text{OAc})_3$) and thiourea ($\text{CH}_4\text{N}_2\text{S}$) as the Rh and S precursors. Following the impregnation step, the samples were thermally treated under a flowing argon atmosphere to form the rhodium sulfide nanoparticles.

Optimization of synthesis conditions

To optimize the synthesis conditions, initial efforts were directed toward the preparation of silica-supported $\text{Rh}_{17}\text{S}_{15}$ nanoparticles. A relatively high Rh loading of 10 wt.% was chosen to facilitate a facile phase identification *via* PXRD. To account for any potential sulfur loss during thermal treatment, an excess of sulfur precursor, beyond the stoichiometric S/Rh ratio required for the target phase, was used to ensure a proper phase formation. Interestingly, several factors were found to influence the formation of the target phase and the activity of the resulting catalyst. First of all, the impact of the sulfur precursor amount on the phase formation was studied. The synthesis performed using precursors with 20 %, 30 %, and 50 % molar excess of thiourea were thermally treatment under a flowing argon atmosphere at 700 °C for 6 h. When a 20 mol% excess of thiourea was used, the product consisted of a mix of metallic Rh and $\text{Rh}_{17}\text{S}_{15}$. This finding can be attributed to the loss of sulfur at the high temperature treatment (Figure 33a, I). In contrast, a 50 mol% excess of thiourea indicated the formation of the sulfur rich Rh_2S_3 phase (Figure 33a, III), whereas the use of 30 mol% excess thiourea resulted in the formation of phase pure $\text{Rh}_{17}\text{S}_{15}$, indicating the optimum quantity of sulfur precursor for the successful synthesis (Figure 33a, II).

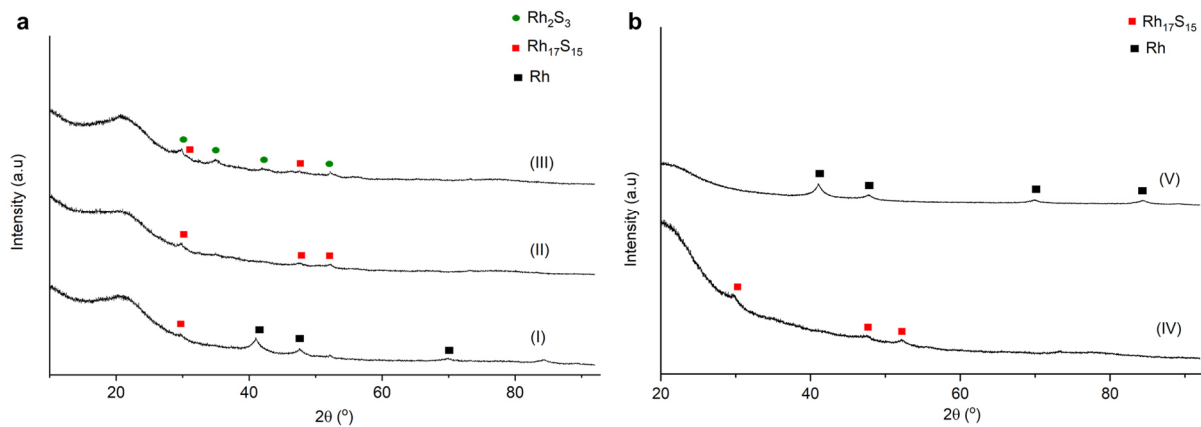


Figure 33: PXRD patterns showing a) the influence of quantity of sulfur precursor on the Rh₁₇S₁₅ phase formation applying I) 20 mol% excess, II) 30 mol% excess and III) 50 mol% excess of thiourea, b) phases formed at thermal treatment temperature of IV) 700 °C and V) 750 °C. Reference for phase identification: Rh₁₇S₁₅ - ICSD: 410838, Rh - ICSD: 171677, Rh₂S₃ - ICSD: 56882. This figure has been adapted from^[255] (license CC BY 4.0).

Even though a high Rh loading was used throughout the synthesis, the PXRD analysis posed some challenges, due to the low crystallinity of the synthesized nanoparticles as shown by the broadened reflexes, and therewith involved small crystallites. In order to enhance the crystallinity through sintering, thereby enabling a more facile phase identification, the thermal treatment temperature was increased further to 750 °C. This however resulted in the formation of metallic Rh, due to the loss of S at this temperature (Figure 33b, V). This experiment revealed the critical nature of the temperature, and showed that 700 °C can be considered as the optimum temperature for the target phase formation.

To investigate the influence of the gas flow rate on the phase formation, the argon flow rate during thermal treatment was systematically varied. The thermal treatment at 700 °C using the impregnated precursor with 30 mol% excess of thiourea and a low argon flow rate of 15 Nl/h resulted in the formation of both Rh₁₇S₁₅ and Rh₂S₃ (Figure 34b, III). In contrast, increasing the flow rate significantly to 450 Nl/h yielded phase pure Rh₁₇S₁₅ (Figure 34b, IV). At this higher flow rate, the formation of smaller, more finely dispersed nanoparticles on the support is highly likely to occur.^[243] Furthermore, the high argon flow can have a surface cleaning effect, mitigating potential catalyst poisoning by reducing the adsorption of excess sulfur species on Rh active sites during the synthesis.

Based on the results of the above described experiments, the optimum conditions for the synthesis of Rh₁₇S₁₅ nanoparticles were determined to be: 30 mol% excess thiourea in the impregnated precursor, thermal treatment at 700 °C, and an argon flow rate of 450 Nl/h.

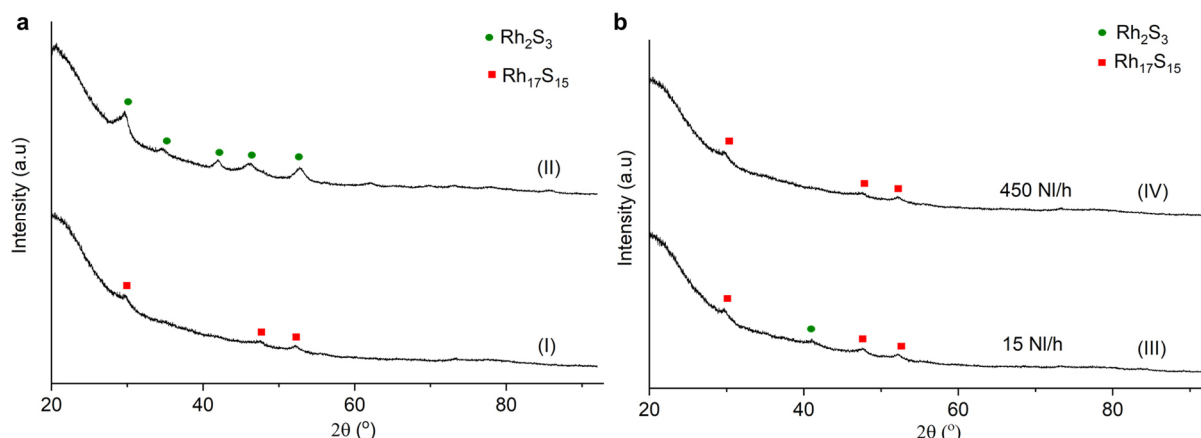


Figure 34: a) PXRD patterns of I) Rh₁₇S₁₅/SiO₂ (10 wt.% Rh) and II) Rh₂S₃/SiO₂ (10 wt.% Rh) and b) PXRD patterns showing the influence of the argon flow rate on the Rh₁₇S₁₅ phase formation with flow rates of III) 15 NI/h and IV) 450 NI/h. Reference for phase identification: Rh₁₇S₁₅ - ICSD: 410838, Rh₂S₃ - ICSD: 56882. This figure has been adapted from reference^[255] (license CC BY 4.0).

In contrast, the successful formation of Rh₂S₃ nanoparticles on silica required a 50 mol% excess of thiourea (Figure 34a, II), while the other synthesis parameters, including temperature and argon flow rate, remained identical to those used for Rh₁₇S₁₅.

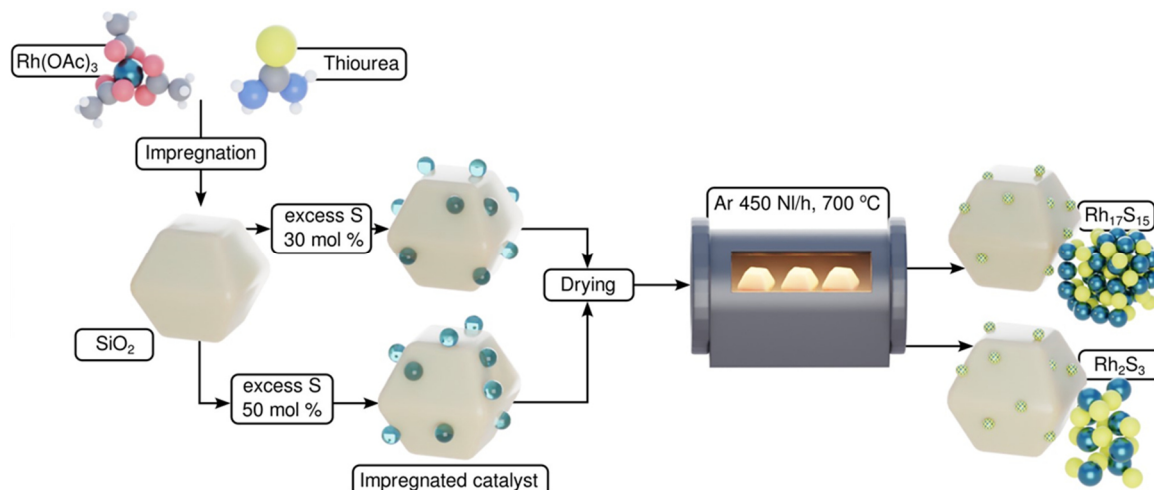


Figure 35: Schematic diagram demonstrating the synthesis route and optimum conditions for the supported rhodium sulfide nanoparticles investigated in this work. This figure has been adapted from reference^[255] (license CC BY 4.0).

After the successful synthesis of 10 wt.% Rh-containing supported rhodium sulfide catalysts, the syntheses were performed with lower metal loadings following the same procedures, however varying the silica quantity to adjust the loading. Herein, Rh₁₇S₁₅/SiO₂ catalysts with 10, 5 and 1 wt.% Rh loading were prepared. Similarly, Rh₂S₃/SiO₂ catalysts with 10 and 1 wt.% Rh loading catalysts were prepared. The PXRD analyses of the materials with lower Rh loading did not show any reflexes, indicating the formation of smaller crystallites in comparison to the 10 wt.% metal-containing samples (Figure S21).

A supported Rh reference catalyst was synthesized with 1 wt.% Rh loading (Rh/SiO_2 , 1 wt.% Rh) adapting the same synthesis conditions as that of rhodium sulfides, however without the addition of S precursor. A PXRD analysis indicated the formation of Rh nanoparticles on silica (Figure S22). When compared with the PXRD results of rhodium sulfides, the formation of bigger crystallites can be seen for the supported rhodium catalyst from the observed reflexes. This observation implies that the sulfur incorporation into rhodium during the synthesis may contribute to an enhanced sintering resistance at high temperatures.

Advanced characterization

To obtain a more distinct identification of the phases present, selected area electron diffraction (SAED) was performed in conjunction with transmission electron microscopy (TEM). The obtained SAED patterns for $\text{Rh}_{17}\text{S}_{15}/\text{SiO}_2$ (10 wt.% Rh) and $\text{Rh}_{17}\text{S}_{15}/\text{SiO}_2$ (5 wt.% Rh) clearly provided the evidence for the formation of target $\text{Rh}_{17}\text{S}_{15}$ phase (Figure S23a). Similarly, the formation of the Rh_2S_3 phase was confirmed from the SAED analysis (Figure S23b) for $\text{Rh}_2\text{S}_3/\text{SiO}_2$ (10 wt.% Rh). However, the analysis of the rhodium sulfide samples with 1 wt.% Rh content did not give any meaningful data due to the very small crystallites/particles formed, leading to a lack of signals during the measurements. HRTEM lattice fringe-based analysis was additionally performed for the catalysts in order to confirm the formation of phases (Figure S24 to Figure S27). For instance, a lattice fringe distance of 0.26 nm measured for the $\text{Rh}_2\text{S}_3/\text{SiO}_2$ (1 wt.% Rh) sample and is in good agreement with the d-spacing corresponding to Rh_2S_3 (112), which clearly indicates the formation of the corresponding phase (Figure S27).

The elemental composition and distribution in the sample was measured by EDX spectroscopy in connection with TEM (Figure S24 to Figure S27). An elemental mapping performed for the samples indicated a uniform distribution of rhodium and sulfur over silica, with an estimated average Rh/S ratio close to 1.13 for $\text{Rh}_{17}\text{S}_{15}/\text{SiO}_2$ (1 and 10 wt.% Rh) and 0.66 for $\text{Rh}_2\text{S}_3/\text{SiO}_2$ (1 and 10 wt.% Rh), proving the integrity of the samples. Moreover, no nitrogen-containing species were detected in the EDX analysis, which confirms the complete decomposition of thiourea. Herein an indicative mechanism of formation of target phases can be proposed. Under the applied thermal treatment conditions, thiourea is expected to decompose, generating sulfur-containing species, such as CS_2 and H_2S ,^[256] which can subsequently react with Rh to form rhodium sulfide nanoparticles.

The synthesized rhodium sulfide materials were further characterized using HAADF-STEM to gain detailed insights into the particle morphology and distribution (Figure S24 to Figure S27). Z-contrast imaging performed revealed spherically shaped rhodium sulfide nanoparticles dispersed on the silica support. Notably, variations in particle size were observed depending on the Rh loading (Figure S30). Figure 36 indicates an increase in particle size with respect to the impregnation loading. For instance, the estimated average particle sizes for $\text{Rh}_{17}\text{S}_{15}/\text{SiO}_2$

(1 wt.% Rh) and $\text{Rh}_2\text{S}_3/\text{SiO}_2$ (1 wt.%) were 2.2 nm and 3.0 nm, whereas larger particle sizes of 6.3 nm and 3.6 nm were observed for their 10 wt.% loaded counterparts. This increase in particle size can be attributed to an enhanced sintering resulting from the higher metal concentration on the support, which promotes particle migration and coalescence as well as Ostwald ripening.^[257,258]

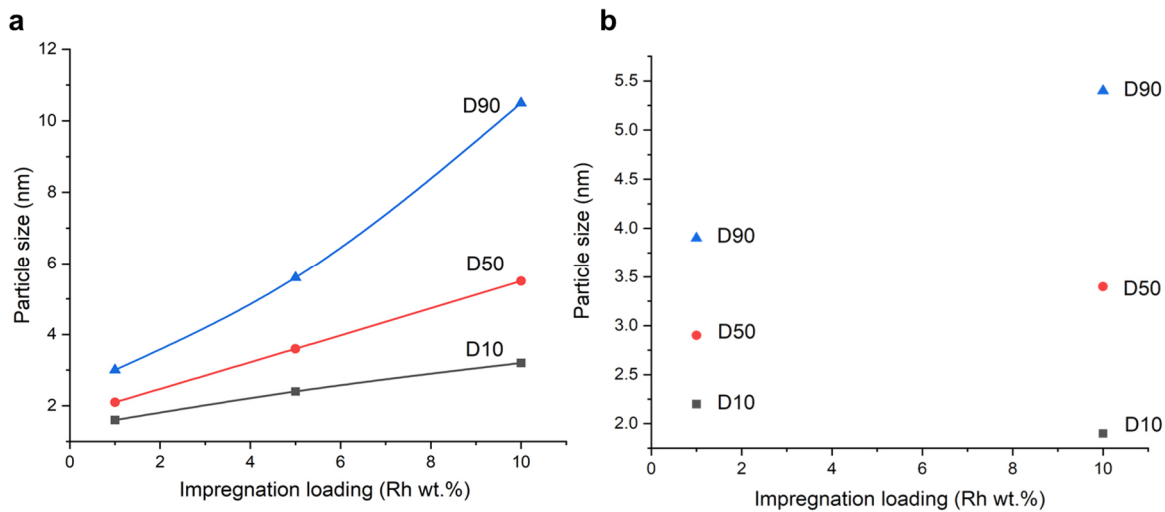


Figure 36: Dependency of the particle size on the Rh loading on the support for a) $\text{Rh}_{17}\text{S}_{15}/\text{SiO}_2$ and b) $\text{Rh}_2\text{S}_3/\text{SiO}_2$. D10 implies, 10 % of the particle are smaller than the corresponding particle size, similarly D 50 (median) and D 90. This figure has been adapted from reference^[255] (license CC BY 4.0).

An interesting observation was made during the high resolution HAADF-STEM imaging of a single particle of $\text{Rh}_{17}\text{S}_{15}/\text{SiO}_2$ (10 wt.% Rh) (Figure 37c and d). A periodically arranged layer of Rh atoms with an approximate average inter planar spacing of 4 Å is visible, which is considerably higher than the spacing of 1.9 Å^[259] observed for metallic rhodium. This expanded Rh layer separation, attributed to sulfur incorporation, suggests the potential isolation of active sites on the particle surface, despite the fact that the imaging primarily reflects bulk characteristics. Additionally, the observed atomic arrangement hints at the possible formation of surface structural motifs.

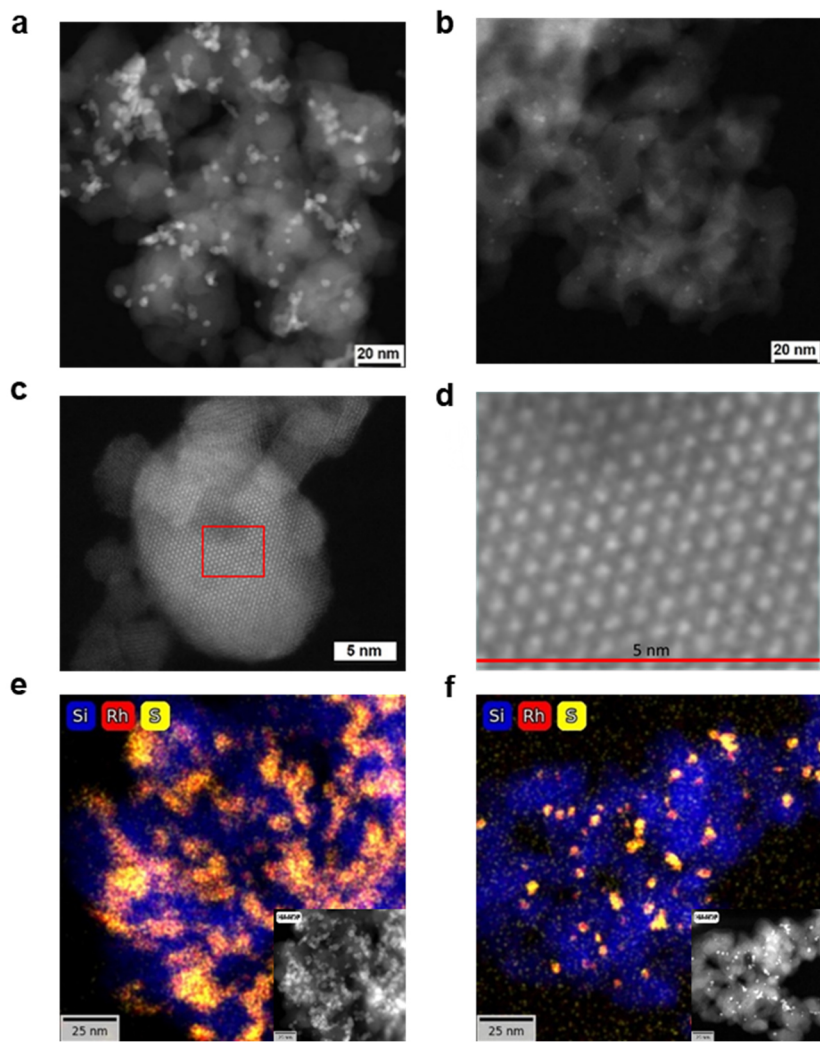


Figure 37: HAADF-STEM mages showing rhodium sulfide nanoparticles distributed on silica obtained with a) $\text{Rh}_{17}\text{S}_{15}/\text{SiO}_2$ (10 wt.% Rh) and b) $\text{Rh}_{17}\text{S}_{15}/\text{SiO}_2$ (1 wt.% Rh). HR-HAADF-STEM imaging performed for c) $\text{Rh}_{17}\text{S}_{15}/\text{SiO}_2$ (10 wt.% Rh) and d) magnified section marked in the red exhibiting separated Rh atomic layers. EDX elemental mapping of e) $\text{Rh}_{17}\text{S}_{15}/\text{SiO}_2$ (10 wt.% Rh) and b) $\text{Rh}_{17}\text{S}_{15}/\text{SiO}_2$ (1 wt.% Rh). The HAADF-STEM images corresponding to the EDX mappings are provided at the inset. This figure has been adapted from references^[255] (license CC BY 4.0).

The electronic environment and structure of the rhodium sulfide catalysts were further investigated using X-ray absorption spectroscopy analysis (Figure 38). The X-ray absorption near edge structure (XANES) analysis of $\text{Rh}_{17}\text{S}_{15}/\text{SiO}_2$ (1 wt.% Rh) and $\text{Rh}_2\text{S}_3/\text{SiO}_2$ (1 wt.% Rh) led to similar observations for both catalysts (Figure 38a). In comparison to metallic Rh and Rh_2O_3 , used as references, where Rh exists in 0 and +3 oxidation states respectively, an oxidation state lying between these values can be concluded for the rhodium sulfides ($\text{Rh}^{\delta+}$). This observation is line with the XANES investigation performed by Ziegelbauer *et al.* on rhodium sulfide, where a combination of features of Rh and Rh_2O_3 were observed for Rh_xS_y and the bulk oxidation state of Rh was assigned to +1.2.^[260] Such a partially charged Rh indicates electron transfer from Rh to S and an electronic structure modulation achieved

through sulfur incorporation. The characteristic broad white line observed in the spectra around 23,240 eV is consistent with previously reported XANES features of Rh_xS_y species.^[260–262]

To investigate the structural characteristics of the materials further, extended X-ray absorption fine structure (EXAFS) spectroscopy was employed, and the corresponding Fourier-transformed spectra (FT-EXAFS) were analyzed (Figure 38b). The results provided further evidence for the formation of rhodium sulfide phases in the synthesized catalysts. A prominent feature, observed at a backscattering distance of 1.8 Å (not corrected for scattering phase shift), corresponds to Rh-S interactions^[262] confirming the presence of such bonds in $\text{Rh}_{17}\text{S}_{15}/\text{SiO}_2$ (1 wt.% Rh) and $\text{Rh}_2\text{S}_3/\text{SiO}_2$ (1 wt.% Rh). Additionally, a peak at 2.3 Å attributed to Rh-Rh backscattering in the $\text{Rh}_{17}\text{S}_{15}$ crystal structure was observed in the $\text{Rh}_{17}\text{S}_{15}/\text{SiO}_2$ (1 wt.% Rh) catalyst. Notably, the Rh-Rh backscattering distance is shifted to a lower value with respect to pure Rh, where the feature can be observed at 2.4 Å. In the case of $\text{Rh}_2\text{S}_3/\text{SiO}_2$ (1 wt.% Rh), the Rh-Rh backscattering feature was less prominent, indicating a reduced metallic character compared to $\text{Rh}_{17}\text{S}_{15}$. This observation aligns with the reduced Rh content and the band gap of Rh_2S_3 (0.19 eV), supporting its lower metallic character relative to $\text{Rh}_{17}\text{S}_{15}$. The feature at 1.5 Å, corresponding to Rh-O, most likely results from the prolonged storage of the sample under atmospheric condition prior to the measurement, leading to surface oxidation.

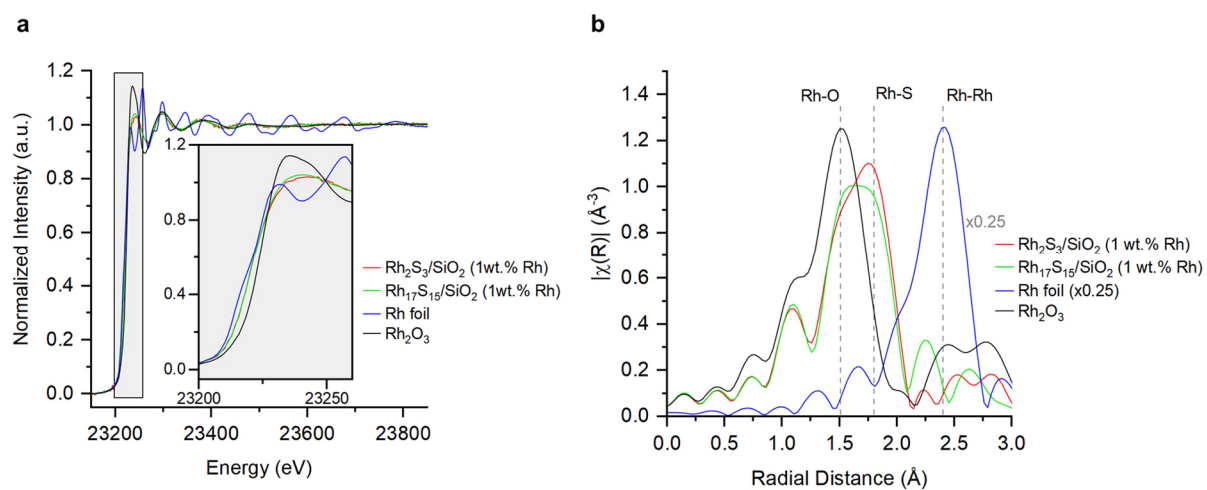


Figure 38: Ex situ XAS spectra recorded for the rhodium sulfide samples at the Rh-K edge a) with an inset showing the XANES region and b) FT-EXAFS spectra (k^2 -weighted, not phase corrected). The spectra obtained for the reference samples (Rh foil and Rh_2O_3) are also provided for the comparison purpose. This figure has been adapted from reference^[255] (license CC BY 4.0).

Surface analysis

To gain further insights into the surface properties of the synthesized catalysts, XPS analysis was conducted to study the oxidation states of Rh and S in the rhodium sulfide catalysts. Both the 1 wt.% and 10 wt.% Rh loaded samples, ($\text{Rh}_x\text{S}_y/\text{SiO}_2$, $x = 17$, $y = 15$ or $x = 2$, $y = 3$ with 1 and 10 wt.% Rh) were analysed *via* XPS. On deconvolution of the Rh 3d signals of the 10 wt.%

Rh loaded samples ($\text{Rh}_x\text{S}_y/\text{SiO}_2$, $x = 17$, $y = 15$ or $x = 2$, $y = 3$ with 10 wt.% Rh), the possible presence of two Rh species was identified (Figure S32a and Figure S34a). The doublet observed at binding energies of 309.5 eV and 314.4 eV corresponds to $3d_{5/2}$ and $3d_{3/2}$ states, which can be assigned to rhodium sulfides, as the signal at 309.5 eV is generally associated with covalently bonded Rh in an oxidized form.^[65,263] This observation can be substantiated by the S 2p signals observed for $\text{Rh}_x\text{S}_y/\text{SiO}_2$ ($x = 17$, $y = 15$ or $x = 2$, $y = 3$ with 10 wt.% Rh) samples at 161.9 eV and 162.9 eV, corresponding to polysulfides. Therefore, the analysis provides indication on covalently bound rhodium and sulfur, confirming the presence of rhodium sulfides in the sample.^[65,263] Herein, a partially positive oxidation state can be assigned to rhodium ($\text{Rh}^{\delta+}$), which is in good agreement with the XANES analysis of Rh_xS_y . The absence of the S 2p signal at 164 eV^[65] indicates the lack of elemental sulfur on the surface of the sample. The other doublet of Rh 3d at binding energies 307.5 eV and 312.2 eV corresponding to $3d_{5/2}$ and $3d_{3/2}$ states and can be assigned to metallic rhodium (Rh^0). Furthermore, the Rh to S ratio was determined by XPS for the samples containing 10 wt.% Rh loading. A ratio of 1.11 was obtained for $\text{Rh}_{17}\text{S}_{15}/\text{SiO}_2$ (10 wt.% Rh) and 0.53 for $\text{Rh}_2\text{S}_3/\text{SiO}_2$ (10 wt.% Rh) which are consistent with the expected Rh to S ratios based on the stoichiometry of the respective phases (Table S11).

The observations associated with the Rh 3d signals are identical for the lower Rh loaded samples $\text{Rh}_x\text{S}_y/\text{SiO}_2$ ($x = 17$, $y = 15$ or $x = 2$, $y = 3$ with 1 wt.% Rh). Hereby, again the presence of Rh^0 and $\text{Rh}^{\delta+}$ species can be confirmed (Figure S33a and Figure S 35a). However, no S 2p signals were observed (Figure S33b and Figure S 35b), possibly due to the very low concentration of sulfur in the sample (below the detection limit). The existence of Rh^0 and $\text{Rh}^{\delta+}$ in Rh_xS_y has also been observed with the reported XPS spectra of Rh_xP_y systems.^[25] This may therefore be considered a characteristic feature of rhodium chalcogenide and pnictogenide phases and demonstrated the structural diversity of metal sites in metal sulfides and phosphides. The observed oxygen signal in the spectra can be attributed to the silica support, thereby ruling out the presence of Rh_2O_3 within the detection limits of XPS. Additionally, no nitrogen species were detected by XPS analysis, in line with the EDX analysis, confirming the complete decomposition of the thiourea precursor during the synthesis process.

The surface chemistry of the rhodium sulfide samples was further investigated using DRIFTS with CO as a probe molecule, providing more surface specific information (Figure 39a and Figure S38). Differences in the surface characteristics are evident from the comparison of DRIFT spectra of $\text{Rh}_{17}\text{S}_{15}$, Rh_2S_3 and Rh. The band observed in the initial scan at 2105 cm^{-1} in the $\text{Rh}_{17}\text{S}_{15}/\text{SiO}_2$ (1 wt.% Rh) can be assigned to the symmetric stretching mode of gem-dicarbonyl species ($\text{Rh}^{3+}(\text{CO})_2$).^[264,265] This species is formed through the interaction of two CO molecules with a highly oxidized Rh centre. On exposure to CO a reduction of the surface species is observed leading to the shift in the symmetric stretching mode to a lower wave

number (2102 cm^{-1}). Therefore, the bands at 2102 cm^{-1} and 2036 cm^{-1} can be assigned to the symmetric and asymmetric stretching modes of $\text{Rh}^{\delta+}(\text{CO})_2$ species. The signal near 2067 cm^{-1} corresponds to linearly bonded CO on metallic rhodium ($\text{Rh}^0\text{-CO}$).^[264,265] Similarly, the analysis of $\text{Rh}_2\text{S}_3/\text{SiO}_2$ (1 wt.% Rh) showed (Figure S38) the symmetric stretching mode corresponding to gem-dicarbonyl species ($\text{Rh}^{3+}(\text{CO})_2$) at 2104 cm^{-1} , and the subsequent reduction of this species on CO exposure leading to the shift in symmetric stretching mode to 2086 cm^{-1} . The signals at 2086 cm^{-1} and 2036 cm^{-1} correspond to the symmetric and asymmetric stretching modes of $\text{Rh}^{\delta+}(\text{CO})_2$. Further, the coordination of CO in a linear fashion to Rh^0 can be seen from the signal at 2073 cm^{-1} .^[264,265] The immediate formation of the signal near 2086 cm^{-1} (sudden shift of the wave number from the initial value of 2104 cm^{-1}) underlines the facile reducibility of the Rh_2S_3 surface species in contrast to $\text{Rh}_{17}\text{S}_{15}$ on exposure to CO, showing the difference in surface chemistry with respect to the S incorporation.

- Further to analyze the effect of the sulfur incorporation on the CO adsorption behaviour, Rh/SiO_2 (1 wt.% Rh) was analyzed *via* DRIFT spectroscopy (Figure 39, b). The results are in line with the reported spectrum of Rh/SiO_2 .^[265] In comparison to the rhodium-rich $\text{Rh}_{17}\text{S}_{15}/\text{SiO}_2$ (1 wt.% Rh) sample, two major findings were observed: A blue shift in the symmetric and asymmetric stretching vibrations, corresponding to rhodium gem-dicarbonyl species is observed, shifting from 2098 and 2028 cm^{-1} in pure Rh samples to 2102 and 2036 cm^{-1} in $\text{Rh}_{17}\text{S}_{15}$. This indicates a lower back donation from Rh to CO in $\text{Rh}_{17}\text{S}_{15}$ and suggests an electron deficient rhodium surface (rhodium with higher cationic nature). This indicated electron transfer from Rh to S leading to the formation of $\text{Rh}^{\delta+}$ is in line with the observations from XANES and XPS analyses.
- A bridged CO vibration mode on Rh^0 at 1936 cm^{-1} can be observed in Rh/SiO_2 (1 wt.% Rh) catalyst.^[265] However, such bridged species were absent in $\text{Rh}_{17}\text{S}_{15}/\text{SiO}_2$ (1 wt.% Rh), underlining the Rh separation induced by S. Such a separation of Rh sites through S incorporation were seen in the HR-HAADF-STEM analysis (Figure 37d).

Therefore, the observed differences between the $\text{Rh}_{17}\text{S}_{15}$ and pure Rh surfaces indicate distinct surface properties, which may result in variations in their catalytic performance.

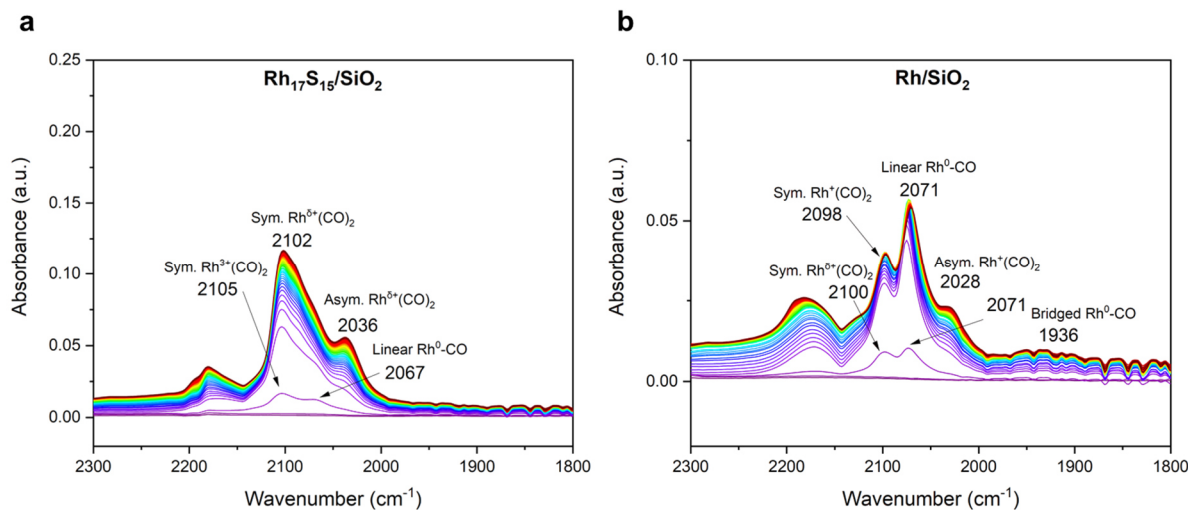
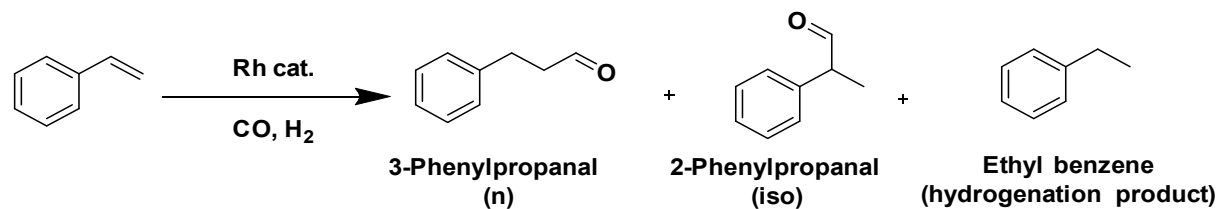


Figure 39: CO-DRIFT spectra of a) $\text{Rh}_{17}\text{S}_{15}/\text{SiO}_2$ (1 wt.% Rh) and Rh/SiO₂ (1 wt.% Rh). Signals around 2200 cm^{-1} corresponds to gas phase CO. This figure has been adapted from reference^[255] (license CC BY 4.0).

6.2 Catalytic performance in olefin hydroformylation reactions

The rhodium sulfide catalysts, $\text{Rh}_x\text{S}_y/\text{SiO}_2$ ($x = 17$, $y = 15$ or $x = 2$, $y = 3$ with 10 and 1 wt.% Rh), were applied in the liquid-phase hydroformylation reaction in batch reactors with styrene as model substrate. During the hydroformylation of styrene with CO and H₂, both the linear product 3-phenylpropanal and the branched isomer 2-phenylpropanal can be formed, along with the undesired hydrogenation side product, ethylbenzene. A key objective in developing hydroformylation catalysts is to modulate the catalytic activity to favor the aldehyde formation, while simultaneously minimizing the competing hydrogenation pathway.^[22,266]



Scheme 9: Hydroformylation of styrene, also indicating the possible hydrogenation side-product.

The performance of the rhodium sulfide catalysts was assessed under the reaction conditions of 40 bar syngas pressure (CO:H₂ 1:1), 0.2 mol% catalyst concentration (Rh basis) at a temperature of 80 °C and a stirring speed of 1200 rpm in batch mode. Reactions performed with $\text{Rh}_{17}\text{S}_{15}/\text{SiO}_2$ (10 wt.% Rh) and $\text{Rh}_2\text{S}_3/\text{SiO}_2$ (10 wt.% Rh) for 80 min resulted in styrene conversions of 18 % and 5 % (Table 12, entries 1 and 2), respectively, with 100 % selectivity towards the aldehyde products. An enhanced conversion of 85 % for $\text{Rh}_{17}\text{S}_{15}$ and 42 % for Rh_2S_3 were achieved (Table 12, entries 3 and 4) upon allowing the reaction to proceed further for 225 min. Hereby a slight drop in aldehyde selectivity to 99 %, due to the formation of trace amounts of hydrogenation product (ethyl benzene), was observed using $\text{Rh}_{17}\text{S}_{15}/\text{SiO}_2$ (10 wt.%

Rh) as catalyst. Interestingly, the selectivity remained the same with $\text{Rh}_2\text{S}_3/\text{SiO}_2$ (10 wt.% Rh). These results show the active nature of the rhodium sulfide catalysts in hydroformylation catalysis with $\text{Rh}_{17}\text{S}_{15}$ outperforming Rh_2S_3 in terms of activity.

The tests were further extended towards supported rhodium sulfide catalysts with a lower Rh loading (1 wt.% Rh). A reaction performed for 80 min with $\text{Rh}_{17}\text{S}_{15}/\text{SiO}_2$ (1 wt.% Rh) resulted in a styrene conversion of 87 %, (Table 12, entry 5), which is almost 5 times higher than the value obtained with $\text{Rh}_{17}\text{S}_{15}/\text{SiO}_2$ (10 wt.% Rh) under similar conditions. A similar observation was made when $\text{Rh}_2\text{S}_3/\text{SiO}_2$ (1 wt.% Rh) was used as catalyst, where a substantially higher conversion of 60 % was obtained (Table 12, entry 7) in comparison to the 10 wt.% Rh loaded counter part (12 times higher). Here, this improvement in catalytic activity can be attributed to the reduction in particle size at lower Rh loadings, as clearly observed *via* electron microscopic analysis. Smaller particles ultimately lead to an increased number of surface metal atoms and thus provide more accessible active sites for the catalytic reaction.^[243,267] Moreover, the reduction in particle size can also lead to an increase in low/under-coordinated metal sites, such as those located at defects, corners, steps, and edges, which may also serve as active sites for catalytic reactions.^[243]

A comparison of the activity of $\text{Rh}_x\text{S}_y/\text{SiO}_2$ ($x = 17, y = 15$ or $x = 2, y = 3$, 1 wt.% Rh) was conducted with a reference Rh catalyst (Rh/SiO_2 , 1wt.% Rh). A substantially lower conversion of 40 % (Table 12, entry 9), in comparison to the rhodium sulfide catalysts (60 % for Rh_2S_3 and 87 % for $\text{Rh}_{17}\text{S}_{15}$), was achieved under similar reaction conditions. The observed differences in catalytic activity, as determined by the styrene conversion to the corresponding aldehydes, were consistent with the pressure profiles recorded in the batch reactors during the reactions (Figure 40c). In this context, the pressure loss reflects the consumption of syngas, indicating the progress of the reaction, where a more rapid pressure decrease corresponds to a higher hydroformylation rate.

These results collectively demonstrate the superior performance of rhodium sulfide catalysts compared to the supported Rh reference catalyst, highlighting the effectiveness of the d-block-p-block element combination strategy. Based on the styrene hydroformylation activity, the catalytic performance follows the order $\text{Rh} < \text{Rh}_2\text{S}_3 < \text{Rh}_{17}\text{S}_{15}$, with $\text{Rh}_{17}\text{S}_{15}$ emerging as the most active phase (Figure 40). Although the catalytic activity is influenced by particle size and size differences are indeed observed among these catalysts, the primary factor contributing to the enhanced performance can be attributed to the electronic and geometric modifications introduced by sulfur incorporation. For example, despite the $\text{Rh}_2\text{S}_3/\text{SiO}_2$ (10 wt.% Rh) catalyst exhibiting smaller particle sizes compared to $\text{Rh}_{17}\text{S}_{15}/\text{SiO}_2$ (10 wt.% Rh), the latter demonstrates superior catalytic activity. Moreover, a plot prepared connecting the activity and

the particle size of several reported catalysts from the literature indicates the superior activity of the rhodium sulfide catalysts, irrespective of the particle size (Figure 43b).

The lead catalyst, $\text{Rh}_{17}\text{S}_{15}/\text{SiO}_2$ (1 wt.% Rh), was evaluated under conditions leading to complete styrene conversion, resulting in 97 % selectivity toward the aldehydes and 3 % formation of ethylbenzene after 3 h of reaction. The ratio of linear to branched aldehydes (n/iso) was determined to be 1.0, indicating no preferential formation of either isomer (Table 12, entry 6). However, an enhanced regioselectivity may potentially be achieved by incorporating ligands^[248] or employing confinement effects,^[268] an interesting aspect which will be part of future studies.

Table 12: Results of the hydroformylation of styrene performed with various catalysts. This table has been adapted from reference^[255] (license CC BY 4.0).

Entry	Catalyst	Time (min)	Conv. (%)	Select.* (%)	n/iso
1	$\text{Rh}_{17}\text{S}_{15}/\text{SiO}_2$ (10 wt.% Rh)	80	18	100	0.7
2	$\text{Rh}_2\text{S}_3/\text{SiO}_2$ (10 wt.% Rh)	80	5	100	-
3	$\text{Rh}_{17}\text{S}_{15}/\text{SiO}_2$ (10 wt.% Rh)	225	85	99	0.88
4	$\text{Rh}_2\text{S}_3/\text{SiO}_2$ (10 wt.% Rh)	225	42	100	0.7
5	$\text{Rh}_{17}\text{S}_{15}/\text{SiO}_2$ (1 wt.% Rh)	80	87	98	0.85
6	$\text{Rh}_{17}\text{S}_{15}/\text{SiO}_2$ (1 wt.% Rh)	180	100	97	1.0
7	$\text{Rh}_2\text{S}_3/\text{SiO}_2$ (1 wt.% Rh)	80	60	99	0.85
8	$\text{Rh}_2\text{S}_3/\text{SiO}_2$ (1 wt.% Rh)	120	93	99	0.85
9	Rh/SiO_2 (1 wt.% Rh)	80	40	99	0.91
10	$\text{Rh}_x\text{S}_y/\text{SiO}_2$ (1 wt.% Rh) ^a	270	40	100	0.67

Reaction conditions: styrene (1 mmol), toluene (1.5 mL), catalyst (0.2 mol%, Rh basis), 40 bar syngas pressure, CO:H₂ 1:1, 80 °C, 1200 rpm. The quantifications were performed using GC-MS analysis and *n*-decane as internal standard. * Aldehyde selectivity ^a Catalyst prepared with low (15 NL/h) Ar flow rate

The applicability of the supported rhodium sulfide catalysts in a solvent free system was examined by performing reactions in neat styrene. At a very low catalyst concentration of 0.06 mol%, a styrene conversion of 40 % with n/iso ratio of 0.95 (100 % aldehyde selectivity) has been observed in 2 h when the reaction was performed at 80 °C with $\text{Rh}_{17}\text{S}_{15}/\text{SiO}_2$ (1 wt.% Rh), indicating the success of this approach (Table S13, entry 1).

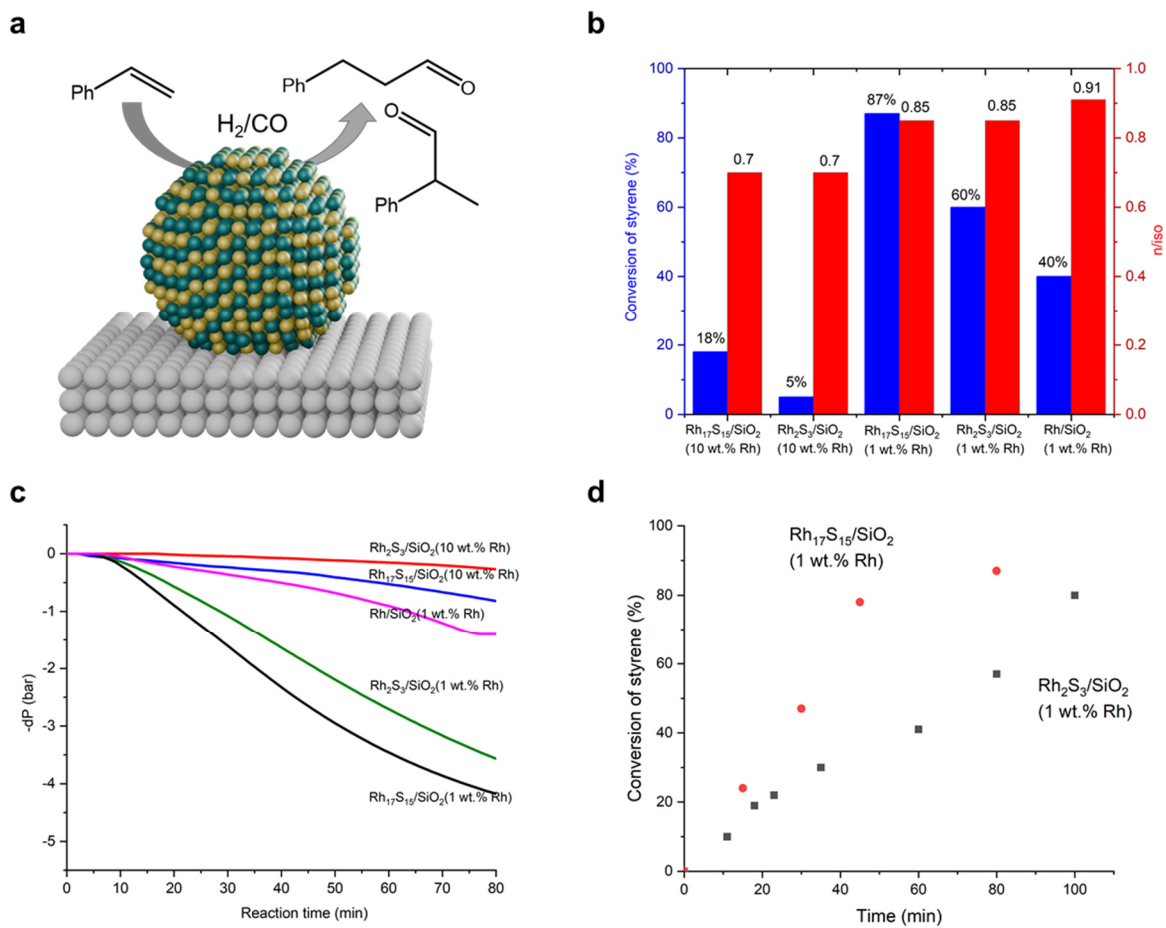


Figure 40: a) Schematic representation of the styrene hydroformylation over rhodium sulfide catalysts. b) performance comparison of various catalysts synthesized in this work providing a reaction time of 80 min, c) pressure loss curve corresponding to syn gas consumption indicating the progress of reaction and d) conversion with respect to time plot prepared for the lead rhodium sulfide catalysts. Reaction conditions: styrene (1 mmol), toluene (1.5 mL), catalyst (0.2 mol%, Rh basis), 40 bar syngas pressure, CO:H₂ 1:1, 80 °C, 1200 rpm. The quantifications were performed using GC-MS analysis and *n*-decane as internal standard. This figure has been adapted from reference^[255] (license CC BY 4.0).

Influence of synthesis conditions

As discussed in the previous section, a higher argon flow rate was necessary to synthesize phase-pure Rh₁₇S₁₅. To investigate the influence of gas flow rate on catalytic performance, a rhodium sulfide catalyst with 1 wt.% Rh was synthesized at a lower Ar flow rate (15 Nl/h), using precursor quantities required for the formation of the Rh₁₇S₁₅ phase. This catalyst achieved only 40 % conversion towards the aldehydes even after 4.5 h of reaction time (Table 12, entry 10). In contrast, both Rh₁₇S₁₅ and Rh₂S₃ prepared with 1 wt.% Rh loading under higher Ar flow rates (450 Nl/h) exhibited significantly improved conversions of 87 % and 60 % within just 80 min (Table 12, entry 5 and 7). Interestingly, a catalyst prepared under stagnant Ar conditions showed no significant conversion. These results suggest that higher Ar flow rates may facilitate surface cleaning by removing excess sulfur, thereby preventing active site poisoning.

Additionally, an increased flow rate appears to improve nanoparticle dispersion on the support,^[243] as evidenced by electron microscopy images. Hence, the importance of carefully tailored synthesis conditions for producing active rhodium sulfide catalysts can be clearly concluded.

Influence of reaction temperature and partial pressure

The influence of the reaction temperature on the hydroformylation activity was systematically investigated (Figure 41) using the lead catalyst candidate $\text{Rh}_{17}\text{S}_{15}/\text{SiO}_2$ (1 wt.% Rh). A clear enhancement in conversion, reflecting an increased reaction rate, was observed at higher temperatures. For example, reactions carried out using $\text{Rh}_{17}\text{S}_{15}/\text{SiO}_2$ (1 wt.% Rh) at 70 °C, 80 °C, and 90 °C for 30 min resulted in styrene conversions of 32 %, 47 %, and 76 %, respectively, clearly demonstrating the positive correlation between temperature and alkene conversion (Figure 41a). Another important observation with regard to the linear to branched aldehyde ratio(n/iso). An increased n/iso ratio was observed with an increase in reaction temperature, indicating higher selectivity towards linear aldehydes (Figure 41b). The increased selectivity towards the linear aldehyde can be attributed to the greater reversibility of the formation of the branched alkyl–Rh intermediate, leading to the regeneration of styrene aduct through β -hydride elimination.^[269] Whereas, limited β -hydride elimination (reversibility to styrene aduct) takes place in the case of the linear alkyl–Rh species.^[269] Accordingly, a part of the branched species isomerizes to linear alkyl–Rh species resulting in the enhanced formation of linear aldehydes at elevated temperatures.^[269–271]

The regioselectivity of hydroformylation can be generally influenced by tuning the catalytic system, varying the ligand (in homogeneous catalysis) or changing the solvent.^[266,272] However, the results above demonstrate that the formation of a target product can be selectively enhanced also by varying reaction conditions. In this context, it is worth to note that the dominant formation of a specific product at elevated temperatures indicates the thermodynamic effects of the reaction. Moreover, the undesired side reaction of hydrogenation is thermodynamically more favorable than the hydroformylation reaction.^[12] For instance, the calculated ΔG values associated with the hydroformylation product of 1-decene (n-undecanal) is -16 kJ.mol⁻¹ whereas, the hydrogenation product (n-decane) is -23 kJ.mol⁻¹.^[273] This underscores the need for highly selective catalysts to steer the reaction toward the desired aldehyde product.

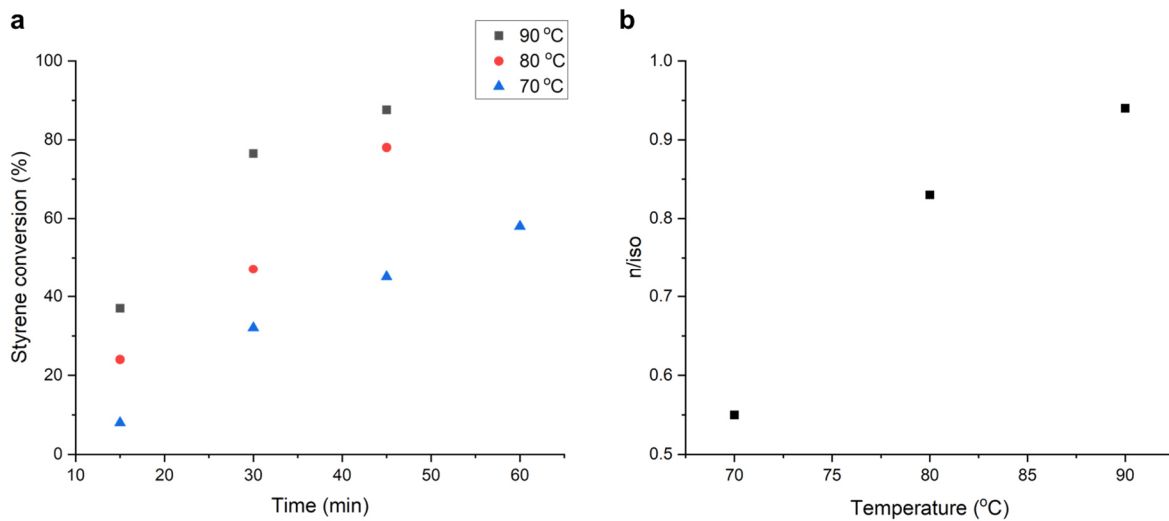


Figure 41: Temperature dependency of the hydroformylation reaction demonstrating a) an enhanced conversion with increased temperature and b) a change in regioselectivity (*n*/iso determined at 40 % styrene conversion). Reaction conditions: styrene (1 mmol), toluene (1.5 mL), Rh₁₇S₁₅/SiO₂ (1 wt.% Rh) (0.2 mol%, Rh basis), 40 bar syngas pressure, CO:H₂ 1:1, 1200 rpm. The quantifications were performed using GC-MS analysis and *n*-decane as internal standard. This figure has been adapted from reference^[255] (license CC BY 4.0).

Subsequently, the effect of CO and H₂ partial pressures on the reaction was examined using the lead catalyst, Rh₁₇S₁₅/SiO₂ (1 wt.% Rh). An enhanced styrene conversion was observed under equal partial pressures of CO and H₂ (Figure 42a).

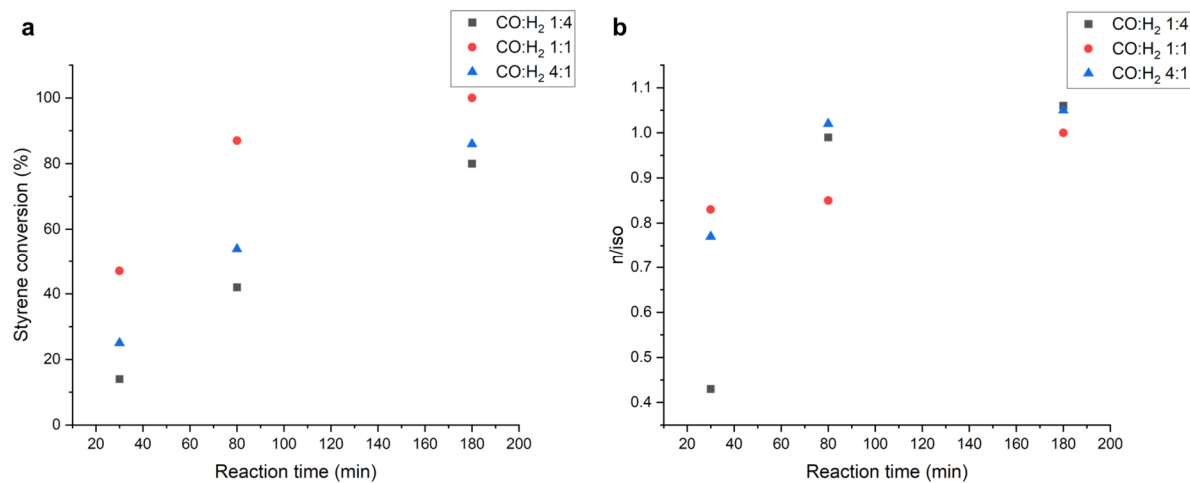


Figure 42: Influence of CO and H₂ partial pressure on the a) styrene conversion and b) the corresponding *n*/iso ratio. Reaction conditions: styrene (1 mmol), toluene (1.5 mL), Rh₁₇S₁₅/SiO₂ (1 wt.% Rh) (0.2 mol%, Rh basis), 40 bar syngas pressure, 80 °C, 1200 rpm. The quantifications were performed using GC-MS analysis and *n*-decane as internal standard. This figure has been adapted from reference^[255] (license CC BY 4.0).

In contrast, increasing the H₂ partial pressure (CO:H₂ = 1:4) led to an enhanced hydrogenation activity, as evidenced by the formation of 5 % ethylbenzene at 80 % styrene conversion, in comparison to a maximum of 3 %, which was observed with an equimolar gas composition.

Substrate scope

Various substrates, such as 1-hexene, 1-octene, 2-octene, allyl benzene, and diisobutylene, were tested in the hydroformylation reaction with Rh₁₇S₁₅/SiO₂ (1 wt.% Rh) as catalyst. In all cases excellent conversions and selectivities towards the aldehyde products were observed, while the hydrogenation side reaction was suppressed (Table 13). For instance, the hydroformylation of 1-hexene performed at 80 °C resulted in an aldehyde selectivity of 87 % at 100 % conversion, with an n/iso ratio of 1.05 (Table 13, entry 1). The side products formed were the isomerized olefins (13 %), which will eventually get converted to corresponding branched aldehydes giving sufficient reaction time. The hydroformylation of diisobutylene is an industrially important reaction as the resulting aldehyde are useful raw materials for the production of plasticizers, surfactants, spices and detergents.^[274] Therefore, the hydroformylation of diisobutylene performed with Rh₁₇S₁₅/SiO₂ (1 wt.% Rh) resulted in 38 % conversion to the aldehyde products (Table 13, entry 6).

Table 13: Results of hydroformylation performed with various substrates using Rh₁₇S₁₅/SiO₂ (1 wt.% Rh) catalyst. This table has been adapted from reference^[255] (license CC BY 4.0).

Entry	Olefin	Reaction	Conversion	Isomerized	Aldehydes	n/iso
		time (min)	(%)	olefin (%)	(%)	
1	1-hexene	45	100	13	87	1.05
2	1-octene	45	100	30	70	1.47
3	2-octene	45	62	38	62	0.35
4	Allyl benzene	45	100	30	70	1.23
5	Allyl benzene	960	100	10	90	0.88
6	Diisobutylene*	420	38	0	100	only n

*Diisobutylene used here is a 70:30 mixture of 2,4,4-trimethylpent-1-ene and 2,4,4-trimethylpent-2-ene. The conversion of 2,4,4-trimethylpent-1-ene is provided in the table and only 8% conversion was observed for 2,4,4-trimethylpent-2-ene.

Reaction conditions: substrate (1 mmol), toluene (1.5 mL), catalyst (0.2 mol%, Rh basis), 40 bar syngas pressure, CO:H₂ 1:1, 80 °C, 1200 rpm.

Benchmarking the catalysts

In order to compare the performance of the rhodium sulfide catalysts with the other literature reported catalysts, the TOF values were calculated. These calculations were based on the dispersion values calculated from the average particle sizes. By using this approach, TOF values of 2620 h⁻¹ for Rh₁₇S₁₅/SiO₂ (1 wt.% Rh) and 1450 h⁻¹ for Rh₂S₃/SiO₂ (1 wt.% Rh) at 80 °C and 40 bar were determined. The values enabled a facile comparison of the activities

with other reported heterogeneous and homogeneous catalysts (Figure 43). For instance, the TOF value reported (1469 h^{-1}) for the styrene hydroformylation by Liu *et al.*^[25] for the silica supported Rh₂P catalyst is lower in comparison to Rh₁₇S₁₅/SiO₂ (1 wt.% Rh). As illustrated in Figure 43a, the lead candidate of this study Rh₁₇S₁₅/SiO₂ (1 wt.% Rh) demonstrates superior performance, surpassing many catalysts reported in the literature in terms of TOF. Additionally, a comparison was made by evaluating the turnover frequency (TOF) with respect to particle size (Figure 43b). Notably, Rh₁₇S₁₅/SiO₂ (1 wt.% Rh) outperformed many reported catalysts, including those with similar or even smaller particle sizes. This clearly indicates that the enhanced activity originates from sulfur incorporation rather than from differences in particle size.

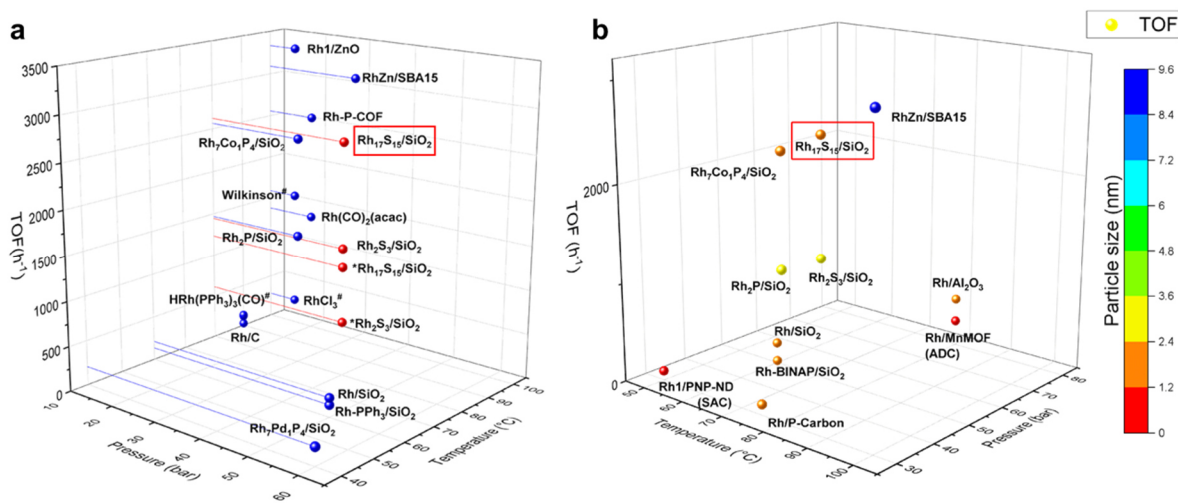


Figure 43: a) Plot showing a comparison of TOF values of rhodium sulfide catalysts synthesized in this work (1 wt.% Rh) with other literature reported catalysts^[25,186,189,191,275–278] and b) plot prepared demonstrating particle size dependency of hydroformylation activity.^[25,183,184,191,248,275,277,279,280] SAC = single atom catalysts, ADC = atomically dispersed catalyst, Rh1/PNP-ND: phosphorus-coordinated rhodium by metal-ligand coordination on a nano diamond support, BINAP: (R)-2,2'-bis(diphenylphosphino)-1,1'-binaphthyl, SBA-15 = mesoporous silica. This figure has been adapted from reference^[255] (license CC BY 4.0). * TOF estimated based on total Rh content, [#]homogeneous catalysts

Further, the apparent activation energies of the reactions with rhodium sulfide catalysts were estimated from the Arrhenius plot (ln (rate) vs 1/T) in the temperature range from 60 °C to 84 °C. Values of $82 \pm 25\text{ kJ}\cdot\text{mol}^{-1}$ and $132 \pm 19\text{ kJ}\cdot\text{mol}^{-1}$ were determined for the styrene hydroformylation reaction performed with Rh₁₇S₁₅/SiO₂ (1 wt.% Rh) and Rh₂S₃/SiO₂ (1 wt.% Rh), respectively, under an applied syngas pressure of 40 bar (CO: H₂ 1:1) and a stirring speed of 1200 rpm (Figure 44, Figure S40 and Figure S41). The comparison with previously reported values for the styrene hydroformylation supports the reliability of the estimated apparent activation energies (Table S14).

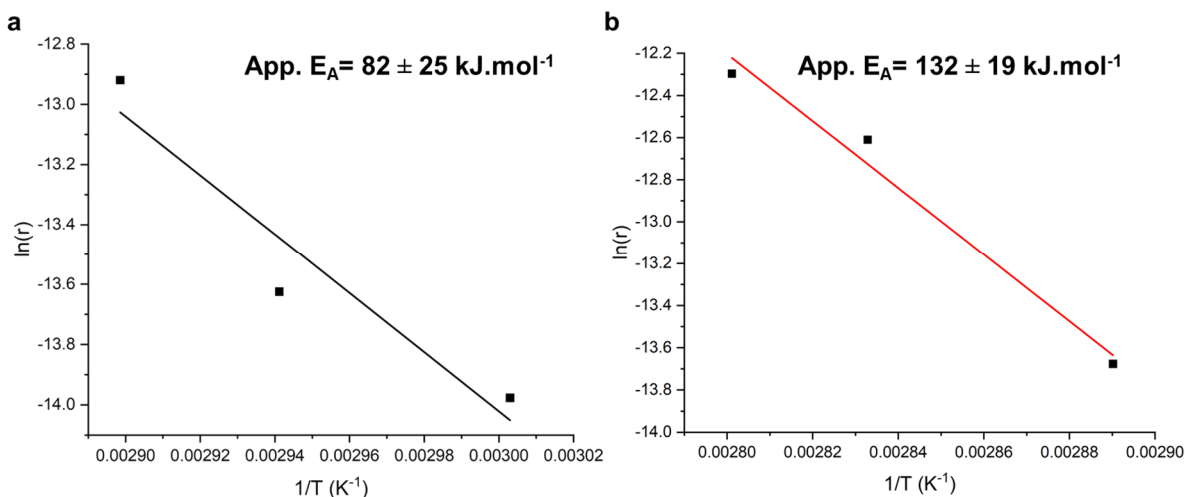


Figure 44: Arrhenius plot for the estimation of the apparent activation energy of the styrene hydroformylation with a) $\text{Rh}_{17}\text{S}_{15}/\text{SiO}_2$ (1 wt.% Rh) and b) $\text{Rh}_2\text{S}_3/\text{SiO}_2$ (1 wt.% Rh). Reaction conditions: styrene (1 mmol), toluene (1.5 mL), catalyst (0.2 mol%, Rh basis), 40 bar syngas pressure, $\text{CO}:\text{H}_2$ 1:1, 1200 rpm. The quantifications were performed using GC-MS analysis and *n*-decane as internal standard. This figure has been adapted from reference^[255] (license CC BY 4.0).

Further comparison of the $\text{Rh}_{17}\text{S}_{15}/\text{SiO}_2$ (1 wt.% Rh) catalyst with respect to other reported catalysts in terms of hydroformylation performance is provided in the appendix (Table S15 and Table S16). For instance, the hydroformylation of 1-hexene at 60 °C with Rh/C and $[\text{RhCl}(\text{PPh}_3)_3]$ resulted in 63 % (Table S15, entry 6) and 82 % (Table S15, entry 1) conversion with 72 % and 67 % aldehyde selectivity, respectively, after 5 h reaction time.^[281] In contrast, the reaction performed with $\text{Rh}_{17}\text{S}_{15}/\text{SiO}_2$ (1 wt.% Rh) under similar conditions resulted in 100 % 1-hexene conversion with 92 % aldehyde selectivity within 4 h, completely outperforming both the heterogeneous and homogeneous catalysts (Table S15, entry 8). The results presented above, along with comparisons to other reported catalysts, highlight the effectiveness of sulfur incorporation into Rh forming a crystalline Rh_xS_y phase, leading to the development of a highly active hydroformylation catalyst.

6.3 Recovery and stability tests

The reusability of the rhodium sulfide catalysts was evaluated *via* recovery experiments. After the initial (fresh) run, the catalysts were recovered by centrifugation, thoroughly washed with acetone, and reused in a subsequent reaction (first recovery). The catalytic reactions were carried out at 80 °C and allowed to proceed to higher conversion levels to assess any potential catalyst deactivation over time. Interestingly, both the $\text{Rh}_{17}\text{S}_{15}/\text{SiO}_2$ (1 wt.% Rh) and $\text{Rh}_2\text{S}_3/\text{SiO}_2$ (1 wt.% Rh) catalysts were successfully reused for three rounds without any decline in conversion. Also, the aldehyde selectivity with the same n/iso ratios was maintained (Figure 45). For example, with the lead performer $\text{Rh}_{17}\text{S}_{15}/\text{SiO}_2$ (1 wt.% Rh) a styrene conversion of 87 %, 83 % and slightly higher 94 % were achieved in the fresh test, first recovery and second recovery test after allowing each run to proceed for 80 min. The n/iso ratios (0.85, 0.91 and 0.92) and aldehyde selectivities remained the same in all three runs.

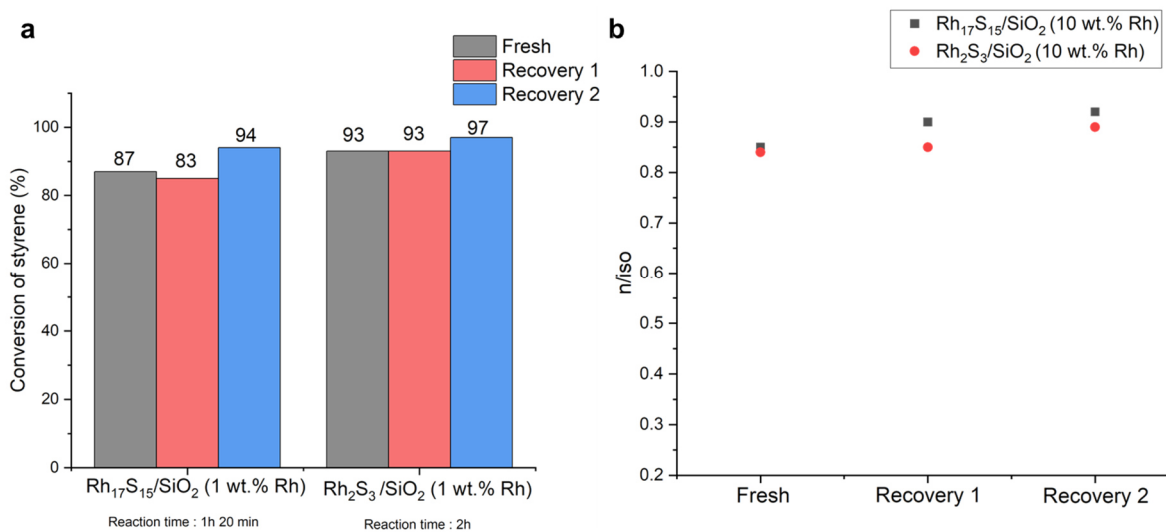


Figure 45: Results of recovery tests using the rhodium sulfide catalysts showing a) the conversion of styrene after each run and b) the n/iso ratios at the corresponding conversions. Reaction conditions: styrene (1 mmol), toluene (1.5 mL), catalyst (0.2 mol%, Rh basis), 40 bar syngas pressure, CO:H₂ 1:1, 80 °C, 1200. The quantifications were performed using GC-MS analysis and *n*-decane as internal standard. This figure has been adapted from reference^[255] (license CC BY 4.0).

The TOF values for each run were assessed at lower conversion levels (<30 %), thereby providing insights into the intrinsic catalytic activity during the recycling. No considerable decline in activity was observed using $\text{Rh}_{17}\text{S}_{15}/\text{SiO}_2$ (1 wt.% Rh) as catalyst (Figure 46).

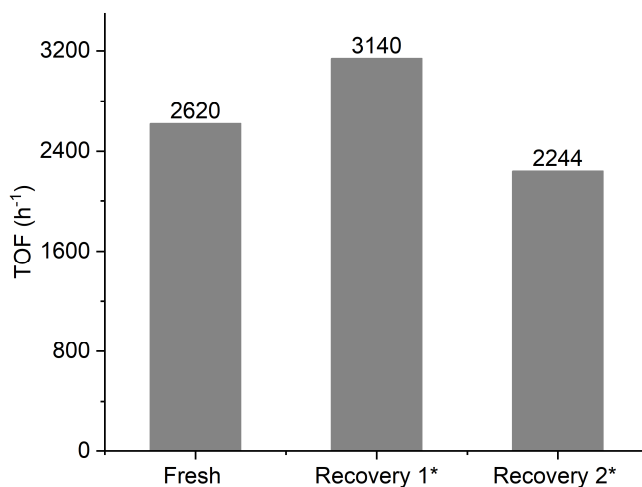


Figure 46: TOF values estimated for the recovery experiment using the $\text{Rh}_{17}\text{S}_{15}/\text{SiO}_2$ (1 wt.% Rh) catalyst. Reaction conditions: styrene (1 mmol), toluene (1.5 mL), catalyst (0.2 mol%, Rh basis), 40 bar syngas pressure, CO:H₂ 1:1, 80 °C, 1200 rpm. The quantifications were performed using GC-MS analysis and *n*-decane as internal standard. *The dispersion was calculated using the average particle size of 2.6 nm obtained from TEM analysis for the recovered catalysts. The same particle size was considered for the catalysts in recovery 1 and 2.

The stability of the catalysts was further assessed by performing electron microscopy-based analyses of the recovered rhodium sulfide catalysts. The lattice fringe-based analysis performed through HRTEM revealed the stability of the rhodium sulfide phases. A lattice fringe *d* spacing of 2.27 Å corresponding to $\text{Rh}_{17}\text{S}_{15}$ (331) and 2.59 Å assigned to Rh_2S_3 (112) were estimated for the recovered $\text{Rh}_{17}\text{S}_{15}/\text{SiO}_2$ (1 wt.% Rh) and $\text{Rh}_2\text{S}_3/\text{SiO}_2$ (1 wt.% Rh) catalysts (Figure S29 and Figure S28). The average particle size of the recovered catalysts, determined *via* STEM analysis, indicated a slight increase of particle size from 2.2 nm to 2.6 nm for $\text{Rh}_{17}\text{S}_{15}/\text{SiO}_2$ (1 wt.% Rh) and a substantial decrease from 3 nm to 1.6 nm for $\text{Rh}_2\text{S}_3/\text{SiO}_2$ (1 wt.% Rh). The post reaction catalyst characterization was further extended towards XAS, where the XANES region still indicated the Rh^{5+} oxidation state (Figure S36) for the recovered $\text{Rh}_x\text{S}_y/\text{SiO}_2$ ($x = 17, y = 15$ or $x = 2, y = 3$ with 1 wt.% Rh) catalysts. In the FT-EXAFS analysis, especially for the recovered $\text{Rh}_2\text{S}_3/\text{SiO}_2$ (1 wt.% Rh) catalyst, the back-scattering event at 2.3 Å, corresponding to Rh-Rh contributions, has increased pointing towards more metallic character (Figure S37). This might stem from the partial decomposition of the Rh_2S_3 phase to $\text{Rh}_{17}\text{S}_{15}$ and a therewith increase in metallic character under the applied reaction conditions.

ICP-AES analyses were performed to estimate the Rh leaching during the reaction. Hereby the estimation of the rhodium content in the fresh catalyst and recovered catalyst (after the first run) indicated a significant precious metal loss. A rhodium loss from 1.02 wt.% to 0.78 wt.% for $\text{Rh}_{17}\text{S}_{15}/\text{SiO}_2$ (1 wt% Rh) and from 0.88 wt.% to 0.73 wt.% for $\text{Rh}_2\text{S}_3/\text{SiO}_2$ (1 wt.% Rh) was

calculated (Table S17). The loss of rhodium can be attributed to the detachment of rhodium sulfide nanoparticles from the silica support, likely caused by reaction conditions and mechanical milling from stirring, collectively promoting the formation of a RhS-containing colloid. To verify this, the styrene hydroformylation reaction was performed with $\text{Rh}_{17}\text{S}_{15}/\text{SiO}_2$ (1 wt.% Rh) as catalyst and the solid catalyst was separated by centrifugation. A clear Tyndall effect indicates the presence of nanoparticle, which was further confirmed by dynamic light scattering (DLS) analysis (Figure S43a).

To further investigate the metal leaching behaviour of the rhodium sulfide catalysts, hot filtration tests were conducted. Therefore, the catalytic reaction was allowed to proceed to 33 % conversion using the $\text{Rh}_{17}\text{S}_{15}/\text{SiO}_2$ (1 wt.% Rh) catalyst. Extensive efforts were made to remove the leached nanoparticles from the reaction mixture, including filtration through a syringe filter and a Celite bed, followed by centrifugation at 25,000 rpm for 30 min. The resulting filtrate was then used to perform again a hydroformylation reaction, after compensating for the solvent, internal standard, and styrene losses during the filtration process. Following the removal of the solid catalyst, the reaction still progressed slightly, reaching a total styrene conversion of 57 % after 80 min (an additional 24% conversion post filtration). In comparison, a control reaction using the solid catalyst under identical conditions achieved 87% conversion. The visual inspection of the filtrate under visible light revealed the presence of the Tyndall effect, indicating colloidal particles. Subsequently, a DLS analysis performed confirmed this, revealing an average particle diameter of 37 nm of a rhodium sulfide colloid (Figure S43b). These findings highlight the need to minimize nanoparticle loss from the catalyst support.

Initial attempts for minimizing the metal leaching were performed by varying the support material. $\text{Rh}_{17}\text{S}_{15}$ nanoparticles were synthesized on Al_2O_3 and 0.5P-SiO_2 (0.5 wt.% P-modified silica), adapting the procedure for $\text{Rh}_{17}\text{S}_{15}/\text{SiO}_2$. A higher metal loading (10 wt.% Rh) was used for the initial synthesis to verify the phase formation *via* PXRD. With both supports the formation of $\text{Rh}_{17}\text{S}_{15}$ nanoparticles could be seen (Figure S42). Hence, the same procedure was adapted to synthesize the 1 wt.% Rh loaded catalyst. The synthesized $\text{Rh}_{17}\text{S}_{15}/\text{Al}_2\text{O}_3$ (1 wt.% Rh) and $\text{Rh}_{17}\text{S}_{15}/0.5\text{P-SiO}_2$ (1 wt.% Rh) catalysts were then applied in the hydroformylation of styrene and showed an enhanced stability. A rhodium leaching of only 6 % was estimated for $\text{Rh}_{17}\text{S}_{15}/\text{Al}_2\text{O}_3$ (1 wt.% Rh), whereas $\text{Rh}_{17}\text{S}_{15}/0.5\text{P-SiO}_2$ (1 wt.% Rh) exhibited an even smaller metal leaching of just 3 % (Table S17). The enhanced suppression of leaching through support engineering through the use of 0.5P-SiO_2 highlights the success of this approach, not only in Heck coupling (chapter 4), but also in hydroformylation reactions. These findings clearly demonstrate the improved metal-support interactions, leading to an enhanced catalyst stability.

6.4 Theoretical investigations into Rh surface motifs

The remarkable catalytic activity shown by rhodium sulfide nanoparticles prompted a theoretical investigation to gain atomic-level insights into the materials behavior. Theoretical studies were performed with the combination of local environmental descriptors, unsupervised machine learning and density functional theory calculations. Atomistic simulations were initially employed to investigate the structural differences between the Rh, Rh₂S₃ and Rh₁₇S₁₅ phases at the atomic scale, aiming to provide insights into their structure-activity relationships.

The structure of metallic rhodium is determined as face centered cubic (FCC), featuring surface metal centers in close spatial proximity. This arrangement facilitates interactions between reaction intermediates on adjacent sites, which can potentially compromise the catalytic performance, especially with respect to unwanted side reactions.^[282] However, this scenario differs for Rh_xS_y systems, where the sulfur incorporation introduces significant structural diversity.

To gain insight into the potential active sites on the surface of Rh₂S₃ and Rh₁₇S₁₅ phases, all surface termination up to third miller indices were enumerated. This resulted in the identification of over 240,000 potential high symmetry active sites among the 2014 possible surface terminations (using CATKIT^[283]). For understanding the structural diversity of these sites through a visual overview, smooth overlap of atomic positions (SOAP)^[284,285] descriptors were generated for each identified site, considering a 3.0 Å cut-off distance (approximately one nearest neighbor) to capture the local environment. These high dimensional descriptors were subsequently projected into a two dimensional space using t-distributed stochastic neighbor embedding (t-SNE),^[286] with the aim to provide a representation of the structural diversity (Figure 47, a-c).^[287-290] Colour coding the t-SNE maps, according to material origin, S/Rh ratio, and Rh content enabled the distinction between Rh rich and Rh poor potential active sites within an S/Rh ratio range of 1 to 6. Importantly, the presence of non-overlapping clusters (regions) in the descriptor space indicates that, although many structurally similar sites are shared between Rh₂S₃ and Rh₁₇S₁₅, distinct classes of sites exist for each phase. These differences highlight the possible differences in the surface sites of these two materials and led to the subsequent investigations, which focus on understanding these key structural differences.

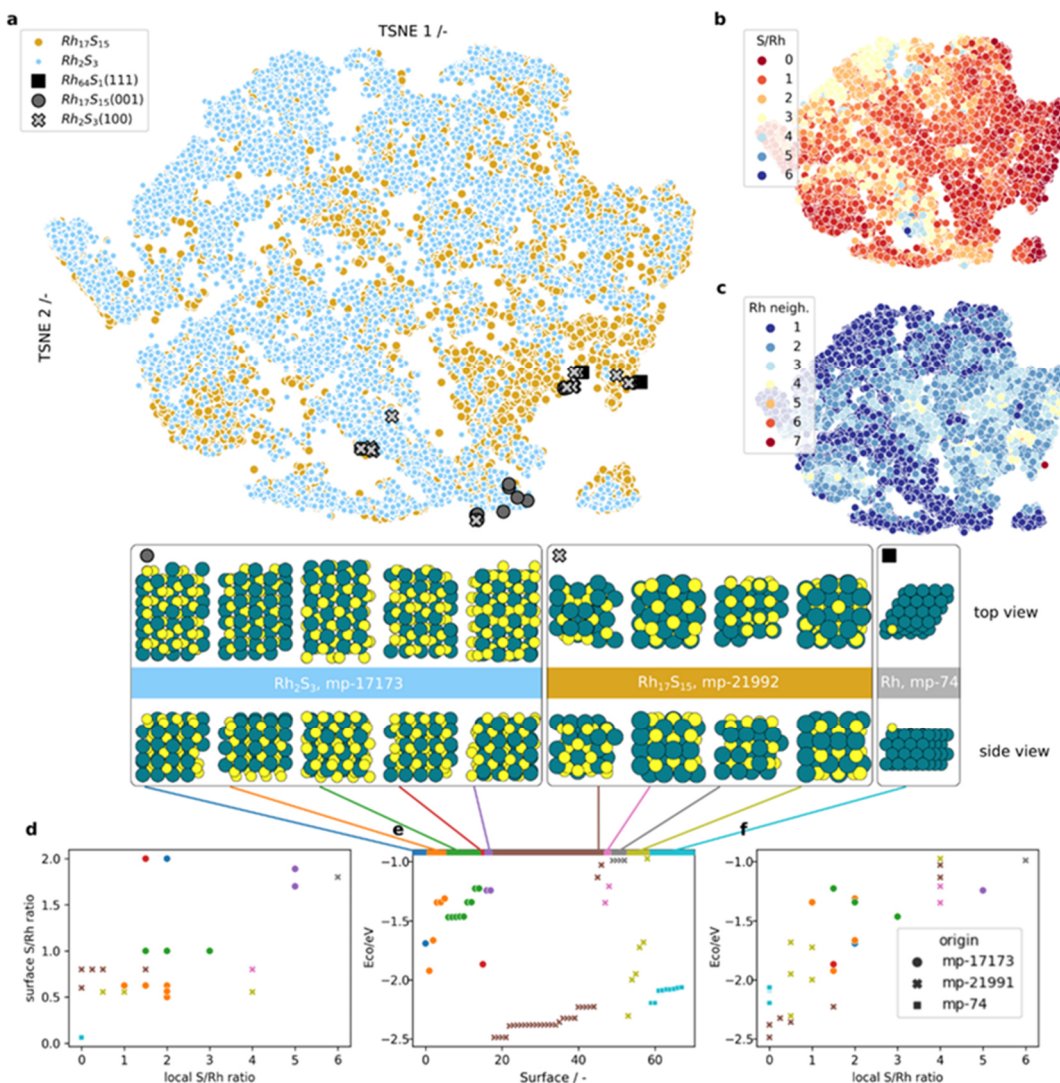


Figure 47: A two-dimensional t-SNE map was generated based on the SOAP descriptors of a representative subset of 20,000 active sites selected from a total of 240,000 enumerated possibilities. These sites span all surface terminations up to Miller index=3 for $\text{Rh}_{17}\text{S}_{15}$ (mp-21991) and Rh_2S_3 (mp-17173). Each point in the t-SNE plot corresponds to a potential active site, with the proximity of points reflecting structural similarity. Based on the standard for such analyses, absolute distances between points are not quantitatively meaningful; therefore, axis labels have been omitted.^[287,289,291] The maps are visualized as follows: (a) colour coded by material origin, (b) by local S/Rh atomic ratio within a 3 Å radius of the site, (c) by the number of Rh atoms within this radius, (d) the ratio of surface S/Rh atoms to the local S/Rh composition, (e) CO adsorption energy ($E_{\text{CO}} = E^*_{\text{CO}} - E_{\text{CO}} - E^*$) at various surface sites, and (f) as a function of local composition. Binding energy estimations are performed considering (100) $\text{Rh}_{17}\text{S}_{15}$ (mp-21991), (001) Rh_2S_3 (mp-17173), and S-doped (111) Rh (mp-74) surfaces. Rh and S atoms are represented by blue and yellow spheres, respectively. This figure has been adapted from reference^[255] (license CC BY 4.0).

To quantitatively evaluate the energetics of the large number of potential catalytic surfaces, DFT calculations were performed. While DFT is widely regarded as the benchmark method for studying reaction energetics in heterogeneous catalysis, its high computational cost imposes practical limitations on the number of surface configurations that can be feasibly explored. This

can result in under sampling of the available structural space for complex materials, such as rhodium sulfides, leading to inaccurate results (Figure 47 a). To address this challenge, a hypothesis was arrived that the local atomic composition at an active site is a primary determinant of its chemical reactivity. Further, the computations were performed for the most thermodynamically favorable crystallographic orientations, the (001) surface for Rh_2S_3 and the (100) surface for $\text{Rh}_{17}\text{S}_{15}$.^[292] This resulted in an investigation focusing on 9 rhodium sulfide surface terminations and approximately 70 surface Rh sites, with varying S/Rh ratio representing metal rich and S rich sites. A Rh (111) slab with an S add-atom was also considered for the calculations as a reference surface.

For these investigation the carbon monoxide binding energy (E_{CO}) was regarded as one of the key descriptors for describing the hydroformylation activity of the catalyst surfaces.^[25] Therefore, through the application of DFT, CO binding energies on the surface sites were calculated. A clear variation in CO binding energy was observed across the different surface terminations of $\text{Rh}_{17}\text{S}_{15}$, which were strongly influenced by the local S/Rh ratio. Surfaces enriched in sulfur exhibited a weaker CO adsorption, whereas Rh rich surfaces showed a significantly stronger binding. Specifically, the CO binding energies ranged from as low as -1.3 eV on S rich terminations to as high as -2.25 eV on Rh rich ones, highlighting the material's potential for a tunable catalytic behavior.

Hence, sites with predominantly rhodium neighbors are more likely to exhibit higher activity toward hydroformylation reactions, indicating the need for Rh ensembles on the surface. Through a detailed comparison of the surfaces of the materials under investigation, rhodium ensembles consisting of four atoms (Rh_4), which are spatially isolated (Figure 48), were computationally identified at the Rh rich termination of $\text{Rh}_{17}\text{S}_{15}$. Here, a trade-off is observed: spatial isolation is achieved through sulfur incorporation, yet the surrounding environment at the surface still provides only Rh atoms, enabling a strong CO binding (-2.25 eV). Similarly, other isolated Rh sites with favorable CO binding energies can be identified in $\text{Rh}_{17}\text{S}_{15}$ further supporting its potential as an exceptional hydroformylation catalyst. This conclusion aligns with the CO-DRIFTS analysis (Figure 39) of the lead catalyst candidate $\text{Rh}_{17}\text{S}_{15}/\text{SiO}_2$ (1 wt.% Rh), where the absence of bands corresponding to bridged CO species indicates the presence of isolated Rh sites (CO binding sites). Moreover, the separation of Rh atoms in $\text{Rh}_{17}\text{S}_{15}$ has been clearly visualized using HR-HAADF-STEM imaging (Figure 37), providing strong evidence in support of these findings. These findings emphasize that tailoring the surface S/Rh ratio particularly in $\text{Rh}_{17}\text{S}_{15}$ through carefully selected synthetic strategies is a key aspect in the successful design of rhodium sulfide-based catalysts.

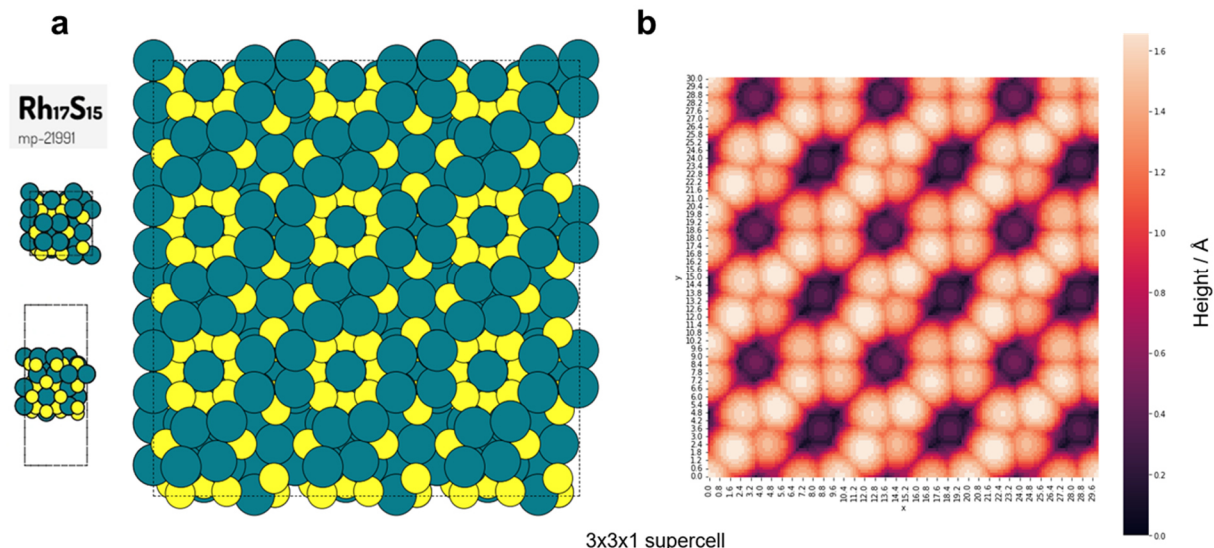


Figure 48: a) The relaxed Rh rich surface termination of $\text{Rh}_{17}\text{S}_{15}$ (mp-21991 and b) visualized as an atomic force microscopy (AFM) style schematic on the right. The surface features spatially resolved Rh₄ motifs distributed across the termination. This figure has been adapted from reference^[255] (license CC BY 4.0).

As mentioned before, the d-band center of a metal catalyst provides can provide insight into its hydroformylation activity by influencing the binding strength of key intermediates, such as CO. Therefore, the the d-band centers were calculated for the $\text{Rh}_{17}\text{S}_{15}$, Rh_2S_3 and Rh surfaces and demonstrate a variation with respect to the Fermi level (Figure S50). When examining the Rh_2S_3 surfaces, it can be observed that the d-band center varies from -1.83 eV to -2.7 eV, representing the highest and lowest values among all the materials studied in this chapter. The calculated d-band center for $\text{Rh}_{17}\text{S}_{15}$ surfaces ranges from -1.99 eV to -2.49 eV, while the Rh surface has a value of -2.37 eV. These values strongly suggest a potentially stronger CO adsorption on the Rh_2S_3 surface, corresponding to the d-band center of -1.83 eV, as higher energy d states, relative to the Fermi level, generally indicate a stronger CO binding.^[49] Surprisingly, the CO binding energy calculated using DFT ($E_{\text{CO}} = E^*_{\text{CO}} - E_{\text{CO}} - E^*$) at the corresponding surface was -1.92 eV, which is lower than -2.25 eV at the most favorable CO adsorption site on $\text{Rh}_{17}\text{S}_{15}$ and -2.20 eV on Rh. This discrepancy clearly highlights the significant contributions of geometric effects in these systems, in addition to the electronic effects seen from the projected density of states (PDOS) diagrams (Figure S50).

6.5 Concluding remarks

The hydroformylation of styrene using rhodium sulfides demonstrated superior performance compared to pure rhodium, with the catalytic activity following the trend $\text{Rh}_{17}\text{S}_{15} > \text{Rh}_2\text{S}_3 > \text{Rh}$. In all cases an excellent selectivity towards the aldehyde products was observed. The lead candidate, $\text{Rh}_{17}\text{S}_{15}/\text{SiO}_2$ (1 wt.% Rh), not only outperformed the supported Rh catalyst (Rh/SiO_2 , 1wt.% Rh), but also surpassed many reported heterogeneous and homogeneous catalysts in terms of hydroformylation activity. This study not only demonstrates the success of the d-block-p-block element combination strategy but also highlights the importance of tailoring the synthesis strategy to create highly active materials by engineering surface terminations that enhance catalytic performance. The use of optimized precursor ratios and thermal treatment conditions proved to be essential for obtaining phase pure and catalytically active rhodium sulfide phases. The incorporation of sulfur into Rh under optimised synthesis conditions resulted in the formation of spatially isolated and tunable $\text{Rh}^{\delta+}$ sites, as confirmed through advanced characterization techniques, such as XPS, XAS, DRIFTS, and electron microscopy, along with in-depth theoretical investigations by machine learning and DFT calculations. These isolated metal motifs were identified as the catalytically active sites, offering valuable insights for the design of next the generation catalysts based on d-block metals and p-block element combinations.

Although, the synthesized rhodium sulfide catalysts could be recovered and reused over three reaction cycles without any significant loss in catalytic activity or selectivity, some nanoparticle detachment from the silica support was observed. This underscores the need to improve the metal-support interaction and further investigate strategies to enhance the catalyst stability. Initial results from support engineering suggest promising improvements in terms of catalyst stability of rhodium sulfide catalysts. However, these efforts should be continued in more detail. Moreover, strategies should be developed to tune the regioselectivity and enable the production of linear or branched aldehydes in a desired ratio. Additionally, the application of Rh-S catalysts in gas-phase hydroformylation remains an area for future exploration. *In-situ* and *operando* investigations should also be carried out to gain insights into the studied systems to gain valuable information of any dynamic catalyst changes under reaction conditions.

7 Conclusions and outlook

This work explored two strategies to enhance the performance of heterogeneous catalysts through the incorporation of a non-metal into either the metal matrix or the support material. Significant improvements in the catalytic activity were observed upon incorporating phosphorus into palladium and sulfur into rhodium, relative to their respective pure metal counterparts. This d-block-p-block element combination strategy has found to be very successful in several catalytic reactions in the liquid phase. Additionally, phosphorus-modified supports demonstrated excellent resistance towards metal leaching, contributing to an enhanced catalyst stability. These findings clearly demonstrate the success of the approaches employed in this study and highlight their potential for large-scale industrial applications. The major results of this work are summarized in Figure 49.

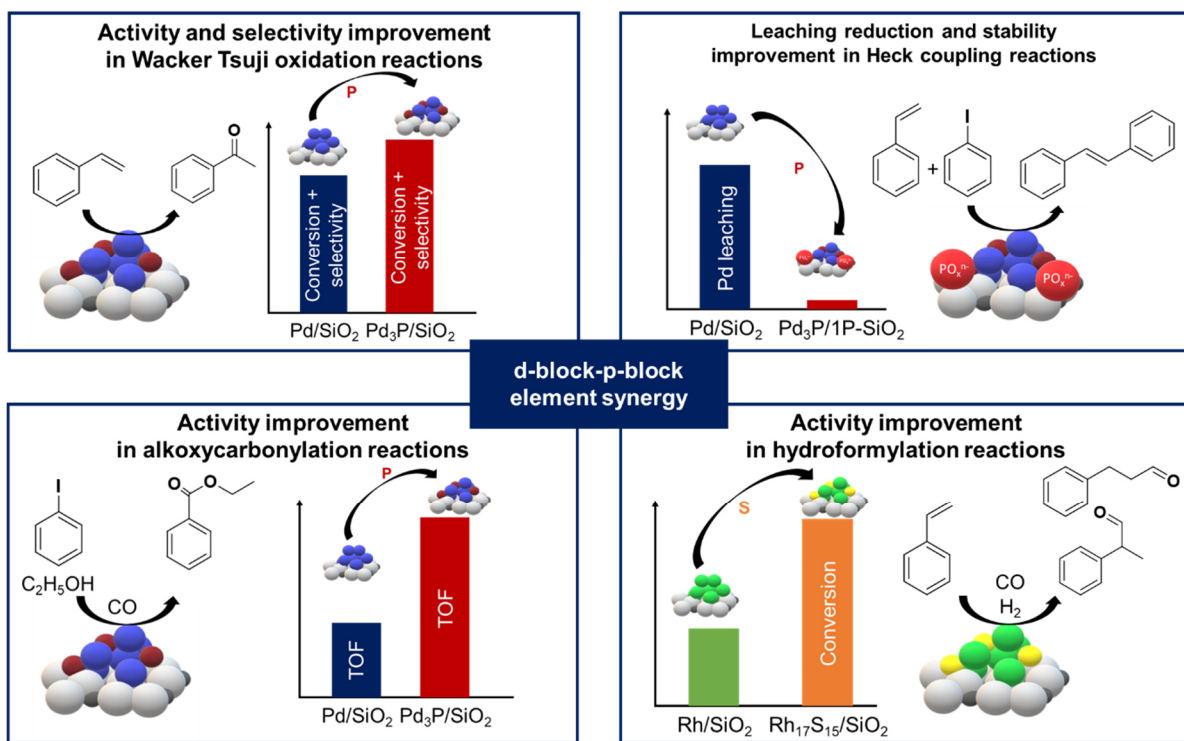


Figure 49: Schematic representation of the results of this work, all under the umbrella of the d-block-p-block element combination strategy.

Element synergy for activity improvement

The combination of a d-block transition metal with a p-block element effectively alters the electronic and geometric properties of the metal center, similar to ligands in molecular complexes. These modifications influence the catalytic behavior, making this element synergy strategy a promising tool for the performance enhancement in heterogeneous catalysis. As part of this work, the success of the d-block-p-block element combination strategy and the underlying element synergy has been demonstrated in several cases for various catalytic reactions. For example, the formation of crystalline palladium phosphide nanoparticles (Pd_3P)

on a silica support resulted in the superior catalytic activity and selectivity in the Wacker-Tsui oxidation of styrene to acetophenone, compared to pure Pd nanoparticles on silica. The structural analysis of Pd_3P revealed an increased separation between the Pd sites relative to pure Pd, leading to an improved catalytic performance. The partial positive charge on Pd, determined *via* XPS analysis, points towards a charge transfer from Pd to P. Such a change in electronic properties of the active metal sites can significantly alter the binding energies of the substrates and intermediates.

This concept was further extended towards carbonylation catalysis. The investigation of the Pd_3P system in the alkoxy carbonylation reaction of iodobenzene resulted in a more than two-fold improvement in the catalytic activity in comparison to the Pd-based reference catalyst. The success of this approach was further validated by the superior activity in comparison to some other well-known reported heterogeneous and homogeneous catalysts. The tests with various aryl halides and alcohols, followed by phenoxy and amino carbonylation, demonstrates the applicability of the developed Pd_3P catalyst in the wide spectrum of carbonylation reactions. The examination of some of the possible surfaces of Pd_3P showed the formation of separated metal ensembles, consisting of Pd dimers, trimers and tetramers, which are well separated and can potentially act as active sites. Herein, a continuity breaking of the metal atoms in the crystal structure is achieved by the P incorporation, enabling the metal site separation. As seen before, a charge transfer from Pd to P is taking place, which leads to a reduced CO binding affinity of the surface. This helped to prevent any catalyst poisoning by CO, resulting in more available active sites for the oxidative addition of aryl halides and the subsequent alkoxy carbonylation reaction.

Through systematic investigations with respect to several synthesis parameters, highly active rhodium sulfide nanoparticles were synthesized on silica. Thereby, a promoting effect through the incorporation of sulfur, usually considered as a catalyst poison, was observed in the hydroformylation reaction of styrene. A phase dependent catalytic activity was seen following the order $\text{Rh} < \text{Rh}_2\text{S}_3 < \text{Rh}_{17}\text{S}_{15}$. The lead candidate $\text{Rh}_{17}\text{S}_{15}/\text{SiO}_2$ (1 wt.% Rh) not only outperformed the Rh-based reference catalysts but also exhibited superior activity in comparison to many reported heterogeneous and homogeneous catalysts. Through the application of unsupervised machine learning and density functional theory, the surfaces of the $\text{Rh}_{17}\text{S}_{15}$ and Rh_2S_3 systems were investigated, revealing the enormous number of possible chemically distinct surface sites, varying from S to Rh-rich. This feature enables the tuning of the CO binding energy on the site based on the surface termination, thereby providing an immense potential for tailoring the catalytic performance. Highly active ensembles, especially site-separated rhodium tetramers (Rh_4), have been identified in the Rh-rich surface terminations of $\text{Rh}_{17}\text{S}_{15}$. These species show a high CO affinity and contribute to an enhanced hydroformylation performance. The existence of such electronically modified and separated

active sites was not only computationally identified, but also confirmed through other characterization techniques, such as CO-DRIFT, XPS, XAS and TEM.

Stability improvement through support engineering

One of the major challenges in catalytic liquid-phase reactions is metal leaching, which leads to catalyst deactivation, product contamination, and a loss of precious metals. In this study, a simple yet highly effective strategy to suppress metal leaching was developed for the Heck coupling reaction through a support engineering approach. Through the addition of ammonium dihydrogen phosphate to the silica support, followed by calcination, P-modified supports, which contained phosphate species on the surface, could be obtained. The synthesis of Pd_3P nanoparticles on this modified support with an optimum phosphorus quantity ($\text{Pd}_3\text{P}/1\text{P}-\text{SiO}_2$, 10 wt.% Pd) resulted in a significant reduction in metal leaching by 85 % in comparison to a conventional silica supported Pd catalyst (Pd/SiO_2 , 10 wt.% Pd) in Heck coupling reactions. The anchoring effect, induced by the phosphate species on the support, stabilized the nanoparticles on the support, resulting in a high resistance towards metal leaching. Furthermore, a reduction in leaching amounting to 62 % was observed in the Pd_3P supported on pure silica ($\text{Pd}_3\text{P}/\text{SiO}_2$, 10 wt.% Pd) in comparison to the Pd counter part, demonstrating the simultaneous stability enhancement achieved through d-metal-p-block combination strategy. Hereby an anchoring of Pd within the crystal structure by P can be assumed. By combining these two results, it can be assumed, that the superior stability shown by $\text{Pd}_3\text{P}/1\text{P}-\text{SiO}_2$ (10 wt.% Pd) could potentially be the result of a “double anchoring” mechanism by phosphorus on the support and with the structure of the binary phosphide phase. This enhanced stability was also visible during the recovery experiments, where $\text{Pd}_3\text{P}/1\text{P}-\text{SiO}_2$ was recovered and reused multiple times without any significant loss of catalytic activity in comparison to the Pd/SiO_2 catalyst.

Outlook

The successful application of the d-block-p-block element combination strategy for developing exceptionally performing catalysts in Wacker-Tsuji oxidation, Heck coupling, carbonylation and hydroformylation reactions has opened up broad possibilities for a novel catalyst design. Metal-p-block combinations beyond phosphorus and sulfur can be investigated in this context to identify the most effective pairs, and a general workflow for such catalyst development can be proposed. Using tools such as “The Materials Project”, other Pd-p-block and Rh-p-block phases can be screened for their thermodynamic stability by evaluating their energy above the hull. By applying machine learning and DFT, and considering the underlying mechanisms of the target reactions, suitable materials can be preliminarily selected. With carefully tailored synthesis methods, these catalysts can then be produced in the laboratory and tested in the relevant reactions to evaluate their performance. Such data-inspired investigations may reveal

reaction-specific periodic trends, potentially accelerating the catalyst discovery for similar types of reactions.

The reactions studied in this work, where Pd-based catalysts were employed, can also be explored using nickel-based catalysts, which are considered as a more economical alternative to palladium. Investigating Ni-p-block combinations in this context would be valuable from an economic and sustainability point of view. Similarly, Co-based phases can be explored for hydroformylation reactions. Another promising strategy involves the development of phosphides and sulfides based on bimetallic systems, such as Pd_xNi_yP , Pd_xCu_yP , and Pd_xCo_yP for Wacker-Tsuji oxidation, carbonylation, and coupling reactions, or Rh_xCo_yS and Rh_xPd_yS for hydroformylation reactions.

A simple yet highly effective strategy for enhancing catalyst stability lies in the support engineering, which holds strong potential for the application across various supports and catalytic reactions. In this approach, a critical challenge in liquid-phase reactions, metal leaching, which leads to both catalyst loss and product contamination can be significantly mitigated, promoting more efficient use of metal resources. Therefore, combining support engineering with the element synergy strategy offers a powerful route toward developing catalysts that are not only highly active and selective, but also exceptionally stable.

8 Experimental details

8.1 Material characterization techniques

Powder X-ray diffraction (PXRD): PXRD measurements were carried out using a Stoe STADI-MP diffractometer equipped with a Ge-monochromatized Cu K α radiation source ($\lambda = 1.54 \text{ \AA}$) in transmission mode. For a typical experiment, approximately 3-5 mg of finely ground sample was placed between thin amorphous films and mounted onto the sample holder. Data were collected over a 2θ range of 2° to 92° , with a step size of 3° and a total acquisition time of 80 min. The sample holder was continuously rotated throughout the measurement. The raw PXRD data were further analyzed for phase identification using the Match! Version 3 software from Crystal Impact.^[293] Crystal structure data for phase identification were obtained from the Inorganic Crystal Structure Database (ICSD)^[294] and “The Materials Project”.^[33]

Inductively coupled plasma atomic emission spectroscopy (ICP-AES): The analysis of samples was performed in collaboration with Mikroanalytisches Labor Pascher. In a typical analysis, the samples were digested in a mixture of nitric acid, hydrofluoric acid, and hydrochloric acid at 130°C for 12 h. The subsequent analysis was carried out using an iCAP 6500 spectrometer from Thermo Fisher Scientific.

Thermogravimetry differential thermal analysis (TG-DTA): The TG-DTA measurements performed in nitrogen (inert) atmosphere were carried out in a Netzsch STA 449 F3 instrument (Netzsch, Germany) with $\alpha\text{-Al}_2\text{O}_3$ as reference material. For a typical measurement, a heating rate of 5 K/min up to 1000°C was applied (chapter 3). For the measurements performed in air (chapter 4), the analysis was conducted up to 650°C at a heating rate of 10 K/min using an empty Al_2O_3 crucible as reference. The instrument from Netzsch (STA 409), equipped with a TASC 414/2 controller and PU 1.851.01 power unit, was used for the measurements in air.

Scanning electron microscopy (SEM): SEM analyses were conducted using a Zeiss Supra 40 VP microscope (Zeiss, Germany), equipped with a Schottky field emitter providing a resolution of 2.0 nm, typically operated at 15 keV. For SEM imaging, powdered samples were dispersed in water, drop casted onto a silicon wafer, mounted on the sample holder, and dried to form a thin particle layer. Energy-dispersive X-ray spectroscopy (EDX) was performed using the same SEM in combination with a Sapphire Si(Li) detector (EDAX Genesis). For EDX, samples were prepared either as a thin powder layer or by drop casting aqueous suspensions onto carbon tape followed by drying.

Transmission electron microscopy (TEM): The analysis of rhodium sulfide catalyst *via* TEM discussed in chapter 6 was performed at BASF, Ludwigshafen

Hereby, samples were prepared on ultra thin carbon coated TEM grids. Finely ground powders were dispersed in ethanol through sonication, and a drop of the suspension was placed

between two glass microscope slides (objective slides) and gently spread for the purpose of forming a thin film. The TEM grids were then dipped onto the resulting film to collect the sample. The analysis was performed using a probe corrected Themis Z 3.1 microscope (Thermo Fisher Scientific, Waltham, USA) operating at 300 kV. Both high angle annular dark-field - scanning transmission electron microscopy (HAADF-STEM) and high-resolution TEM (HRTEM modes were employed to investigate the samples at good resolution. The recovered catalysts showed some contamination, which was treated in a plasma cleaner for 10 seconds. In cases of strong contamination, an additional 1 h electron shower was applied. Elemental analysis was conducted using the integrated SuperX G2 Energy-Dispersive X-ray Spectroscopy (EDXS) detectors, and data processing was carried out with the Velox 3 software (Thermo Fisher Scientific, USA). The silica support material demonstrated sensitivity to the electron beam and occasionally shrank during elemental mapping. Due to the low crystallinity of the sample, PXRD analysis has not provided the complete reflex data. Hence, the phase identification was also performed with selected area electron diffraction (SAED), with a selected area diameter of approximately 200 nm. Adequate crystalline reflections for phase identification were observed only in samples with higher Rh loading (5 and 10 wt.%). For samples with lower Rh content, the phase identification was performed *via* lattice spacing analysis in HRTEM images. Particle size distributions were determined by analyzing 700 to 1500 particles (varied from case to case basis) using automated particle size detection in TEM micrographs with the NanoDefine ParticleSizer plugin in ImageJ (FIJI).

The analysis of Pd based samples (Pd and Pd₃P) was performed at KIT in collaboration with AK Feldmann and the measurements were performed by Dr. Felix Jung. For the sample preparation, the well ground catalyst powders were dispersed in ethanol by ultra sonication, and a drop of the suspension was carefully deposited onto copper grids coated with an amorphous carbon film. The grids were subsequently dried at 60 °C overnight. TEM, STEM, and EDXS analyses were conducted using a FEI Osiris ChemiSTEM operated at an acceleration voltage of 200 kV. TEM images were acquired and analyzed with a Gatan BM Ultrascan CCD camera and Gatan Digital Micrograph 2.3. HAASF-STEM images were obtained using FEI TEM imaging and analysis software version 4.6. To determine particle size distributions, diameters of 200 nanoparticles were measured for each sample. Elemental mapping *via* EDXS was performed using a Bruker Super-X system, subsequently quantification was carried out with Bruker Esprit 2.3 software employing the Cliff-Lorimer method with theoretical k-factors.

Diffuse reflectance infrared Fourier transform spectroscopy (DRIFTS):

The DRIFTS measurements were performed in collaboration with AK Grunwaldt and the measurements were performed by Dr. Daria Gashnikova.

In order to prepare the samples for the measurement, finely ground catalyst samples were mixed with calcium fluoride (CaF_2 , 99.5 %) in a 20:80 ratio (20% catalyst, 80% CaF_2), then pressed and sieved to obtain a particle size fraction of 100-200 μm . Measurements were conducted using a VERTEX 70 Fourier transform infrared (FTIR) spectrometer from Bruker, equipped with Praying Mantis diffuse reflection optics (Harrick) and a liquid nitrogen cooled mercury cadmium telluride (MCT) detector.

Prior to CO adsorption, the samples were pretreated in flowing argon at 150 $^{\circ}\text{C}$ for 1 h to remove physisorbed water and other surface contaminants. Following this, background spectra were recorded in argon at 40 $^{\circ}\text{C}$ under a flow of 100 mL/min. CO adsorption experiments were carried out at 40 $^{\circ}\text{C}$ for 1 h using a 1% CO/Ar mixture at a total flow rate of 100 mL/min. Each set of 130 recorded spectra was averaged into a single scan, yielding an effective resolution of one scan per min during the CO adsorption experiments. Temperature calibration was performed prior to the measurements using an infrared camera (ImageIR® 8300 camera, InfraTec used calibration: M1x (30-150)) to correlate actual sample temperatures with instrument setpoints. This is performed through monitoring the surface temperature of CaF_2 bed under 100 mL/min argon flow. The values provided in the corresponding section (150 $^{\circ}\text{C}$ and 40 $^{\circ}\text{C}$) are based on the values from IR camera.

X-ray photoelectron spectroscopy (XPS): The XPS analysis of the rhodium-based samples in chapter 6 was performed at BASF, Ludwigshafen. The powder samples were initially pressed onto indium foil as a powder and measured in isolation. Monochromatic Al $\text{K}\alpha$ radiation (45 W) was used to perform XPS measurements with Phi Versa Probe 5000 spectrometer. The diameter of the measuring spot was selected as approximately 200 μm . The energetic position of the spectra was calibrated using the Si 2p signal, normalized to 103.5 eV for SiO_2 . Mean values of the measurement points are reported in the corresponding figures, with error bars representing the standard deviation across all analyzed points. Quantification uncertainties were estimated *via* Monte Carlo simulation and are used in the error bars. All samples were analyzed using the built-in Phi charge neutralizer system. To minimize differential charging, the powder samples were pressed into indium foil and mounted onto the sample holder using double sided adhesive tape, ensuring insulation from ground.

Survey scans were performed over a range of 1350 eV to 0 eV with a pass energy of 117 eV, an energy step size of 0.5 eV, and a dwell time of 3500 ms per point. High resolution spectra were recorded from the same analysis area using a pass energy of 23.5 eV and a step size of 0.1 eV, with dwell times per point as follows: O (700 ms), C and Rh (3500 ms), S (3500 ms), and Si (2100 ms). Spectra were charge-corrected by referencing the C 1s peak to 284.8 eV, a standard value for hydrocarbon species. The spectral analysis was conducted using CasaXPS software (version 2.3.22PR1.0). A Shirley background subtraction was applied to all regions.

Quantification was based exclusively on high-resolution spectra. Peak fitting for C + Rh and S was performed using symmetric LA (1,1,900) line shapes. Elemental quantification was conducted using the relative sensitivity factors provided by the instrument manufacturer.

XPS measurements for the palladium phosphide sample in chapter 3 was performed in collaboration with Prof. Helge S. Stein at Helmholtz Institute Ulm and the measurements were performed by Mr. Stefan Fuchs. The measurements were performed using an EnviroESCA model instrument from Specs with Al-K α source (1486.71 eV) operated at 15 kV, 43 W (3 mA emission) and 30 eV pass energy for high resolution spectra. The charging effects were compensated by recording spectra at 7 mbar nitrogen atmosphere in the analysis chamber to compensate for charging effects. The evaluation with Shirley type background and 70 % Gaussian and 30 % Lorentzian profile was performed with CasaXPS version 2.3.24PR1.0.

X-ray absorption spectroscopy (XAS): The XAS measurements were performed in collaboration with AK Grunwaldt and the measurements were performed by Dr. Florian Maurer.

Except of the Rh foil reference, which was recorded at BM23 (ESRF), all X-ray absorption spectroscopic measurements were conducted at the CATACT beamline^[295] at the KIT light source (KIT, Germany). X-ray absorption near-edge structure (XANES) and extended X-ray absorption fine structure (EXAFS) spectra were recorded at the Rh-K edge in transmission mode. The Si (311) double-crystal monochromator was used to tune the energy of the incident photons. For sample measurements, the beam size was set to 2 (vertical) x 2 (horizontal) mm². The catalyst powder filled into a quartz capillary (outer diameter: 1.5 mm; wall thickness: 0.02 mm) was used for the measurement. ATHENA application from the IFFEFIT software package was used for the normalization and background subtraction for the EXAFS evaluation.^[296]

CO chemisorption: The XAS measurements were performed in collaboration with AK Grunwaldt and the measurements were performed by Ms. Kathrin Schaefer. The measurements were performed with an instrument made at KIT, occupied with an analyzer for the CO and CO₂ from Rosemount Xstream in order to determine the dispersion of the samples. Two measurements for each sample was made and the average value was used in this work.

Dynamic light scattering (DLS): The measurements were carried out using a Zetasizer Nano ZS (Malvern Panalytical, Malvern), equipped with a He-Ne laser (λ = 633 nm). The scattering intensities required for the calculation were detected at an angle of 173° in backscatter geometry. For particle size determination, approximately 2 mL dilute filtrate sample after the reaction was transferred into a polystyrene cuvette and placed into the device's measurement cell. The analysis was conducted using the Zetasizer software (Version 7.10, Malvern Panalytical, Malvern).

8.2 Synthesis of materials

8.2.1 Chemicals

Palladium acetate ($\text{Pd}(\text{OAc})_2$) with a purity of $\geq 99.9\%$, methyl acrylate (purity 99 %), styrene (purity $\geq 99\%$), potassium carbonate (purity $\geq 99\%$), ammonium dihydrogen phosphate (purity $\geq 99\%$), cuprous chloride (CuCl), cupric chloride (CuCl_2), phosphoric acid (85 wt.%), rhodium acetate ($\text{Rh}(\text{OAc})_3$) with purity $\geq 98\%$, and thiourea (purity $\geq 99\%$) were purchased from Sigma Aldrich. Iodobenzene (purity $\geq 99\%$) and methyl 4-iodobenzoate (purity $\geq 98\%$) were purchased from TCI. Acetone (HPLC grade), ethanol (purity $\geq 99.8\%$) and potassium phosphate trihydrate (purity $\geq 99\%$) were purchased from Carl Roth and *n*-decane and triethylamine (Et_3N) with a purity of 99 % from abcr GmbH. Silica (Cariact, Q 20 C) was purchased from Fuji Silysia Chemical Ltd. Acetic acid (99 %), hydrogen peroxide (30 %) and sulfuric acid (70 %) were purchased from VWR International. Acetonitrile (HPLC grade) and dimethyl sulphoxide (purity $\geq 99.9\%$) were purchased from Fischer Scientific GmbH. *N*-Methyl-2-pyrrolidone (purity $\geq 99.5\%$), hydrochloric acid (37 %), toluene (purity $\geq 99.85\%$) and *N,N*-dimethylformamide (purity $\geq 99.8\%$) were obtained from Acros and dimethyl acetamide with a purity 99 % was purchased from Alfa Aesar.

Hydrogen gas (purity 99.999 %) carbon monoxide (purity 98 %) argon gas (99.999%) and syngas gas (95 % and rest Argon, CO: H_2 : 50:50) were purchased from Air Liquide.

8.2.2 Preparation of phosphorus-modified supports

Phosphorus modified supports, also referred in this work as “engineered supports” were prepared following the procedure below:

In a typical procedure for the preparation of 1 wt.% phosphorus-modified silica, 1P- SiO_2 , a solution of 37.1 mg (0.32 mmol) of $\text{NH}_4\text{H}_2\text{PO}_4$ in 0.9 mL of water was added drop wise to the support material silica (Cariact, Q 20 C from Fuji Silysia Chemical Ltd.). The impregnated silica was subsequently dried at 60 °C for 12 h and calcined under air in a box furnace at 600 °C for 6 h with a temperature ramp of 15 K/min. The P-modified silica with a lower phosphorus loading of 0.5 wt.% was prepared following the same procedure, however using half the amount of $\text{NH}_4\text{H}_2\text{PO}_4$. The prepared support materials were denoted by the quantity of phosphorus added to the sample: 0.5P- SiO_2 and 1P- SiO_2 . Only for the purpose of examining the success of the synthetic approach through characterization, 5 wt.% phosphorus modified silica (5P- SiO_2) was also prepared using 185.5 mg of $\text{NH}_4\text{H}_2\text{PO}_4$.

8.2.3 Synthesis of supported Pd_xP_y nanoparticles

The supported palladium phosphide nanoparticles ($\text{Pd}_3\text{P}/\text{SiO}_2$, 10 wt.% Pd) as catalysts for Wacker-Tsuji oxidation reactions (chapter 3) were prepared as follows:

The material was prepared using a wet impregnation method, in which 100 mg (0.45 mmol) of $\text{Pd}(\text{OAc})_2$ dissolved in HCl and 104 mg (0.9 mmol) $\text{NH}_4\text{H}_2\text{PO}_4$ dissolved in water were mixed in a round bottom flask. In to this solution 450 mg of silica, providing a metal impregnation loading (Pd/silica) of 10 wt.%, was added and stirred overnight. Further, the solvent was removed from the mixture using a rotary evaporator and applying vacuum and dried overnight at 50 °C. The dried precursors were then reduced in stagnant pure H_2 (99.9999 % purity) at 400 °C for 4 h with a heating rate of 5 K/min. The Pd/SiO_2 (10 wt.% Pd) was synthesized following the procedure mentioned above, without the addition of a $\text{NH}_4\text{H}_2\text{PO}_4$ solution.

Supported palladium phosphide nanoparticles as catalysts for the Heck coupling reaction (chapter 4) reaction was prepared as follows:

In a typical synthesis for the preparation of $\text{Pd}_3\text{P}/\text{SiO}_2$ (10 wt.% Pd) *via* incipient wetness impregnation method, 100 mg (0.45 mmol) of $\text{Pd}(\text{OAc})_2$ and 10 μL (0.15 mmol) of H_3PO_4 (85 %) were dissolved upon sonication in 2 mL of concentrated HCl and added drop wise to 450 mg of silica support. The substance was further dried at 60 °C for 12 h in a drying oven and reduced in stagnant pure H_2 at 400 °C for 8 h with a heating ramp of 50 K/min. To perform the thermal treatment in H_2 atmosphere (reduction), the dried impregnated precursors were taken in a quartz glass Schlenk tube, equipped with a pressure relief valve and two stopcocks. The Schlenk tube was then connected to a Schlenk line and the hydrogen gas bottle. Prior to introducing hydrogen, the entire apparatus underwent evacuation. A box furnace was used to heat the Schlenk tube containing the dried impregnated precursor in order to facilitate the catalyst formation. Intermittent dosing of hydrogen was employed during the thermal treatment to maintain a consistent hydrogen atmosphere. To synthesize, $\text{Pd}_3\text{P}/0.5\text{P}-\text{SiO}_2$ (10 wt.% Pd) and $\text{Pd}_3\text{P}/1\text{P}-\text{SiO}_2$ (10 wt.% Pd), the same procedure was applied, however with using the P-modified supports. The procedure for the preparation of Pd/SiO_2 (10 wt.% Pd) and $\text{Pd}/1\text{P}-\text{SiO}_2$ (10 wt.% Pd) was the same, however without the addition of phosphoric acid to the precursor solution.

The $\text{Pd}_3\text{P}/\text{SiO}_2$ (5 wt.% Pd) catalyst used for the alkoxy carbonylation reaction (chapter 5) was also synthesized as above, however with the precursor quantities as 100 mg $\text{Pd}(\text{OAc})_2$ and 10 μL H_3PO_4 and 0.94 g silica, in order to adjust the Pd loading on silica. Similarly, Pd/SiO_2 (5 wt.% Pd) was synthesized, however without the addition of H_3PO_4 .

To prevent the surface oxidation, all the catalysts were stored in an Argon-filled glovebox (MBraun) prior to use.

8.2.4 Synthesis of supported Rh_xS_y nanoparticles

The supported rhodium sulfide nanoparticles were prepared *via* an incipient wetness impregnation method. For the synthesis of $\text{Rh}_{17}\text{S}_{15}/\text{SiO}_2$ (10 wt.% Rh) catalyst, 50 mg (0.18

mmol) of Rh(OAc)_3 and 16 mg (0.21 mmol) thiourea ($\text{CH}_4\text{N}_2\text{S}$) were dissolved in water and added to 200 mg of silica. The impregnated silica was dried at 60 °C for 12 h in a drying oven. The dried material was further heated in a flowing stream of argon (450 NL/h) to 700 °C for 6 h with a heating ramp of 10 K/min in a tube furnace. For the synthesis of $\text{Rh}_2\text{S}_3/\text{SiO}_2$ (10 wt.% Rh), 50 mg (0.18 mmol) of Rh(OAc)_3 and 30 mg (0.4 mmol) thiourea ($\text{CH}_4\text{N}_2\text{S}$) were dissolved in water and added to 200 mg of silica. Further drying and thermal treatment was performed similar to $\text{Rh}_{17}\text{S}_{15}/\text{SiO}_2$ (10 wt.% Rh) as explained above. Rhodium sulfide with 1 wt.% Rh loading catalysts were prepared with same procedure, however using 2 g silica. Further, following the similar procedure Rh/SiO_2 (1 wt.% Rh) was prepared as reference catalyst, but without the addition of thiourea.

8.3 Catalyst testing procedures

8.3.1 General procedure for the Wacker Tsuji oxidation reactions

The Wacker-Tsuji oxidation reaction was performed in a Microbatch Reactor 2500 setup purchased from the Parr Instrument Company equipped with magnetic stirring, a gas inlet, a pressure indicator and a temperature control facility.

System A and B: The procedure for these reactions was adapted from Donck *et al.*^[121] In a typical reaction, 1 mmol of styrene was added to the solvent mixture containing 2 mL of THF and 0.5 mL of H_2O taken in an autoclave (micro-batch reactor). To this solution 2 mol % Pd catalyst (based on Pd with respect to styrene) and 20 mol% co-catalysts (CuCl or CuCl_2) were added. Further, the autoclave was pressurized with pure oxygen heated to the desired temperature with continuous stirring (800 rpm). After the assigned reaction time, the autoclave was removed from the heat source and allowed to cool down to room temperature. Subsequently, the pressure was released.

System C: The procedure used for the reactions was adapted from Xia *et al.*^[205] In a typical test, 1 mmol of styrene, 0.31 mL of H_2O_2 (30 %), 0.013 mL of H_2SO_4 (70 %) and 2.5 mL of MeCN were added to an autoclave (micro-batch reactor). After the addition of 2 mol % Pd catalyst (based on Pd with respect to styrene), the autoclave was heated to the desired temperature with continuous stirring (800 rpm). After the assigned reaction time, the autoclave was removed from the heat source and allowed to cool down to room temperature.

System D: The procedure used here for the reaction was adapted from Vafaeenezadeh *et al.*^[126] In a typical test, 1 mmol of styrene, 1.4 mL of acetic acid, 0.6 mL of water and 0.31 mL of hydrogen peroxide (30 %) were added to an autoclave (micro-batch reactor). After addition of 2 mol % Pd catalyst (Pd with respect to styrene), the autoclave was heated to the desired temperature with continuous stirring (800 rpm). After the assigned reaction time, the autoclave was removed from the heat source and allowed to cool down to room temperature.

8.3.2 General procedure for Heck coupling reactions

For a typical Heck reaction, 10 mL of DMSO was taken in a 25 mL round-bottom flask. To this flask 1 mmol of styrene, 0.65 mmol of iodobenzene, 100 μ L of *n*-decane (internal standard) and base (256 mg of K_3PO_4 or 133 μ L of Et_3N) were added. Finally, 1 mol% Pd catalyst (Pd with respect to styrene) was added to the reaction mixture and heated using oil bath to the desired temperature for the specific time while continuously stirring. After the reaction time, the flask was removed from the oil bath and allowed to cool down.

8.3.3 General procedure for alkoxy carbonylation reactions

Alkoxy carbonylation reactions were performed in Parr 5500 series compact reactors with a capacity of 25 mL and equipped with an overhead stirrer, gas inlet, pressure indicator and temperature control facility. In a typical reaction, 1 mmol of iodobenzene, 420 μ L of Et_3N , 100 μ L of *n*-decane (internal standard) and 0.5 mol % of Pd catalyst (Pd with respect to iodobenzene) were added to 4 mL of ethanol in the reactor. The reactor was further flushed three times with carbon monoxide to purge air from the system, then pressurized to the desired pressure and heated to the reaction temperature under continuous stirring at 1000 rpm. After completion of the reaction, the heater was turned off and the reactor was allowed to cool to ambient temperature. The gas was vented in the fume hood prior opening the reactor and preparing for further analysis.

8.3.4 General procedure for hydroformylation reactions

Hydroformylation reactions were performed in a Microbatch Reactor 2500 setup purchased from the Parr Instrument Company equipped with magnetic stirring, a gas inlet, a pressure indicator and a temperature control facility. In a typical test, 1 mmol of styrene, 1.5 mL of toluene, 0.5 mL *n*-decane (internal standard) and 0.2 mol % of Rh catalyst (Rh with respect to styrene) were added to the autoclave. The reactor was further flushed three times with syn gas to purge air from the system, then pressurized to the desired pressure and heated to the reaction temperature under continuous stirring at 1200 rpm. After completion of the reaction, the autoclave was removed from the heat source and allowed to cool to ambient temperature. The gas was vented in the fume hood prior opening the reactor and preparing for further analysis. During the reaction, the pressure inside the autoclave was recorded using the integrated SpecView software.

8.3.5 Catalyst recovery tests

To evaluate the reusability of the synthesized catalysts, recovery tests were conducted. In a typical test, the fresh solid catalyst was used in the reaction (first run). After the reaction, the catalyst was separated by centrifugation at 12,000 rpm, washed at least twice with a solvent, such as acetone, and dried at 60 °C for 12 h. The recovered catalyst was then reused under identical reaction conditions, and its performance was assessed in terms of conversion and

selectivity. To obtain sufficient catalyst for the recovery cycles, accounting for potential loss during separation and washing, parallel reactions were carried out and the resulting catalysts were combined.

8.3.6 Filtration tests

Insights into the heterogeneous nature of the catalyst can be obtained from filtration tests. In a typical filtration test, the reaction was allowed to proceed with the catalyst to reach a lower level of conversion. Further, the reaction was stopped and catalyst was removed *via* filtration. Here, particular care should be taken to maximize the removal of catalyst particles from the liquid using suitable techniques. The filtration was performed with a syringe filter of 200 nm for reactions conducted at round bottom flask. However, for reactions conducted at autoclaves a series of catalyst separation techniques using a syringe filter, celite bed prepared in the glass pipette, and centrifugation at high rpm was performed. Further, the reaction was allowed to proceed with the filtrate without the addition of a catalyst. Further progress of the reaction in the filtrate was monitored to obtain insight into the heterogeneous nature of the catalyst.

8.3.7 GC-MS analysis of the reaction products

The products obtained after the catalytic reactions were analyzed qualitatively and quantitatively with gas chromatography-mass spectrometry (GC-MS). An Agilent GC-MS, model 8860 GC and 5977B MSD with fused silica capillary column (ID: 0.25 mm, film thickness: 0.25 μ m, and length: 30 m) operating in He (99.9999% purity) carrier gas was used for the analysis of samples. For a typical analysis, the reaction mixture was filtered through a 200 nm syringe filter, and a 20 μ L aliquot (80 μ L for alkoxycarbonylation) was added to 1 mL of acetone in a GC vial using a microliter syringe. Using an automatic liquid sampler facility in the GC-MS, 1 μ L sample was injected for analysis and a split ratio of 1:100 was applied. The method parameter used for specific reactions are provided below:

Wacker- Tsuji reaction, Heck coupling and hydroformylation reactions - injection temperature: 250 °C, oven temperature programing: 2.25 min at 50 °C followed by increase to 240 °C at 40 K/min and holding at 240 °C for 1 min.

Alkoxycarbonylation reactions - injection temperature: 310 °C, oven temperature programing: 2.25 min at 50 °C followed by increase to 290 °C at 40 K/min and holding at 290 °C fro 1 min.

The qualitative analysis to identify the products were performed with Agilent Mass Hunter software integrated with NIST library. Quantitative analysis was performed using *n*-decane as internal standard. The integration of peaks and determination of areas in the chromatogram were performed with the Agilent Mass Hunter software.

8.4 Estimation of performance parameters

The dispersion for $\text{Pd}_3\text{P}/\text{SiO}_2$ (5 wt.% Pd) and Pd/SiO_2 (5 wt.% Pd) in chapter 5 were determined *via* CO chemisorption analysis.

The dispersions of the rhodium sulfide catalysts in chapter 6 were determined from particle sizes obtained from TEM as follows:

Dispersion of Rh = $\frac{4d}{d_{np}}$, where d is the distance between rhodium atoms and dnp is the average particle diameter (area based) from the TEM analysis^[278]

Dispersion of $\text{Rh}_{17}\text{S}_{15}/\text{SiO}_2$ (1 wt.% Rh) calculated as 47 % (d=0.258 nm and dnp=2.2 nm) and for $\text{Rh}_2\text{S}_3/\text{SiO}_2$ (1 wt.% Rh) as 42 % (d=0.3208 nm and dnp=3 nm).

The general formula used for the determination of TOF is given below:

$$\text{TOF (h}^{-1}\text{)} = \frac{\text{Converted substrate(mol)}}{\text{Total metal (mol)} \times \text{Dispersion of metal} \times \text{time (h)}}$$

TOF values were determined at conversions lower than 30 %.

Conversion, selectivity and n/iso ratio were estimated based on the equations provided below using the integrated peak area from chromatogram.

$$\text{Conversion (\%)} = \frac{\text{Reactant converted (mol)}}{\text{Reactant intially present (mol)}}$$

$$\text{Selectivity (\%)} = \frac{\text{Desired product formed (mol)}}{\text{Reactant converted (mol)}}$$

$$\text{n/iso} = \frac{\text{Linear aldehyde formed (mol)}}{\text{Branched aldehyde formed (mol)}}$$

8.5 Theoretical calculations

The calculation for the determination of CO binding energies demonstrated in chapter 5 was performed with the “Open Catalyst Project”.^[246] The model EquiformerV2^[297] was used for determining the binding energy.

The theoretical calculations with DFT and machine learning in chapter 6 was performed at BASF by Dr. Edvin Fako and Dr. Sandip De. QuantumEspresso was used to perform all DFT calculations.^[298] The functional used was the Perdew-Becke-Ernzerhof (PBE)^[299] functional and core electrons were by projector augmented-waves (PAW).^[300,301] The valence monoelectric states expansion was carried out as plain waves with a maximum kinetic energy of 450 eV. As suggested by Standard Solid State Pseudopotentials (SSSP) library, core electrons were represented by pseudopotentials,^[302] whereas the representation of valence shells are done with 4, 6, 6, and 17 electrons for C, O, S, and Rh. Grimme-D3 approach was used to introduce dispersion.^[303] A dense reciprocal-space mesh was employed with a

maximum spacing of 0.25 \AA^{-1} and Gaussian smearing of 0.1 eV with 10^{-6} eV selected as self consistent field (SCF) calculation convergence criteria. The maximal force criterion of 0.05 eV/ \AA was selected for ionic convergence. To ensure consistency, bulk Rh_xS_y and Rh structures obtained from “The Materials Project” [33] were relaxed using the same DFT settings prior to constructing the corresponding slab models.

9 References

- [1] X. Cui, W. Li, P. Ryabchuk, K. Junge, M. Beller, *Nat. Catal.* **2018**, *1*, 385–397.
- [2] J. G. de Vries, S. D. Jackson, *Catal. Sci. Technol.* **2012**, *2*, 2009.
- [3] H.-Y. Jeong, M. Balamurugan, C. H. Choi, K. T. Nam, in *Carbon Dioxide Electrochem. Homog. Heterog. Catal.* (Eds.: M. Robert, C. Costentin, K. Daasbjerg), The Royal Society Of Chemistry, **2020**, pp. 226–286.
- [4] Y. Li, J. Yu, *Nat. Rev. Mater.* **2021**, *6*, 1156–1174.
- [5] M. S. Alhumaimess, *J. Saudi Chem. Soc.* **2020**, *24*, 461–473.
- [6] S. Zhou, L. Wang, S. Gao, X. Chen, C. Zhang, D. Yu, X. Fan, X. Yu, Z. Zhao, *ACS Catal.* **2024**, *14*, 6062–6127.
- [7] W. Juszczyk, Z. Karpiński, D. Łomot, J. Pielaśek, *J. Catal.* **2003**, *220*, 299–308.
- [8] L. Courthéoux, V. Hétier, A. Carvalho, J. Rousseau, P. Lacroix Desmazes, E. Girard, D. Uzio, S. Brunet, A. Pradel, *ChemCatChem* **2023**, *15*, e202300535.
- [9] M. Muraleedharan Nair, S. Kaliaguine, *New J. Chem.* **2016**, *40*, 4049–4060.
- [10] A. Z. Fadhel, P. Pollet, C. L. Liotta, C. A. Eckert, *Molecules* **2010**, *15*, 8400–8424.
- [11] C. Vogt, B. M. Weckhuysen, *Nat. Rev. Chem.* **2022**, *6*, 89–111.
- [12] S. Hanf, L. Alvarado Rupflin, R. Gläser, S. Schunk, *Catalysts* **2020**, *10*, 510.
- [13] T. Cuk, *ACS Cent. Sci.* **2018**, *4*, 1084–1086.
- [14] D. B. Burueva, L. M. Kovtunova, V. I. Bukhtiyarov, K. V. Kovtunov, I. V. Koptyug, *Chem. Eur. J.* **2019**, *25*, 1420–1431.
- [15] R. Kukawka, A. Pawłowska-Zygarowicz, J. Dzialekowska, M. Pietrowski, H. Maciejewski, K. Bica, M. Smiglak, *ACS Sustain. Chem. Eng.* **2019**, *7*, 4699–4706.
- [16] A. Riisager, R. Fehrmann, M. Haumann, P. Wasserscheid, *Eur. J. Inorg. Chem.* **2006**, *2006*, 695–706.
- [17] J. Yu, G. Yang, M. Gao, H. Wang, H. Jiang, *Angew. Chem. Int. Ed.* **2024**, *63*, e202412643.
- [18] M. A. Ortuño, N. López, *Catal. Sci. Technol.* **2019**, *9*, 5173–5185.
- [19] A. Ota, M. Armbrüster, M. Behrens, D. Rosenthal, M. Friedrich, I. Kasatkin, F. Girgsdies, W. Zhang, R. Wagner, R. Schlögl, *J. Phys. Chem. C* **2011**, *115*, 1368–

[20] H. Li, H. Yang, H. Li, *J. Catal.* **2007**, *251*, 233–238.

[21] D. Albani, M. Shahrokh, Z. Chen, S. Mitchell, R. Hauert, N. López, J. Pérez-Ramírez, *Nat. Commun.* **2018**, *9*, 1–11.

[22] L. Alvarado Rupflin, J. Mormul, M. Lejkowski, S. Titlbach, R. Papp, R. Gläser, M. Dimitrakopoulou, X. Huang, A. Trunschke, M. G. Willinger, R. Schlögl, F. Rosowski, S. A. Schunk, *ACS Catal.* **2017**, *7*, 3584–3590.

[23] Y. Nakaya, S. Furukawa, *Chem. Rev.* **2023**, *123*, 5859–5947.

[24] B. Liu, X. Lan, Q. Zhong, T. Wang, *ACS Catal.* **2024**, *14*, 757–775.

[25] B. Liu, N. Huang, Y. Wang, X. Lan, T. Wang, *ACS Catal.* **2021**, *11*, 1787–1796.

[26] V. B. John, in *Underst. Phase Diagrams*, Palgrave, London, **1974**, pp. 1–7.

[27] E. Svanidze, T. Besara, M. F. Ozaydin, C. S. Tiwary, J. K. Wang, S. Radhakrishnan, S. Mani, Y. Xin, K. Han, H. Liang, T. Siegrist, P. M. Ajayan, E. Morosan, *Sci. Adv.* **2016**, *2*, e1600319.

[28] A. R. Paul, M. Mukherjee, D. Singh, *Cryst. Res. Technol.* **2022**, *57*, 2100159.

[29] M. Gutnyk, F. Nürnberger, *Hist. Sci. Technol.* **2023**, *13*, 243–262.

[30] Y. Liu, A. J. McCue, D. Li, *ACS Catal.* **2021**, *11*, 9102–9127.

[31] Z. Li, J. Wang, in *Handb. Energy Mater.*, Springer Nature Singapore, Singapore, **2022**, pp. 1–32.

[32] M. Cui, X. Meng, *Nanoscale Adv.* **2020**, *2*, 5516–5528.

[33] A. Jain, S. P. Ong, G. Hautier, W. Chen, W. D. Richards, S. Dacek, S. Cholia, D. Gunter, D. Skinner, G. Ceder, K. A. Persson, *APL Mater.* **2013**, *1*, 11002.

[34] M. Armbrüster, K. Kovnir, M. Behrens, D. Teschner, Y. Grin, R. Schlögl, *J. Am. Chem. Soc.* **2010**, *132*, 14745–14747.

[35] C. Li, Y. Chen, S. Zhang, J. Zhou, F. Wang, S. He, M. Wei, D. G. Evans, X. Duan, *ChemCatChem* **2014**, *6*, 824–831.

[36] T. Gong, G. Qiu, M.-R. He, O. V. Safonova, W.-C. Yang, D. Raciti, C. Oses, A. S. Hall, *J. Am. Chem. Soc.* **2025**, *147*, 510–518.

[37] L. A. Rupflin, C. Boscagli, S. A. Schunk, *Catalysts* **2018**, *8*, 122.

[38] B. Liu, X. Lan, Q. Zhong, T. Wang, *ACS Catal.* **2024**, 757–775.

[39] N. Marcella, J. S. Lim, A. M. Płonka, G. Yan, C. J. Owen, J. E. S. van der Hoeven, A. C. Foucher, H. T. Ngan, S. B. Torrisi, N. S. Marinkovic, E. A. Stach, J. F. Weaver, J. Aizenberg, P. Sautet, B. Kozinsky, A. I. Frenkel, *Nat. Commun.* **2022**, 13, 832.

[40] R. Li, Y. Yue, Z. Chen, X. Chen, S. Wang, Z. Jiang, B. Wang, Q. Xu, D. Han, J. Zhao, *Appl. Catal. B Environ.* **2020**, 279, 119348.

[41] G. Vilé, N. Almora-Barrios, S. Mitchell, N. López, J. Pérez-Ramírez, *Chem. Eur. J.* **2014**, 20, 5926–5937.

[42] D. Albani, K. Karajovic, B. Tata, Q. Li, S. Mitchell, N. López, J. Pérez-Ramírez, *ChemCatChem* **2019**, 11, 457–464.

[43] S. Hu, Z. Gao, S. Gao, J. Wang, X. Zhang, *ACS Appl. Energy Mater.* **2023**, 6, 11051–11060.

[44] P. Yin, J. Shi, M. Zuo, W. Zhang, B. Peng, B. Jiang, X.-Z. Fu, H.-W. Liang, *J. Phys. Chem. Lett.* **2024**, 15, 4501–4507.

[45] S. Furukawa, A. Suga, T. Komatsu, *ACS Catal.* **2015**, 5, 1214–1222.

[46] R. Burch, *Acc. Chem. Res.* **1982**, 15, 24–31.

[47] K. Yang, X. Chen, J. Qi, Z. Bai, L. Zhang, C. Liang, *J. Catal.* **2019**, 369, 363–371.

[48] L. Casillas-Trujillo, B. Osinger, R. Lindblad, D. Karlsson, A. I. Abrikosov, S. Fritze, K. von Fieandt, B. Alling, I. Hotz, U. Jansson, I. A. Abrikosov, E. Lewin, *Mater. Chem. Front.* **2021**, 5, 5746–5759.

[49] J. K. Nørskov, F. Abild-Pedersen, F. Studt, T. Bligaard, *Proc. Natl. Acad. Sci.* **2011**, 108, 937–943.

[50] S. Bhattacharjee, U. V. Waghmare, S.-C. Lee, *Sci. Rep.* **2016**, 6, 35916.

[51] R. Qi, Q. Jiang, M. Zhong, W. Li, S. Ren, Y. Wang, M. Feng, X. Lu, *Chem. Eng. J.* **2024**, 496, 154094.

[52] M.-L. Yang, Y.-A. Zhu, X.-G. Zhou, Z.-J. Sui, D. Chen, *ACS Catal.* **2012**, 2, 1247–1258.

[53] R. M. Kluge, R. W. Haid, A. Riss, Y. Bao, K. Seufert, T. O. Schmidt, S. A. Watzele, J. V. Barth, F. Allegretti, W. Auwärter, F. Calle-Vallejo, A. S. Bandarenka, *Energy Environ. Sci.* **2022**, 15, 5181–5191.

[54] Y. Liu, A. J. McCue, D. Li, *ACS Catal.* **2021**, 11, 9102–9127.

[55] D. Evans, J. A. Osborn, G. Wilkinson, *J. Chem. Soc. A Inorganic, Phys. Theor.* **1968**, 3133.

[56] S. Tang, C. Liu, A. Lei, *Chem. Commun.* **2013**, *49*, 2442.

[57] J. Tappen, I. Rodstein, K. McGuire, A. Großjohann, J. Löffler, T. Scherpf, V. H. Gessner, *Chem. Eur. J.* **2020**, *26*, 4281–4288.

[58] S. Lapointe, A. Sarbajna, V. H. Gessner, *Acc. Chem. Res.* **2022**, *55*, 770–782.

[59] G. Rangits, L. Kollár, *J. Mol. Catal. A Chem.* **2005**, *242*, 156–160.

[60] S. E. Habas, F. G. Baddour, D. A. Ruddy, C. P. Nash, J. Wang, M. Pan, J. E. Hensley, J. A. Schaidle, *Chem. Mater.* **2015**, *27*, 7580–7592.

[61] J. R. Hayes, R. H. Bowker, A. F. Gaudette, M. C. Smith, C. E. Moak, C. Y. Nam, T. K. Pratum, M. E. Bussell, *J. Catal.* **2010**, *276*, 249–258.

[62] L. S. Escandón, S. Ordóñez, A. Vega, F. V. Díez, *J. Hazard. Mater.* **2008**, *153*, 742–750.

[63] X. Cui, H. He, D. Xie, L. Zheng, X. Wang, Z. Jiang, D. Xu, Y. Guo, *Chem. Eng. J.* **2023**, *464*, 142622.

[64] A. J. McCue, A. Guerrero-Ruiz, I. Rodríguez-Ramos, J. A. Anderson, *J. Catal.* **2016**, *340*, 10–16.

[65] J. Masud, T. Van Nguyen, N. Singh, E. McFarland, M. Ikenberry, K. Hohn, C.-J. Pan, B.-J. Hwang, *J. Electrochem. Soc.* **2015**, *162*, F455–F462.

[66] E. Aslan, I. Akin, I. H. Patir, *Chem. Eur. J.* **2016**, *22*, 5342–5349.

[67] C. Bara, A.-F. Lamic-Humblot, E. Fonda, A.-S. Gay, A.-L. Taleb, E. Devers, M. Digne, G. D. Pirngruber, X. Carrier, *J. Catal.* **2016**, *344*, 591–605.

[68] Y. Liu, A. J. McCue, C. Miao, J. Feng, D. Li, J. A. Anderson, *J. Catal.* **2018**, *364*, 406–414.

[69] T. F. Jaramillo, K. P. Jørgensen, J. Bonde, J. H. Nielsen, S. Horch, I. Chorkendorff, *Science (80-.)* **2007**, *317*, 100–102.

[70] W. Hu, L. Xie, C. Gu, W. Zheng, Y. Tu, H. Yu, B. Huang, L. Wang, *Coord. Chem. Rev.* **2024**, *506*, 215715.

[71] Y. Kim, Y. Kim, A. Choi, S. Woo, D. Mok, N. Choi, Y. S. Jung, J. H. Ryu, S. M. Oh, K. T. Lee, *Adv. Mater.* **2014**, *26*, 4139–4144.

[72] J. F. Callejas, J. M. McEnaney, C. G. Read, J. C. Crompton, A. J. Biacchi, E. J. Popczun, T. R. Gordon, N. S. Lewis, R. E. Schaak, *ACS Nano* **2014**, *8*, 11101–11107.

[73] Z. Guo, R. Wang, Y. Guo, J. Jiang, Z. Wang, W. Li, M. Zhang, *ACS Catal.* **2022**, *12*, 15193–15206.

[74] F. Chen, B. Zhao, M. Sun, C. Liu, Y. Shi, Y. Yu, B. Zhang, *Nano Res.* **2022**, *15*, 10134–10141.

[75] M. Wang, C.-L. Dong, Y.-C. Huang, S. Shen, *J. Catal.* **2019**, *371*, 262–269.

[76] J. Ryu, N. Jung, J. H. Jang, H.-J. Kim, S. J. Yoo, *ACS Catal.* **2015**, *5*, 4066–4074.

[77] L. A. King, M. A. Hubert, C. Capuano, J. Manco, N. Danilovic, E. Valle, T. R. Hellstern, K. Ayers, T. F. Jaramillo, *Nat. Nanotechnol.* **2019**, *14*, 1071–1074.

[78] Y.-F. Xu, P. N. Duchesne, L. Wang, A. Tavasoli, F. M. Ali, M. Xia, J.-F. Liao, D.-B. Kuang, G. A. Ozin, *Nat. Commun.* **2020**, *11*, 5149.

[79] J. Xing, H. Li, M. Ming-Cheng Cheng, S. M. Geyer, K. Y. S. Ng, *J. Mater. Chem. A* **2016**, *4*, 13866–13873.

[80] J. A. Aliaga, J. F. Araya, H. Lozano, E. Benavente, G. Alonso-Nuñez, G. González, *Mater. Chem. Phys.* **2015**, *151*, 372–377.

[81] D. R. Cummins, H. B. Russell, J. B. Jasinski, M. Menon, M. K. Sunkara, *Nano Lett.* **2013**, *13*, 2423–2430.

[82] C. Levard, B. C. Reinsch, F. M. Michel, C. Oumahi, G. V. Lowry, G. E. Brown, *Environ. Sci. Technol.* **2011**, *45*, 5260–5266.

[83] Z. Yang, L. Li, Y. Wang, J. Liu, X. Feng, X. Lu, *Chinese J. Catal.* **2012**, *33*, 508–517.

[84] M. F. Delley, Z. Wu, M. E. Mundy, D. Ung, B. M. Cossairt, H. Wang, J. M. Mayer, *J. Am. Chem. Soc.* **2019**, *141*, 15390–15402.

[85] J. Ann Aitken, V. Ganzha-Hazen, S. L. Brock, *J. Solid State Chem.* **2005**, *178*, 970–975.

[86] Y. Hu, B. Li, C. Yu, H. Fang, Z. Li, *Mater. Today* **2023**, *63*, 288–312.

[87] I. Sádaba, M. López Granados, A. Riisager, E. Taarning, *Green Chem.* **2015**, *17*, 4133–4145.

[88] T. Okuhara, *Chem. Rev.* **2002**, *102*, 3641–3666.

[89] B. Urbán, M. Papp, R. Skoda-Földes, *Curr. Green Chem.* **2019**, *6*, 78–95.

[90] Y. Zhang, P. Cao, H.-Y. Zhang, G. Yin, J. Zhao, *Catal. Commun.* **2019**, *129*, 105747.

[91] J. Zhao, Y. He, F. Wang, Y. Yang, W. Zheng, C. Huo, H. Jiao, Y. Yang, Y. Li, X. Wen, *J. Catal.* **2021**, *404*, 244–249.

[92] I. Agirrezabal-Telleria, J. Requies, M. B. Güemez, P. L. Arias, *Appl. Catal. B Environ.* **2014**, *145*, 34–42.

[93] J. Zhao, Y. He, F. Wang, W. Zheng, C. Huo, X. Liu, H. Jiao, Y. Yang, Y. Li, X. Wen, *ACS Catal.* **2020**, *10*, 914–920.

[94] S. Nandi, P. Patel, N. H. Khan, A. V. Biradar, R. I. Kureshy, *Inorg. Chem. Front.* **2018**, *5*, 806–813.

[95] C. Galdeano-Ruano, S. Gutiérrez-Tarriño, C. W. Lopes, J. Mazarío, L. E. Chinchilla, G. Agostini, J. J. Calvino, J. P. Holgado, E. Rodríguez-Castellón, A. Roldan, P. Oña-Burgos, *J. Catal.* **2024**, *431*, 115374.

[96] J. Han, J. Duan, P. Chen, H. Lou, X. Zheng, H. Hong, *Green Chem.* **2011**, *13*, 2561.

[97] H. Neumann, A. Brennführer, P. Groß, T. Riermeier, J. Almena, M. Beller, *Adv. Synth. Catal.* **2006**, *348*, 1255–1261.

[98] B. Liu, P. Hu, F. Xu, L. Cheng, M. Tan, W. Han, *Commun. Chem.* **2019**, *2*, 5.

[99] F. Hebrard, P. Kalck, *Chem. Rev.* **2009**, *109*, 4272–4282.

[100] R. A. Fernandes, A. K. Jha, P. Kumar, *Catal. Sci. Technol.* **2020**, *10*, 7448–7470.

[101] N. G. Schmidt, E. Eger, W. Kroutil, *ACS Catal.* **2016**, *6*, 4286–4311.

[102] M. Beller, B. Cornils, C. D. Frohning, C. W. Kohlpaintner, *J. Mol. Catal. A Chem.* **1995**, *104*, 17–85.

[103] A. Vavasori, L. Calgaro, G. Quartarone, L. Ronchin, C. Tortato, *Pure Appl. Chem.* **2016**, *88*, 445–455.

[104] A. Siva Prasad, B. Satyanarayana, *J. Mol. Catal. A Chem.* **2013**, *370*, 205–209.

[105] F. Maurer, J. Jelic, J. Wang, A. Gänzler, P. Dolcet, C. Wöll, Y. Wang, F. Studt, M. Casapu, J.-D. Grunwaldt, *Nat. Catal.* **2020**, *3*, 824–833.

[106] G. J. Hutchings, *Faraday Discuss.* **2021**, *229*, 9–34.

[107] M. L. Schulte, V. Truttmann, D. E. Doronkin, L. Baumgarten, A. Nicolai, D. A. Montalvo Beltran, F. J. Summ, C. Kiener, L. Warmuth, S. Pitter, E. Saraçi, J. Grunwaldt, *Angew. Chemie* **2025**, *137*, e202423281.

[108] J. Imbao, J. A. van Bokhoven, A. Clark, M. Nachtegaal, *Nat. Commun.* **2020**, *11*, 1118.

[109] P. A. Runeberg, P. C. Eklund, *Org. Lett.* **2019**, *21*, 8145–8148.

[110] S. Keshipour, S. Nadervand, *RSC Adv.* **2015**, *5*, 47617–47620.

[111] J. Albarrán-Velo, V. Gotor-Fernández, I. Lavandera, *Adv. Synth. Catal.* **2021**, *363*, 4096–4108.

[112] T. Brunzel, J. Heppekausen, J. Panten, A. Köckritz, *RSC Adv.* **2019**, *9*, 27865–27873.

[113] K. E. Kim, J. Li, R. H. Grubbs, B. M. Stoltz, *J. Am. Chem. Soc.* **2016**, *138*, 13179–13182.

[114] B. W. Michel, A. M. Camelio, C. N. Cornell, M. S. Sigman, *J. Am. Chem. Soc.* **2009**, *131*, 6076–6077.

[115] D. A. Chaudhari, R. A. Fernandes, *J. Org. Chem.* **2016**, *81*, 2113–2121.

[116] X.-Y. Zhou, X. Chen, L.-G. Wang, *Synlett* **2016**, *27*, 2742–2746.

[117] K. Pandey, K. Rangan, A. Kumar, *J. Org. Chem.* **2018**, *83*, 8026–8035.

[118] Z. Zhang, Y. Kumamoto, T. Hashiguchi, T. Mamba, H. Murayama, E. Yamamoto, T. Ishida, T. Honma, M. Tokunaga, *ChemSusChem* **2017**, *10*, 3482–3489.

[119] P. H. Espeel, G. De Peuter, M. C. Tielen, P. A. Jacobs, *J. Phys. Chem.* **1994**, *98*, 11588–11596.

[120] A. Evnin, *J. Catal.* **1973**, *30*, 109–117.

[121] S. Donck, E. Gravel, N. Shah, D. V. Jawale, E. Doris, I. N. N. Namboothiri, *ChemCatChem* **2015**, *7*, 2318–2322.

[122] R. S. Phatake, C. V. Ramana, *Tetrahedron Lett.* **2015**, *56*, 3868–3871.

[123] V. Bethi, R. A. Fernandes, *J. Org. Chem.* **2016**, *81*, 8577–8584.

[124] M. G. Kulkarni, Y. B. Shaikh, A. S. Borhade, S. W. Chavhan, A. P. Dhondge, D. D. Gaikwad, M. P. Desai, D. R. Birhade, N. R. Dhatrak, *Tetrahedron Lett.* **2013**, *54*, 2293–2295.

[125] A. Vasseur, J. Muzart, J. Le Bras, *European J. Org. Chem.* **2015**, *2015*, 4053–4069.

[126] M. Vafaeenezadeh, R. Saynisch, A. Lösch, W. Kleist, W. R. Thiel, *Molecules* **2021**, *26*, 26216450.

[127] P. H. Espeel, M. C. Tielen, P. A. Jacobs, *J. Chem. Soc., Chem. Commun.* **1991**, 669–671.

[128] C. R. Reilly, J. J. Lerou, *Catal. Today* **1998**, *41*, 433–441.

[129] T. V. Baiju, E. Gravel, E. Doris, I. N. N. Namboothiri, *Tetrahedron Lett.* **2016**, *57*, 3993–4000.

[130] A. Koranne, S. Turakhia, V. K. Jha, S. Gupta, R. Ravi, A. Mishra, A. K. Aggarwal, C. K. Jha, N. Dheer, A. K. Jha, *RSC Adv.* **2023**, *13*, 22512–22528.

[131] K. W. Wellington, S. A. Benner, *Nucleosides, Nucleotides and Nucleic Acids* **2006**, *25*, 1309–1333.

[132] A. Biffis, M. Zecca, M. Basato, *J. Mol. Catal. A Chem.* **2001**, *173*, 249–274.

[133] A. Kumar, G. Kumar Rao, A. K. Singh, *RSC Adv.* **2012**, *2*, 12552–12574.

[134] S. Jagtap, *Catalysts* **2017**, *7*, 267.

[135] P. J. Anju, M. Neetha, G. Anilkumar, *ChemistrySelect* **2022**, *7*, e202103564.

[136] R. F. Heck, *Acc. Chem. Res.* **1979**, *12*, 146–151.

[137] K. U. Rao, J. Lakshmidhi, R. M. Appa, S. S. Prasad, M. Narasimhulu, R. Vijitha, K. S. V. K. Rao, K. Venkateswarlu, *ChemistrySelect* **2017**, *2*, 7394–7398.

[138] B. M. Bhanage, S. Fujita, M. Arai, *J. Organomet. Chem.* **2003**, *687*, 211–218.

[139] S. J. Sabounchei, M. Ahmadi, *Inorganica Chim. Acta* **2013**, *405*, 15–23.

[140] S. Yaşar, E. Ö. Özcan, N. Gürbüz, B. Çetinkaya, İ. Özdemir, *Molecules* **2010**, *15*, 649–659.

[141] A. F. Littke, G. C. Fu, *J. Org. Chem.* **1999**, *64*, 10–11.

[142] A. Hallberg, L. Westfelt, *J. Chem. Soc. Perkin Trans. 1* **1984**, 933.

[143] M. Beller, K. Kühlein, *Synlett* **1995**, *1995*, 441–442.

[144] M. Wagner, K. Köhler, L. Djakovitch, S. Weinkauf, V. Hagen, M. Muhler, *Top. Catal.* **2000**, *13*, 319–326.

[145] H. Fan, Z. Qi, D. Sui, F. Mao, R. Chen, J. Huang, *Chinese J. Catal.* **2017**, *38*, 589–596.

[146] B. Tamami, F. N. Dodeji, *J. Iran. Chem. Soc.* **2012**, *9*, 841–850.

[147] C.-A. Wang, Y.-W. Li, X.-M. Hou, Y.-F. Han, K. Nie, J.-P. Zhang, *ChemistrySelect*

2016, 1, 1371–1376.

- [148] X. Liu, X. Zhao, M. Lu, *J. Organomet. Chem.* **2014**, 768, 23–27.
- [149] P. R. Sruthi, V. Sarika, A. Suku, A. Krishnan, S. Anas, *Inorganica Chim. Acta* **2020**, 502, 119305.
- [150] B. Altava, M. I. Burguete, E. García-Verdugo, N. Karbass, S. V. Luis, A. Puzary, V. Sans, *Tetrahedron Lett.* **2006**, 47, 2311–2314.
- [151] S. Zhao, *J. Mol. Catal. A Chem.* **2004**, 211, 139–142.
- [152] R. Chanthateyanonth, H. Alper, *J. Mol. Catal. A Chem.* **2003**, 201, 23–31.
- [153] C. González-Arellano, A. Corma, M. Iglesias, F. Sánchez, *Adv. Synth. Catal.* **2004**, 346, 1758–1764.
- [154] P. Vinod Kumar, S. Mohana Roopan, G. Madhumitha, *Monatshefte für Chemie* **2024**, 155, 1–15.
- [155] I. Bucsi, Á. Mastalir, Á. Molnár, K. L. Juhász, A. Kunfi, *Struct. Chem.* **2017**, 28, 501–509.
- [156] V. Polshettiwar, C. Len, A. Fihri, *Coord. Chem. Rev.* **2009**, 253, 2599–2626.
- [157] C. Gnad, A. Abram, A. Urstöger, F. Weigl, M. Schuster, K. Köhler, *ACS Catal.* **2020**, 10, 6030–6041.
- [158] D. B. Eremin, V. P. Ananikov, *Coord. Chem. Rev.* **2017**, 346, 2–19.
- [159] J. Richardson, C. Jones, *J. Catal.* **2007**, 251, 80–93.
- [160] R. Sang, Y. Hu, R. Razzaq, R. Jackstell, R. Franke, M. Beller, *Org. Chem. Front.* **2021**, 8, 799–811.
- [161] M. Beller, W. Mägerlein, A. F. Indolese, C. Fischer, *Synthesis (Stuttg.)* **2004**, 2001, 1584–1584.
- [162] P. E. Garrou, R. F. Heck, *J. Am. Chem. Soc.* **1975**, 4115, 4115–4127.
- [163] E. Mizushima, T. Hayashi, M. Tanaka, *Green Chem.* **2001**, 3, 76–79.
- [164] T. Xu, H. Alper, *J. Am. Chem. Soc.* **2014**, 136, 16970–16973.
- [165] J. R. Martinelli, D. A. Watson, D. M. M. Freckmann, T. E. Barder, S. L. Buchwald, *J. Org. Chem.* **2008**, 73, 7102–7107.
- [166] C. F. J. Barnard, *Org. Process Res. Dev.* **2008**, 12, 566–574.

[167] B. Apanda, S. Zolezzi, G. Valdebenito, J. Cáceres-vásquez, S. A. Moya, P. Aguirre, *J. Chil. Chem. Soc.* **2013**, *58*, 2136–2137.

[168] W. Mägerlein, M. Beller, A. F. Indolese, *J. Mol. Catal. A Chem.* **2000**, *156*, 213–221.

[169] V. Dufaud, J. Thivolle-Cazat, J.-M. Basset, *J. Chem. Soc. Chem. Commun.* **1990**, 426.

[170] J. Liu, J. Chen, C. Xia, *J. Catal.* **2008**, *253*, 50–56.

[171] F. Chen, T. Li, X. Pan, Y. Guo, B. Han, F. Liu, B. Qiao, A. Wang, T. Zhang, *Sci. China Mater.* **2020**, *63*, 959–964.

[172] Q. Hu, L. Wang, C. Wang, Y. Wu, Z. Ding, R. Yuan, *RSC Adv.* **2017**, *7*, 37200–37207.

[173] I. Ziccarelli, H. Neumann, C. Kreyenschulte, B. Gabriele, M. Beller, *Chem. Commun.* **2016**, *52*, 12729–12732.

[174] S. Antebi, P. Arya, L. E. Manzer, H. Alper, *J. Org. Chem.* **2002**, *67*, 6623–6631.

[175] H. Mei, S. Xiao, T. Zhu, Y. Lei, G. Li, *Transit. Met. Chem.* **2014**, *39*, 443–450.

[176] V. V. Gaikwad, V. B. Saptal, K. Harada, T. Sasaki, D. Nishio-Hamane, B. M. Bhanage, *ChemNanoMat* **2018**, *4*, 575–582.

[177] M. B. Ibrahim, R. Suleiman, M. Fettouhi, B. El Ali, *RSC Adv.* **2016**, *6*, 78826–78837.

[178] M. V. Khedkar, T. Sasaki, B. M. Bhanage, *ACS Catal.* **2013**, *3*, 287–293.

[179] C. F. J. Barnard, *Organometallics* **2008**, *27*, 5402–5422.

[180] B. Zhang, D. Peña Fuentes, A. Börner, *ChemTexts* **2022**, *8*, 2.

[181] R. Franke, D. Selent, A. Börner, *Chem. Rev.* **2012**, *112*, 5675–5732.

[182] S. K. Pedersen, H. G. Gudmundsson, D. U. Nielsen, B. S. Donslund, H. C. D. Hammershøj, K. Daasbjerg, T. Skrydstrup, *Nat. Catal.* **2020**, *3*, 843–850.

[183] Y. Liu, Z. Liu, Y. Hui, L. Wang, J. Zhang, X. Yi, W. Chen, C. Wang, H. Wang, Y. Qin, L. Song, A. Zheng, F.-S. Xiao, *Nat. Commun.* **2023**, *14*, 2531.

[184] B. Liu, Y. Wang, N. Huang, X. Lan, Z. Xie, J. G. Chen, T. Wang, *Chem* **2022**, *8*, 2630–2658.

[185] Y. Liu, J. Zhao, Y. Zhao, H.-M. Liu, H. Fu, X. Zheng, M. Yuan, R. Li, H. Chen, *RSC Adv.* **2019**, *9*, 7382–7387.

[186] J. Amsler, B. B. Sarma, G. Agostini, G. Prieto, P. N. Plessow, F. Studt, *J. Am. Chem. Soc.* **2020**, *142*, 5087–5096.

[187] P. Samanta, A. Solé-Daura, R. Rajapaksha, F. M. Wisser, F. Meunier, Y. Schuurman, C. Sassoye, C. Mellot-Draznieks, J. Canivet, *ACS Catal.* **2023**, *13*, 4193–4204.

[188] M. Schörner, P. Rothgängel, K. Mitländer, D. Wisser, M. Thommes, M. Haumann, *ChemCatChem* **2021**, *13*, 4192–4200.

[189] R. Lang, T. Li, D. Matsumura, S. Miao, Y. Ren, Y. Cui, Y. Tan, B. Qiao, L. Li, A. Wang, X. Wang, T. Zhang, *Angew. Chem. Int. Ed.* **2016**, *55*, 16054–16058.

[190] W. Shang, B. Qin, M. Gao, X. Qin, Y. Chai, G. Wu, N. Guan, D. Ma, L. Li, *CCS Chem.* **2023**, *5*, 1526–1539.

[191] M. Chen, G. Gupta, C. W. Ordonez, A. R. Lamkins, C. J. Ward, C. A. Abolafia, B. Zhang, L. T. Roling, W. Huang, *J. Am. Chem. Soc.* **2021**, *143*, 20907–20915.

[192] Z. Mao, H. Guo, Z. Xie, P. Liu, J. G. Chen, *Catal. Sci. Technol.* **2022**, 4988–4992.

[193] J. A. Varela, S. A. Vázquez, E. Martínez-Núñez, *Chem. Sci.* **2017**, *8*, 3843–3851.

[194] X. Xia, X. Gao, J. Xu, C. Hu, X. Peng, *Synlett* **2017**, *28*, 607–610.

[195] M. G. Kulkarni, S. M. Bagale, M. P. Shinde, D. D. Gaikwad, A. S. Borhade, A. P. Dhondge, S. W. Chavhan, Y. B. Shaikh, V. B. Ningdale, M. P. Desai, D. R. Birhade, *Tetrahedron Lett.* **2009**, *50*, 2893–2894.

[196] P. S. Shinde, P. S. Suryawanshi, K. K. Patil, V. M. Belekar, S. A. Sankpal, S. D. Delekar, S. A. Jadhav, *J. Compos. Sci.* **2021**, *5*, 75.

[197] Z. Wu, T. Pan, Y. Chai, S. Ge, Y. Ju, T. Li, K. Liu, L. Lan, A. C. K. Yip, M. Zhang, *J. Catal.* **2018**, *366*, 80–90.

[198] A. P. Ortiz, J. Romero, E, *J. Phys. Conf. Ser.* **2017**, *935*, 12050.

[199] A. Neyyathala, F. Flecken, S. Hanf, *Chempluschem* **2023**, *88*, e2022004.

[200] M. C. Militello, S. J. Simko, *Surf. Sci. Spectra* **1994**, *3*, 387–394.

[201] T. Bell, H. Fleisch, *J. Catal.* **1984**, *413*, 398–413.

[202] Y. Liu, A. J. McCue, C. Miao, J. Feng, D. Li, J. A. Anderson, *J. Catal.* **2018**, *364*, 406–414.

[203] M. A. Andrade, L. M. D. R. S. Martins, *Molecules* **2021**, *26*, 1680.

[204] L. Nie, K. K. Xin, W. S. Li, X. P. Zhou, *Catal. Commun.* **2007**, *8*, 488–492.

[205] X. Xia, X. Gao, J. Xu, C. Hu, X. Peng, *J. Saudi Chem. Soc.* **2017**, *21*, 334–340.

[206] A. W. Stobbe-Kreemers, M. Makkee, J. J. F. Scholten, *Appl. Catal. A: Gen.* **1997**, *156*, 219–238.

[207] M. S. Batra, R. Dwivedi, R. Prasad, *ChemistrySelect* **2019**, *4*, 11636–11673.

[208] Y. Ma, Y. Li, F. Wang, *Corros. Sci.* **2009**, *51*, 997–1006.

[209] S. Byun, J. Chung, Y. Jang, J. Kwon, T. Hyeon, B. M. Kim, *RSC Adv.* **2013**, *3*, 16296–16299.

[210] U. Jadhav, C. Su, M. Chakankar, H. Hocheng, *Bioresour. Bioprocess.* **2017**, *4*, 42.

[211] S. Rundqvist, L.-O. Gullman, A. Kjekshus, R. Söderquist, *Acta Chem. Scand.* **1960**, *14*, 2246–2247.

[212] S. Jain, Y. Ji, R. J. Davis, *J. Phys. Chem. B* **2005**, *109*, 17232–17238.

[213] A. Ellert, F. Ding, A. Hutzler, F. Herold, L. Piccirilli, M. Rønning, T. V. W. Janssens, D. Wisser, P. Schühle, *Appl. Catal. A: Gen.* **2025**, *696*, 120199.

[214] J. Dong, J. Wang, J. Wang, M. Yang, W. Li, M. Shen, *Catal. Sci. Technol.* **2017**, *7*, 5038–5048.

[215] J.-H. Park, S. Yeo, T.-J. Kang, I. Heo, K.-Y. Lee, T.-S. Chang, *Fuel* **2018**, *212*, 77–87.

[216] Y. Wen, B. Wang, C. Huang, L. Wang, D. Hulicova-Jurcakova, *Chem. Eur. J.* **2015**, *21*, 80–85.

[217] C. Zhang, N. Mahmood, H. Yin, F. Liu, Y. Hou, *Adv. Mater.* **2013**, *25*, 4932–4937.

[218] J. C. Roy, M. Al-Mamun, H. Yin, Y. Dou, L. Zhang, P. Liu, Y. Wang, Y. L. Zhong, H. Zhao, *Chempluschem* **2020**, *85*, 1602–1611.

[219] R. Huang, C. H. Liang, D. S. Su, B. Zong, J. Rong, *Catal. Today* **2015**, *249*, 161–166.

[220] A. Abdel-Kader, A. A. Ammar, S. I. Saleh, *Thermochim. Acta* **1991**, *176*, 293–304.

[221] Y. Maki, K. Sato, A. Isobe, N. Iwasa, S. Fujita, M. Shimokawabe, N. Takezawa, *Appl. Catal. A: Gen.* **1998**, *170*, 269–275.

[222] V. Bokade, H. Moondra, P. Niphadkar, *SN Appl. Sci.* **2020**, *2*, 51.

[223] A. Neyyathala, F. Flecken, F. Rang, C. Papke, S. Hanf, *Chem. Eur. J.* **2024**, *30*, e202302825.

[224] A. Nuri, N. Vucetic, J.-H. Smått, Y. Mansoori, J.-P. Mikkola, D. Y. Murzin, *Catal. Letters* **2019**, *149*, 1941–1951.

[225] S. P. Bhatia, G. A. Wellington, J. Cocchiara, J. Lalko, C. S. Letizia, A. M. Api, *Food Chem. Toxicol.* **2007**, *45*, S113–S119.

[226] R. G. Heidenreich, J. G. E. Krauter, J. Pietsch, K. Köhler, *J. Mol. Catal. A Chem.* **2002**, *182–183*, 499–509.

[227] A. Biffis, M. Zecca, M. Basato, *Eur. J. Inorg. Chem.* **2001**, *2001*, 1131–1133.

[228] Á. Molnár, *Chem. Rev.* **2011**, *111*, 2251–2320.

[229] J.-D. Grunwaldt, M. Caravati, S. Hannemann, A. Baiker, *Phys. Chem. Chem. Phys.* **2004**, *6*, 3037.

[230] F. Zaera, *J. Catal.* **2021**, *404*, 900–910.

[231] A. Ellert, F. Herold, M. Rønning, A. Hutzler, L. Piccirilli, T. V. W. Janssens, P. N. R. Vennestrøm, P. Wasserscheid, P. Schühle, *J. Catal.* **2024**, *436*, 115607.

[232] Y. Ma, B. Chi, W. Liu, L. Cao, Y. Lin, X. Zhang, X. Ye, S. Wei, J. Lu, *ACS Catal.* **2019**, *9*, 8404–8412.

[233] J. M. Tukacs, B. Marton, E. Albert, I. Tóth, L. T. Mika, *J. Organomet. Chem.* **2020**, *923*, 121407.

[234] A. Brennführer, H. Neumann, M. Beller, *Angew. Chem. Int. Ed.* **2009**, *48*, 4114–4133.

[235] A. Neyyathala, F. Jung, C. Feldmann, S. A. Schunk, S. Hanf, **2025**, DOI 10.26434/chemrxiv-2025-46zsr.

[236] S. Carenco, Y. Hu, I. Florea, O. Ersen, C. Boissière, N. Mézailles, C. Sanchez, *Chem. Mater.* **2012**, *24*, 4134–4145.

[237] T. Ito, K. Mori, T. Mizoroki, A. Ozaki, *Bull. Chem. Soc. Jpn.* **1975**, *48*, 2091–2094.

[238] R. A. Morrison, K. A. Krieger, *J. Catal.* **1968**, *12*, 25–34.

[239] R. S. Mane, T. Sasaki, B. M. Bhanage, *RSC Adv.* **2015**, *5*, 94776–94785.

[240] S. M. Islam, K. Ghosh, A. S. Roy, R. A. Molla, *RSC Adv.* **2014**, *4*, 38986–38999.

[241] P. Mäki-Arvela, D. Y. Murzin, *Appl. Catal. A: Gen.* **2013**, *451*, 251–281.

[242] M. Che, C. O. Bennett, in *Adv. Catal.*, **1989**, pp. 55–172.

[243] P. Munnik, P. E. De Jongh, K. P. De Jong, *Chem. Rev.* **2015**, *115*, 6687–6718.

[244] G. C. Bond, *Surf. Sci.* **1985**, *156*, 966–981.

[245] C. Ramesh, R. Nakamura, Y. Kubota, M. Miwa, Y. Sugi, *Synthesis (Stuttg.)* **2003**,

501–504.

[246] L. Chanussot, A. Das, S. Goyal, T. Lavril, M. Shuaibi, M. Riviere, K. Tran, J. Heras-Domingo, C. Ho, W. Hu, A. Palizhati, A. Sriram, B. Wood, J. Yoon, D. Parikh, C. L. Zitnick, Z. Ulissi, *ACS Catal.* **2021**, *11*, 6059–6072.

[247] L. Wang, W. Zhang, S. Wang, Z. Gao, Z. Luo, X. Wang, R. Zeng, A. Li, H. Li, M. Wang, X. Zheng, J. Zhu, W. Zhang, C. Ma, R. Si, J. Zeng, *Nat. Commun.* **2016**, *7*, 14036.

[248] P. Gao, G. Liang, T. Ru, X. Liu, H. Qi, A. Wang, F.-E. Chen, *Nat. Commun.* **2021**, *12*, 4698.

[249] M. Zhao, C. Li, D. Gómez, F. Gonell, V. M. Diaconescu, L. Simonelli, M. L. Haro, J. J. Calvino, D. M. Meira, P. Concepción, A. Corma, *Nat. Commun.* **2023**, *14*, 7174.

[250] X. Zhang, T. Yan, H. Hou, J. Yin, H. Wan, X. Sun, Q. Zhang, F. Sun, Y. Wei, M. Dong, W. Fan, J. Wang, Y. Sun, X. Zhou, K. Wu, Y. Yang, Y. Li, Z. Cao, *Nature* **2024**, *629*, 597.

[251] N. Huang, B. Liu, X. Lan, T. Wang, *Ind. Eng. Chem. Res.* **2020**, *59*, 18771–18780.

[252] L. Jia, X. Tan, T. Yu, J. Ye, *Energy & Fuels* **2022**, *36*, 11308–11322.

[253] A. Calafat, J. Laine, *Catal. Letters* **1994**, *28*, 69–77.

[254] S. P. Ong, L. Wang, B. Kang, G. Ceder, *Chem. Mater.* **2008**, *20*, 1798–1807.

[255] A. Neyyathala, E. Fako, S. De, D. Gashnikova, F. Maurer, J. Grunwaldt, S. A. Schunk, S. Hanf, *Small Struct.* **2025**, *6*, 2400260.

[256] Z. D. Wang, M. Yoshida, B. George, *Comput. Theor. Chem.* **2013**, *1017*, 91–98.

[257] P. Yin, S. Hu, K. Qian, Z. Wei, L.-L. Zhang, Y. Lin, W. Huang, H. Xiong, W.-X. Li, H.-W. Liang, *Nat. Commun.* **2021**, *12*, 4865.

[258] T. W. Hansen, A. T. DeLaRiva, S. R. Challa, A. K. Datye, *Acc. Chem. Res.* **2013**, *46*, 1720–1730.

[259] C.-H. Li, J. Wu, A. B. Getsoian, G. Cavataio, J. R. Jinschek, *Chem. Mater.* **2022**, *34*, 2123–2132.

[260] J. M. Ziegelbauer, V. S. Murthi, C. O'Laoire, A. F. Gullá, S. Mukerjee, *Electrochim. Acta* **2008**, *53*, 5587–5596.

[261] J. Liang, A. Levina, J. Jia, P. Kappen, C. Glover, B. Johannessen, P. A. Lay, *Inorg. Chem.* **2019**, *58*, 4880–4893.

[262] J. M. Ziegelbauer, D. Gatewood, A. F. Gullá, M. J.-F. Guinel, F. Ernst, D. E. Ramaker, S. Mukerjee, *J. Phys. Chem. C* **2009**, *113*, 6955–6968.

[263] Y. Li, N. Li, K. Yanagisawa, X. Ding, X. Li, *J. Mater. Chem. A* **2014**, *2*, 1484–1492.

[264] G. Srinivas, S. S. C. Chuang, *J. Catal.* **1993**, *144*, 131–147.

[265] J. W. Niemantsverdriet, *Spectroscopy in Catalysis: An Introduction*, 2nd, Completely Revised Edition, Wiley-VCH, Weinheim, **2000**.

[266] T. Li, F. Chen, R. Lang, H. Wang, Y. Su, B. Qiao, A. Wang, T. Zhang, *Angew. Chem. Int. Ed.* **2020**, *59*, 7430–7434.

[267] A. Bano, A. Dawood, Rida, F. Saira, A. Malik, M. Alkholief, H. Ahmad, M. A. Khan, Z. Ahmad, O. Bazighifan, *Sci. Rep.* **2023**, *13*, 12359.

[268] X. Dou, T. Yan, L. Qian, H. Hou, M. Lopez-Haro, C. Marini, G. Agostini, D. M. Meira, X. Zhang, L. Zhang, Z. Cao, L. Liu, *Nat. Catal.* **2024**, *7*, 666–677.

[269] P. E. Goudriaan, M. Kuil, X.-B. Jiang, P. W. N. M. van Leeuwen, J. N. H. Reek, *Dalt. Trans.* **2009**, 1801–1805.

[270] S. Güven, M. M. L. Nieuwenhuizen, B. Hamers, R. Franke, M. Priske, M. Becker, D. Vogt, *ChemCatChem* **2014**, *6*, 603–610.

[271] R. Lazzaroni, P. Pertici, S. Bertozzi, G. Fabrizi, *J. Mol. Catal.* **1990**, *58*, 75–85.

[272] S. Yu, Y. Chie, Z. Guan, Y. Zou, W. Li, X. Zhang, *Org. Lett.* **2009**, *11*, 241–244.

[273] F. Jameel, M. Stein, *Mol. Catal.* **2021**, *503*, 111429.

[274] *Method for Preparing Isononanal by Diisobutylene Hydroformylation*, **2021**, CN112794796A.

[275] B. Liu, Y. Wang, N. Huang, X. Lan, T. Wang, *ACS Catal.* **2021**, *11*, 9850–9859.

[276] Y. Liu, A. Dikhtiarenko, N. Xu, J. Sun, J. Tang, K. Wang, B. Xu, Q. Tong, H. J. Heeres, S. He, J. Gascon, Y. Fan, *Chem. Eur. J.* **2020**, *26*, 12134–12139.

[277] D. Han, X. Li, H. Zhang, Z. Liu, G. Hu, C. Li, *J. Mol. Catal. A Chem.* **2008**, *283*, 15–22.

[278] B. Liu, N. Huang, Y. Wang, X. Lan, T. Wang, *Chem. Eng. J.* **2022**, *441*, 136101.

[279] P. Tang, S. Paganelli, F. Carraro, M. Blanco, R. Riccò, C. Marega, D. Badocco, P. Pastore, C. J. Doonan, S. Agnoli, *ACS Appl. Mater. Interfaces* **2020**, *12*, 54798–54805.

[280] S. Alini, A. Bottino, G. Capannelli, A. Comite, S. Paganelli, *Appl. Catal. A: Gen.* **2005**,

292, 105–112.

- [281] C. Galdeano-Ruano, C. W. Lopes, D. Motta Meira, A. Corma, P. Oña-Burgos, *ACS Appl. Nano Mater.* **2021**, *4*, 10743–10753.
- [282] H. Lindlar, *Helv. Chim. Acta* **1952**, *35*, 446–450.
- [283] “GitHub - SUNCAT-Center/CatKit: General purpose tools for high-throughput catalysis,” DOI <https://github.com/SUNCAT-Center/CatKit> can be found under <https://github.com/SUNCAT-Center/CatKit>, **n.d.**
- [284] A. P. Bartók, R. Kondor, G. Csányi, *Phys. Rev. B* **2013**, *87*, 184115.
- [285] L. Himanen, M. O. J. Jäger, E. V. Morooka, F. Federici Canova, Y. S. Ranawat, D. Z. Gao, P. Rinke, A. S. Foster, *Comput. Phys. Commun.* **2020**, *247*, 106949.
- [286] L. Van Der Maaten, G. Hinton, *J. Mach. Learn. Res.* **2008**, *9*, 2579–2605.
- [287] S. De, A. P. Bartók, G. Csányi, M. Ceriotti, *Phys. Chem. Chem. Phys.* **2016**, *18*, 13754–13769.
- [288] A. P. Bartók, S. De, C. Poelking, N. Bernstein, J. R. Kermode, G. Csányi, M. Ceriotti, *Sci. Adv.* **2017**, *3*, e1701816.
- [289] S. De, F. Musil, T. Ingram, C. Baldauf, M. Ceriotti, *J. Cheminform.* **2017**, *9*, 1–14.
- [290] P. O. Dral, *Quantum Chemistry in the Age of Machine Learning*, Elsevier Inc., **2024**.
- [291] F. Musil, S. De, J. Yang, J. E. Campbell, G. M. Day, M. Ceriotti, *Chem. Sci.* **2018**, *9*, 1289–1300.
- [292] N. Singh, D. C. Upham, R. F. Liu, J. Burk, N. Economou, S. Buratto, H. Metiu, E. W. McFarland, *Langmuir* **2014**, *30*, 5662–5668.
- [293] “MATCH! Version 3, Crystal Impact GbR, Bonn,” DOI <https://www.crystalimpact.com/match>, **2020**.
- [294] FIZ Karlsruhe – Leibniz Institute for Information Infrastructure, “Inorganic Crystal Structure Database (ICSD),” DOI <https://doi.org/10.34726/209>, **2023**.
- [295] A. Zimina, K. Dardenne, M. A. Denecke, D. E. Doronkin, E. Huttel, H. Lichtenberg, S. Mangold, T. Pruessmann, J. Rothe, T. Spangenberg, R. Steininger, T. Vitova, H. Geckeis, J.-D. Grunwaldt, *Rev. Sci. Instrum.* **2017**, *88*, 113113.
- [296] B. Ravel, M. Newville, *J. Synchrotron Rad.* **2005**, *12*, 537–541.
- [297] Y. L. Liao, B. Wood, A. Das, T. Smidt, *12th Int. Conf. Learn. Represent. ICLR 2024*

[298] P. Giannozzi, O. Andreussi, T. Brumme, O. Bunau, M. Buongiorno Nardelli, M. Calandra, R. Car, C. Cavazzoni, D. Ceresoli, M. Cococcioni, N. Colonna, I. Carnimeo, A. Dal Corso, S. De Gironcoli, P. Delugas, R. A. Distasio, A. Ferretti, A. Floris, G. Fratesi, G. Fugallo, R. Gebauer, U. Gerstmann, F. Giustino, T. Gorni, J. Jia, M. Kawamura, H. Y. Ko, A. Kokalj, E. Küçükbenli, M. Lazzeri, M. Marsili, N. Marzari, F. Mauri, N. L. Nguyen, H. V. Nguyen, A. Otero-De-La-Roza, L. Paulatto, S. Poncé, D. Rocca, R. Sabatini, B. Santra, M. Schlipf, A. P. Seitsonen, A. Smogunov, I. Timrov, T. Thonhauser, P. Umari, N. Vast, X. Wu, S. Baroni, *J. Phys. Condens. Matter* **2017**, *29*, 465901.

[299] J. P. Perdew, K. Burke, M. Ernzerhof, *Phys. Rev. Lett.* **1996**, *77*, 3865–3868.

[300] P. E. Blöchl, *Phys. Rev. B* **1994**, *50*, 17953–17979.

[301] G. Kresse, D. Joubert, *Phys. Rev. B* **1999**, *59*, 1758–1775.

[302] G. Prandini, A. Marrazzo, I. E. Castelli, N. Mounet, E. Passaro, J. Yu, N. Marzari, *Mater. Cloud Arch. 2023.65* **2023**, DOI 10.24435/materialscloud:f3-ym.

[303] S. Grimme, J. Antony, S. Ehrlich, H. Krieg, *J. Chem. Phys.* **2010**, *132*, 154104.

[304] Y. Wan, F. Song, T. Ye, G. Li, D. Liu, Y. Lei, *Appl. Organomet. Chem.* **2019**, *33*, 1–10.

[305] Y. Zhang, Y. Xiong, J. Ge, R. Lin, C. Chen, Q. Peng, D. Wang, Y. Li, *Chem. Commun.* **2018**, *54*, 2796–2799.

[306] V. S. Nair, S. P. Mathew, R. V. Chaudhari, *J. Mol. Catal. A Chem.* **1999**, *143*, 99–110.

[307] S. Feng, Q. Yu, X. Ma, X. Yu, N. Yan, *Natl. Sci. Open* **2023**, *2*, 20220064.

[308] M. D. Khokhar, R. S. Shukla, R. V. Jasra, *React. Kinet. Mech. Catal.* **2015**, *114*, 265–277.

[309] T. Borrman, H. W. Roesky, U. Ritter, *J. Mol. Catal. A Chem.* **2000**, *153*, 31–48.

10 Appendix

10.1 Chapter 3: Supported palladium phosphides as oxidation catalysts

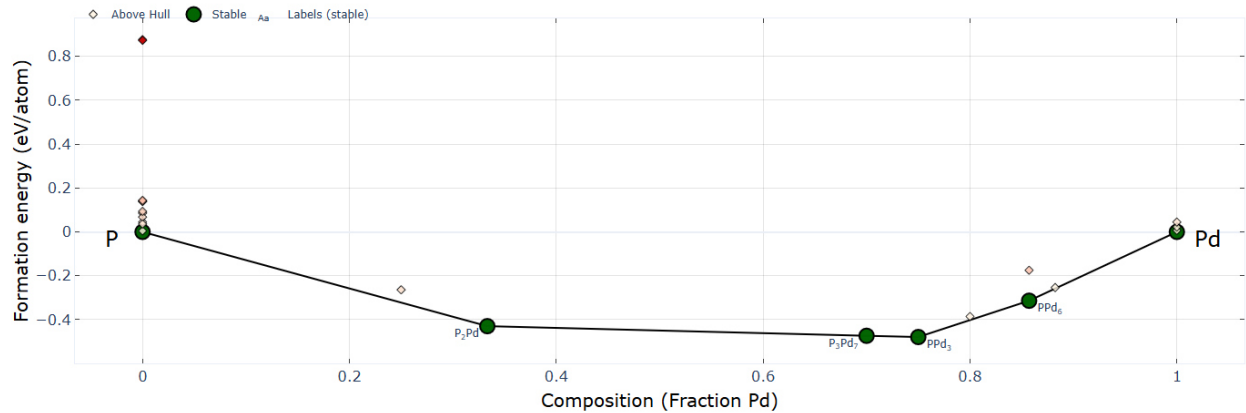


Figure S1: Calculated phase stability diagram generated using the phase diagram application of “The Materials Project”.^[33,254]

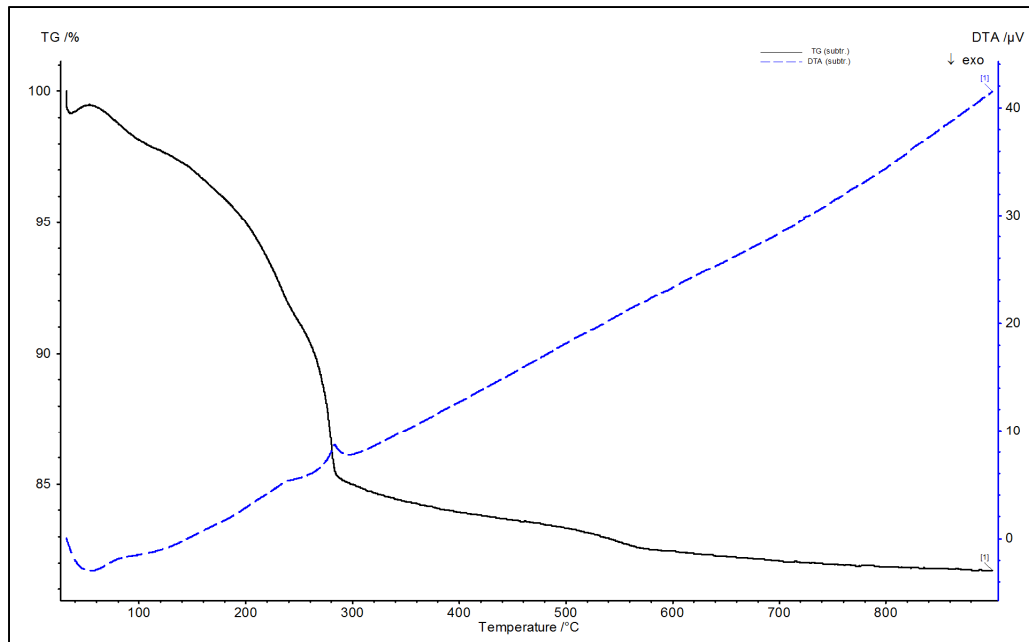


Figure S2: Result of TG-DTA analysis performed in inert atmosphere with the impregnated precursors for the Pd₃P catalyst (Pd₃P/SiO₂, 10 wt.% Pd). This figure has been adapted from reference^[199] (license CC BY-NC 4.0).

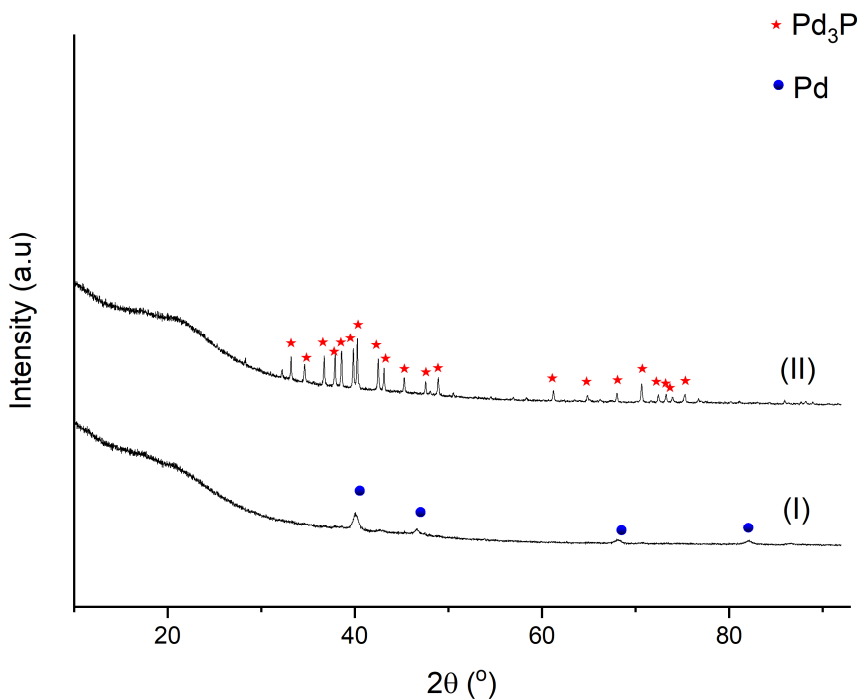


Figure S3: PXRD pattern of the catalysts synthesized and used for the Wacker-Tsui oxidation of styrene with I) Pd/SiO₂ (10 wt.% Pd) and II) Pd₃P/SiO₂ (10 wt.% Pd). Reference patterns for the phase identification - Pd₃P: ICSD 85525 and Pd: ICSD 52251. This figure has been adapted from reference^[199] (license CC BY-NC 4.0).

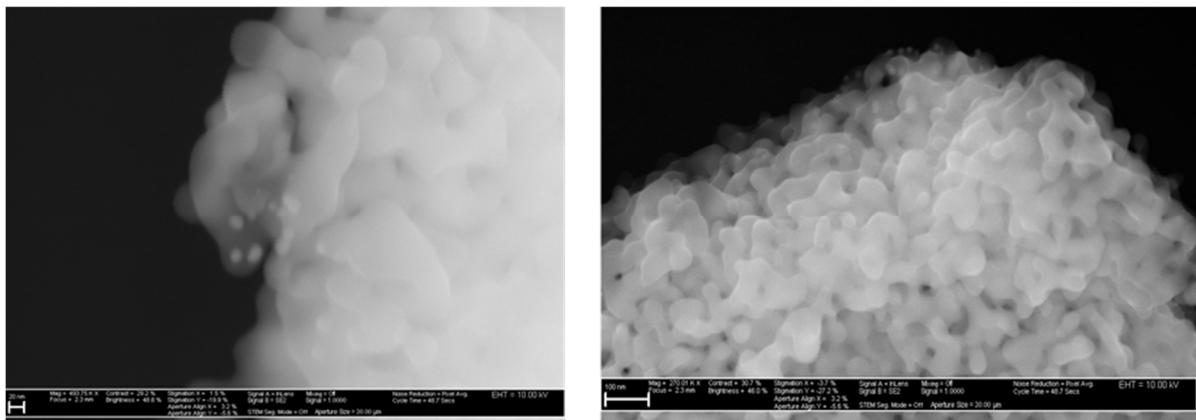


Figure S4: Example SEM images of Pd₃P/SiO₂, (10 wt.% Pd) used as catalyst for the Wacker-Tsui oxidation reaction. This figure has been adapted from reference^[199] (license CC BY-NC 4.0).

Table S1: The binding energies observed in the XPS analysis of the $\text{Pd}_3\text{P}/\text{SiO}_2$ (10 wt.% Pd) catalyst, along with the corresponding assigned species. The binding energy values were calibrated using the O 1s peak of SiO_2 at 532.6 eV. This table has been adapted from reference^[199] (license CC BY-NC 4.0).

Region	Assignment	Binding energy [eV]
O1s	PO_4	531.2
	SiO_2	532.6
	O_2 (atmospheric)	536.8
Si2p	SiO_2	102.9
		103.4
P2p	PO_4^{3-}	134.0
		134.9
Pd3d	$\text{Pd}^{\delta+}$	335.6
		340.9

10.2 Chapter 4: Support engineering for Heck coupling reactions

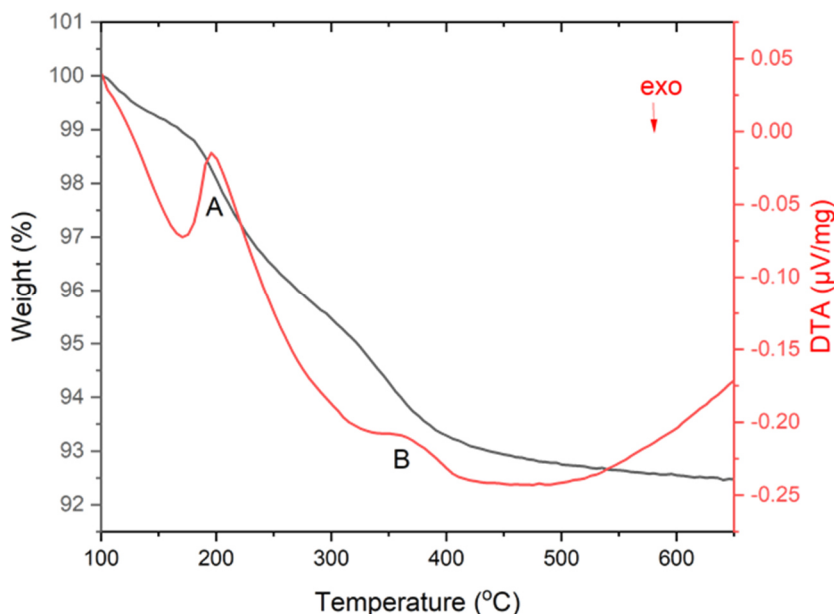


Figure S5: Result of TG-DTA analysis performed with impregnated precursor for 5P- SiO_2 showing two endothermic events. This figure has been adapted from reference^[223] (license CC BY-NC 4.0).

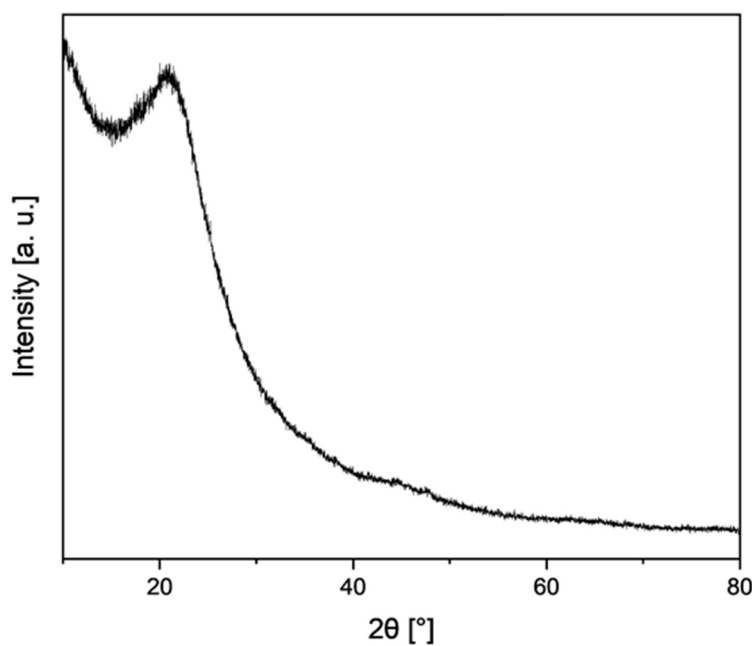


Figure S6: PXRD pattern for the 5P-SiO₂ support, indicating amorphous nature of the support. This figure has been adapted from reference^[223] (license CC BY-NC 4.0).

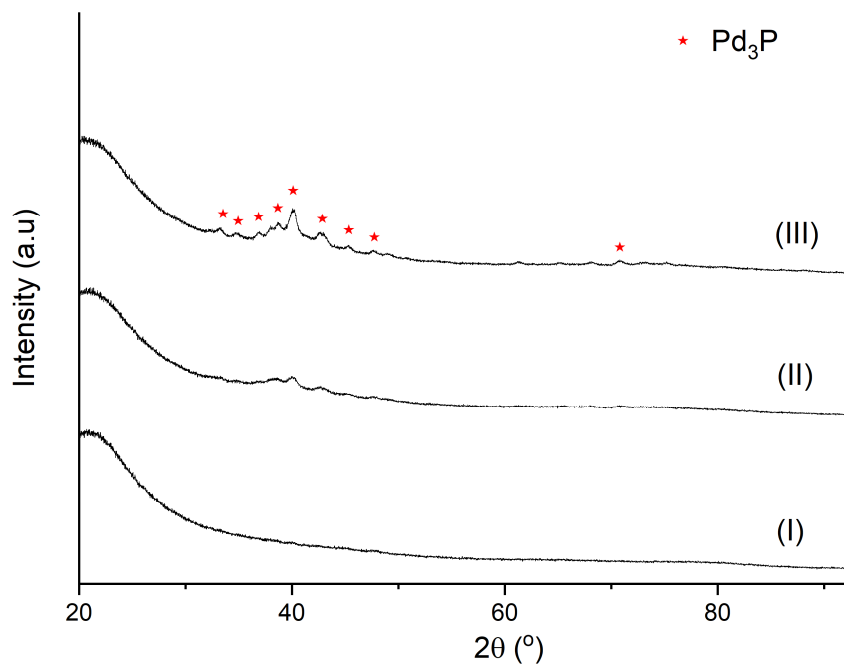


Figure S7: PXRD pattern of Pd₃P nanoparticles on 1P-SiO₂ prepared with Pd loadings of I) 1 wt.%, II) 5 wt.% and III) 10 wt.%. Reference for the phase identification - Pd₃P: ICSD 85525. This figure has been adapted from reference^[223] (license CC BY-NC 4.0).

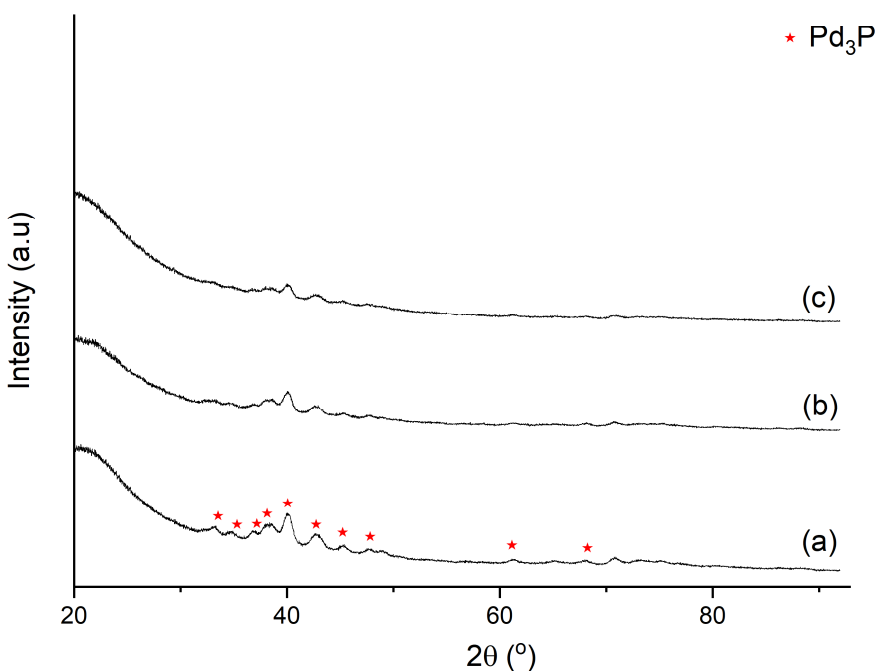


Figure S8: PXRD pattern of $\text{Pd}_3\text{P}/0.5\text{P}-\text{SiO}_2$ (10 wt.% Pd) catalyst: a) fresh, b) first recovery and c) second recovery. Reaction conditions: styrene ($0.1 \text{ mmol} \cdot \text{mL}^{-1}$), iodobenzene ($0.06 \text{ mmol} \cdot \text{mL}^{-1}$), Et_3N ($0.1 \text{ mmol} \cdot \text{mL}^{-1}$), solvent (DMSO), catalyst ($10^{-3} \text{ mmol} \cdot \text{mL}^{-1}$, Pd basis). Reactions were carried out at 140°C for 60 min. Reference for the phase identification - Pd_3P : ICSD 85525. This figure has been adapted from reference^[223] (license CC BY-NC 4.0).

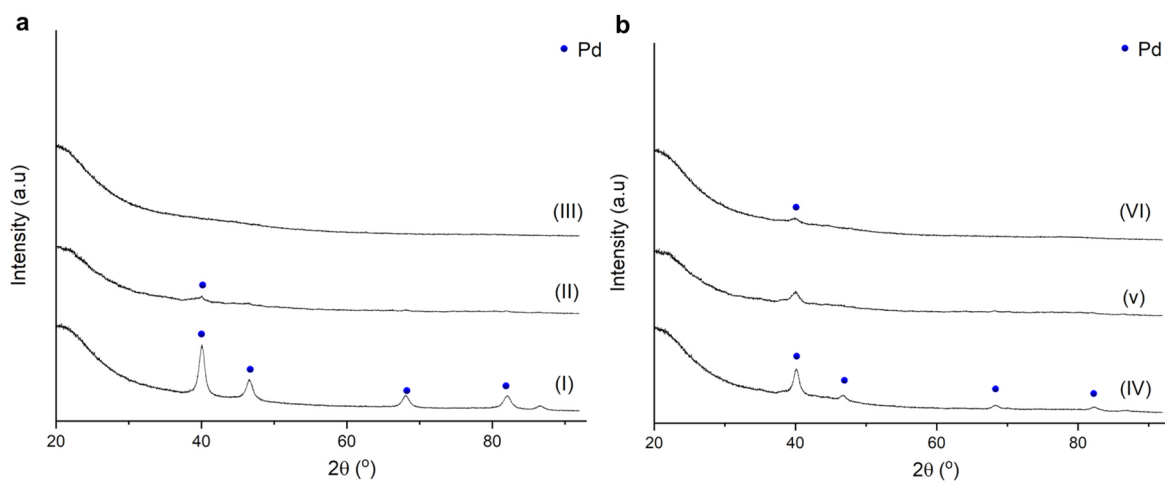


Figure S9: PXRD pattern of a) Pd/SiO_2 (10 wt.% Pd) with I) fresh, II) first recovery, III) second recovery and b) $\text{Pd}/1\text{P}-\text{SiO}_2$ (10 wt.% Pd) with IV) fresh, V) first recovery and VI) second recovery. Reaction conditions: styrene ($0.1 \text{ mmol} \cdot \text{mL}^{-1}$), iodobenzene ($0.06 \text{ mmol} \cdot \text{mL}^{-1}$), Et_3N ($0.1 \text{ mmol} \cdot \text{mL}^{-1}$), solvent (DMSO), catalyst ($10^{-3} \text{ mmol} \cdot \text{mL}^{-1}$, Pd basis). Reactions were carried out at 140°C for 60 min. Reference for the phase identification - Pd: ICSD 52251. This figure has been adapted from reference^[223] (license CC BY-NC 4.0).

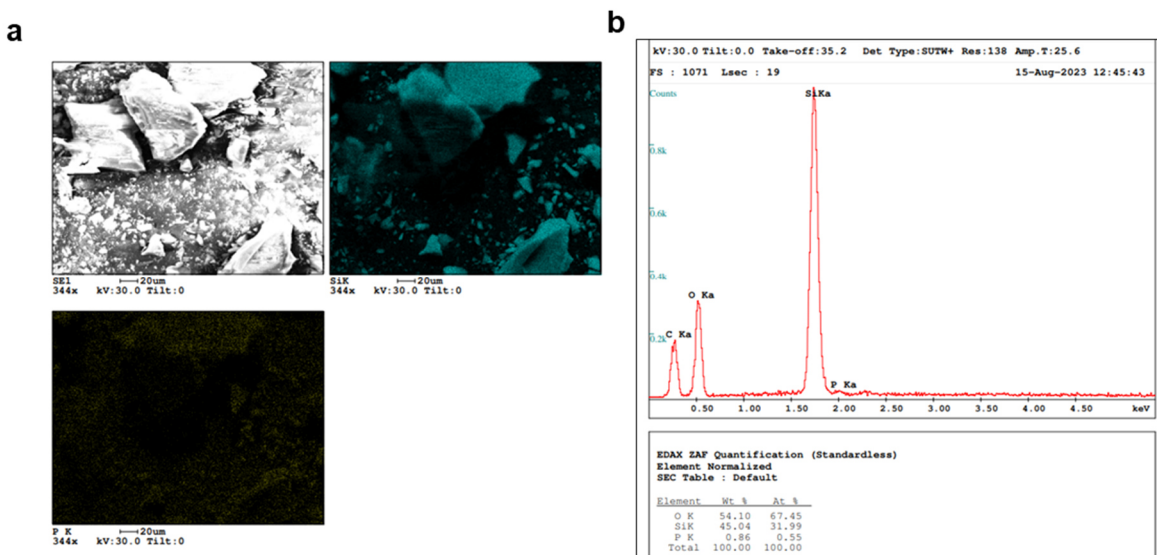


Figure S10: a) SEM image and EDX mapping of 1P-SiO₂ and b) sample EDX spectra for the elemental quantification. This figure has been adapted from reference^[223] (license CC BY-NC 4.0).

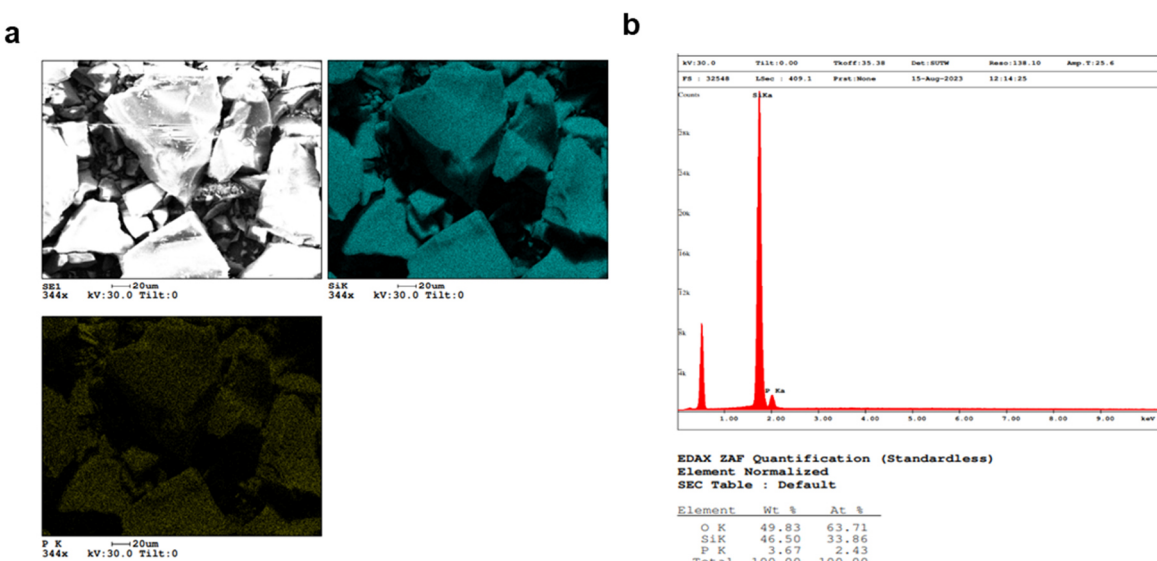


Figure S11: a) SEM image and EDX mapping of 5P-SiO₂ and b) sample EDX spectra for the elemental quantification. This figure has been adapted from reference^[223] (license CC BY-NC 4.0).

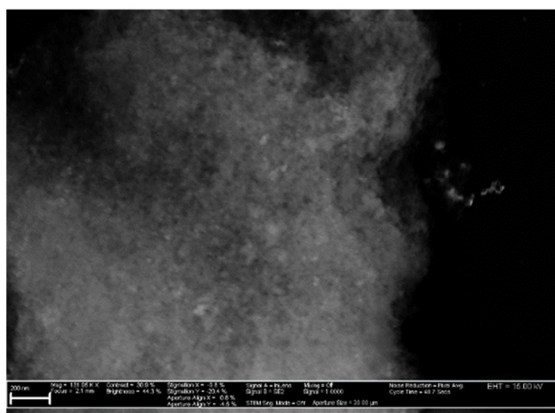
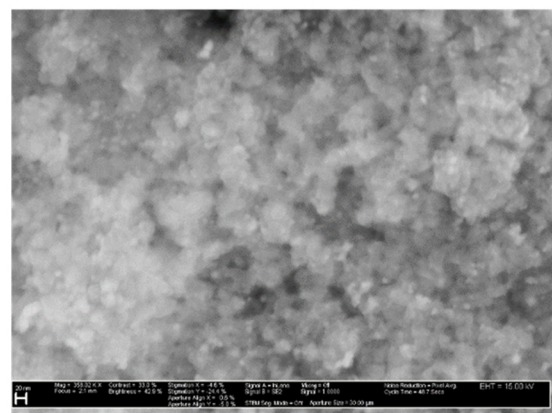
a**b**

Figure S12: SEM images of a) $\text{Pd}_3\text{P}/\text{SiO}_2$ (10 wt.% Pd) and b) Pd/SiO_2 (10 wt.% Pd). This figure has been adapted from reference [223] (license CC BY-NC 4.0).

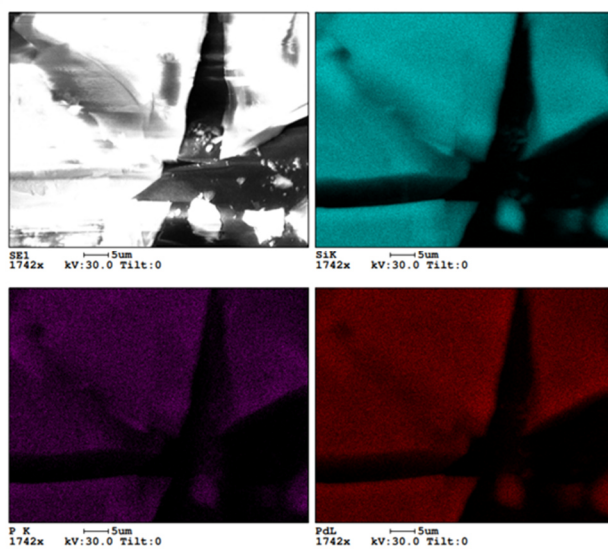
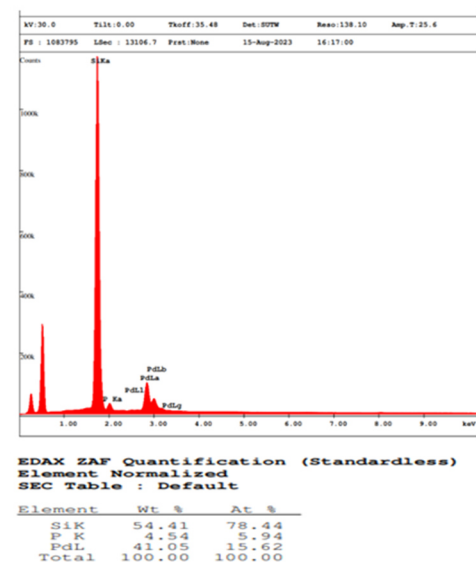
a**b**

Figure S13: a) SEM-EDX mapping of $\text{Pd}_3\text{P}/\text{SiO}_2$ (10 wt.% Pd) and b) sample EDX spectra and elemental quantification. This figure has been adapted from reference [223] (license CC BY-NC 4.0).

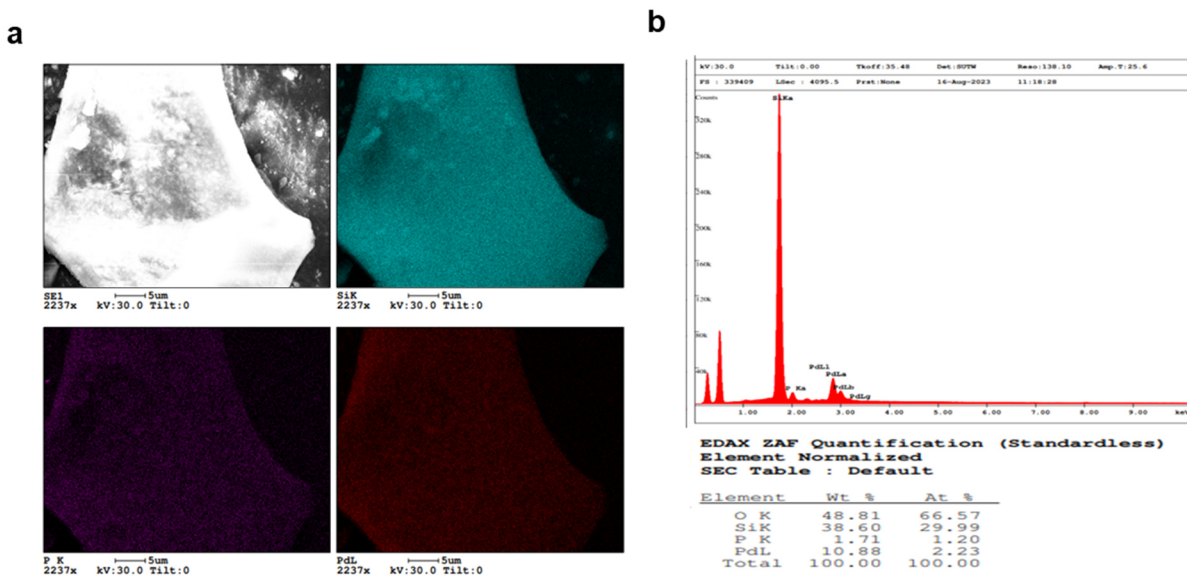


Figure S14: a) SEM-EDX mapping of $\text{Pd}_3\text{P}/1\text{P}-\text{SiO}_2$ (10 wt.% Pd), b) sample EDX spectra and elemental quantification. This figure has been adapted from reference^[223] (license CC BY-NC 4.0).

Table S2: Catalyst test results of the Heck coupling reaction of styrene and methyl-4-iodobenzoate using various catalysts. This table has been adapted from reference^[223] (license CC BY-NC 4.0).

Entry	Catalyst	Conversion (%)
1	Pd/SiO_2 (10 wt.% Pd)	95
2	$\text{Pd}_3\text{P/SiO}_2$ (10 wt.% Pd)	82
3	Pd/1P-SiO_2 (10 wt.% Pd)	95
4	$\text{Pd}_3\text{P/1P-SiO}_2$ (10 wt.% Pd)	85

Reaction conditions: styrene ($0.1 \text{ mmol} \cdot \text{mL}^{-1}$), methyl 4-iodobenzoate ($0.06 \text{ mmol} \cdot \text{mL}^{-1}$), Et_3N ($0.1 \text{ mmol} \cdot \text{mL}^{-1}$), solvent (DMSO), catalyst ($10^{-3} \text{ mmol} \cdot \text{mL}^{-1}$, Pd basis), 140°C , 60 min. Conversions were assessed based on the concentration methyl-4-iodobenzoate (limiting reagent). The quantifications were performed using GC-MS analysis and *n*-decane as internal standard.

Table S3: Results of ICP-AES analysis with weight percentages [wt.-%] of phosphorus (P), palladium (Pd) and silicon (Si). This table has been adapted from reference^[223] (license CC BY-NC 4.0).

Entry	Catalyst	State	P	Pd	Si
1	Pd/SiO ₂ (10 wt.% Pd)	Fresh	n. d.	9.455	39
2	Pd/SiO ₂ (10 wt.% Pd)	Recovered	n. d.	7.555	39.25
3	Pd ₃ P/SiO ₂ (10 wt.% Pd)	Fresh	1.085	8.595	38.55
4	Pd ₃ P/SiO ₂ (10 wt.% Pd)	Recovered	0.68	7.675	37.55
5	Pd/1P-SiO ₂ (10 wt.% Pd)	Fresh	0.715	9.295	39.35
6	Pd/1P-SiO ₂ (10 wt.% Pd)	Recovered	0.31	6.805	38.3
7	Pd ₃ P/1P-SiO ₂ (10 wt.% Pd)	Fresh	n. d.	8.225	38.15
8	Pd ₃ P/1P-SiO ₂ (10 wt.% Pd)	Recovered	n. d.	8.125	38.75

n.d : not determined

Reaction conditions: styrene (0.1 mmol · mL⁻¹), iodobenzene (0.06 mmol · mL⁻¹), Et₃N (0.1 mmol · mL⁻¹), solvent (DMSO), catalyst (10⁻³ mmol · mL⁻¹, Pd basis), 140 °C, 60 min.

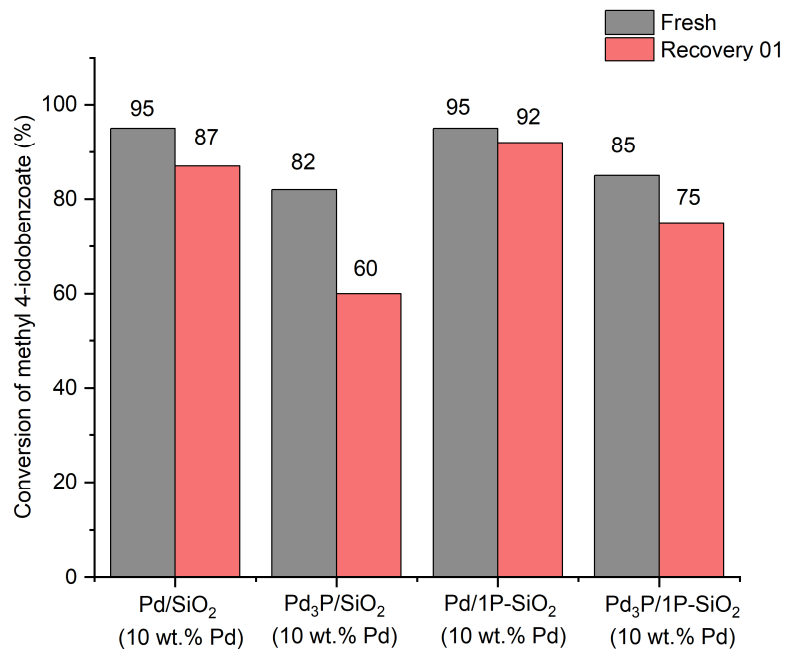


Figure S15: Results of recovery test with methyl-4-iodobenzoate and styrene. Reaction conditions: styrene (0.1 mmol · mL⁻¹), methyl 4-iodobenzoate (0.06 mmol · mL⁻¹), Et₃N (0.1 mmol · mL⁻¹), solvent (DMSO), catalyst (10⁻³ mmol · mL⁻¹, Pd basis), 140°C, 60 min. Conversions were calculated considering the concentration of methyl-4-iodobenzoate. The quantifications were performed using GC-MS analysis and *n*-decane as internal standard. This figure has been adapted from reference^[223] (license CC BY-NC 4.0).

Table S4: Results of the hot filtration tests allowing total reaction time of 60 min. This table has been adapted from reference [223] (license CC BY-NC 4.0).

Entry	Catalyst	Conversion of	Conversion of
		iodobenzene with catalyst after 20 min (%)	iodobenzene after 60 min after catalyst removal (%)
1	Pd/SiO ₂ (10 wt.% Pd)	58	59
2	Pd ₃ P/SiO ₂ (10 wt.% Pd)	60	63
3	Pd ₃ P/0.5P-SiO ₂ (10 wt.% Pd)	52	58
4	Pd ₃ P/1P-SiO ₂ (10 wt.% Pd)	51	60

Reaction conditions: styrene (0.1 mmol · mL⁻¹), iodobenzene (0.06 mmol · mL⁻¹), K₃PO₄ (0.1 mmol · mL⁻¹), solvent (DMSO), catalyst (10⁻³ mmol · mL⁻¹, Pd basis), 140°C. The quantifications were performed using GC-MS analysis and *n*-decane as internal standard

10.3 Chapter 5: Alkoxy carbonylation reactions with supported palladium phosphide nanoparticles

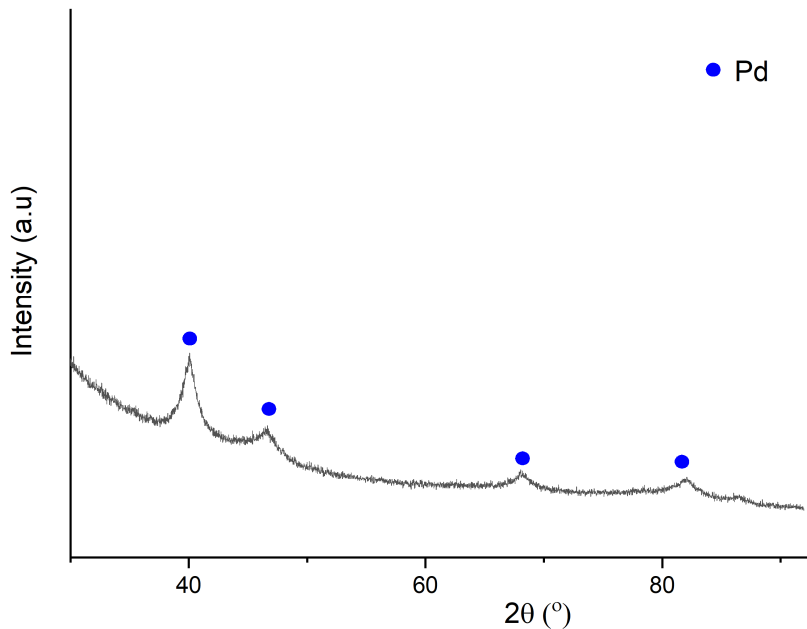


Figure S16: PXRD pattern of Pd/SiO₂ (5 wt.% Pd) used as catalyst for the alkoxy carbonylation reaction. Reference for the phase identification - Pd: ICSD 52251. This figure has been adapted from reference^[235] (license CC BY-NC ND 4.0).

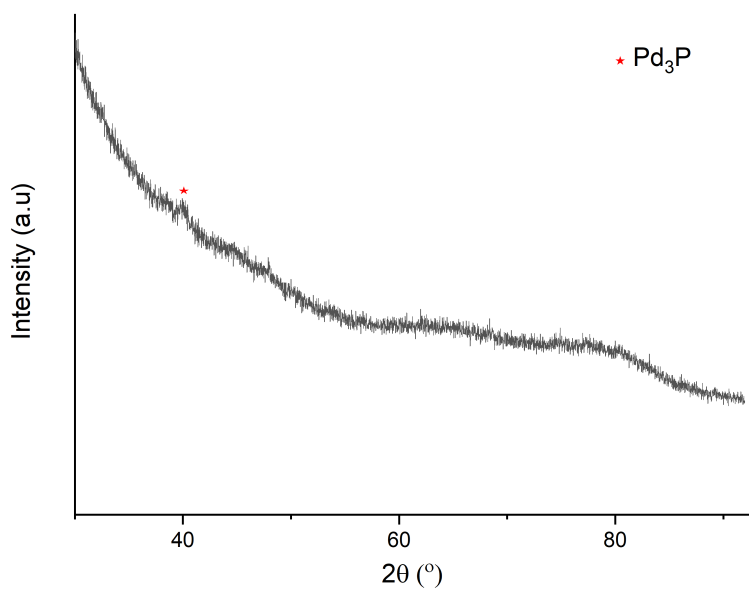


Figure S17: PXRD pattern of $\text{Pd}_3\text{P}/\text{SiO}_2$ (1 wt.% Pd) catalyst used for the alkoxy carbonylation reaction. Reference for the phase identification - Pd_3P : ICSD 85525. This figure has been adapted from reference^[235] (license CC BY-NC ND 4.0).

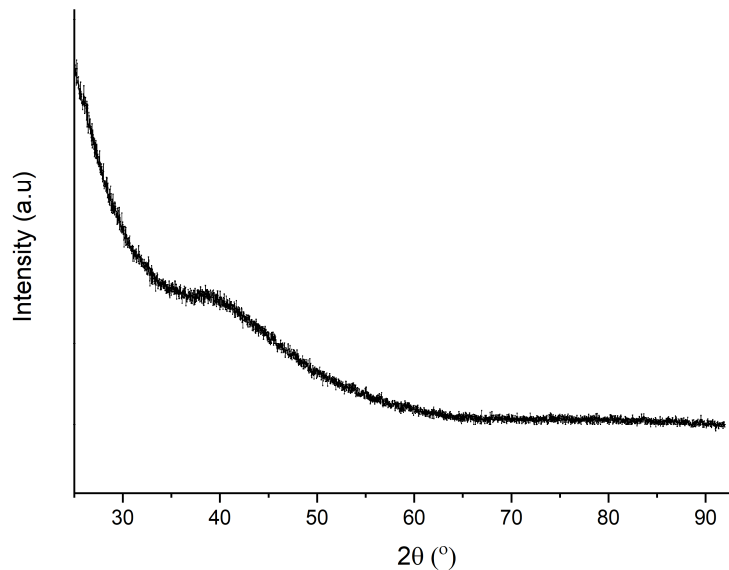


Figure S18: PXRD pattern of $\text{Pd}_3\text{P}/\text{C}$ (5 wt.% Pd) used as catalyst for the alkoxy carbonylation reaction. This figure has been adapted from reference^[235] (license CC BY-NC ND 4.0).

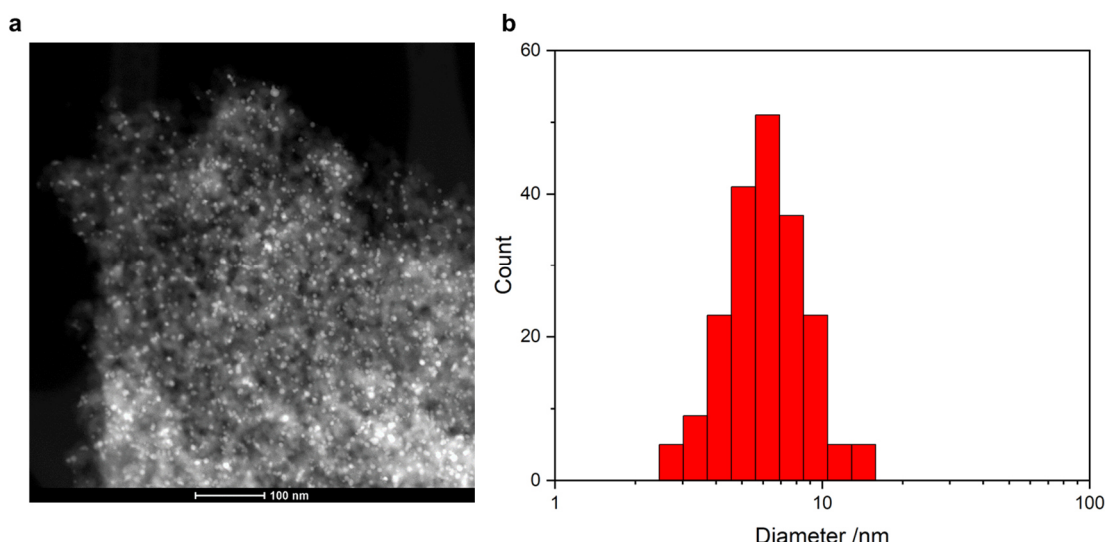


Figure S 19: a) Sample HAADF-STEM image of Pd/SiO₂ (5 wt.% Pd) and b) particle size distribution showing an average particle size of 6.6 ± 2.5 nm. This figure has been adapted from reference^[235] (license CC BY-NC ND 4.0).

Table S5: Influence of CO pressure and base concentration on alkoxy carbonylation reaction of iodobenzene with Pd₃P/SiO₂ (5 wt.% Pd). This table has been adapted from reference^[235] (license CC BY-NC ND 4.0).

Entry	Iodobenzene (mmol)	Et ₃ N (mmol)	CO pressure (bar)	TOF (h ⁻¹)
1	1	3	24	820
2	1	3	6	7600
3	1	1	24	295
4	1	1	6	7800

Reaction conditions: ethanol (4 mL), catalyst concentration (0.5 mol%, Pd basis), 100 °C, 1000 rpm.

Table S6: Results of the aminocarbonylation performed with Pd₃P/SiO₂ (5 wt.% Pd) as catalyst. This figure has been adapted from reference^[235] (license CC BY-NC ND 4.0).

Temperature	Conversion
100 °C	10 %
120 °C	56 %
140 °C	78 %

Note: In all cases 100 % selectivity to benzalilide. Reaction conditions: iodobenzene (1 mmol) and aniline (4 mmol), Et₃N (3 mmol), CO (10 bar), toluene (4 mL), catalyst (0.5 mol%, Pd basis), 5h.

Table S7: Comparison of the activity of $\text{Pd}_3\text{P}/\text{SiO}_2$ (5 wt.% Pd) and Pd/SiO_2 (5 wt.% Pd) with homogeneous catalysts. This table been adapted from reference^[235] (license CC BY-NC ND 4.0).

Entry	Catalyst	TOF (h ⁻¹)
1	$\text{Pd}(\text{OAc})_2$	620
2	$\text{Pd}(\text{NO}_3)_2$	700
3	$\text{Pd}_3\text{P}/\text{SiO}_2$ (5 wt.% Pd)	7680*
4	Pd/SiO_2 (5 wt.% Pd)	2830*

*Calculated based on the dispersion estimated through CO chemisorption measurements.

Reaction conditions: iodobenzene (1 mmol), Et_3N (3 mmol), CO (6 bar), ethanol (4 mL), catalyst (0.5 mol %, Pd basis), 100 °C.

Table S8: Performance comparison with the other reported heterogeneous palladium catalysts for the alkoxycarbonylation of iodobenzene. BOX: bis(oxazoline), GO: graphene oxide, IL: ionic liquid, PK: polyketone, phen: 1,10-phenanthroline, Y: Y zeolite, POP: porous organic polymer, KAP: knitting aryl network polymers, ImmPd: immobilized palladium. This table been adapted from reference^[235] (license CC BY-NC ND 4.0).

Entry	Catalyst	T	P	Time	Pd	NuH	Yield
		(°C)	(bar)	(h)	(mol %)		
1	$\text{Pd-BOX}^{[177]}$	100	6	3	0.5	MeOH	85 %
2	$\text{Pd/C}^{[239]}$	100	5	3	1	MeOH	73 %
3	$\text{Pd}(\text{OAc})_2\text{-PPh}_2\text{Et@SiO}_2^{[239]}$	100	5	3	1	MeOH	92 %
4	$\text{PdCl}_2\text{-PPh}_2\text{Et@SiO}_2^{[239]}$	100	5	3	1	MeOH	99 %
5	$\text{Pd@GOIL}^{[176]}$	100	3	2	0.5	MeOH	98 %
6	5% $\text{Pd/C}^{[245]}$	140	10	6	1	EtOH	80 %
7	$\text{Pd/Fe}_3\text{O}_4/\text{PK}^{[103]}$	120	50	2.5	0.1	MeOH	89 %
8	$\text{PdCl}_2(\text{phen})@\text{Y}^{[175]}$	100	5	1	0.6	MeOH	99 %
9	$\text{Pd@POP-Ph}_3\text{P}^{*[304]}$	80	1	4	0.25	EtOH	99 %
10	$\text{Pd@KAPs (Ph-PPh}_3)^{*[304]}$	80	1	4	0.25	EtOH	36 %
11	ImmPd-IL ^[178]	80	5	3	2	EtOH	95 %
12	$\text{Pd@CC3-R-MeOH}^{[305]}$	80	Balloon	12	2	EtOH	96 %
13	$\text{Pd}_3\text{P}/\text{SiO}_2$ (5 wt.% Pd)	100	6	2	0.5	EtOH	97%
14	$\text{Pd}_3\text{P}/\text{SiO}_2$ (5 wt.% Pd)	100	6	2	0.5	MeOH	98%

*DBU is used as base

10.4 Chapter 6: Olefin hydroformylation reactions with supported rhodium sulfide nanoparticles

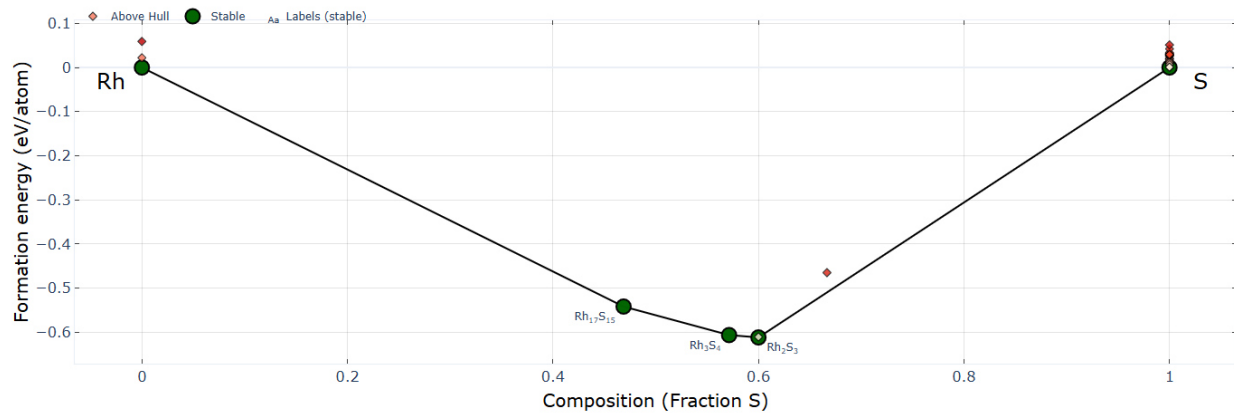


Figure S20: Phase stability diagram for the Rh-S system generated with “The Materials Project”. [33,254]

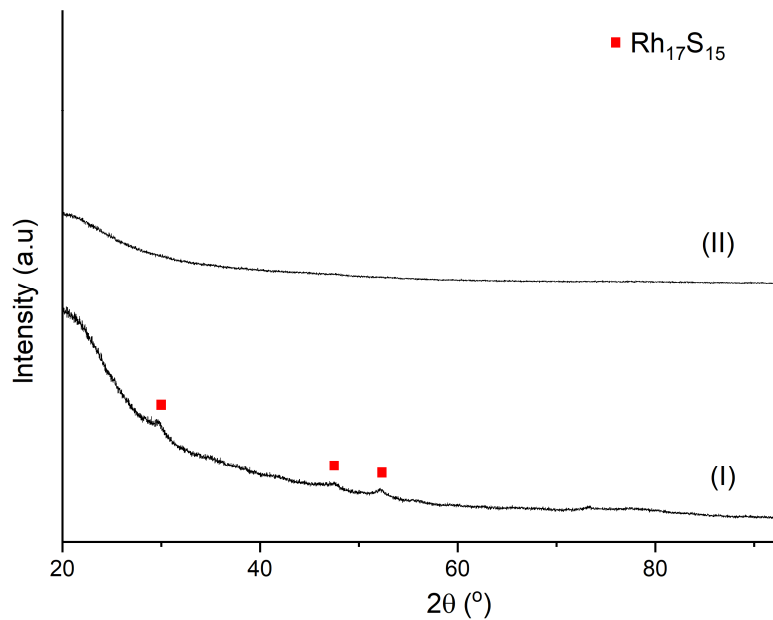


Figure S21: PXRD patterns for I) $\text{Rh}_{17}\text{S}_{15}/\text{SiO}_2$ (10 wt.% Rh) and II) $\text{Rh}_{17}\text{S}_{15}/\text{SiO}_2$ (1 wt.% Rh). Reference for phase identification - $\text{Rh}_{17}\text{S}_{15}$: ICSD 410838. This figure has been adapted from reference^[255] (license CC BY 4.0).

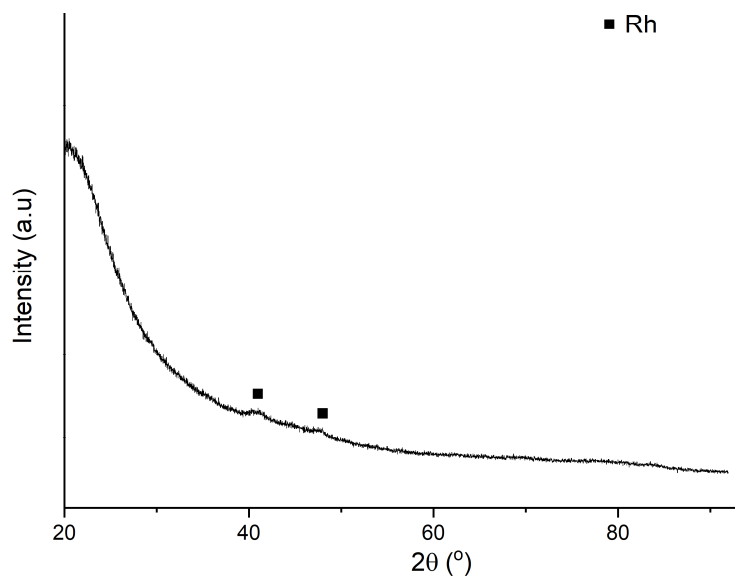


Figure S22: PXRD pattern of the reference Rh/SiO₂ (1 wt.% Rh) catalyst. Reference for phase identification- Rh: ICSD 171677. This figure has been adapted from reference^[255] (license CC BY 4.0).

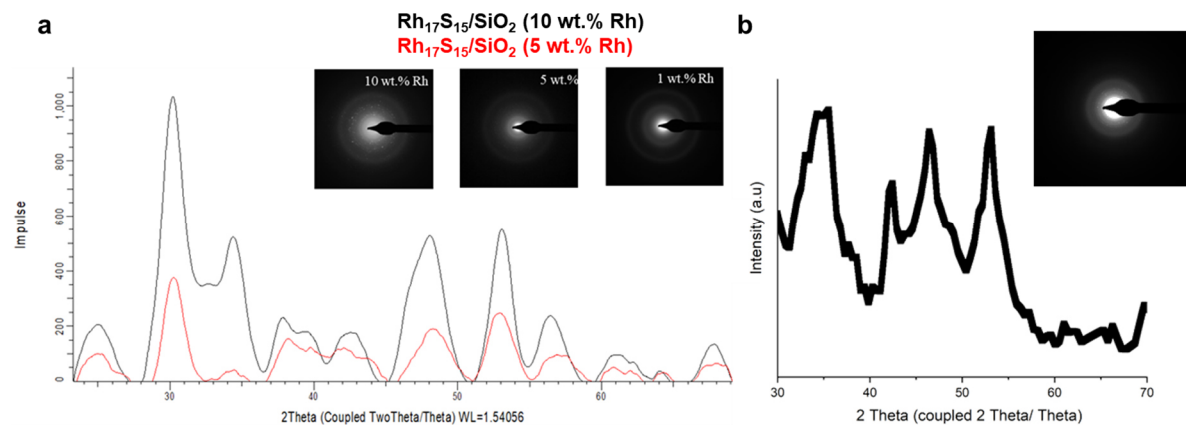


Figure S23: SAED analysis results a) Rh₁₇S₁₅/SiO₂ (10 wt.% Rh)-black pattern, Rh₁₇S₁₅/SiO₂ (5 wt.% Rh)- red pattern and b) Rh₂S₃/SiO₂ (10 wt.% Rh). This figure has been adapted from reference^[255] (license CC BY 4.0).

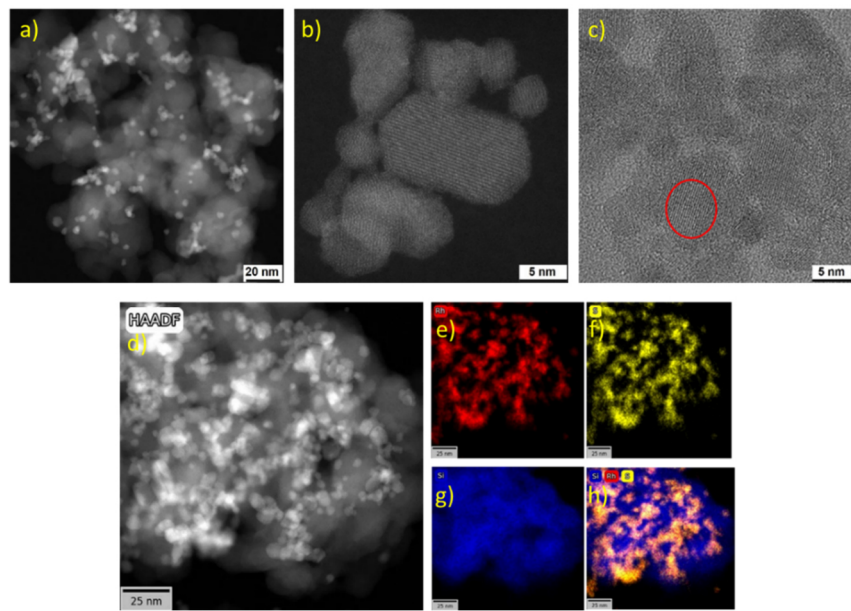


Figure S24: TEM analysis performed for $\text{Rh}_{17}\text{S}_{15}/\text{SiO}_2$ (10 wt.% Rh) catalyst comprising of a) HAADF-STEM image, b) HR-HAADF-STEM image, c) HRTEM image showing example lattice fringes highlighted d) HAADF-STEM image and corresponding EDX mappings of elements e) Rh, f) S, g) Si and h) combined Rh, S and Si. This figure has been adapted from reference^[255] (license CC BY 4.0).

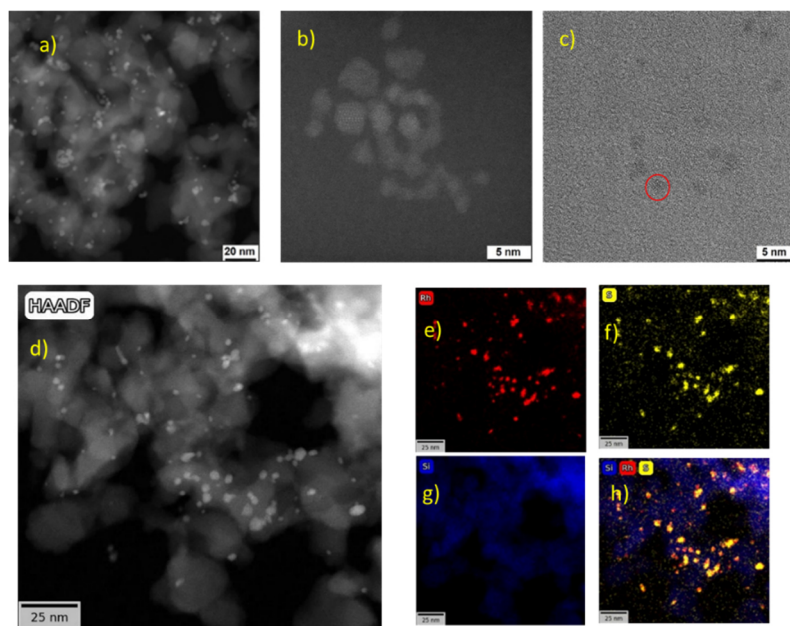


Figure S25: TEM analysis performed for $\text{Rh}_{17}\text{S}_{15}/\text{SiO}_2$ (1 wt.% Rh) catalyst comprising of a) HAADF-STEM image, b) HR-HAADF-STEM image, c) HRTEM image showing example lattice fringes highlighted d) HAADF-STEM image and corresponding EDX mappings of elements e) Rh, f) S, g) Si and h) combined Rh, S and Si. This figure has been adapted from reference^[255] (license CC BY 4.0).

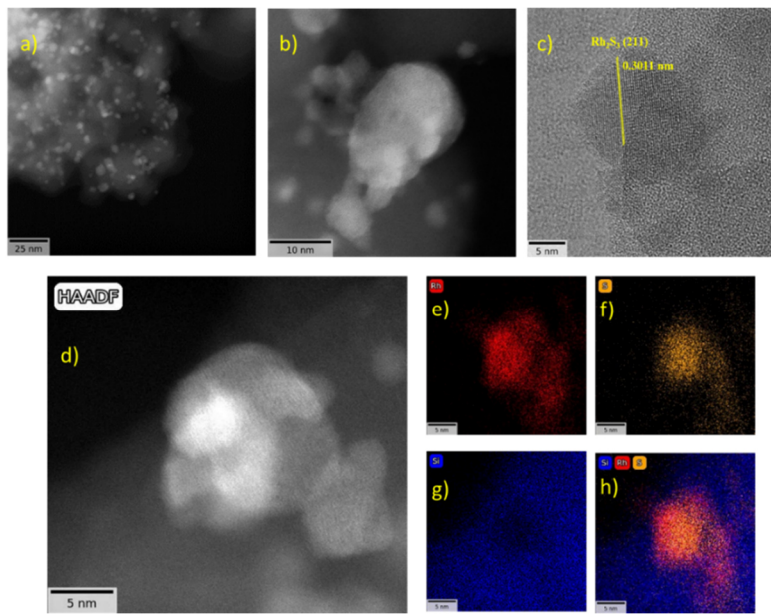


Figure S26: TEM analysis performed for $\text{Rh}_2\text{S}_3/\text{SiO}_2$ (10 wt.% Rh) catalyst comprising of a) HAADF-STEM image, b) HR-HAADF-STEM image, c) HRTEM image showing example lattice fringes with d spacing 0.301 nm corresponding to $\text{Rh}_2\text{S}_3(211)$ highlighted d) HAADF-STEM image and corresponding EDX mappings of elements e) Rh, f) S, g) Si and h) combined Rh, S and Si. This figure has been adapted from reference^[255] (license CC BY 4.0).

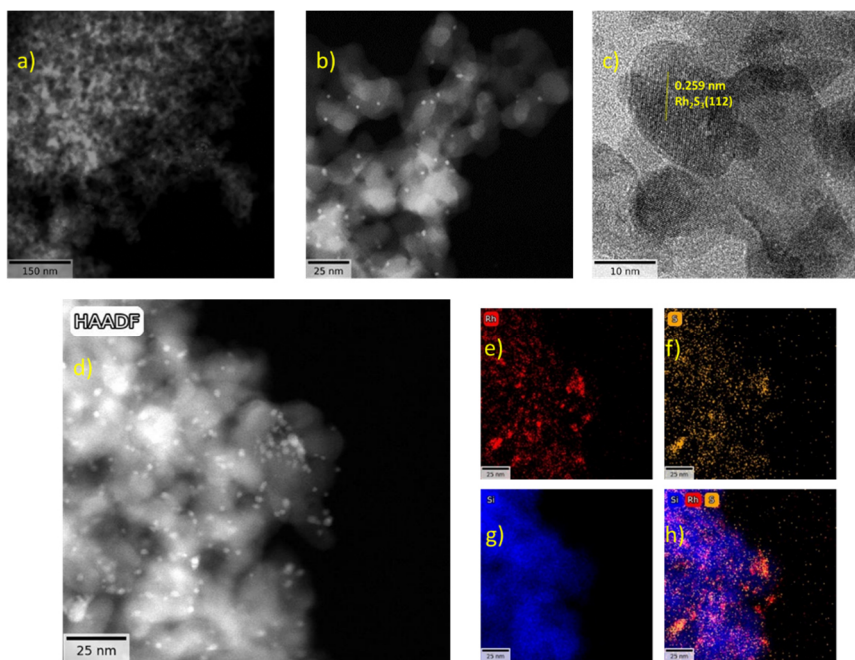


Figure S27: TEM analysis performed for $\text{Rh}_2\text{S}_3/\text{SiO}_2$ (1 wt.% Rh) catalyst comprising of a) HAADF-STEM image, b) HR-HAADF-STEM image, c) HRTEM image showing example lattice fringes with d spacing 0.259 nm corresponding to $\text{Rh}_2\text{S}_3(112)$ highlighted d) HAADF-STEM image and corresponding EDX mappings of elements e) Rh, f) S, g) Si and h) combined Rh, S and Si. This figure has been adapted from reference^[255] (license CC BY 4.0).

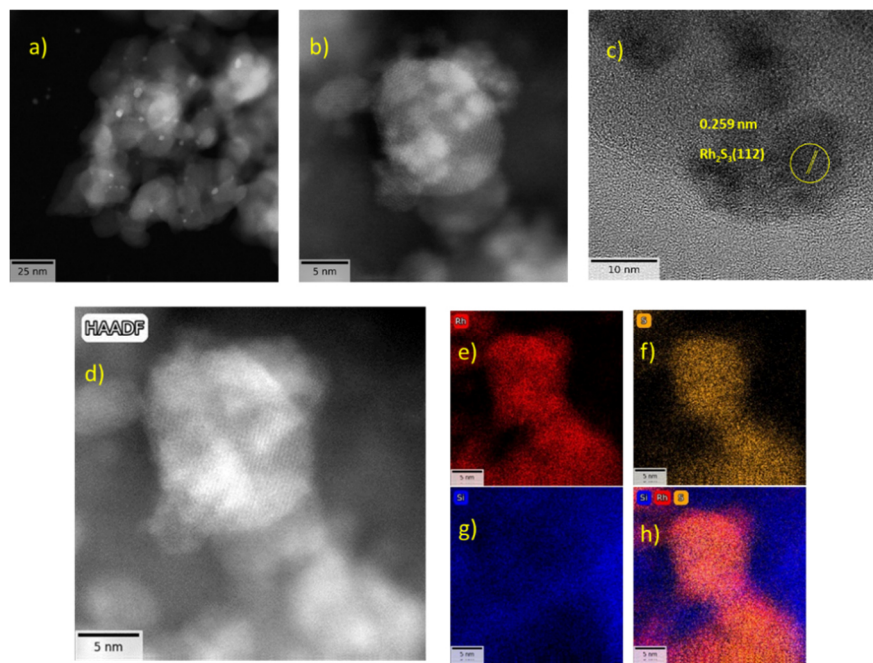


Figure S28: TEM analysis performed for recovered $\text{Rh}_2\text{S}_3/\text{SiO}_2$ (1 wt.% Rh) catalyst comprising of a) HAADF-STEM image, b) HR-HAADF-STEM image, c) HRTEM image showing example lattice fringes with d spacing 0.259 nm corresponding to Rh_2S_3 (112) highlighted, d) HAADF-STEM image and corresponding EDX mappings of elements e) Rh, f) S, g) Si and h) combined Rh, S and Si. Reaction conditions: styrene (1 mmol), toluene (1.5 mL), catalyst (0.2 mol%, Rh basis), 40 bar syngas pressure, CO:H_2 1:1, 80 °C, 1200 rpm. This figure has been adapted from reference^[255] (license CC BY 4.0).

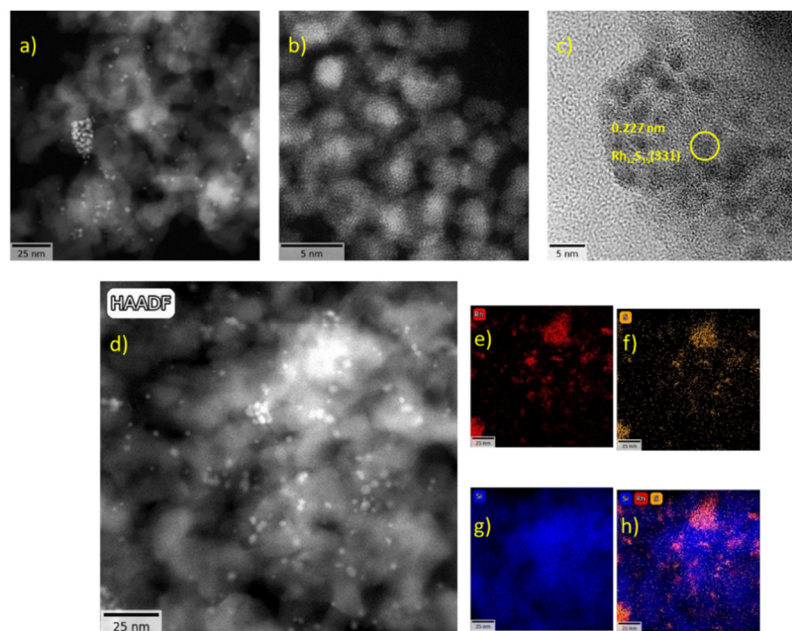


Figure S29: TEM analysis performed for recovered $\text{Rh}_{17}\text{S}_{15}/\text{SiO}_2$ (1 wt.% Rh) catalyst comprising of a) HAADF-STEM image, b) HR-HAADF-STEM image, c) HRTEM image showing example lattice fringes with d spacing 0.227 nm corresponding to $\text{Rh}_{17}\text{S}_{15}$ (331) highlighted, d) HAADF-STEM image and corresponding EDX mappings of elements e) Rh, f) S, g) Si and h) combined Rh, S and Si. Reaction

conditions: styrene (1 mmol), toluene (1.5 mL), catalyst (0.2 mol%, Rh basis), 40 bar syngas pressure, CO:H₂ 1:1, 80 °C, 1200 rpm. This figure has been adapted from reference^[255] (license CC BY 4.0).

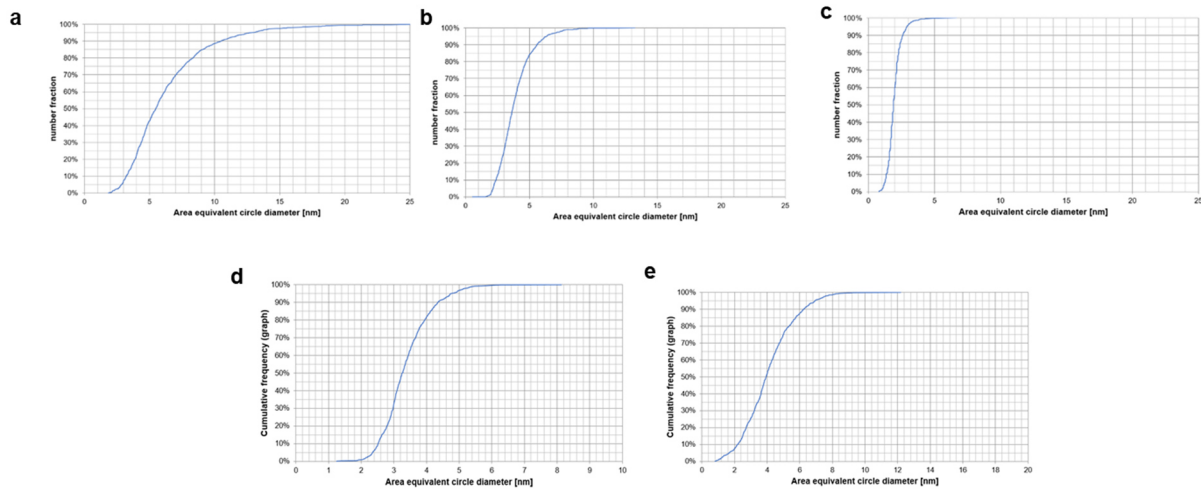


Figure S30: Cumulative particle size distribution of Rh₁₇S₁₅/SiO₂ with a Rh loading of a) 10 wt.%, b) 5 wt.% and c) 1 wt.% and Rh₂S₃/SiO₂ with Rh loading d) 10 wt.% and e) 1 wt.%. At least 1100 particles for Rh₁₇S₁₅ and 700 particles for Rh₂S₃ were considered for preparing the size distribution graphs and estimating the statistical descriptors. This figure has been adapted from reference^[255] (license CC BY 4.0).

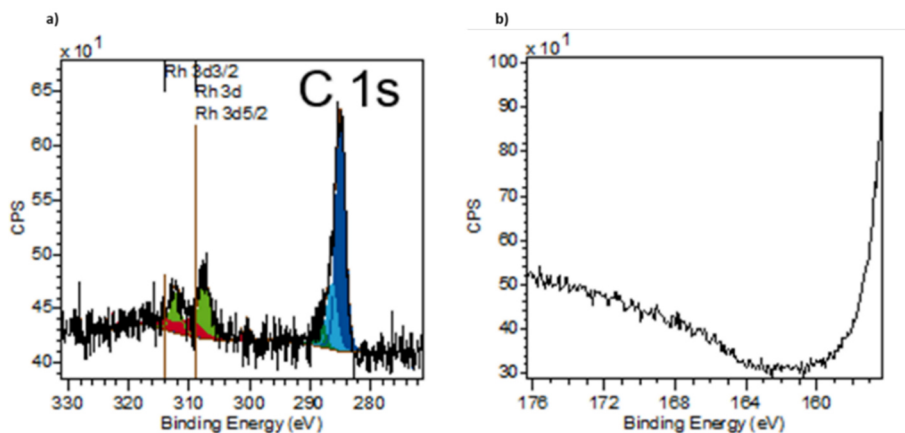


Figure S31: XPS analysis of the Rh/SiO₂ (1 wt.% Rh) reference catalyst with a) Rh 3d and b) S 2p spectra. This figure has been adapted from reference^[255] (license CC BY 4.0).

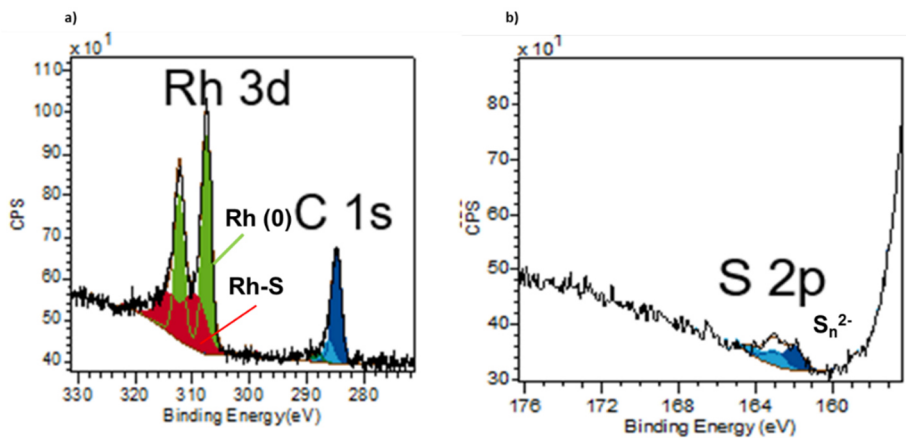


Figure S32: XPS analysis of $\text{Rh}_{17}\text{S}_{15}/\text{SiO}_2$ (10 wt.% Rh) with a) Rh 3d and b) S 2p spectra. This figure has been adapted from reference [255] (license CC BY 4.0).

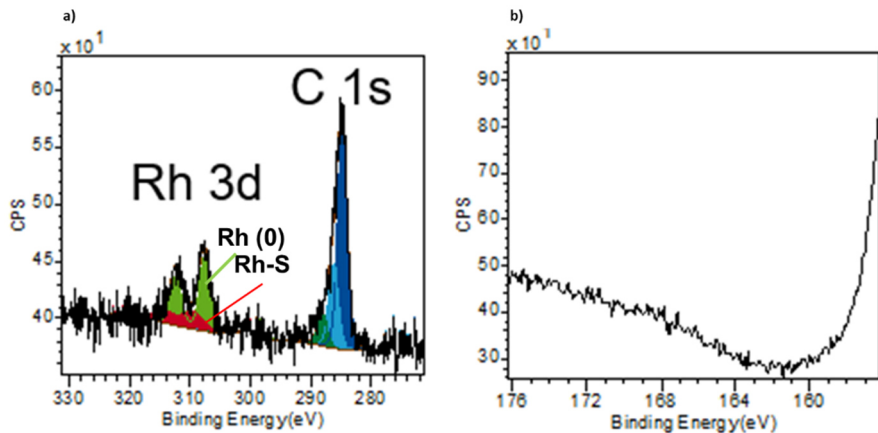


Figure S33: XPS analysis of $\text{Rh}_{17}\text{S}_{15}/\text{SiO}_2$ (1 wt.% Rh) with a) Rh 3d and b) S 2p spectra. This figure has been adapted from reference [255] (license CC BY 4.0).

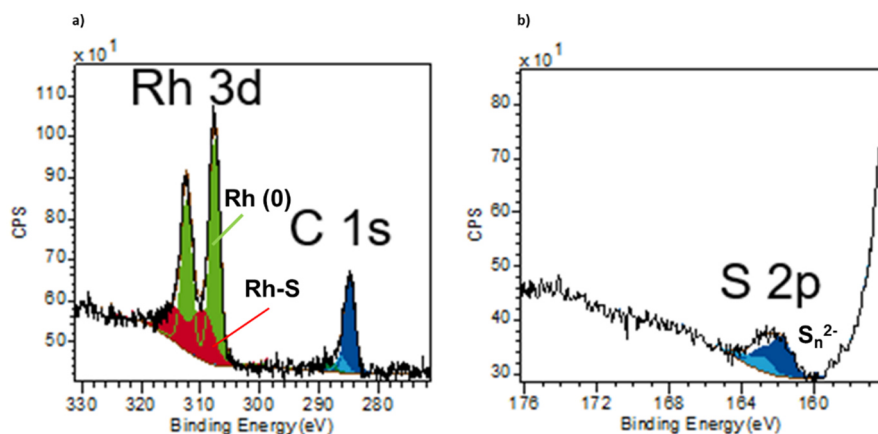


Figure S34: XPS analysis of $\text{Rh}_2\text{S}_3/\text{SiO}_2$ (10 wt.% Rh) with a) Rh 3d and b) S 2p spectra. This figure has been adapted from reference [255] (license CC BY 4.0).

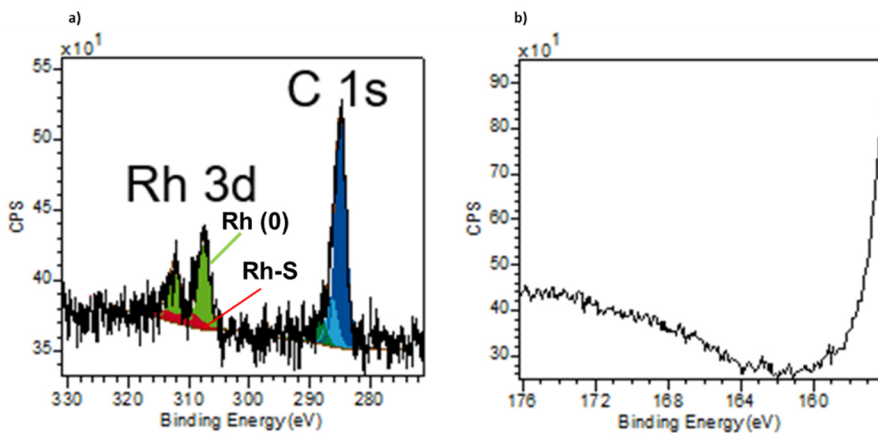


Figure S 35: XPS analysis of $\text{Rh}_2\text{S}_3/\text{SiO}_2$ (1 wt.% Rh) with a) Rh 3d and b) S 2p spectra. This figure has been adapted from reference^[255] (license CC BY 4.0).

Table S9: Composition determined *via* XPS measurements. This table has been adapted from reference^[255] (license CC BY 4.0).

Catalyst	Composition in at.% and wt.%				
	C 1s	O 1s	Rh 3d	S 2p	Si 2p
Rh/SiO_2 (1 wt.% Rh)	5.3 at.% 3.3 wt.%	66.7 at.% 55.4 wt.%	0.1 at.% 0.7 wt.%	-	27.9 at.% 40.7 at.%
$\text{Rh}_{17}\text{S}_{15}/\text{SiO}_2$ (10 wt.% Rh)	6.1 at.% 3.6 wt.%	64.5 at.% 50.8 wt.%	1.3 at.% 6.4 wt.%	0.4 at.% 0.7 wt.%	27.8 at.% 38.5 wt.%
$\text{Rh}_{17}\text{S}_{15}/\text{SiO}_2$ (1 wt.% Rh)	4.9 at.% 3.0 wt.%	66.6 at.% 55.0 wt.%	0.2 at.% 0.9 wt.%	-	28.3 at.% 41.0 wt.%
$\text{Rh}_2\text{S}_3/\text{SiO}_2$ (10 wt.% Rh)	5.5 at.% 3.3 wt.%	64.8 at.% 51.2 wt.%	1.1 at.% 5.8 wt.%	0.6 at.% 0.9 wt.%	28.0 at.% 38.8 wt.%
$\text{Rh}_2\text{S}_3/\text{SiO}_2$ (1 wt.% Rh)	4.2 at.% 2.6 wt.%	67.6 at.% 55.8 wt.%	0.2 at.% 0.9 wt.%	-	28.1 at.% 40.7 wt.%

Sulfur signals were not detected in the XPS spectra of rhodium sulfide samples containing 1 wt.% Rh, due to the low sulfur concentration.

Table S10: Quantification of Rh and S species based on the XPS measurements. This table has been adapted from reference^[255] (license CC BY 4.0).

Catalyst	Rh 3d (at.% / wt.%)				S 2p (at.% / wt.%)			
	Rh (0)	Error	Rh-S	Error	S1	Error	S2	Error
	307.5 eV	(+/-)	309.5 eV	(+/-)	161.9 eV	(+/-)	162.9 eV	(+/-)
$\text{Rh}_{17}\text{S}_{15}/\text{SiO}_2$ (10 wt.% Rh)	0.8/ 4.1	0.1/ 0.3	0.4/ 2.3	0.1/ 0.3	0.3/ 0.4	0.1/ 0.1	0.2/ 0.3	0.1/ 0.1
$\text{Rh}_{17}\text{S}_{15}/\text{SiO}_2$ (1 wt.% Rh)	0.1/ 0.6	-	0.1/ 0.3	-	0.1/ 0.1	-	0.2/ 0.3	0.1/ 0.1
$\text{Rh}_2\text{S}_3/\text{SiO}_2$ (10 wt.% Rh)	0.8/ 4.1	-	0.3/ 1.7	-	0.4/ 0.6	0.1/ 0.1	0.2/ 0.3	0.1/ 0.1
$\text{Rh}_2\text{S}_3/\text{SiO}_2$ (1 wt.% Rh)	0.1/ 0.6	-	0.1/ 0.3	-	0.1/ 0.1	-	0.2/ 0.3	0.1/ 0.1

Table S11: Determination of the Rh/S ratios in the sample from Rh-S related signals. This table has been adapted from reference [255] (license CC BY 4.0).

Catalyst	Measurement	Rh as Rh-S (at.%)	S 2p (at.%)	Rh-S/S	Average Rh-S/S	Expected Rh/ S value
$\text{Rh}_{17}\text{S}_{15}/\text{SiO}_2$ (10 wt.% Rh)	1	0.4	0.3	1.33	1.11	1.13
	2	0.5	0.5	1.0		
	3	0.4	0.4	1.0		
$\text{Rh}_2\text{S}_3/\text{SiO}_2$ (10 wt.% Rh)	1	0.3	0.6	0.5	0.53	0.67
	2	0.3	0.6	0.5		
	3	0.3	0.5	0.6		

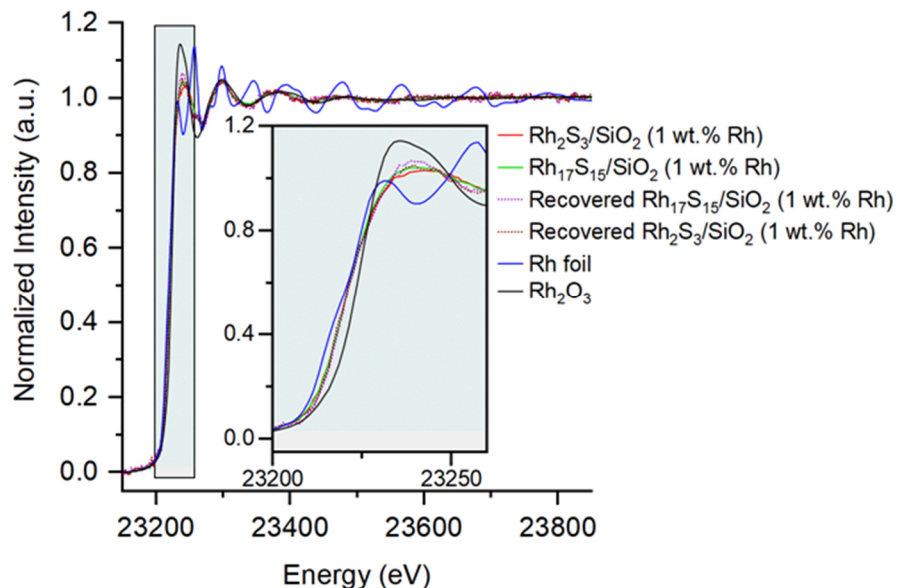


Figure S36: *Ex-situ* XAS results (recorded at Rh-K edge) of the fresh and recovered rhodium sulfide catalysts. XANES region is highlighted for better view and analysis. Reaction conditions: styrene (1 mmol), toluene (1.5 mL), catalyst (0.2 mol%, Rh basis), 40 bar syngas pressure, CO:H₂ 1:1, 80 °C, 2 h, 1200 rpm. This figure has been adapted from reference [255] (license CC BY 4.0).

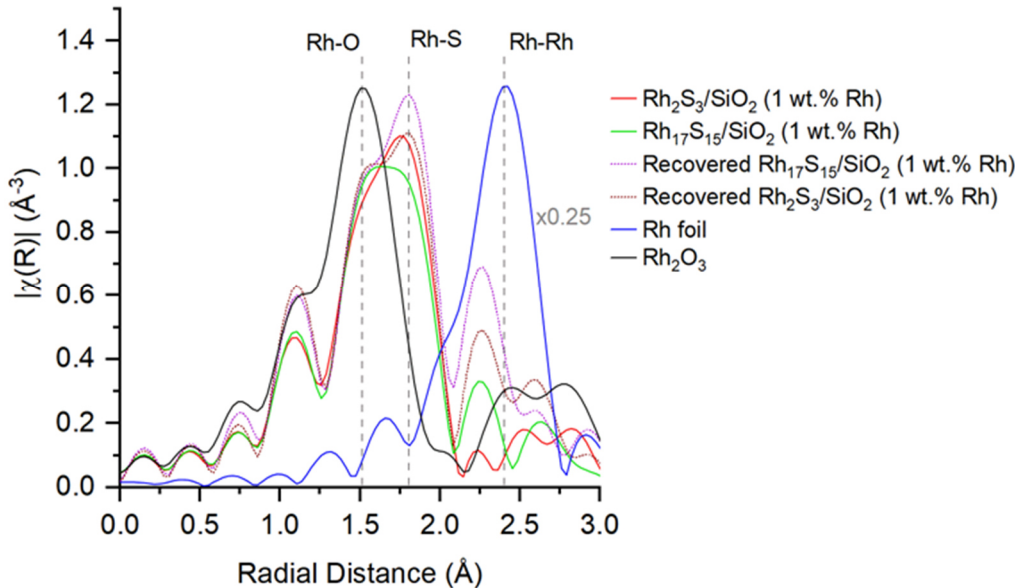


Figure S37: FT-EXAFS spectra (k^2 -weighted), not corrected for scattering phase shift, obtained for the fresh and recovered rhodium sulfide catalysts. Reaction conditions: styrene (1 mmol), toluene (1.5 mL), catalyst (0.2 mol%, Rh basis), 40 bar syngas pressure, CO:H₂ 1:1, 80 °C, 2 h, 1200 rpm. This figure has been adapted from reference^[255] (license CC BY 4.0).

Table S12: Calculated EXAFS path^[296] for the Rh₂O₃ and Rh₁₇S₁₅ bulk structure. Aggregate function was used to generate the paths for Rh₁₇S₁₅. This table has been adapted from reference^[255] (license CC BY 4.0).

Structure	Included paths	Effective path length (Å)	Degeneracy
Rh ₂ O ₃	*O*	2.041	6
Rh ₁₇ S ₁₅	*S1*	2.285	1.4
	S2	2.353	2.3
	Rh	2.840	2.1

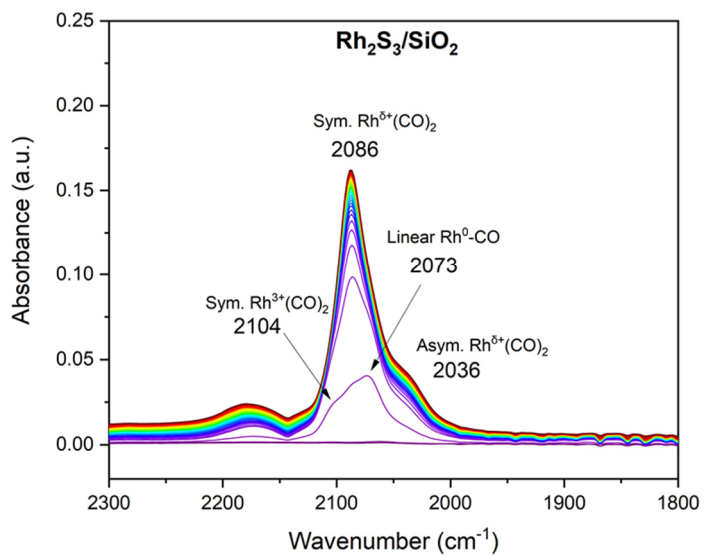


Figure S38: CO-DRIFT spectra of $\text{Rh}_2\text{S}_3/\text{SiO}_2$ (1 wt.% Rh). This figure has been adapted from reference^[255] (license CC BY 4.0).

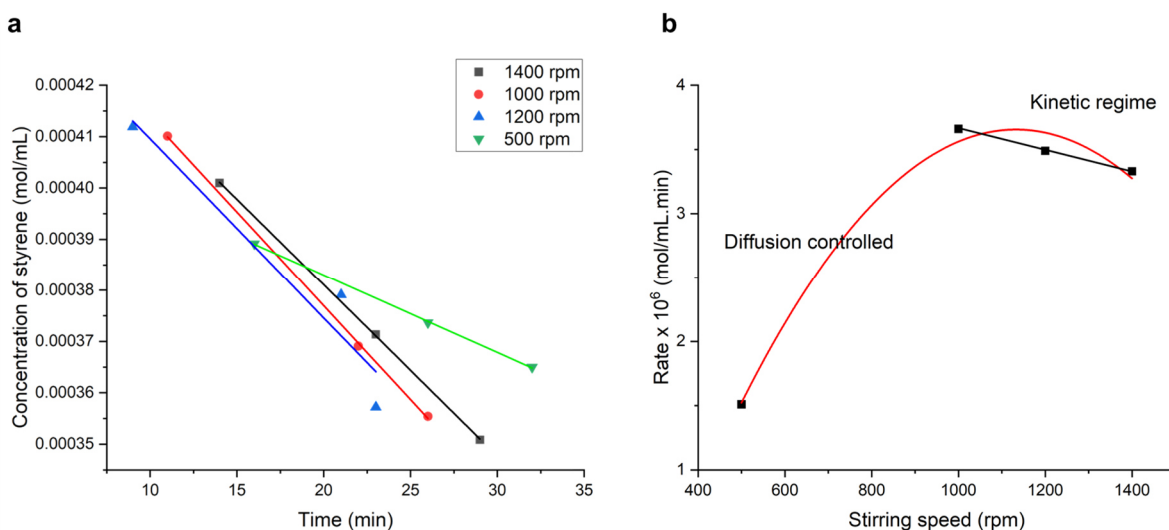


Figure S39: Study of the influence of rate of reaction with respect to stirrer speed. a) Determination of rate of reaction carried out with varying rpm and b) plot showing the dependency of reaction rate and stirrer speed. Reaction conditions: styrene (1 mmol), toluene (1.5 mL), $\text{Rh}_2\text{S}_3/\text{SiO}_2$ (1 wt.% Rh) (0.2 mol%, Rh basis), 40 bar syngas pressure, CO:H₂ 1:1, 80 °C. Analysis performed at lower conversions (less than 20%) to ensure differential conditions. This figure has been adapted from reference^[255] (license CC BY 4.0).

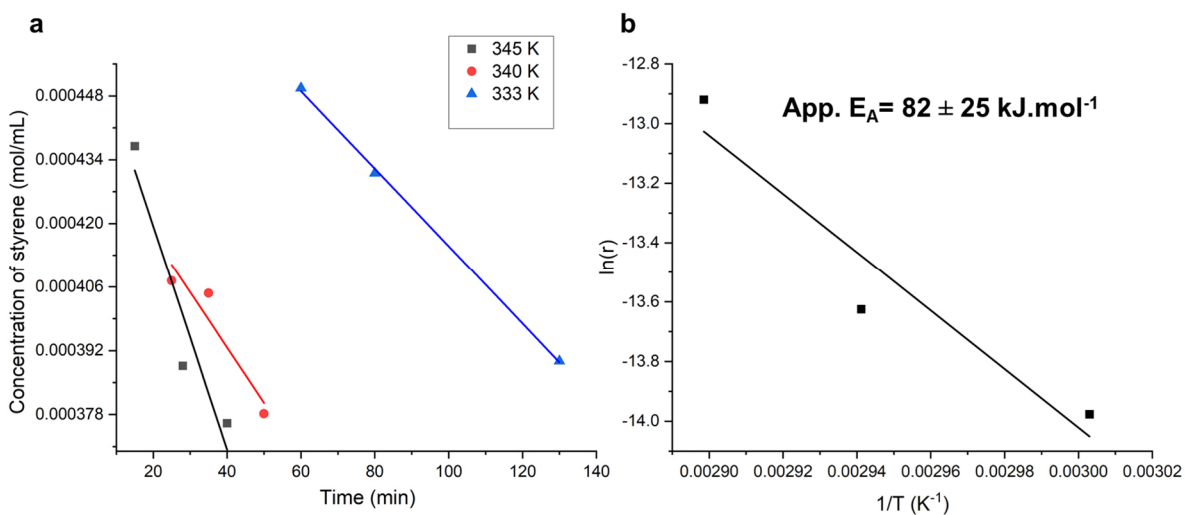


Figure S40: Estimation of apparent activation energy for the styrene hydroformylation using $\text{Rh}_{17}\text{S}_{15}/\text{SiO}_2$ (1 wt.% Rh) as catalyst. a) Determination of rate of reaction and b) Arrhenius plot. Reaction conditions: styrene (1 mmol), toluene (1.5 mL), catalyst (0.2 mol%, Rh basis), 40 bar syngas pressure, CO:H_2 1:1, 1200 rpm. Rates were determined at lower conversions (less than 20%) to ensure differential conditions. This figure has been adapted from reference^[255] (license CC BY 4.0).

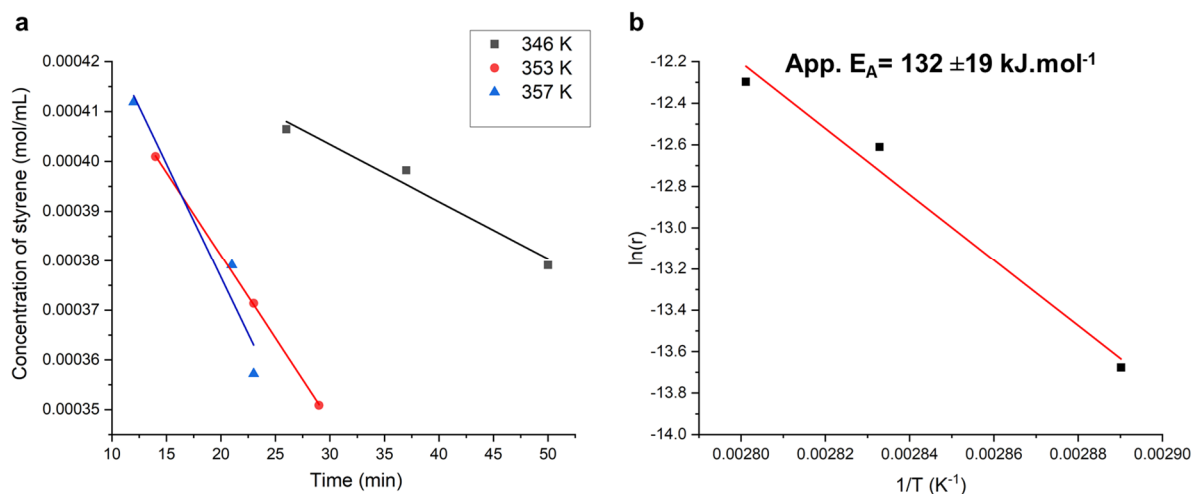


Figure S41: Estimation of apparent activation energy for the styrene hydroformylation with $\text{Rh}_2\text{S}_3/\text{SiO}_2$ (1 wt.% Rh) as catalyst. a) Determination of rate of reaction and b) Arrhenius plot. Reaction conditions: styrene (1 mmol), toluene (1.5 mL), catalyst (0.2 mol%, Rh basis), 40 bar syngas pressure, CO:H_2 1:1, 1200 rpm. Rates were determined at lower conversions (less than 20%) to ensure differential conditions. This figure has been adapted from reference^[255] (license CC BY 4.0).

Table S13: Hydroformylation performed with neat styrene and 1-hexene (solvent free) using $\text{Rh}_{17}\text{S}_{15}/\text{SiO}_2$ (1 wt.% Rh) catalyst. This table has been adapted from reference^[255] (license CC BY 4.0).

Catalyst concentration (mol%)	Substrate	Reaction time (h)	Conversion (%)	n/iso
0.06	styrene	2	40	0.95
0.014*	styrene	16	60	1.08
0.014	1-hexene	16	90	2.62

* Polymerization of styrene was observed.

Reaction conditions: 40 bar syngas pressure, CO:H₂ 1:1, 80 °C, 1200 rpm stirring speed

Table S14: Experimentally determined activation energies for various reported catalyst for the styrene hydroformylation. PTA = phosphotungstic acid, HMS = hexagonal mesoporous silica, PEG = polyethylene glycolate. This table has been adapted from^[255] (license CC BY 4.0).

Entry	Catalyst	Catalyst type	E_A
1	$\text{HRh}(\text{CO})(\text{PPh}_3)_3$ ^[306]	Homogeneous	68.8 kJ.mol ⁻¹
2	Rh ₁ /Cs-PTA ^[307]	Heterogeneous	50.4 kJ.mol ⁻¹ (b) 74.4 kJ.mol ⁻¹ (l)
3	$\text{HRh}(\text{CO})(\text{PPh}_3)_3$ -HMS ^[308]	Heterogeneous	32.50 kJ.mol ⁻¹
4	$\text{Rh}(\text{PEG})_x$ ^[309]	Homogeneous	34.1 kJ.mol ⁻¹
5	Rh_1/CeO_2 ^[186]	Heterogeneous	56.0 kJ.mol ⁻¹

Table S15: Performance comparison of the synthesized catalysts with other reported catalysts in the hydroformylation of 1-hexene. This table has been adapted from reference^[255] (license CC BY 4.0).

Entry	Catalyst	Rh loading on support	Reaction time (h)	Conversion (%)	Selectivity to aldehyde (%)	n/iso
1	$\text{RhCl}(\text{PPh}_3)_3$ ^[281] *		5	82	67	2.33
2	$\text{Rh}_2\text{P}/\text{C}$ ^[281]	1 wt.%	5	96	94	2.03
3	$\text{Rh}_2\text{P}/\text{C}$ ^[281]	5 wt.%	5	77	69	2.22
4	$\text{Rh-PPh}_3/\text{C}$ ^[281]	1 wt.%	5	100	83	1.22
5	$\text{Rh-PPh}_3/\text{C}$ ^[281]	5 wt.%	5	67	61	2.22
6	Rh/C ^[281]	1 wt.%	5	63	72	2.03
7	Rh/C ^[281]	5 wt.%	5	4	-	-
8	$\text{Rh}_{17}\text{S}_{15}/\text{SiO}_2$	1 wt.%	4	100	92**	1.05
9	Rh/SiO_2	1 wt.%	5	67	84**	2.51

* Homogeneous catalyst, ** only isomerized olefins are formed as the side products.

Reaction conditions: 1- hexene (1 mmol), toluene (1.5 mL), catalyst (0.2 mol%), 40 bar syngas pressure, CO:H₂ 1:1, 60°C, 1200 rpm stirring speed. The catalyst in bold are synthesized in this work.

Table S16: Activity comparison of synthesized catalysts in hydroformylation of styrene. This table has been adapted from^[255] (license CC BY 4.0).

Entry	Catalyst	Rh loading on support (wt.%)	Pressure (bar)	Temperature (°C)	TOF (h ⁻¹)
1	Wilkinson ^{*[189]}	-	16	100	1583
2	Wilkinson ^{*[183]}	-	30	110	15000
3	HRh(PPh ₃) ₃ (CO) ^{*[186]}	-	10	90	117
4	Rh(CO) ₂ (acac) ^{*[276]}	-	20	100	1368
5	RhCl ₃ ^{*[189]}	-	16	100	277
6	Rh/C ^[186]	5	10	90	24
7	Rh/SiO ₂ ^[277]	Not given	50	60	212
8	Rh ₁ /ZnO ^[189]	0.006	16	100	3333
9	Rh ₁ /CeO ₂ ^[186]	1 Rh at nm ⁻²	10	90	130
10	Rh ₂ P/SiO ₂ ^[25]	1.4	30	80	1469
11	Rh ₇ Co ₁ P ₄ /SiO ₂ ^[275]	1	30	80	2563
12	RhZn/SBA-15 ^[191]	3	30	100	3090
13	Rh-PPh ₃ /SiO ₂ ^[277]	Not given	50	60	135
14	Rh-P-COF ^[276]	Not given	20	100	2557
15	Rh ₇ Pd ₁ P ₄ /SiO ₂ ^[278]	Not given	60	40	204
16	Rh₁₇S₁₅/SiO₂**	1	40	80	1232
17	Rh₂S₃/SiO₂**	1	40	80	607
18	Rh₁₇S₁₅/SiO₂	1	40	80	2620
19	Rh₂S₃/SiO₂	1	40	80	1450

* Homogeneous catalyst, ** TOF estimated considering total Rh content

The catalyst in bold are synthesized in this work.

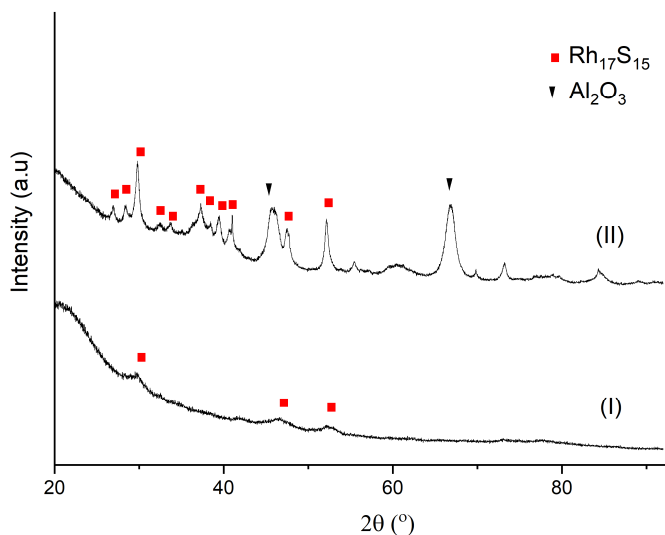


Figure S42: PXRD patterns of $\text{Rh}_{17}\text{S}_{15}$ with 10 wt.% loading prepared on I) 0.5P- SiO_2 and II) Al_2O_3 . Reference for phase identification- $\text{Rh}_{17}\text{S}_{15}$: ICSD 410838. This figure has been adapted from reference^[255] (license CC BY 4.0).

Table S17: Results of ICP-AES analysis performed for the metal leaching investigation. This table has been adapted from reference^[255] (license CC BY 4.0).

Entry	Catalyst	State	Rh (wt.%)	Si (wt.%)	Al (wt.%)
1	$\text{Rh}_{17}\text{S}_{15}/\text{SiO}_2$ (1 wt.% Rh)	Fresh	1.03	43.55	
2	$\text{Rh}_{17}\text{S}_{15}/\text{SiO}_2$ (1 wt.% Rh)	Recovered	0.78	41.70	
3	$\text{Rh}_2\text{S}_3/\text{SiO}_2$ (1 wt.% Rh)	Fresh	0.88	43.3	
4	$\text{Rh}_2\text{S}_3/\text{SiO}_2$ (1 wt.% Rh)	Recovered	0.73	42.0	
5	Rh/SiO_2 (1 wt.% Rh)	Fresh	0.92	43.9	
6	Rh/SiO_2 (1 wt.% Rh)	Recovered	0.85	42.7	
7	$\text{Rh}_{17}\text{S}_{15}/\text{Al}_2\text{O}_3$ (1 wt.% Rh)*	Fresh	0.80		48.3
8	$\text{Rh}_{17}\text{S}_{15}/\text{Al}_2\text{O}_3$ (1 wt.% Rh)*	Recovered	0.72		46.4
9	$\text{Rh}_{17}\text{S}_{15}/0.5\text{P-}\text{SiO}_2$ (1 wt.% Rh)**	Fresh	0.89	44.3	
10	$\text{Rh}_{17}\text{S}_{15}/0.5\text{P-}\text{SiO}_2$ (1 wt.% Rh)**	Recovered	0.85	43.4	

Reaction conditions: styrene (1 mmol), toluene (1.5 mL), catalyst (0.2 mol%, Rh basis), 40 bar syngas pressure, CO:H₂ 1:1, 80°C, 2 h, 1200 rpm stirring speed.

* 18 % Conversion of styrene to aldehydes with a n/iso ratio of 0.62 was obtained under the applied conditions.

** 10 % conversion of styrene to aldehydes with a n/iso ratio of 0.71 has estimated

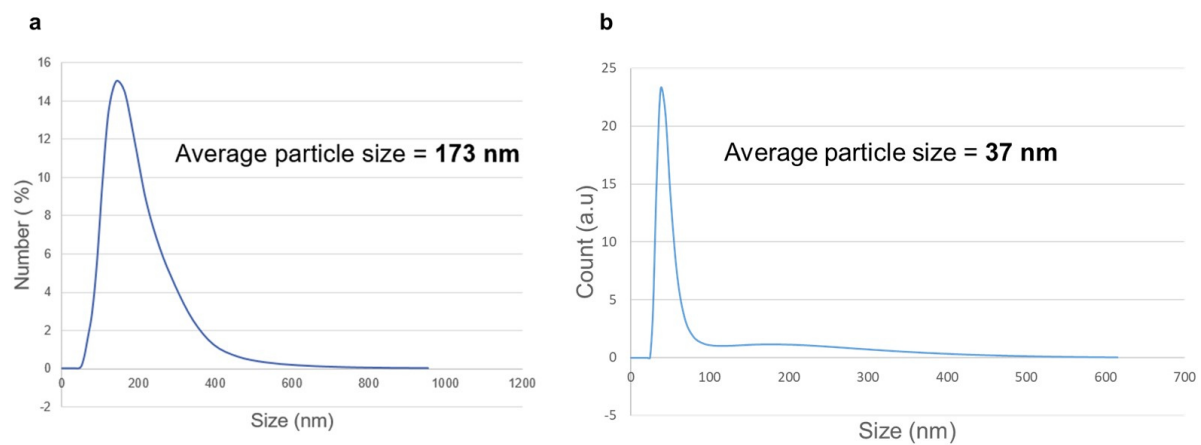


Figure S43: Results of the DLS measurement performed with the a) supernatant liquid after the centrifugation of reaction mixture with solid rhodium sulfide catalyst and b) after filtration with syringe filter (200 nm), celite bed followed by centrifugation. All results indicating the formation of rhodium sulfide colloid after the hydroformylation reaction.

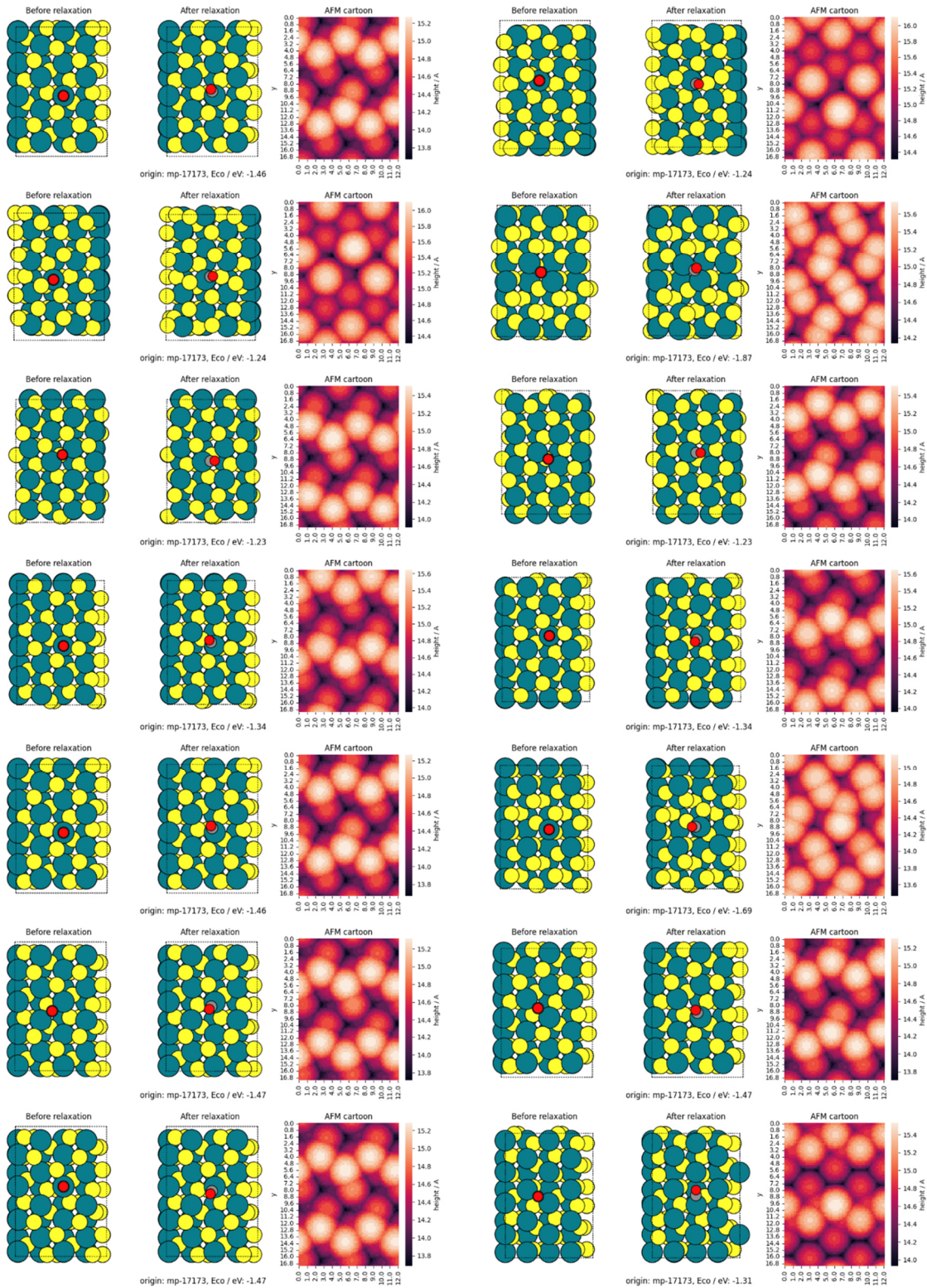


Figure S44: Part 1/2 illustration of CO adsorption on possible sites of Rh₂S₃ (mp-17173) with estimated binding energies (Rh: blue, S: yellow, C: grey, O: red) and AFM cartoon showing the surface. This figure has been adapted from reference^[255] (license CC BY 4.0).

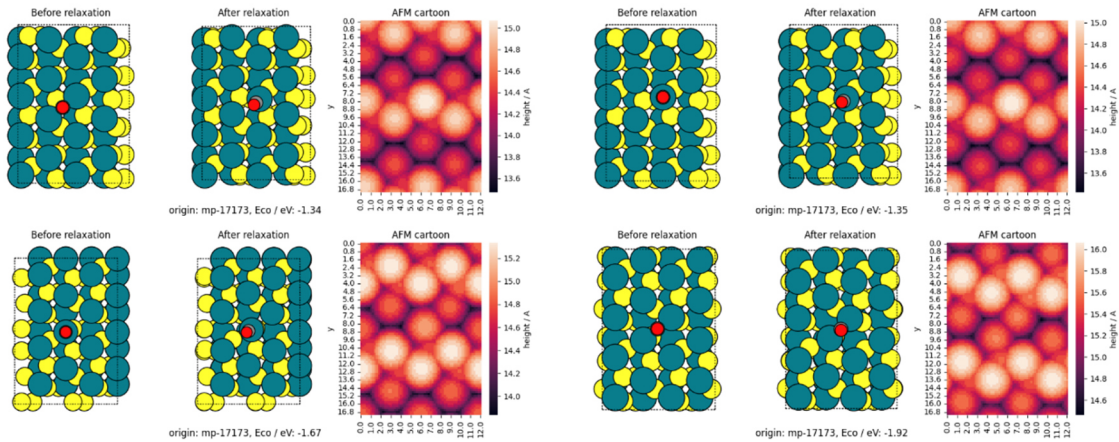


Figure S45: Part 2/2 illustration of CO adsorption on possible sites of Rh₂S₃ (mp-17173) with estimated binding energies (Rh: blue, S: yellow, C: grey, O: red) and AFM cartoon showing the surface. This figure has been adapted from reference^[255] (license CC BY 4.0).

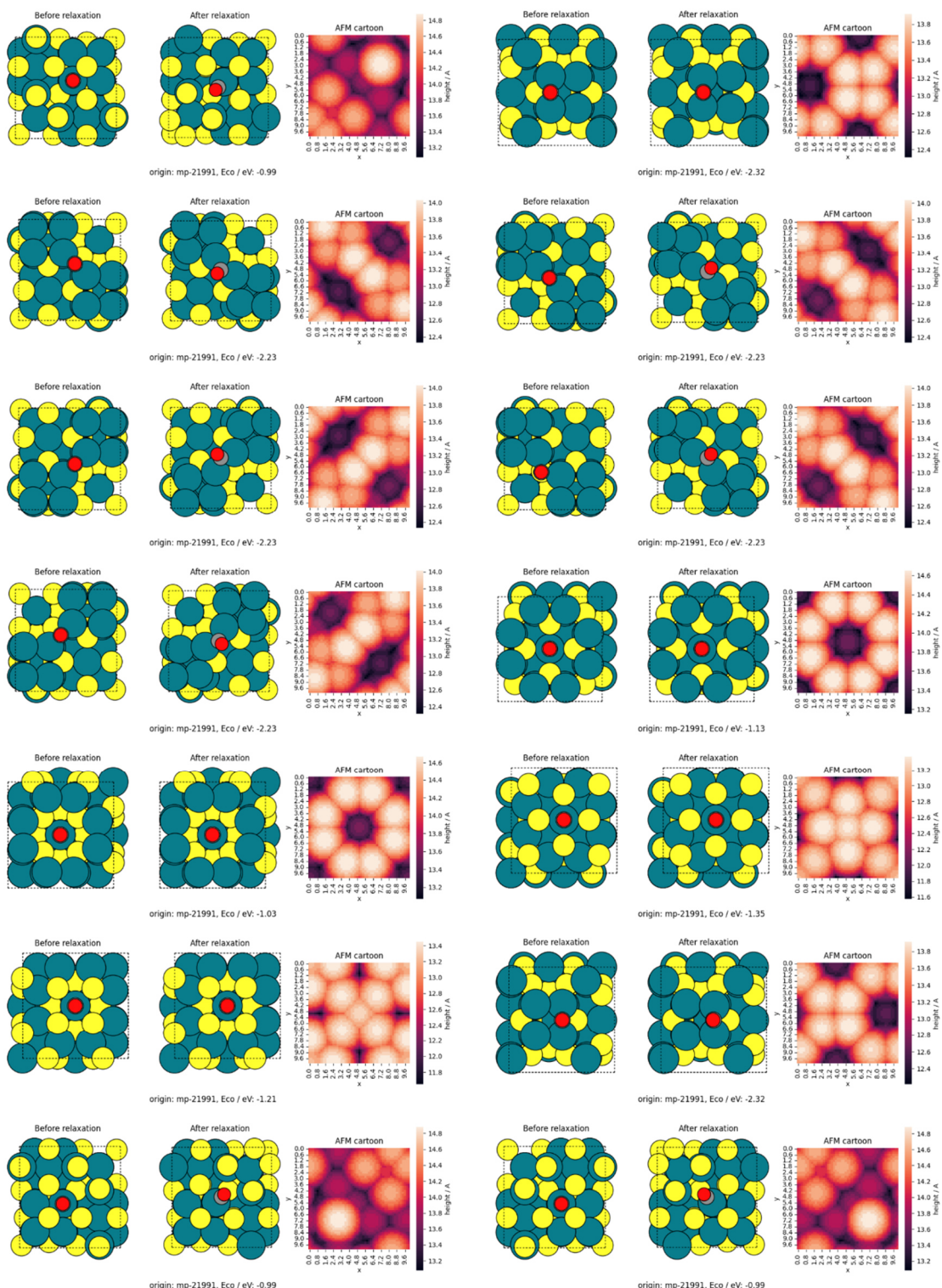


Figure S46: Part 1/3 illustration of CO adsorption on possible sites of Rh₁₇S₁₅ (mp-21991) with estimated binding energies (Rh: blue, S: yellow, C: grey, O: red) and AFM cartoon showing the surface. This figure has been adapted from reference^[255] (license CC BY 4.0).

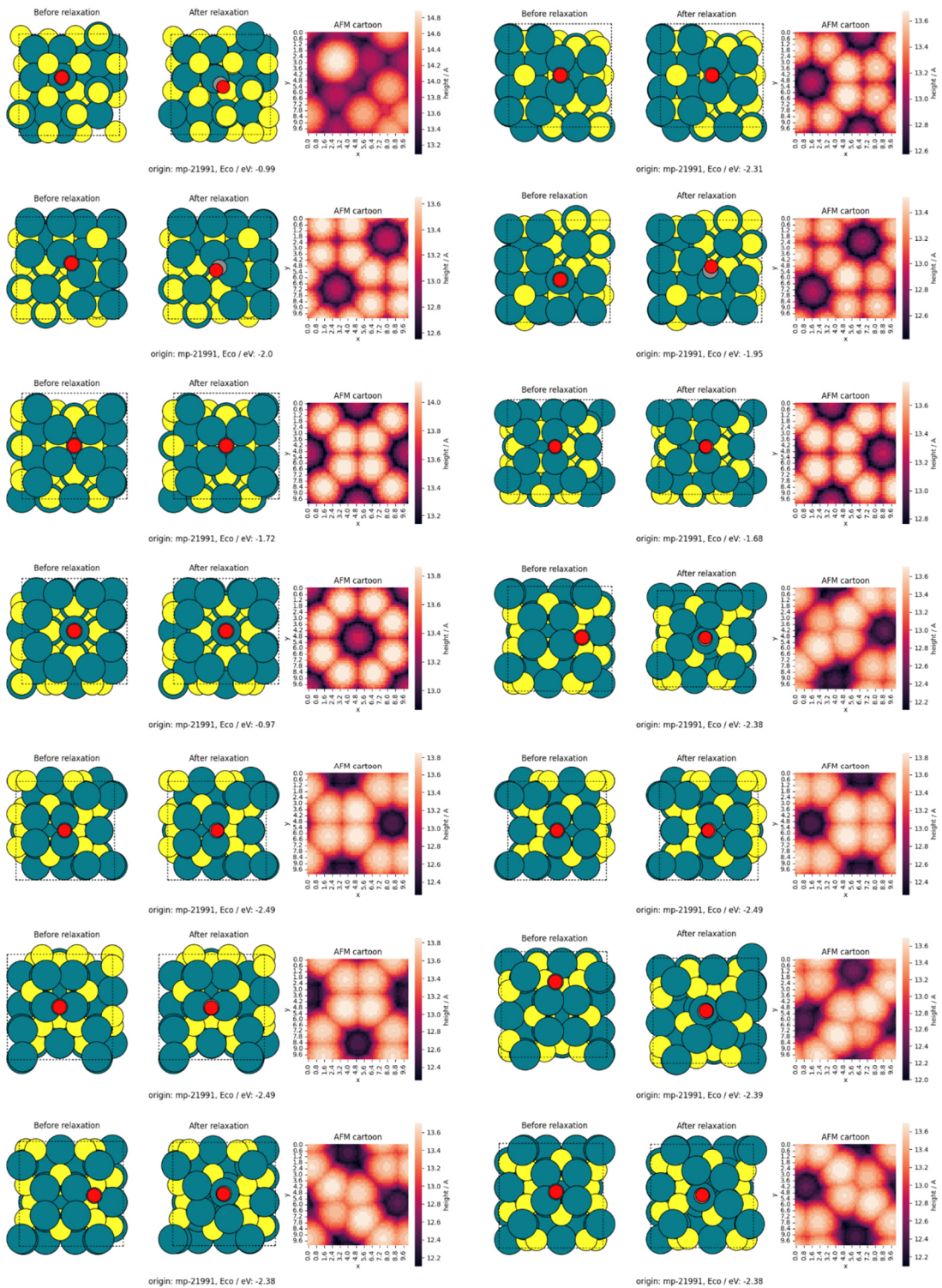


Figure S47: Part 2/3 illustration of CO adsorption on possible sites of $\text{Rh}_{17}\text{S}_{15}$ (mp-21991) with estimated binding energies (Rh: blue, S: yellow, C: grey, O: red) and AFM cartoon showing the surface. This figure has been adapted from reference^[255] (license CC BY 4.0).

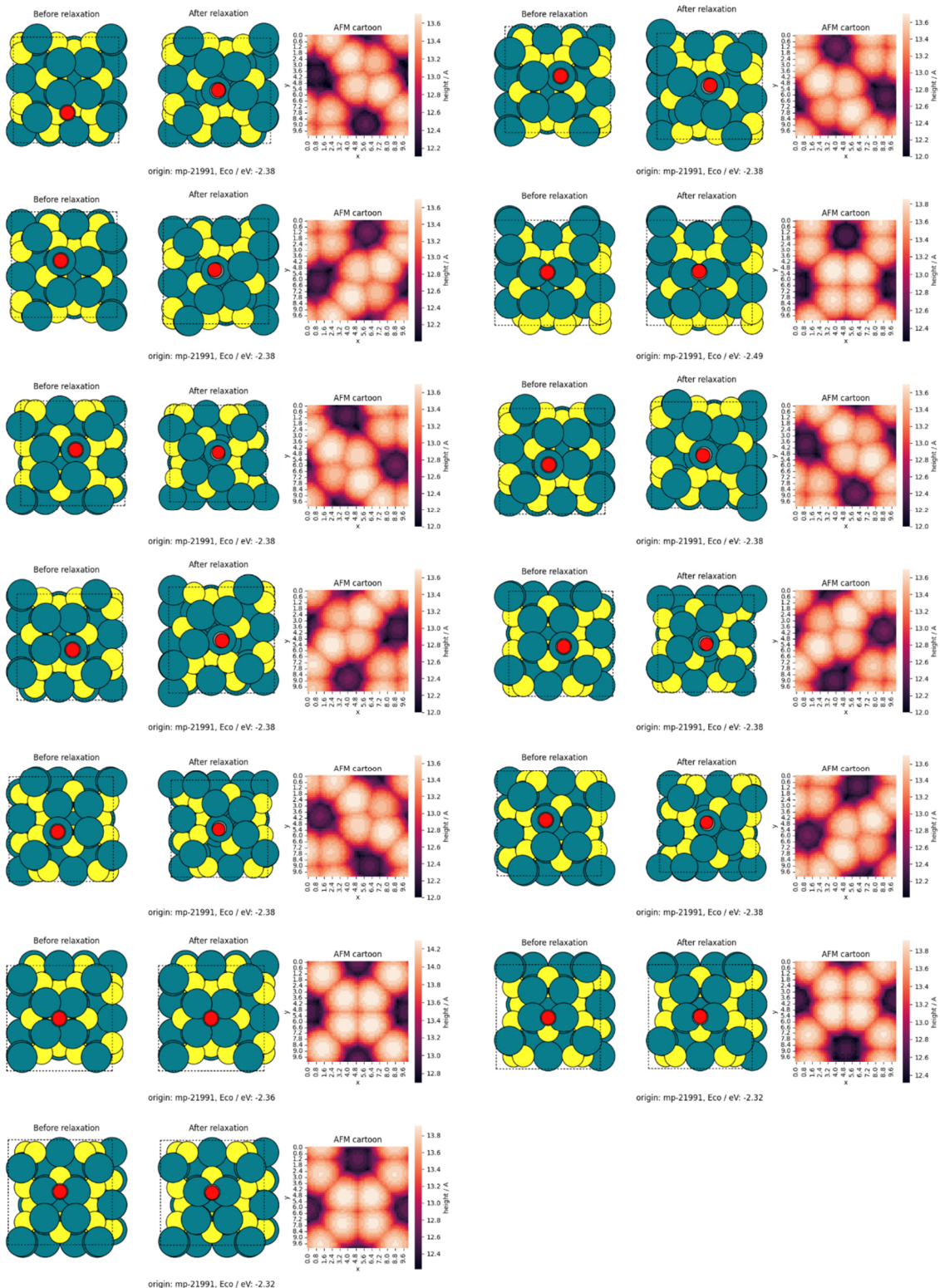


Figure S48: Part 3/3 illustration of CO adsorption on possible sites of Rh₁₇S₁₅ (mp-21991) with estimated binding energies (Rh: blue, S: yellow, C: grey, O: red) and AFM cartoon showing the surface. This figure has been adapted from reference^[255] (license CC BY 4.0).

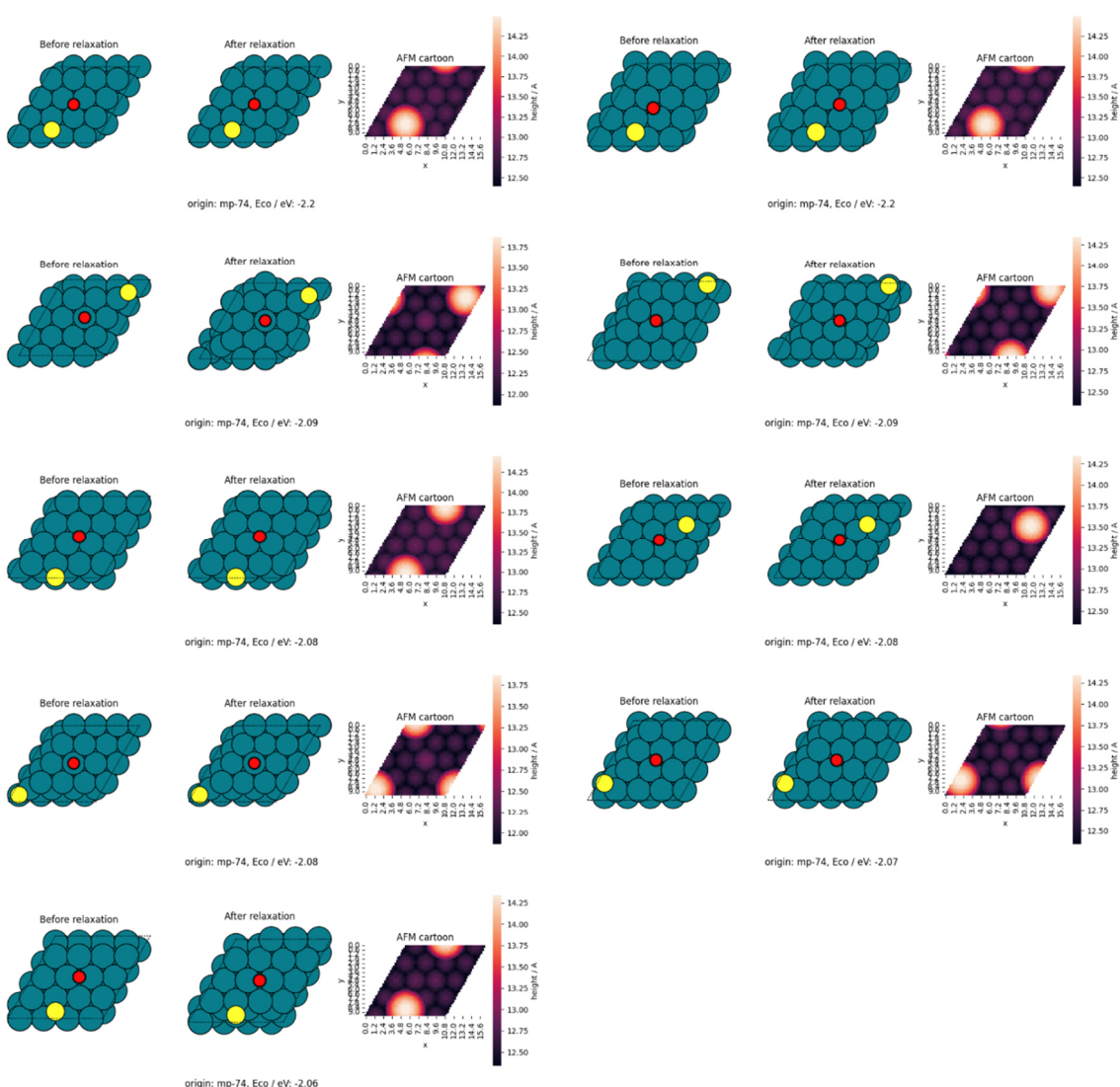


Figure S49: Illustration of CO adsorption on possible sites of S doped Rh (mp-74) with estimated binding energies (Rh: blue, S: yellow, C: grey, O: red) and AFM cartoon showing the surface. This figure has been adapted from reference^[255] (license CC BY 4.0).

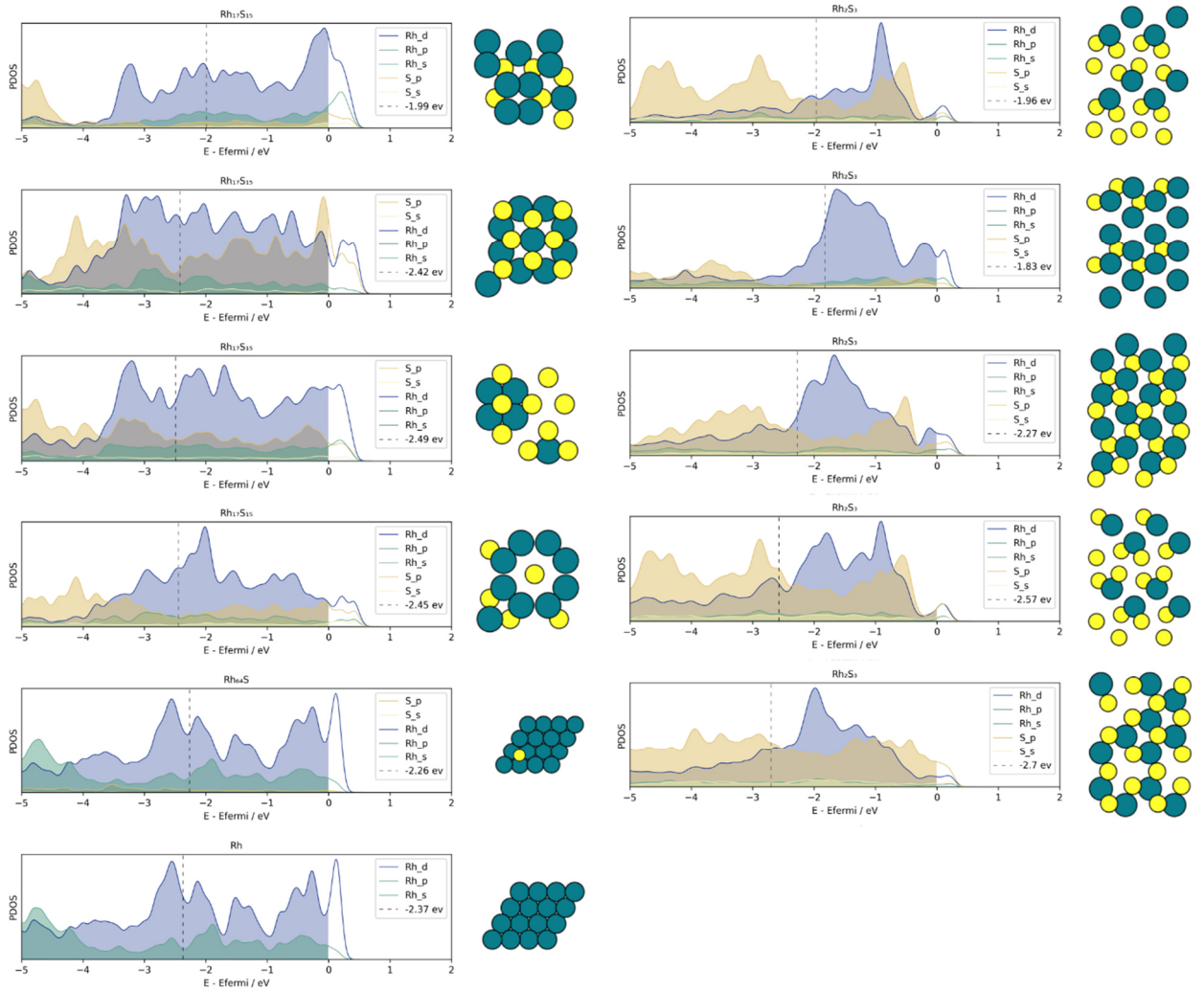


Figure S50: Projected density of states (PDOS) for all surface atoms of the investigated catalytic surface terminations are shown alongside each structure. The dark blue shaded regions highlight the d band population of the surface Rh atoms and the d band centre is represented as dark dotted lines. Calculations were performed considering (100) Rh₁₇S₁₅ (mp-21 991), (001) Rh₂S₃ (mp-17 173), and S-doped (111) Rh (mp-74) surfaces. This figure has been adapted from reference^[255] (license CC BY 4.0).

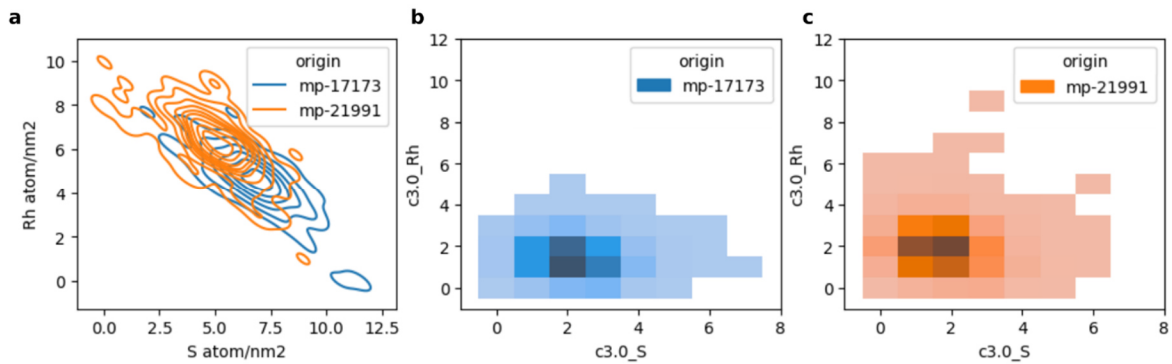


Figure S51: Surface compositions of all enumerated slabs of Rh₁₇S₁₅ (mp-21991) and Rh₂S₃ (mp-17173) up to Miller index 3 are shown as a) representation of the local compositions defined as all neighboring atoms within a 3 Å cut-off radius from the generated adsorption site are presented for (b) Rh₂S₃ and (c) Rh₁₇S₁₅. This figure has been adapted from reference^[255] (license CC BY 4.0).

11 Abbreviations

BOX	Bisoxazoline
BINAP	2,2'-Bis(diphenylphosphino)-1,1'-binaphthyl
CNT	Carbon nanotube
dba	dibenzalacetone
DBT	Dibenzothiophene
DFT	Density functional theory
DIBPP	1,3-bis(diisobutylphosphino)propane
dppe	1,2-bis(diphenylphosphino)ethane
dppf	1,1'-bis(diphenylphosphino)ferrocene
dppp	1,3-bis(diphenylphosphino)propane
DRIFTS	Diffuse reflectance infrared spectroscopy
DTA	Differential Thermal Analysis
EDXS	Energy dispersive X-ray spectroscopy
EXAFS	Extended X-ray absorption fine structure
FCC	Face centred cubic
GC	Gas chromatography
HAADF	High angle annular dark field
HDS	Hydrodesulfurization
HER	Hydrogen evolution reaction
HRTEM	High resolution transmission electron microscopy
ICSD	Inorganic crystal structure database
ImmPd	immobilized palladium
KAP	Knitting aryl network polymers
MeCN	Acetonitrile
ML	Machine learning
MOF	Metal organic framework
MS	Mass spectrometry
NMP	<i>N</i> -Methylpyrrolidone
PDOS	Projected density of states
PEG	Polyethylene glycolate
PK	Polyketone
POP	Porous organic polymer
PTA	Phosphotungstic acid
PXRD	Powder X-ray diffraction

SAED	Selected area electron diffraction
SCF	Self consistent field
SEM	Scanning electron microscopy
SILP	Supported ionic liquid phase
SOAP	Smooth overlap of atomic positions
STEM	Scanning transmission electron microscopy
TEM	Transmission electron microscopy
TFA	Trifluoroacetate
TGA	Thermogravimetric analysis
TOF	Turn over frequency
TON	Turn over number
TPPTS	Phosphanetriyltris(benzenesulfonic acid) trisodium salt
t-SNE	t-distributed stochastic neighbor embedding
XANES	X-ray absorption near edge structure
XAS	X-ray absorption spectroscopy
XPS	X-ray photoelectron spectroscopy

12 Personal data

12.1 Curriculum vitae

Name	Arjun Neyyathala
Date of birth	14.04.1992
Place of birth	Kerala, India
Marital status	Single
Gender	Male
Nationality	Indian
Education	
12/2021 - Present	Ph.D. studies in chemistry Karlsruhe Institute of Technology (KIT) Institute for Inorganic Chemistry in the group of TT.-Prof. Dr. S. Hanf
10/2018 - 10/2021	M.Sc. in chemical and energy engineering from Otto von Guericke University Magdeburg (OvGU), Magdeburg
06/2009 - 03/2013	B. Tech in chemical engineering from Govt. Engineering College, Thrissur
01/2007 - 03/2009	Higher secondary education, H.S.S. Sreekrishnapuram
Work Experience	
06/2013 - 09/2018	Consultant (chemical engineer), KITCO Ltd.
Awards and recognitions	
2021	DAAD scholarship
2013	Calicut university B.Tech 4 th rank

12.2 Attended conferences

- Europacat 2023, Prague:
Poster presentation (Palladium Phosphide Catalysts for the Wacker-Tsuji-Oxidation of Alkenes: A. Neyyathala, F. Flecken, S. Hanf)
- Jahrestreffen Deutscher Katalytiker 2024, Weimar:
Flash talk (Pd₃P as versatile heterogeneous catalysts for oxidation and C–C bond formation reactions: A. Neyyathala, F. Flecken, F. Rang, C. Papke, S. Hanf)
Poster (Pd₃P as versatile heterogeneous catalysts for oxidation and C–C bond formation reactions: A. Neyyathala, F. Flecken, F. Rang, C. Papke, S. Hanf)
Poster (Bridging homogeneous and heterogeneous catalysis through a d-block/p-block combination strategy: a theoretical investigation: A. Neyyathala, E. Fako, S. De, S. A. Schunk, S. Hanf).
- Jahrestreffen Deutscher Katalytiker 2025, Weimar:
Talk (Boosting carbonylation chemistry through tunable active sites via d-block metal-p-block element synergy: A. Neyyathala, E. Fako, S. De, S. A. Schunk, S. Hanf)

12.3 List of publications and patents

Peer-reviewed articles

- A supported Palladium Phosphide Catalyst for the Wacker-Tsuji-Oxidation of Styrene, A. Neyyathala, ^[+] F. Flecken, ^[+] S. Hanf, *ChemplusChem*, **2023**, 88, e202200431. ^[+]Both authors contributed equally.
- Support Engineering for the Stabilisation of Heterogeneous Pd₃P-Based Catalysts for Heck Coupling Reactions, A. Neyyathala, ^[+] F. Flecken, ^[+] F. Rang, C. Papke, S. Hanf, *Chem. Eur. J.*, **2024**, 30, e202402825. ^[+]Both authors contributed equally.
- From Poison to Promotor: Spatially Isolated Metal Sites in Supported Rhodium Sulfides as Hydroformylation Catalysts, A. Neyyathala, E. Fako, S. De, D. Gashnikova, F. Maurer, J.-D. Grunwaldt, S. A. Schunk, S. Hanf, *Small Struct.* **2025**, 6, 2400260.
- Generating knowledge graphs through text mining of catalysis research related literature, A. S. Behr, D. Chernenko, D. Koßmann, A. Neyyathala, S. Hanf, S. A. Schunk, N. Kockmann, *Catal. Sci. Technol.*, **2024**, 14, 5699-5713.
- A Bench-stable Fluorophosphine Nickel (0) Complex and Its Catalytic Application, F. Flecken, A. Neyyathala, T. Grell, S. Hanf, *Angew. Chem. Int. Ed.*, **2025**, e202510369.

Pre-print

- A. Neyyathala, F. Jung, C. Feldmann, S.A. Schunk, S. Hanf, *ChemRxiv* **2025**, DOI: 10.26434/chemrxiv-2025-46zsr.

Patent applications

- Patent application 230651EP01, Rhodium Sulfides as Hydroformylation Catalysts, BASF SE and KIT, 08.12.2023.
- Patent application EP25161927, Process for performing alkoxy carbonylation reactions, BASF SE and KIT, 05.03.2025.

13 Acknowledgements

Firstly, I would like to thank JProf. Dr. Schirin Hanf for supervising my thesis. Thank you so much for this opportunity, your support, energy, motivation, wisdom, great leadership and everything. It is always great working with you. There is lot more to say, may be words are not enough.

I also would like to sincerely acknowledge Prof. Dr. Jan-Dierk Grunwaldt for acting as the co-referee of my thesis and his continuous support during my research work.

Thank you Prof. Dr. Stephan Schunk for your continuous support and guidance throughout my work.

I hereby also acknowledge BASF for partially funding the projects and hte GmbH for the guidance and supports.

I also would like to thank Prof. Dr. Claus Feldmann, Prof. Dr. Peter Roesky, Prof. Dr. Annie K. Powell, Dr. Alexander Hinz and Dr. Silke Wolf for your supports during my work in terms of facilities and advices.

I would like to acknowledge Dr. Sandip De and Dr. Edvin Fako for the calculations performed and technical discussions.

My family, team Hanf (Hanfsomes), thank you and love you all, Franzi...buddy, thanks for everything, friendship and collaboration. Fabi, Ria, Pascal, Christina, Ankit, Lena, Sven, Lorena, thank you guys for all your supports. I can't even think of a journey without you people. Once again, "this is 17 Hanf to the team, thank you very much". This team means a lot to me. It is a "family (net) thing".

I would like to thank Felix Jung, Daria, Simon Barth, Florian, Marc, David Rudolf for performing and helping to perform measurements.

Team AK Feldmann, thank you all for your supports for helping for the measurments and technical discussions.

Team AK Roesky thank you for all your supports.

Lucas, Tom and Francesca thank you mates for all our time together.

Anette Baust and Isabella Vogelbacher, thanks for the organizational supports.

Thanks to

The students I supervised during this time.

Gabi Leichle and Lena for the chemicals and gas bottles.

The team workshop for all your support.

Bernhard, Melina, Perrine,

“Single Malt Members”, “Vishu Family”, “WG Hollis”

My dear neighbours and friends Chelsea, Anton, Zaid.

Acha and Amma, thank you so much. I know it is hard for you that I am far away. Your blessings are with me always. I want to tell you, that you both are the greatest thing happened in my life.

I love you.

Megha, thank you for being with me and all your supports.

Thanks to all...who supported me in this journey.